Development of an optical setup for measuring heat diffusivity in bi-dimensional systems

Joan Younes

N°d'ordre NNT : 2021LYSEI078

THESE de DOCTORAT DE L'UNIVERSITE DE LYON
opérée au sein de
INSA LYON

Ecole Doctorale EDA34
Matériaux de Lyon

Spécialité/ discipline de doctorat :

Matériaux

Soutenue publiquement le 26/11/2021, par :
Joan Younes

Development of an optical setup for measuring heat diffusivity in bi-dimensional systems

Devant le jury composé de :

TABBAL, Malek,	Professeur	AUB	Président
BRUYANT, Aurélien	Maître de conférences HDR	UTT	Rapporteur
NAJEM, Sara	Assistant Professor	AUB	Rapporteure
GOMES, Séverine	Directrice de recherche	INSA-LYON	Examinatrice
TABBAL, Malek	Professeur	AUB	Examinateur
FABRÈGUE, Damien	Professeur des Universités	INSA-LYON	Directeur de thèse
SOUEIDAN, Maher	Directeur de recherche	UL	co-Directeur de thèse
KAZAN, Michel	Associate Professor	AUB	Invité
ZAATAR, Youssef	Associate Professeur	UL	Invité

To my wife who inspired me every single day with her determination and passion for life…

Acknowledgements

I would like to extend my appreciation and deepest gratitude for the professional and unlimited support of Prof. Michel Kazan and for his dedication and guidance throughout my PhD. This work would not have been possible without his continuous help and availability.

I would like to thank my thesis director Prof. Damien Fabrègue, my co-director Prof. Youssef Zaatar, and my Supervisor Prof. Maher Soueidan for their help and support, their insightful comments and criticism, and for setting the boundaries for this Thesis.

I present my acknowledgement to the American University of Beirut management and staff, particularly at the physics department, especially Mr. Sahag Bozoian and Dr. Sobhi Hamyeh for their support, and to the INSA-LYON staff as well in different departments for their continuous support.

I would like to recognize the Thesis Jury for their time and consideration and their constructive comments.

A special gratitude goes to my wife and kids for their unconditional moral support and understanding, their enthusiasm and encouragement despite the hard times they went through.

Finally, I am thankful to my Lord for his unlimited blessings throughout my life.

Table of Contents

Abstract

Semiconductors are essential to all technology fields. The continuous need for higher speeds and higher power semiconductors, coupled with the continuous miniaturization trend has led to the necessity of proper thermal management in semiconductors, to minimize component failure.

Thermal characterization tools are essential for proper thermal management and component design. This Thesis is dedicated to describing a developed non-contact photothermal beam deflection technique, employing a mid-IR laser as a modulated pump beam, and a visible laser as a probe beam. The modulated Laser beam creates a temperature gradient on both sides of the sample's surface, causing a deflection of the probe beam which is synchronized with the modulation of the pump beam. A position sensitive detector allows the measurement of the probe beam deflection through synchronous lock-in amplification.

For a given modulation frequency, the offset distance between the probe and heating beam is varied, and the deflection components (Transverse and longitudinal deflections) are recorded through a home-made software. Measurements are repeated for different frequencies and data are fitted to theoretical mathematical models to retrieve the thermal diffusivity of the measured sample.

Using a mid-IR heating laser has given the technique developed in this thesis unique features, such as the ability to measure most types of samples without the need of any metal layer on the sample's surface, as is the case with other non-contact thermal characterization techniques.

The Technique was validated successfully on different samples with known thermal diffusivities. Another unique feature is the ability of this technique to perform subsurface imaging and subsurface profiling. This feature was used to successfully image subsurface defects.

Two other applications were also investigated to prove the power of this technique:

- Measurement of in-plane and cross-plane thermal diffusivities for a set of samples.
- Measurement thermal transport by surface modes in ultra-thin layers (down to 3nm in thickness).

Résumé

Les semi-conducteurs sont essentiels à tous les domaines de technologie. Le besoin continuel pour des semi-conducteurs plus rapides et plus puissants, associé à la tendance à la miniaturisation, a conduit à la nécessité d'une gestion thermique efficace des semi-conducteurs, afin de minimiser les défauts des composants.

Les outils de caractérisation thermique sont essentiels pour une bonne gestion thermique et pour la conception des différents composants. Cette thèse est consacrée à la description d'une technique photo-thermique de déviation de faisceau (sans contact), basée sur l'effet mirage, utilisant un laser moyen IR comme faisceau de pompe de chauffage modulé, et un laser visible comme faisceau de sonde rasant la surface de l'échantillon.

Le faisceau laser modulé crée un gradient de température dans l'air au voisinage de la surface de l'échantillon, provoquant ainsi une déviation du faisceau de sonde. Cette déviation est synchronisée avec la modulation du faisceau de pompe. Un détecteur de position permet de mesurer la déviation du faisceau de sonde grâce à une amplification synchrone à verrouillage.

Pour une fréquence de modulation donnée, la distance pompe-sonde est variée et les composantes de la déflexion (déflexions transversale et longitudinale) du faisceau de sonde, sont enregistrées en fonction de la distance de décalage des deux faisceau pompe-sonde.

Les mesures sont répétées pour différentes fréquences. Un logiciel spécialisé permet d'adapter les données à des modèles mathématiques théoriques et d'obtenir ainsi le paramètre de diffusivité thermique de l'échantillon.

L'utilisation du laser infrarouge a donné à cette technique des caractéristiques uniques, telles que la capacité à mesurer la plupart des types d'échantillons, sans qu'il soit nécessaire de prendre des mesures spéciales ou de déposer une couche métallique sur la surface de l'échantillon, comme c'est le cas avec d'autres techniques de caractérisation thermique sans contact.

La technique a été validée avec succès sur différents échantillons présentant des diffusivités thermiques connues. Une autre caractéristique unique est la capacité de cette technique à réaliser une imagerie et un profil de la sous-surface. Cette caractéristique a été utilisée pour imager avec succès des défauts de sous-surface.

Deux autres applications ont également été étudiées pour illustrer la capacité de cette technique:

- Mesure de diffusivités thermiques dans le plan et en travers du plan pour un ensemble d'échantillons (in-plane and cross-plane thermal diffusivity).

- Mesure de la diffusivité thermique pour des couches ultra-minces (jusqu'à 3 nm d'épaisseur), permettant également d'identifier une autre caractéristique pour cette technique: la génération d'ondes de surface qui augmentent considérablement la diffusivité thermique du matériau.

Introduction

Semiconductors have become an essential aspect of our lives since the invention of the transistor in 1948. They can be found in all sorts of electronic devices: computers, mobile phones, vehicles, trains, aircraft, bank cards, television sets, etc.

Semiconductors manufacturing and optimization are in continuous progress with the need for higher power devices, faster multi-cores CPUs, greater performance GPUs, complicated ASICs, etc.

Also, the constant miniaturization trend of semiconductor chips, was Accentuated during the past 10 years, especially with the prevalence of internet and wireless devices, 4G and 5G enabled mobile phones and networks, and the newly emerging internet of things (IOT), and connected devices, etc. In fact, CPUs are being manufactured with billions of transistors in each chip, with a size of 7nm for each transistor, operating at clock speeds of several GHz.

Efficient thermal management strategy is a key step toward a better performance of semiconductor-based electronics described above. The primary goal of thermal management is to evacuate heat generated by microchips via external heat diffusion channels with the highest possible conductivity. The success of thermal management materials has a significant impact on the lifetime and reliability of electronic components. Nevertheless, proper thermal managements requires the measurement of the thermal transport characteristics of thin films and understanding of the laws governing heat flow at a small scale.

Nowadays, many thermal characterization techniques are available. Some of them are contact methods, which lead to considerable errors. Other methods are non-contact techniques, such as thermo-reflectance, opto-thermal Raman and photothermal beam deflection techniques. However, most of these techniques are either restricted to certain types of samples, limited to bulk sample characterization only, used for specially suspended 2D materials, or require special sample handling, such as the deposition of metal layers on the sample surface, which limits their versatility. This lack of a "universal" or "near universal" technique was the main motivation for this work.

Among the non-contact thermal characterization techniques, the photothermal beam deflection technique (also known as the mirage effect) has been successfully used to measure the thermal diffusivity of bulk materials and later of thin films. The mirage effect, or the deflection of light beams caused by thermal gradients in the refractive index of air, has been known since antiquity. It began with the Greek historian Diodorus Siculus and has been reported in several publications and research works. It was also mentioned in ancient China

and Japan, as well as in the tale of Northern. In contemporary times, the mirage has been detailed in Wood's famous textbook.

Gaspard Monge (1746-1818), the designer of descriptive geometry and founder of the École Polytechnique in France, was the first to scientifically describe the phenomenon of mirage. While in Egypt following Napoleon, he noticed the phenomenon and detailed it in an article: During a walk from Alexandria to Cairo, he noticed what appeared to be lakes in the distance. He also saw an inverted reflection of distant villages. He explained the phenomenon by stating that the light beams were distorted by the superheated layer of air directly above the sand. The heat radiated from the desert surface warms the air directly above it and decreases its density. There is a separating layer between the hottest and coldest layers, which acts as a lens and deflects or refracts light rays from the sky to the coldest layer. The greater the temperature difference, the greater the impact of the mirage. He introduced the French expression "se mirer" (to look at oneself), and "Mirage" is its English translation [1].

Two groups discussed almost simultaneously the new method of measuring the temperature rise of a material irradiated by a modulated light beam using the mirage effect. Fournier et al. revealed the concepts of the method at the Topical Meeting on Photoacoustic Spectroscopy in Ames. Later, they published an extended version in Applied Physics Letters [2]. Murphy and Aamodt [3] detailed the same procedure and cite Fournier's paper in a study published in the Journal of Applied Physics. Boccara et al [4] developed a technique to calculate the absorption coefficient of the sample from the thermal gradient in the air layer near the sample surface. In this approach, the periodic heat created by a modulated pump laser beam on the sample causes a refractive index gradient of the medium above, which periodically deflects a probe beam passing over the solid surface (the mirage effect).

Available photothermal beam deflection techniques, as well as other techniques, are not capable of measuring certain types of samples (polar, transparent samples, etc.). This gap in available techniques motivated us to venture into the development of a new versatile optical configuration for thermal diffusivity measurement that would allow the measurement of a wide range of samples (including bulk samples, thin films, etc.) without the need for special sample preparation or deposition of layers.

This thesis describes the work done to develop a mid-infrared photothermal beam deflection technique, a non-contact thermal characterization technique that allowed us to measure the thermal diffusivity of various materials. We used a mid-infrared heating beam, which differentiates our approach from available photothermal beam deflection techniques that normally use a pumping beam in the visible region.

Using a mid-infrared pump laser improves accuracy and makes the approach suitable for a wider range of materials, since the vast majority of materials are opaque in the mid-infrared spectral region due to vibrational resonances. Furthermore, a mid-infrared laser promotes greater interaction with the vibrational modes of the atoms, inducing more heating in the sample, and allowing higher modulation frequencies to be achieved for the pump beam, when thin films need to be measured.

The developed technique offers a unique capability for immediate and sensitive detection of defects buried at great depths below the measured surface. Unlike previous photothermal beam deflection studies, which most often require the deposition of a metal layer to generate a heating point and thermal waves on the surface of an optically thin material, the proposed methodology can induce periodic heating on the surface without the deposition of an absorbing metal layer since most materials in the mid-infrared spectral region are optically thick.

In addition, the complex mid-infrared dielectric function is particularly sensitive to defects. Therefore, the suggested methodology is suitable for highly sensitive and direct detection of subsurface defects. We have successfully applied the proposed technique to measure the thermal diffusivities of extremely transparent and highly reflective materials easily and without any deposition. Another unprecedented feature is the simultaneous ability of this technique to perform subsurface imaging and profiling, and this has been applied for subsurface defect detection and imaging.

This manuscript consists of five chapters, organized as follows:

- The first chapter presents the theoretical background and relevant optical and physical concepts.

- The second chapter introduces common non-contact thermal characterization techniques: thermoreflectance, opto-thermal Raman, and the photothermal beam deflection technique (Mirage effect), laying the groundwork for our own mid-infrared photothermal beam deflection technique (conveniently called IR-PBD). Section 2.3 of the second chapter describes the theory and mathematical model of this technique.

- The third chapter builds on Section 2.3 and presents our own implementation of IR-PBD. Verification of the technique for measuring thermal diffusivity for different samples was done for silicon (Si) substrate, polycrystalline quartz (α-SiO2) and sintered aluminum nitride (AlN) substrates. Another major development we describe is the unique subsurface imaging

capability of the proposed technique, whereby we imaged subsurface structural defects and damage generated by H+ ion bombardment at about 62 µm below the surface of a 4H-SiC substrate. (The results highlighted in this chapter are published in a peer-reviewed journal (J. Younes et al., 2020) [5]).

- The fourth chapter also discusses another application of the developed IR-PBD: the measurement of in-plane and cross-plane thermal diffusivities for four samples bombarded with proton ions with different irradiation doses. This chapter also highlights the ability of the developed technique to measure anisotropic thermal diffusivities.

- The fifth chapter describes another application of the developed IR-PBD: the measurement of in-plane thermal diffusivity by surface electromagnetic mode in quasi two-dimensional thin films.

- A conclusion at the end summarizes the thesis work and presents future perspectives.

1 Optical Theory and Physics for Semiconductor Characterization

1.1 Motivation

In this chapter, we provide an overview of the physics of elementary excitations in semiconductors, which is crucial to understand the functionality and applications of the technique developed in this thesis. We describe the interaction of light with semiconductors and discuss the physics of the elementary excitations that determine the response of the material under examination in each spectral range. We formulate the response function on the basis of classical physics to clearly present the main phenomena resulting from the light-matter interaction to a wide audience.

1.2 Electromagnetic waves in free space

Before discussing the optical properties of semiconductors, it would be instructive to review the fundamental properties of electromagnetic waves. The relatively simple behavior of these waves in free space underlies their much more complex interaction with solids. It will be shown how to relate the electromagnetic behavior of a semiconductor to quantities characteristic of the microscopic nature of the solid, such as the dielectric function $\varepsilon(\omega)$ and the frequency dependent absorption coefficient $\alpha(\omega)$. These can then be related to reflectance, transmittance, and absorbance, which are key properties for photothermal measurements.

Maxwell's equations describe the fundamental electromagnetic behavior. In free space, their solutions describe undamped transverse waves consisting of electric and magnetic fields oscillating perpendicularly and propagating at the fixed speed of light. However, the electromagnetic field interacts with the constituent charges of a solid to produce new phenomena that do not exist in space: the waves are damped when they transmit energy to the solid, the speed of propagation depends on the frequency and longitudinal electromagnetic waves can appear.

In this chapter, Maxwell's equations in free space are presented before focusing on their solutions in solids, which require the constitutive equations. These relate current and charge to the electric field, thus defining the physics

of the light-matter interaction. With the exception of magnetic effects, the presentation is general. After this discussion, expressions for reflectivity, transmission and absorption coefficient are provided.

In SI units, Maxwell's equations are as follows:

$$\nabla \times \boldsymbol{H} = \boldsymbol{j} + \frac{\partial \boldsymbol{D}}{\partial t}$$
$$\nabla \times \boldsymbol{E} = -\frac{\partial \boldsymbol{B}}{\partial t} \qquad \textit{Eq. 1.1}$$
$$\nabla \cdot \boldsymbol{D} = \rho$$
$$\nabla \cdot \boldsymbol{B} = 0$$

where **H** is magnetic field strength, **j** is current density, **D** is the displacement vector, **E** is the electric field, **B** is magnetic induction, ρ is the free carrier charge density, t is time, and ∇ is the vector gradient operator, which in cartesian coordinates is $\hat{\boldsymbol{\imath}}\frac{\partial}{\partial x} + \hat{\boldsymbol{\jmath}}\frac{\partial}{\partial y} + \hat{\boldsymbol{k}}\frac{\partial}{\partial z}$.

These equations are written in a solvable form when relations between **D** and **E**, and **B** and **H**, are known. The basic definitions are of the fields in these equations are presented below:

$$\boldsymbol{D} = \boldsymbol{\varepsilon_0 E} + \boldsymbol{P} = \boldsymbol{\varepsilon \varepsilon_0 E} \qquad \textit{Eq. 1.2}$$
$$\boldsymbol{B} = \mu_0 \boldsymbol{H} + \boldsymbol{M} = \mu \mu_0 \boldsymbol{B} \qquad \textit{Eq. 1.3}$$

where $\boldsymbol{\varepsilon_0}$ is the permittivity of free space ($\boldsymbol{8.85 \times 10^{-2}\, C^2\, N^{-1}\, m^{-2}}$), **P** is electric dipole per unit volume, $\boldsymbol{\mu_0}$ is the permeability of free space ($\boldsymbol{4\pi \times 10^{-7} Ns^2 C^{-2}}$), **M** is magnetic dipole per unit volume, **ε** is the electrical permittivity of a medium other than the vacuum, and **μ** is the magnetic permeability of a medium other than vacuum.

These formal constitutive equations can only be written in detail if the details of the medium are known.

In the most elementary medium, vacuum (or free space), in which there is no free charge density or current flow, j = 0 and ρ= 0. Because there is no electrostatic or magnetic polarization, the constitutive equations written as:

$$\boldsymbol{D} = \boldsymbol{\varepsilon_0 E} \qquad \textit{Eq. 1.4}$$
$$\boldsymbol{B} = \mu_0 \boldsymbol{H} \qquad \textit{Eq. 1.5}$$

Upon using the expressions of **D** and **B** in equations ***Eq. 1.1***, we obtain

$$\nabla^2 \boldsymbol{E} = \varepsilon_0 \mu_0 \frac{\partial^2 \boldsymbol{E}}{\partial t^2} \qquad \textit{Eq. 1.6}$$

$$\nabla^2 \boldsymbol{B} = \varepsilon_0 \mu_0 \frac{\partial^2 \boldsymbol{B}}{\partial t^2} \qquad \textit{Eq. 1.7}$$

which have the standard wave equations form. These show that there is some parallelism between the **E** and **B** fields, and that any electromagnetic wave contains both fields. As the discussion is limited to non-magnetic media, it will focus only on E, which is responsible for important physical effects in a semiconductor.

An oscillatory disturbance propagating at a speed determined by the medium is the standard solution for a wave equation of the form shown in ***Eq. 1.6***. The oscillatory form solution is the following: $e^{i(\boldsymbol{q}.\boldsymbol{r}-\omega t)}$, where **r** is the displacement vector; t is time; the wave vector **q** points in the direction of wave propagation and has a magnitude $2\pi/\lambda = 2\pi f$ where λ is wavelength and $f = 1/\lambda$ is the wavenumber (expressed in Number of waves per centimeter, or cm^{-1}); and ω is the radian frequency $2\pi\nu$, with ν the frequency of wave oscillation in hertz. The speed of wave propagation is ω/q.

If the wave is assumed to propagate along the positive z-axis, the wave behavior is easier to visualize, and the solution remains completely general. The supposed solution is then:

$$\boldsymbol{E}(z,t) = \boldsymbol{E_0} e^{i(qz-\omega t)} \qquad \textit{Eq. 1.8}$$

where the vector $\mathbf{E_0}$ denotes the direction and maximum strength of the electric field. When this is used in equation ***Eq. 1.6***, it can be found that:

$$q^2 = \varepsilon_0 \mu_0 \omega^2 \qquad \textit{Eq. 1.9}$$

which gives for the electric field:

$$\boldsymbol{E} = \boldsymbol{E_0} e^{i\omega\left(z\sqrt{\varepsilon_0\mu_0}-t\right)} \qquad \textit{Eq. 1.10}$$

Eq. 1.9 determines a dispersion relation between q and ω, or, from a quantum perspective, between photon momentum and energy. In semiconductors, however, more complex dispersion relations emerge, resulting in frequency-dependent velocities.

When Maxwell's equations for **B** are solved, the magnetic field follows the electric field, propagating at the same speed but oscillating perpendicular to **E**. Both **E** and **B** oscillate perpendicular to the propagation direction, resulting in transverse electromagnetic waves. The fact that they are transverse is directly derived from Maxwell's third equation, which gives $\nabla \cdot \boldsymbol{D} = \varepsilon_0 \nabla \cdot \boldsymbol{E} = 0$ when ρ = 0; this gives immediately $q \cdot \boldsymbol{E} = 0$, that is, the **E** field is perpendicular to the direction of propagation. In a semiconductor, ∇·D is not necessarily zero, with the result that the electric field can acquire a longitudinal component. Finally, it is worth noting that nothing in the solution for **E**(z,t), in equation ***Eq. 1.10***, causes energy loss. In other words, a wave propagating in free space and encountering nothing but vacuum never loses amplitude.

1.3 Electromagnetic waves in semiconductors

A solid, as opposed to free space, contains both moving free charges and bound charges. Conduction electrons and valence band holes are the free charges in a semiconductor. The bound charges are stuck in the lattice structure, as are the atomic charges that make up the lattice and the internal electrons that are tightly localized at the atomic level. Maxwell's equations are affected by the current and charge density caused by the free charges, as well as by the polarizability of the bound charges.

The effect of bound charges in Maxwell's equations will be considered at first. These charges generate a dipole moment per unit volume, resulting in a polarization vector **P**. The magnitude of **P** to the first approximation is proportional to the magnitude of E and these two vectors are both in the same direction, so the relationship between **P** and **E** becomes:

$$\boldsymbol{P} = \chi \varepsilon_0 \boldsymbol{E} \qquad \textit{Eq. 1.11}$$

where χ is called the 'susceptibility'. The full relationship between **P** and **E** is more complicated, with **P** relying on higher orders of **E**. If only the linear approximation is used, the equation ***Eq. 1.2*** becomes:

$$\boldsymbol{D} = \varepsilon_0 \boldsymbol{E} + \boldsymbol{P} = \varepsilon_0 (1 + \chi) \boldsymbol{E} = \varepsilon_{lat}(\omega) \varepsilon_0 \boldsymbol{E} \qquad \textit{Eq. 1.12}$$

where $\varepsilon_{\mathrm{lat}} = (1 + \chi)$ is the dielectric response function describing the polarization. It is called ε_{lat} to remind us that it is due to electrons bound into

the lattice and lattice atoms. The polarization is frequency-dependent, as demonstrated in Section 1.6, and thus ε_{lat} is frequency-dependent.

The effects of free electrons and holes current could also be incorporated into ***Eq. 1.12***, but it is more helpful to consider them by taking advantage of the relation between the charge current and the electric field according to the microscopic variant of Ohm's law:

$$\boldsymbol{j} = \sigma(\omega)\boldsymbol{E} \qquad \textit{Eq. 1.13}$$

where σ(ω) is the electrical conductivity, which is also frequency-dependent. More complex non-linear relationships, and even spatially non-local relationships, are possible, but they will not be discussed in this manuscript. By substituting the linear relations ***Eq. 1.12*** and ***Eq. 1.13*** into Maxwell's equations ***Eq. 1.1*** and maneuvering to eliminate **B**, the wave equation for the electric field **E** in a solid is obtained:

$$\boldsymbol{\nabla \times \nabla \times E} = \boldsymbol{\nabla^2 E - \nabla(\nabla . E)} = \boldsymbol{\varepsilon_{lat}\varepsilon_0\mu_0 \frac{\partial^2 E}{\partial t^2} + \sigma\mu_0 \frac{\partial E}{\partial t}} \qquad \textit{Eq. 1.14}$$

where the term $\boldsymbol{\nabla^2 E - \nabla(\nabla . E)}$ is a standard expansion of the double cross-product $\nabla \times \nabla \times \boldsymbol{E}$.

This equation for **E** differs from the result obtained in free space (***Eq. 1.6***) in that the term $\nabla . \boldsymbol{E}$, which was zero in free space, may be finite nonzero here, implying the existence of longitudinal waves. It also differs from (***Eq. 1.6***) in that the last term on the right, includes the current of free charges. Effect of charges can be understood by considering a plane-wave solution, so that the electric field can be written as $\boldsymbol{E} = \boldsymbol{E_0} e^{i(qz-\omega t)}$. The substitution of this solution in ***Eq. 1.14*** gives:

$$q^2 E - \boldsymbol{q(q . E)} = \varepsilon_{lat}\varepsilon_0\mu_0\omega^2\boldsymbol{E} + \sigma\mu_0 i\omega\boldsymbol{E} = \omega^2\varepsilon(\omega)\varepsilon_0\mu_0\boldsymbol{E} \qquad \textit{Eq. 1.15}$$

In the right-side term, the newly defined quantity $\varepsilon(\omega)$ is the total dielectric response function, given by:

$$\varepsilon(\omega) = \varepsilon_{lat}(\omega) + \frac{i\sigma(\omega)}{\varepsilon_0\omega} \qquad \textit{Eq. 1.16}$$

It combines the effects of bound charge polarization and free carrier current in the semiconductor and is frequency-dependent due to $\varepsilon_{lat}(\omega)$, σ(ω), and the denominator in the second term. In the linear response limit, ε(ω) turns out to

be the central quantity that describes the electromagnetic-semiconductor interaction.

Because of the longitudinal term $\boldsymbol{q}(\boldsymbol{q}.\boldsymbol{E})$, equation ***Eq. 1.15*** cannot be solved immediately for **q** versus ω. However, the solution becomes clear when **E** is written as the sum of transverse and longitudinal components as

$$\boldsymbol{E} = E_t\hat{\boldsymbol{t}} + E_q\hat{\boldsymbol{q}} \qquad \textit{Eq. 1.17}$$

where $\hat{\boldsymbol{t}}$ is a unit vector perpendicular to the propagation direction located in the x-y plane, and $\hat{\boldsymbol{q}}$ is a unit vector along **q**. Equation ***Eq. 1.15*** can be re-written in the form:

$$\left[\left(\frac{\omega}{c}\right)^2 \varepsilon(\omega) - q^2\right] E_t\hat{\boldsymbol{t}} + \left(\frac{\omega}{c}\right)^2 \varepsilon(\omega) E_q\hat{\boldsymbol{q}} = 0 \qquad \textit{Eq. 1.18}$$

Because the components are linearly independent, ***Eq. 1.18*** can only be satisfied if the coefficients of $\hat{\boldsymbol{t}}$ and $\hat{\boldsymbol{q}}$ are both zero. As a result:

$$q^2 = \frac{\omega^2}{c^2}\varepsilon(\omega) \qquad \textit{Eq. 1.19}$$

is the generalized dispersion relation for transverse waves in a solid of total dielectric function ε(ω), and

$$\varepsilon(\omega) = 0 \qquad \textit{Eq. 1.20}$$

is the requirement for longitudinal modes to exist. When the explicit forms of ε(ω) are derived later in Section 1.5, these two abstract statements will make more sense. ***Eq. 1.20*** provides conditions for existence of longitudinal waves.

It is also important to realize that $\varepsilon(\omega)$ is a complex quantity. It is usually written as $\varepsilon = \varepsilon_R + i\varepsilon_I$. If the polarization and conduction processes in the semiconductor are lossy, which is always the case, ε_{lat} and σ each also include imaginary parts. This means that the wave vector's magnitude q is also a complex quantity $q = q_R + iq_I$. When this is applied to the plane wave $E = E_0 e^{i(qz-\omega t)}$used to solve equation ***Eq. 1.14***, the result is:

$$\boldsymbol{E} = \boldsymbol{E_0} e^{-q_I z} e^{i(q_R z - \omega t)} \qquad \textit{Eq. 1.21}$$

This demonstrates that the imaginary part of the wavevector derived from equation ***Eq. 1.19*** describes the damping of the electrical field while penetrating the medium, whereas the real part relates to the propagation of

the electromagnetic radiation within the medium. These observations can be translated into a more familiar form for optical use by defining a new quantity known as the complex index of refraction, $\bar{n} = n + ik$ as follows:

$$\bar{n} = n + ik = \sqrt{\varepsilon(\omega)} \qquad \textit{Eq. 1.22}$$

Combining equations Eq. 1.19, Eq. 1.21, and Eq. 1.22 one obtains

$$\boldsymbol{E} = \boldsymbol{E_0} e^{-kq_0 z} e^{i(nq_0 z - \omega t)} \qquad \textit{Eq. 1.23}$$

where $q_0 = \omega/c$ is the vacuum wavevector. The complex refractive index and the complex wave vector have an immediate physical meaning in Equation ***Eq. 1.23***. It can be readily noticed that the real part of $\bar{n}$ is related to the wave propagation via the definition of propagation velocity $v = \omega/(nq_0)$. It is therefore in the familiar elementary definition for the refractive index $n = c/v$, which is the ratio of the speed of light in vacuum to that in a solid.

The imaginary part of $\bar{n}$, on the other hand, describes the decrease in the electric field as the wave penetrates the medium. This field attenuation is expressed by the damping term $e^{-kq_0 z}$. This explains why k is known as the 'extinction coefficient.' It will make more sense when the transmittance of a semiconductor is considered in the following section.

1.4 Quantities for semiconductor optical characterization

1.4.1 Reflectance, transmittance, and absorbance

It should now be obvious that if we understand the dielectric function of a solid as a function of frequency, we will know everything about its microscopic optical response. Real measurements, on the other hand, are made under macroscopic conditions. The light is projected on the surface of a sample, which is usually a slab with flat faces. Spectroscopy, (visible or infrared), measures the amount of light reflected from the front surface or transmitted through the back surface, depending on the geometry of the sample. Although reflectance and transmittance are not measured in photoluminescence and Raman spectroscopy, the behavior of light at the air-semiconductor interfaces is important in determining the conditions and significance of the measurement. If the sample is not a slab of a single material but consists of layers of

semiconductors, each interface between different materials affects the incoming electromagnetic waves in any type of spectroscopy.

Boundary conditions used with Maxwell's partial differential equations govern the behavior of electromagnetic waves at interfaces. They can be used to calculate the fraction of incident light that is reflected at an interface between two materials and the fraction that is transmitted across the interface. Consider a typical sample, a slab of thickness d made of a single type of semiconductor, as shown in **Figure 1.1**. The reflectance and transmittance of radiation are affected by the angle of incidence. The behavior at the interface depends on the polarization of the light at any angle other than normal incidence. Only normal incidence is considered here, but the full equations can be found in many references [6]. However, at normal incidence, the polarization is insignificant. The interface is considered to be perpendicular to the +z-direction of wave propagation. The Fresnel amplitude coefficients for reflectance and transmittance at the front surface, derived from Maxwell's boundary conditions, are:

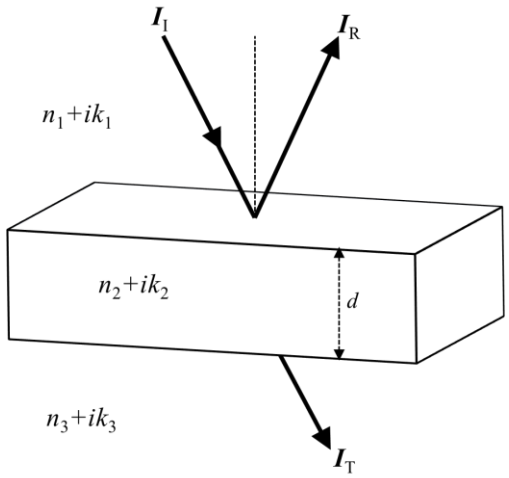

Figure 1.1 *A semiconductor sample of thickness d (medium 2) between media 1 and 3, showing the incident, reflected, and transmitted intensities. Each medium is described by its complex refractive index* $n_j + ik_j$ *(j = 1, 2, 3). These determine the reflectance and transmittance of the sample.*

$$r = \frac{E_r}{E_i} = \frac{\bar{n}_1 - \bar{n}_2}{\bar{n}_1 + \bar{n}_2}$$
$$t = \frac{E_t}{E_i} = \frac{2\bar{n}_1}{\bar{n}_1 + \bar{n}_2} \qquad \textit{Eq. 1.24}$$

where E_i, E_r, and E_t are the incident, reflected, and transmitted electric field amplitudes respectively, and n_1 and n_2 are the two media's complex refractive

indices. In a real experiment, we measure the fraction of the incident intensity that is reflected (denoted here as R) or the fraction of the incident intensity that is transmitted (denoted here as T). The intensity is proportional to the amplitude squared, so that $R = rr^* = |r|^2$ and $T = tt^* = |t|^2$. To put this in a familiar form, medium 1 is considered to be the air, with $n_1 = 1$ and $k_1 = 0$, and the slab to be a semiconductor with $\bar{n} = n + ik$. Then the reflectance can be expressed as:

$$R = \frac{(n-1)^2 + k^2}{(n+1)^2 + k^2} \qquad \textbf{\textit{Eq. 1.25}}$$

This only gives the reflectance from the first surface, or the total reflectance from a semi-infinite medium. This is approximated by a finite sample that absorbs light heavily, resulting in little light reaching the back surface, which then has little effect on the front surface reflection. Another assumption which often stands, at least over part of a spectral range, is that $n > 1$ and $k \ll 1$. Then equation ***Eq. 1.25*** becomes:

$$R = \frac{(n-1)^2}{(n+1)^2} \qquad \textbf{\textit{Eq. 1.26}}$$

In this case, the reflectance represents the real part of the refractive index rather than the absorbing part. The reflectance can be total, i.e., R=1, under two conditions: whenever k≫n and near a longitudinal mode, where ε(ω)=0 and thus n=0.

In some cases, the light can be reflected or transmitted at the back side of the slab. In these cases interference fringes are created and the reflectance R' and transmittance T' of the semiconductor slab in the air should be written as:

$$R' = \frac{4R\,sin^2\,\theta}{(1-R^2)^2 + 4R^2\,sin^2\,\theta} \qquad \textbf{\textit{Eq. 1.27}}$$
$$T' = \frac{(1-R^2)}{(1-R^2)^2 + 4R^2\,sin^2\,\theta}$$

where R is the front surface reflectance from ***Eq. 1.25***. The $sin\,\theta$ terms in these expressions are related to interference effects. When the reflectance is at its lowest and the transmittance is at its highest, $sin\,\theta = 0$. Reflectance minima and transmittance maxima (i.e., a bright fringe) occurs when f = m/2nd where m = 0, 1, 2, ... The distance between two successive bright fringes is $\Delta f = 1/2nd$. As a result, observing such interference fringes provides a simple method for determining layer thickness if n is known.

For a medium with significant absorption, ***Eq. 1.27*** becomes overly complicated. There is, however, a simplifying case that occurs frequently in actual measurements. If the spectrometer's resolution is greater than the spacing between the interference fringes, the equations can be averaged over the phase angle. The transmittance of an absorbing slab becomes:

$$T' = \frac{[(1-R)^2 + 4R\,sin^2\,\phi]e^{-\alpha d}}{1 - R^2 e^{-2\alpha d}} \qquad \textbf{Eq. 1.28}$$

in which two new quantities have been defined: $\phi = tan^{-1}[2k/(1-n^2-k^2)]$ and the absorption coefficient:

$$\alpha = \frac{2\omega k}{c} = 4\pi f k \qquad \textbf{Eq. 1.29}$$

When wavenumber f is used, the term on the right is more convenient. The term $sin\,\phi$ in equation ***Eq. 1.28*** is frequently small enough to be ignored, resulting in an even simpler form:

$$T' = \frac{(1-R)^2 e^{-\alpha d}}{1 - R^2 e^{-2\alpha d}} \qquad \textbf{Eq. 1.30}$$

The intensity transmitted through the slab is affected both by the reflectance of the front surface R and by an exponential decay, as shown in ***Eq. 1.30***, which refers to ***Eq. 1.23*** that includes the extinction coefficient. The meaning of the term $e^{-\alpha d}$, can be made clearer if equation ***Eq. 1.30*** is considered in the limit where there is no front surface reflection (R = 0), implying that reflection losses do not reduce the transmitted intensity at the front surface. The incident intensity I_i and the transmitted intensity leaving the back surface I_t are related by:

$$I_t = I_i e^{-\alpha d} \qquad \textbf{Eq. 1.31}$$

The absorption coefficient is defined as the fractional change in intensity per unit length of penetration caused solely by absorption in the semiconductor. Because of this direct connection to physical processes, the absorption coefficient is a more useful spectroscopic quantity than transmittance. Absorption is often proportional to the concentration N of absorbing entities, which can be useful for quantitative characterization. As such, it is useful to define an absorption cross-section $\sigma = \alpha/N$. When the front surface reflectance

R and thickness d is known, equation ***Eq. 1.30*** can be used to calculate α when the transmittance is measured under appropriate conditions.

Eq. 1.25 to ***Eq. 1.30*** cover the most common cases encountered in practice for a slab of bulk semiconductor in air. For structures with two or three layers, there are similar expressions, but with a high complexity that require preferably dedicated computer evaluation software (such as MATLAB). In most cases, it is more efficient to use a computer program that traces through the Fresnel coefficients (equation ***Eq. 1.24***) at each interface, eventually calculating the structure's total reflectance or transmittance. This 'interface-by-interface' approach has the advantage of being able to be applied to as many layers as required, allowing for the analysis of complex layered semiconductor microstructures. However, as the following section will show, it is not always necessary to analyze the entire structure (depending on the wavelength).

1.4.2 Penetration depth

The absorption coefficient α, defined by ***Eq. 1.31*****,** can be expressed in a way more suitable for studying what optical radiation probes in a semiconductor structure. A quantity known as the skin depth or penetration depth can be defined as $\delta = 1/\alpha$. It is related to the transmitted and incident intensities according to:

$$I_t = I_i e^{-\frac{z}{\delta}} \qquad \textit{Eq. 1.32}$$

Thus, δ is the distance over which the incident intensity drops to 1/e of its value at the semiconductor's surface. This characteristic length would allow the estimation of how far light penetrates a semiconductor. It is usually dependent on the frequency and physical properties of the measured semiconductor. δ is typically between 0.1 – 1 μm in silicon and around 0.1 μm in GaAs in the visible light region [7]. The strongest absorption is usually encountered in the middle and far infrared. Thus, most semiconductor epitaxial layers and microstructures, whose thickness rarely exceeds a few micrometers, are generally permeable to infrared radiation. **Table 1.1** provides values of δ for commonly encountered materials.

1.4.3 Spatial resolution

The diffraction limit sets the lower limit of spatial resolution in optical characterization. The diameter d of the smallest size spot that can be formed by

a light of wavelength λ passing through a lens of focal length F and diameter D is [8]:

$$d = 1.22\frac{F\lambda}{D} \qquad \textit{Eq. 1.33}$$

The spot size for an experiment excited by an Ar^+ laser's 488 nm line could thus be as small as 0.6 μm. Although in practice this ideal value is unlikely to be achieved, visible light (or laser) resolution is sufficient to see spatial detail on a scale appropriate for device geometries. At longer infrared wavelengths, such resolution is not possible, but infrared maps can still provide useful information on the scale of tens of micrometers to millimeters.

1.5 Physics of semiconductors

Electromagnetic radiation can interact with all elementary excitations that make up a semiconductor, as well as the lattice atoms and impurity atoms. The interaction can be expressed in terms of the quantum mechanical properties of the semiconductor, such as the bandgap and phonons, or in terms of the classical effect of an oscillating electric field on a charge. In order to understand fundamental optical properties, a review of fundamental semiconductor physics is first provided. This review briefly highlights the physics of band structure, lattice vibrations, free carrier transport, and impurity effects. Detailed theories of semiconductors can be found in solid-state physics textbooks by Blakemore [9], Ashcroft and Mermin [10], Kittel [11] and others. They all contain enough information about the physics and optical properties of semiconductors. Wooten [13], which deals with the optical properties of solids in general, and Pankove [14], a typical work on the optical properties of semiconductors, are two more specialized works. Other works, for example, Willardson and Beer [12], review the optical properties of specific classes of semiconductors. Superlattices and their optical properties are discussed by Cottam and Tilley [13].

Group IV semiconductors, germanium and silicon, are the oldest, best known and most widely used semiconductors. Binary compounds have also been extensively studied, which has expanded the range of fundamental semiconductor properties and applications. Driven by the need for diverse properties, more complex ternary and quaternary semiconductor alloys have recently been developed. The electro-optics industry relies on $Al_xGa_{1-x}As$. $Hg_{1-x}Cd_xTe$ as an infrared detector material; $In_xGa_{1-x}As_yP_{1-y}$ allows for the selection

of both bandgap and lattice parameters to match a substrate; and $Pb_{1-x}Sn_xTe$ as an early and useful zero-narrow-gap system. Other, uncommon semiconductors exist, such as III-VI chalcopyrites, despite their limited applications.

The introduction of microstructures is a second trend that is emerging in parallel with the increased use of alloys. Microstructures of various types now lead the research topics in new semiconductor physics and the development of new devices.

1.5.1 Bulk crystals

One way to understand the fundamental properties of semiconductors is to compare them to metals, and insulators. At all temperatures, metals are distinguished by their high electrical conductivity, opacity to visible light, and shiny luster. These characteristics result from their high concentrations of free electrons, which are close to 10^{23} cm^{-3}. Electrons move easily in an electric field, and their number does not vary significantly with temperature. Insulators, on the other hand, have a high resistance to current flow and may be transparent. Because almost all the electrons in an insulator are bound into its basic crystalline structure, these properties result from a lack of free carriers.

A semiconductor can switch from insulator-like to metal-like as its free carrier density varies between 10^9 to 10^{21} cm^{-3}. This huge variation can be caused by introducing impurities in the material or by changing its temperature. Both effects are a direct result of a semiconductor's most distinguishing feature, the bandgap. The gap is caused by the quantum physics of the crystalline semiconductor, and the reasons for its presence are briefly explained below.

A crystalline semiconductor is formed of a continual geometric array of atoms, like the diamond structure of a Si or the cubic structure of GaAs. When each component atom is isolated in space, its electrons are housed in discrete energy levels. Nevertheless, in a crystalline structure, the accompanying electrons interact with each other since the atoms are less than a nanometer apart. Pauli exclusion principle dictates that every atomic level be divided into several levels to accommodate the various electrons. Because the new levels are so close together, they form a continuous band of electronic energies. Every atom that joins the array contributes more electrons, each of which enters the band at higher energy. The ‘Fermi energy’ is the energy at which the last electron resides.

However, the electronic energy band does not continue uninterrupted from zero to the ‘Fermi energy’. Quantum mechanics factors impose forbidden energy levels. Electron waves moving through the lattice, like water waves splashing among a regular array of wooden pilings, are successively affected

by the periodic potential from the lattice's ionic cores. Electrons with wavelengths and motion directions that match the geometric constraints of the lattice propagate through the structure, while others are canceled by destructive interference. Canceled wavelengths correspond to missing momenta and therefore missing energies, leading to prohibited regions or gaps within the continuous band of energies.

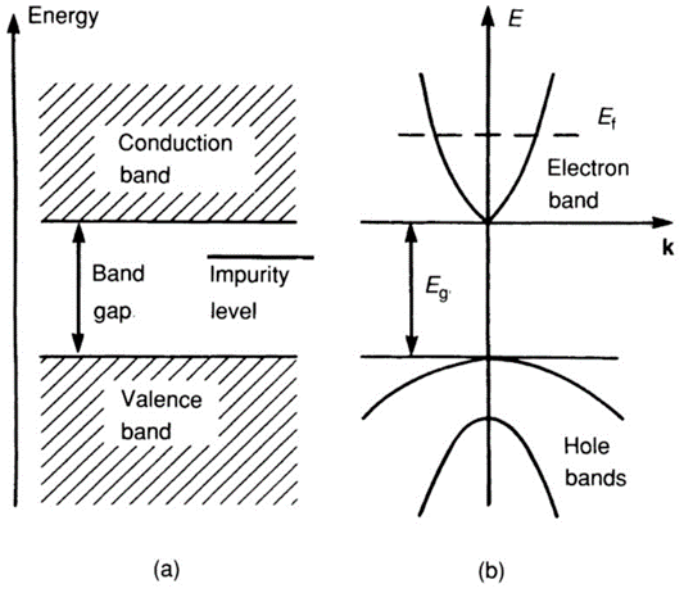

Figure 1.2 (a) *Conduction and valence bands in a semiconductor, with the bandgap and an impurity level in the gap depicted.* ***(b)*** *Diagram of energy versus wave vectors illustrating the quadratic relationship for electrons and holes, the Fermi energy E_f, and multiple hole bands.*

The highest gap and the electron population of the valence band directly below it, determine whether a solid is a metal, conductor, or insulator. If the topmost band is only partially filled with electrons, those electrons with the highest energies can move from valence to higher states in the conduction band with only a small amount of energy added. As a result, they are easily mobile. This defines a metal and explains why, even at low temperatures, movable electrons are always available.

If, on the other hand, the band below the highest gap is filled, the size of the gap determines whether the material is a semiconductor or an insulator. This is outlined schematically in **Figure 1.2(a)**. Thermal energies are too low with a large gap to promote electrons from the lower valence band to the empty conduction band above the gap. At room temperature, such material has very few free carriers. It acts as an insulator. In a solid with a smaller gap, however, thermal energy can excite some electrons to the upper band, where their number

is highly dependent on temperature. This characterizes a semiconductor, that behaves like a poor metal at high temperatures and like an insulator at low temperatures.

Table 1.1 *List of few Semiconductor parameters for photoluminescence, Raman, and infrared characterization*

Semiconductor	Gap type	E_{gap} (eV)	λ_{gap} (μm)	ω_{TO} (cm^{-1})	ω_{LO} (cm^{-1})	ω_{pe} (cm^{-1})	E_d (meV)	δ_{VIS} (nm)	δ_{IR} (μm)
Elemental									
Si	i	1.11	1.1	520	520	55	25	540	2.7×10^4
Ge	i	0.66	1.9	300	300				
III–V									
GaAs	d	1.43	0.87	269	291	101	5.3	93	2500
AlAs	i	2.15	0.58	362	404				
$Al_{0.3}Ga_{0.7}As$	d	1.80	0.69	267, 360†	280, 377†				
InSb	d	0.17	7.3	180	191	181	0.6		
II–VI									
CdTe	d	1.44	0.86	141	168	89	14	100	60
HgTe	d	−0.30	—	119	139				
$Hg_{0.78}Cd_{0.22}Te$	d	0.18	6.9	121, 147‡					
CdS	d	2.42	0.51	242	305				
IV–VI									
PbTe	i	0.29	4.3	32	114				
SnTe	i	0.19	6.5	26	139				

Gap type, direct(d) or indirect(i); E_{gap} , band gap; λ_{gap}, equivalent photon wavelength; ω_{TO}, transverse optical frequency; ω_{LO}, longitudinal optical frequency; ω_{pe}, frequency of the plasma edge at a carrier concentration of 10^{17} cm^{-3}; E_d, impurity ionization energy in the hydrogenic model; δ_{VIS}, penetration depth in nanometers at a wavelength of 0.5 μm; δ_{IR}, penetration depth in micrometers at a wavelength of 100 μm. All quantities are for n-type material at room temperature. Penetration depths are for high-resistivity material, calculated from data in [14]. *Other data come from a variety of sources.*

†GaAs-like and AlAs-like modes, respectively.

‡HgTe-like and CdTe-like modes, respectively.

The value of the gap energy separating semiconductors and insulators is somewhat arbitrary, but it is commonly taken to be around 3eV.

Full quantum calculations provide a detailed picture of valence and conduction band energy **E** as a function of electron momentum **p** or electron wave vector **k**, as defined by the de Broglie relation $\boldsymbol{p} = \hbar \boldsymbol{k}$. The **E** versus **k** diagrams for silicon and GaAs are shown in **Figure 1.3** and **Figure 1.4**, respectively. Due to the change in lattice properties along different crystalline axes, both demonstrate the directional character of the electronic band structure. Various bands are depicted in the figures, for example, along the (100) and (111) directions. Because of the directional nature, the bandgap, or the smallest energy difference between a valence band state and a conduction band state, may not occur at the point of minimum momentum $(k_x, k_y, k_z) = (0,0,0)$. **Figure 1.4** shows that GaAs is a semiconductor with a direct bandgap, with the conduction minimum directly above the valence band maximum. **Figure 1.3** depicts an indirect gap in silicon, with the lowest minimum in the conduction band displaced from (0,0,0). In this case, an electron moving from the valence to the conduction band must undergo a wavevector change.

These band properties have a significant impact on the semiconductor's optical behavior. If an electron absorbs a photon with an energy greater than the gap value, it will be elevated from the valence band to the conduction band. The values range from visible to near infrared. Because momentum must also be conserved, whether the gap is direct or indirect has a significant impact on absorptive and photoluminescent processes near it.

Electrons that enter the conduction band are free to move. Ordinary free electrons of mass m_0 have the following energy-momentum relationship in a vacuum:

$$E = \frac{p^2}{2m_0} \qquad \textit{Eq. 1.34}$$

Mobile electrons in a semiconductor crystal obey a similar quadratic law near the bottom of a band, except that their interaction with the atomic cores gives them an effective electronic mass m* rather than m_0. Their energy-wave vector relationship is as follows:

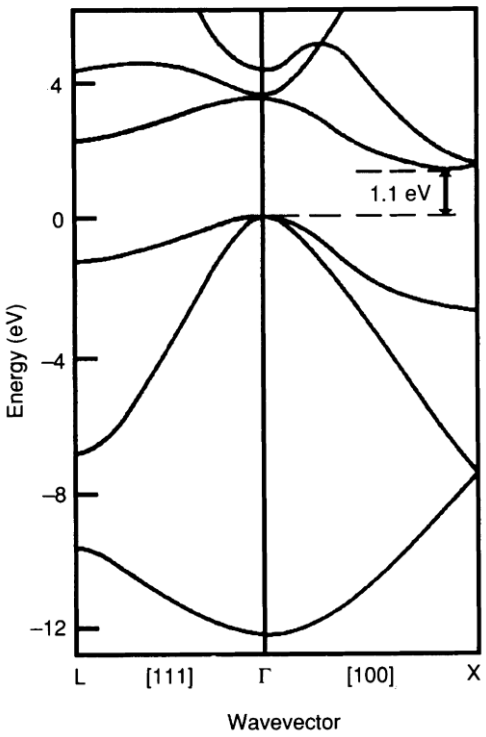

Figure 1.3 *Silicon "energy versus wavevector diagram". The arrow denotes the indirect gap of 1.1 eV (at 300 K), which is the smallest energy separation between the valence and conduction bands. It is distant from the point where the wavevector* ***k*** *=* ***0****.* [15]

$$E = \frac{\hbar^2 k^2}{2m^*} \qquad \textit{Eq. 1.35}$$

Figure 1.2(b) depicts this quadratic relationship. In addition to their effective mass, mobile electrons in the conduction band are described by their concentration n, scattering time τ, or the average time between collisions, and mobility μ, which is defined as the velocity produced per unit electric field. The d.c. mobility is derived from the simple Drude model for electronic behavior. The mobility is related to the scattering time as

$$\mu = \frac{e\tau}{m^*} \qquad \textit{Eq. 1.36}$$

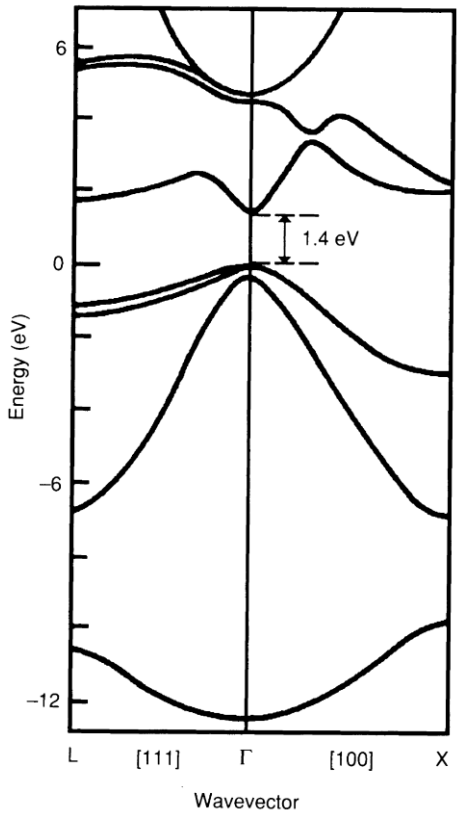

Figure 1.4 *GaAs "energy versus wavevector diagram". The arrow represents the direct gap of 1.4 eV (at 300 K), the smallest energy separation between the valence and conduction bands. It is located at the point where the wavevector* ***k*** *equals zero.* [15]

where e represents the elemental electronic charge. All these parameters combine in the resistivity ρ, which characterizes the electrical properties of a semiconductor, or its inverse, the electrical conductivity σ. These are related in the Drude model and the d.c. limit by:

$$\sigma = \frac{1}{\rho} = ne\mu = \frac{ne^2\tau}{m^*} \qquad \textbf{\textit{Eq. 1.37}}$$

The movement of charged particles is not limited to the conduction band. When an electron is excited from the valence band to the conduction band, an effective positive charge is left behind. This positive charge moves in the opposite direction of the electron when an electric field is applied. The resulting entity, known as a 'hole,' also contributes to a semiconductor's electrical behavior. Electrons and holes have different effective masses, with holes having larger

values. The different curvatures of the electron and hole E-k parabolas are depicted in **Figure 1.2(b).** The holes mobilities are generally much lower than electron mobilities.

Semiconductor crystals consist of a three-dimensional lattice of atoms held together by spring-like joining forces. This lattice supports characteristic normal vibrational modes, the frequency-wavenumber relationship (i.e., the dispersion relationship) being derivable from classical solutions to the equations of atomic motion.

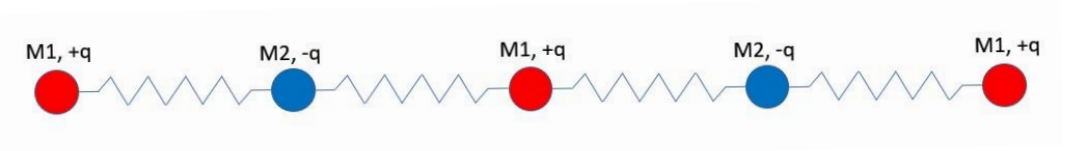

Figure 1.5 : *Linear chain of atoms with alternating masses M_1 and M_2, and alternating charges +q and -q, connected by springs whose force constant is C.*

A linear chain of atoms with alternating masses M_1 and M_2, and alternating charges +q and -q, connected by springs whose force constant is C, is a simple model that describes the lattice vibrations in a binary material like GaAs. The equations of motion for this system produce normal modes. The dispersion relation (ω versus **K)** is depicted in **Figure 1.6.** The modes are: 1- optical, in which atoms of opposite charge vibrate out of phase to produce an oscillating dipole moment that couples to light, 2- or acoustical, which means modes propagating with a constant speed near K=0.

Each type can be transverse or longitudinal. The vibrational frequency of the transverse optical (TO) mode at K = 0 is:

$$\omega_{TO} = \sqrt{2C\left(\frac{1}{M_1} + \frac{1}{M_2}\right)} \qquad \textit{Eq. 1.38}$$

which lies in the infrared for most semiconductors. Resonant absorption occurs when the incoming frequency ω matches ω_{TO}. There is a longitudinal optical (LO) mode as well, whose frequency ω_{LO} also lies in the infrared. Typical LO and TO frequencies are shown in **Table 1.1**. These modes (LO and TO) are important for Raman and photoluminescence processes, where also 2 other types of phonons (transverse and longitudinal acoustic phonons (TA and LA)) may conjointly play a role.

For ternary materials like $Al_xGa_{1-x}As$, each sublattice (in this case, the GaAs and AlAs sublattices) have one TO frequency. Each TO mode is normally visible individually within the infrared and Raman spectra, thus

providing helpful insight for the material. The TO and LO modes coincide both at K= 0 in a single element semiconductor like silicon or germanium (where the charge doesn't alternate sign from atom to atom).

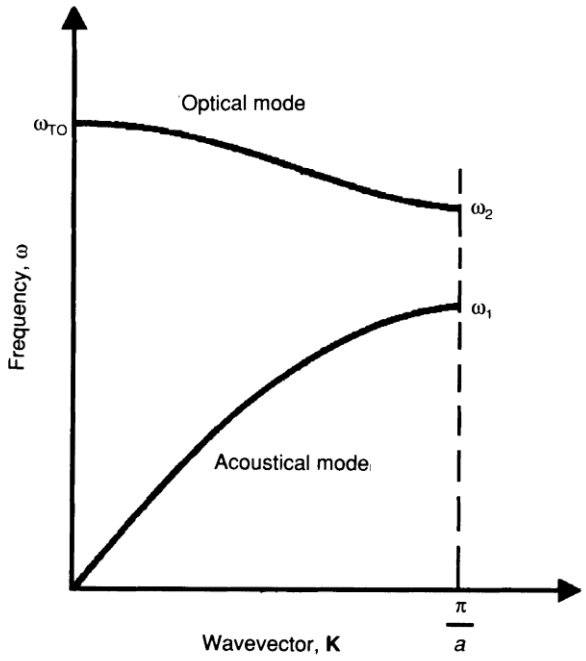

Figure 1.6 *Phonon frequency versus wavevector (dispersion relation) diagram for a linear chain with alternating masses M_1 and M_2, with $M_1 > M_2$. The optical mode frequency ω_{TO} is given by* ***Eq. 1.38****. ω_1 and ω_2 are $(2C/M_1)^{0.5}$ and $(2C/M_2)^{0.5}$, respectively. The maximum wavevector permitted by the cyclic nature of the chain is $K = \pi/a$, where a is the distance between two adjacent masses.*

Although the classical model for lattice normal modes is correct, the vibrations can also be treated as quantized entities. Photons are quanta associated with electromagnetic waves, and similarly, Phonons are quanta associated with mechanical lattice vibrational waves. A phonon with frequency Ω and wavevector **K** has both energy $\hbar\Omega$ and momentum $\hbar\mathbf{K}$. The quantum features become most important in processes such as Raman scattering, where it is useful to speak of phonon creation and destruction, or when electrons and lattice vibrations interact, exchanging energy and momentum.

The most basic type of impurities is substitutional impurity, such as an arsenic atom replacing a silicon atom in the pure silicon lattice. Every silicon atom in the pure material is linked to four of its closest neighbors via covalent bonds, each of which requires a shared electron. An arsenic atom with five valence electrons, has one more electron than what the basic silicon four-hook structure requires. Because the fifth electron is loosely bound, it can easily enter

the conduction band. As a result, arsenic in silicon, and any foreign atom with more electrons than the host atom it replaces, donates an electron to the crystal and is a donor impurity. Similarly, a foreign atom with fewer electrons than the atom it replaces, such as silicon on an arsenic site in GaAs, accepts an electron from the lattice and is an acceptor impurity.

An electron from a substitutional impurity, such as arsenic in silicon, is closer to the conduction band than a valence electron in an energy level diagram like the one shown in **Figure 1.2(a)**. Even at room temperature or lower, thermal energy may be enough to excite the electron across the small energy difference to the conduction band. A photon with at least the same energy as the energy difference can also move an electron from an impurity level to the conduction band. The ionization energy of such an impurity can be calculated using the hydrogen atom theory. In the far-infrared region, the resulting values are a few millielectron-volts. As a result, one-way impurities appear in optical measurements is through infrared absorption caused by photoionization.

A second type of optical effect can occur due to an impurity atom. Such an atom modifies its local lattice environment, influencing the vibrational behavior of its surroundings. This may result in the emergence of new infrared vibrational modes. These new modes are useful for analyzing interstitial impurities that exist between lattice sites. Because their geometry is less obvious and they can form molecule-like complexes, they are more complex than substitutional types. Defects, such as missing or displaced lattice atoms, can also be seen when vibrational modes are created.

1.5.2 Microstructures

All of the physics described for bulk crystalline semiconductors are also present in semiconductor microstructures ranging from epitaxial layers to single and multiple quantum wells to superlattices and other heterostructures. Except near the surfaces and the interfaces, there is generally no significant change in fundamental behavior for layers that are micrometers thick (***Figure 1.6***). However, as the layers shrink to the nanometer levels, fundamental properties change, and thus become more interesting. This is why these nanostructures are built and constructed in the first place. Nonetheless, the general principles of semiconductor optical behavior can also be used to perform a great deal of useful microstructure characterization. This is notably true in the mid- to far-infrared, where some concepts that are applied well for bulk semiconductors additionally work well for complex microstructures.

However, two aspects of microstructure physics influence their optical characterization. One aspect is the shift in energy bands, which can be seen in

a single quantum well. For example, in the case of a thin layer of GaAs sandwiched between two layers of $Al_xGa_{1-x}As$. Because the alloy includes a larger bandgap than the binary structure, electrons tend to stay confined within the GaAs layer. In such a potential well, the electronic energy states lie in the z-direction, that is perpendicular to the plane of the layers, and are quantized. The quantized portion of the energy is as follows:

$$E_n = \frac{\hbar}{2m^*}\left(\frac{n\pi}{L_z}\right)^2 \qquad n = 1, 2, 3, \ \ldots \qquad \textit{Eq. 1.39}$$

where L_z is the well's width. For the confined holes, a similar set of bound energy levels exists. Transitions between these new sets of energy states can be seen in the absorption spectra of quantum wells and superlattices and are important in photoluminescence research. Because the energy levels are related to layer thickness, carrier distribution, and interface quality, such spectra provide fundamental information about the structures as well as characterization data.

A second aspect or effect that differs in microstructures, is the significant change in the phonons in a superlattice. Some may spread throughout the entire microstructure, similar to a bulk crystal, whereas others are restricted to specific layers. For example, if we consider a superlattice made of alternating layers of GaAs and AlAs, the longitudinal modes propagate perpendicular to the plane of the layers in the z-direction. If the properties of the two materials match, they can couple directly across the interfaces between the layers. The longitudinal acoustic (LA) modes of GaAs and AlAs have similar dispersion relations, as shown in **Figure 1.7**, but the LO modes differ in frequency by more than 100 cm^{-1}. As a result, the LA modes continue throughout the structure, whereas the LO modes that originate in each type of material are limited to those layers only. The dispersion relation for both confined and propagating modes is very different from the dispersion relation in the bulk. The largest possible wavevector in the linear diatomic chain, which models a bulk crystal, is $2\pi/2a$, where 2a is the spacing between like atoms and the repeat period for the chain's symmetry (**Figure 1.6**). For a natural crystal, this is typically less than a nanometer. However, the repeat period in a superlattice is significantly longer, lowering the maximum **K** vector. This results in new folded modes, as shown in **Figure 1.7,** which can be significant in microstructure Raman spectra.

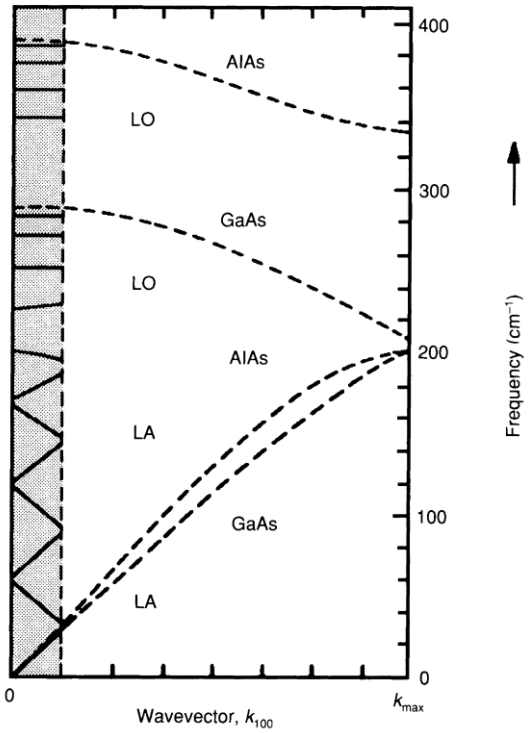

Figure 1.7 *Dispersion relations for the LO and LA phonons in bulk GaAs and AlAs. LO phonons don't propagate throughout a GaAs-AlAs superlattice, however, LA phonons do. The shaded space shows folded dispersion curves for a superlattice whose period is far larger than the lattice spacing.* [16]

1.6 Optical response of semiconductors

Semiconductors interact with light in the 0.1 - 1000 µm spectral range (10 - 10^5 cm^{-1}, 0.001 - 12eV). The dominant effect in the near-ultraviolet-visible-near-infrared region (0.4 - 5 µm, 0.2*10^4 to 2.5*10^4 cm^{-1}, 0.24 - 3.1 eV) is absorption at the gap and by impurities. This causes photoluminescence, providing a sensitive measurement of semiconductor properties, under certain conditions. Absorbed visible light also induces Raman scattering. Raman investigates TO, LO, and other phonon modes, which reflect the semiconductor's crystalline state and provide alloy information. It is also sensitive to carriers and impurities as well. In the middle to far-infrared, the TO and LO modes can also be seen (10 - 300 µm, 30 - 10^3 cm^{-1}, 0.004 - 0.12eV). Also, impurities effects appear here as well, either through the new vibrational modes they induce or through photoexcitation or photoionization of their electrons if they are shallow enough.

Very shallow impurities can be ionized in the more Far Infrared (100-1000 μm, 10 - 10^2 cm^{-1}, 0.001 - 0.01 eV), and free-carrier absorption becomes significant.

Important material properties for device fabrication and manipulation of their optical properties for different applications are the dielectric function and the refractive index. For this purpose, many models have been proposed and used to calculate these properties. This section presents some models based on classical or semi-classical concepts.

1.6.1 Phonons

The Lorentz model provides a classical picture of the energy carrier motion within a material; it simulates the motion of carriers as a classical damped harmonic oscillator, as shown in **Figure 1.8**. Such a model enhances our understanding of semiconductor optical properties. The model begins with the equation of motion of a damped oscillator with a restoring force provided by an applied external field [17–26]:

$$\mu \frac{d}{dt}\left(\frac{dx}{dt}\right) + \mu\Gamma\frac{dx}{dt} + \mu{\omega_j}^2 x = -eE_o e^{-i\omega t} \qquad \textit{Eq. 1.40}$$

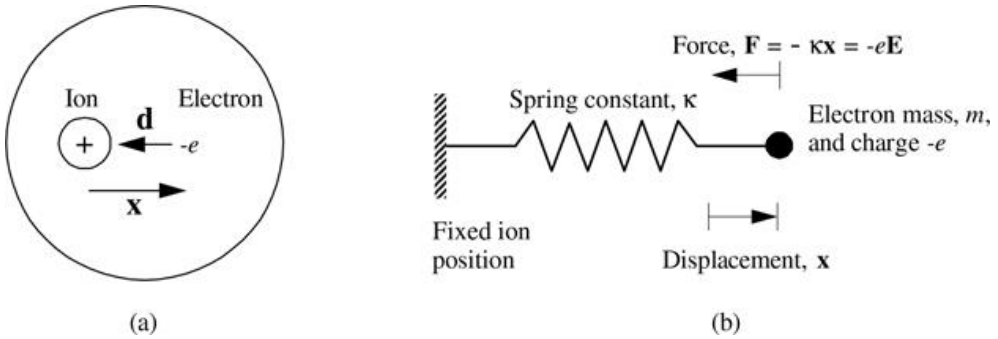

Figure 1.8 *schematic representation of Lorentz oscillator model*

All the components of the above differential equation have the same definition as in the Drude model, with minor differences such as μ used to denote the reduced mass of the carriers and index j to denote the number of the oscillator.

Again, the linear diatomic chain model shown in **Figure 1.5** for a binary semiconductor, that yielded ***Figure 1.6***, also expresses the lattice dielectric function $\varepsilon_{lat}(\omega)$. Under an applied electric field $E = E_0 e^{-i\omega t}$, and assuming a frictional force proportional to velocity, the displacement of the positive ions' u relative to the negative ones is: [17–26]

$$\boldsymbol{u} \propto \frac{E_0 e^{-i\omega t}}{\omega_{TO}^2 - \omega^2 - i\Gamma\omega} \qquad \textit{Eq. 1.41}$$

where the term $\boldsymbol{\omega_{TO}^2}$ refers to the spring restoring force and Γ is the frictional term's strength. According to the definition, this yields the polarization vector **P**, which can be expressed as

$$\boldsymbol{P} = Nq\boldsymbol{u} \qquad \textit{Eq. 1.42}$$

where N denotes the number of ion pairs per cubic centimeter, and q denotes the ionic charge. The lattice dielectric function $\varepsilon_{lat}(\omega)$ in the semiconductor then takes the form given by $\boldsymbol{R} = \boldsymbol{n_i n_f P}$. The solution is as follows [17–26]:

$$\varepsilon_{lat}(\omega) = (n + ik)^2 = \varepsilon(\infty) + \frac{S\omega_{TO}^2}{\omega_{TO}^2 - \omega^2 - i\Gamma\omega} \qquad \textit{Eq. 1.43}$$

The constant $\boldsymbol{\varepsilon}(\infty)$, the high-frequency limit of $\varepsilon_{lat}(\omega)$, is derived from deeply bound valence electrons with a flat frequency response in the infrared. The strength of the oscillator S is proportional to N. It is related to the zero-frequency static dielectric constant $\varepsilon(0)$ and the high-frequency dielectric constant $\boldsymbol{\varepsilon}(\infty)$ by [17–26]:

$$\varepsilon(0) \equiv \varepsilon_{lat}(0) = \varepsilon(\infty) + S \qquad \textit{Eq. 1.44}$$

Eq. 1.43 is the Lorentzian form of the infrared lattice response, which is also useful for impurity-induced local vibrational modes. In the ideal case without damping, i.e., for $\Gamma = 0$, its physical meaning is clear. It develops into:

$$\varepsilon_{lat}(\omega) = \varepsilon(\infty) + \frac{S\omega_{TO}^2}{\omega_{TO}^2 - \omega^2} \qquad \textit{Eq. 1.45}$$

which has a resonance at $\omega = \omega_{TO}$. Moreover, $\varepsilon_{lat}(\omega)$ becomes zero, supporting a longitudinal mode at the longitudinal optical frequency ω_{LO}. The condition $\varepsilon_{lat}(\omega) = 0$ results in [17–26]:

$$\frac{\omega_{LO}^2}{\omega_{TO}^2} = \frac{\varepsilon(0)}{\varepsilon(\infty)} \qquad \textit{Eq. 1.46}$$

This equation is known as the Lyddane-Sachs-Teller relationship. Since $\varepsilon(0) > \varepsilon(\infty), \omega_{LO} > \omega_{TO}$, the increase in the energy of the longitudinal mode is due to the macroscopic electric field associated with the longitudinal oscillations. In binary materials, separate TO and LO modes exist; both are important in infrared and Raman scattering. The oscillator strength S = 0 for covalent group IV semiconductors, so $\varepsilon(0) = \varepsilon(\infty)$ and $\omega_{LO} = \omega_{TO}$ at zero wave-vector.

When n and k are calculated from ***Eq. 1.43*** and used in ***Eq. 1.25*** for reflectance **R**, the result is a reflectance peak very close to ω_{TO}. The peak value is **R** = 1 in the ideal undamped case and very high even in real semiconductors with a small damping term. The minimum in R occurs when n = 1. This minimum R is usually very close to the wavevector defining ω_{LO} for which n = 0. The maximum at ω_{TO} and minimum near ω_{LO} are important features in infrared reflectance spectra interpretation, but there is a fundamental physical difference. The peak denotes resonant energy absorption, whereas the minimum denotes the presence of a longitudinal mode with no resonant absorption.

Curve A in **Figure 1.9** depicts R versus wavevector for a bulk semiconductor with few carriers. This curve clearly displays the lattice TO and LO features. Similar effects would be observed for other semiconductors at any of the TO and LO frequencies shown in **Table 1.1**. [17–26].

Eq. 1.43 can be extended for the ternary or quaternary alloy to include the effects of oscillating sublattices and can be written in the form [17–26]:

$$\varepsilon_{lat}(\omega) = \varepsilon(\infty) + \sum_{j=1}^{J} \frac{S_j \omega_{TOj}^2}{\omega_{TOj}^2 - \omega^2 - i\Gamma_j \omega} \qquad \textit{Eq. 1.47}$$

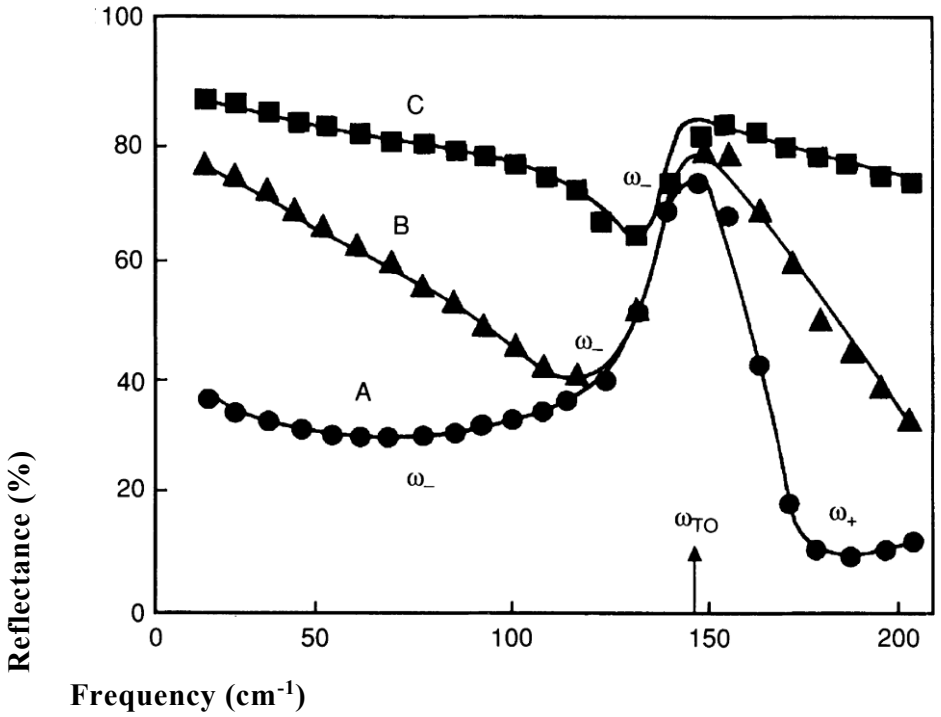

Figure 1.9 *Infrared reflectance for a binary semiconductor, n-CdTe. (■, ▲, ●):Experimental data. (—): Best theoretical fit from Eq. 1.58 and Eq. 1.25. Carrier concentration n in cm^{-3}: curve A, 5.1 x 10^{16}; curve B, 4.1 x 10^{17}; curve C, 1.3 x 10^{18}. Curve A shows nearly pure lattice response, with a TO peak, and an LO minimum at 170 cm^{-1}. As n increases, the minima at the coupled plasmon-phonon frequencies $\omega_{\pm}$ move to higher frequencies, and the low-frequency reflectance increases.* [27]

where j denotes the number of sublattices, each of which has its own TO frequency, oscillator strength, and damping constant. Curve A in ***Figure 1.9*** shows the reflectance for a sample of $Al_{1-x}Ga_xAs$ with few carriers, demonstrating the two lattice TO modes. The intensities and frequencies of the peaks change as x changes, providing a useful characterization tool.

1.6.2 The Drude free carriers model

The Drude model is a simple model developed to describe the motion of free carriers within a semiconductor under the influence of an external electromagnetic field. It assumes that in the absence of this external electromagnetic field, electrons or free carriers within a semiconductor have

random motions with zero average velocity, but that once the field is applied, the electrons align in the direction of this external field, giving rise to non-zero average velocities, carrying current and heat from which the basic properties of the semiconductor, such as electrical conductivity or thermal conductivity, can be measured.
The following classical theories can be used to model the motion of an electron or free carrier in one dimension [17–26]:

$$m_e\ddot{x} = -m_e\gamma\dot{x} - eE \qquad \textit{Eq. 1.48}$$

where m_e is the electron's mass, e is the elemental charge, E is the applied external electric field, and γ is the strength of the electron's collision with neighboring molecules and atoms (or scattering rate, which is equal to the inverse of the scattering time $\gamma = 1/\tau$).

The applied electric field can be a harmonic field of the form: $E = E_o e^{-i\omega t}$ where E_o is the amplitude of the field and ω is the angular frequency. The above differential equation has a solution of the form $x = x_o e^{-i\omega t}$ so that $\ddot{x} = -i\omega\dot{x} = -\omega^2 x$. This leads to [17–26]:

$$dx/dt = (eE/m)/(i\omega - \gamma) \qquad \textit{Eq. 1.49}$$

Using the relationships $J = \sigma E = -n_e e\dot{x}$, one can calculate the conductivity, the dielectric function, and the refractive index as follows [17–26]:

The conductivity:

$$\sigma(\omega) = \frac{\frac{n_e e^2}{m_e}}{\gamma - i\omega} = \frac{\sigma_o}{1 - i(\frac{\omega}{\gamma})} \qquad \textit{Eq. 1.50}$$

where:

$$\sigma_o = \frac{n_e e^2}{m_e \gamma} = \frac{n_e e^2 \tau}{m_e} \qquad \textit{Eq. 1.51}$$

is the DC conductivity.

The dielectric function can now be written in the following form:

$$\varepsilon(\omega) = \varepsilon_\infty - \frac{\sigma_o \gamma}{\varepsilon_o(\omega^2 + i\omega\gamma)} = \varepsilon_\infty - \frac{{\omega_p}^2}{\omega(\omega + i\gamma)} \qquad \textit{Eq. 1.52}$$

where ω_p is defined as the plasma frequency:

$${\omega_p}^2 = \frac{\sigma_o \gamma}{\varepsilon_o} = \frac{n_e e^2}{m_e \varepsilon_o} \qquad \textit{Eq. 1.53}$$

If ω >> γ, the above dielectric function can be approximated by:

$$\varepsilon(\omega) \approx \varepsilon_\infty - \frac{{\omega_p}^2}{\omega^2}\left(1 - i\frac{\gamma}{\omega}\right) \qquad \textit{Eq. 1.54}$$

Finally, the refractive index and extinction coefficient can be approximately given by [17–26]:

$$n \approx k \approx \sqrt{\frac{\sigma_o}{2\omega\varepsilon_o}} \qquad \textit{Eq. 1.55}$$

The Drude model produces reasonably accurate results at room, intermediate, and high temperatures, but fails to produce accurate results at low temperatures as we will be briefly explaining below [17–26]. For these reasons, new models were proposed, one of which is the Lorentz model described quickly in the phonons section.

The analysis of infrared free carriers is aided by the fact that their energies generally exceed those of photons with wavelengths greater than 50μm. This implies that the carriers do not perceive individual photons, and a classical theory is appropriate. The scattering time τ, which depends on the scattering centers in the material, electronic energy, and temperature, is a key component of the free-carrier theory.

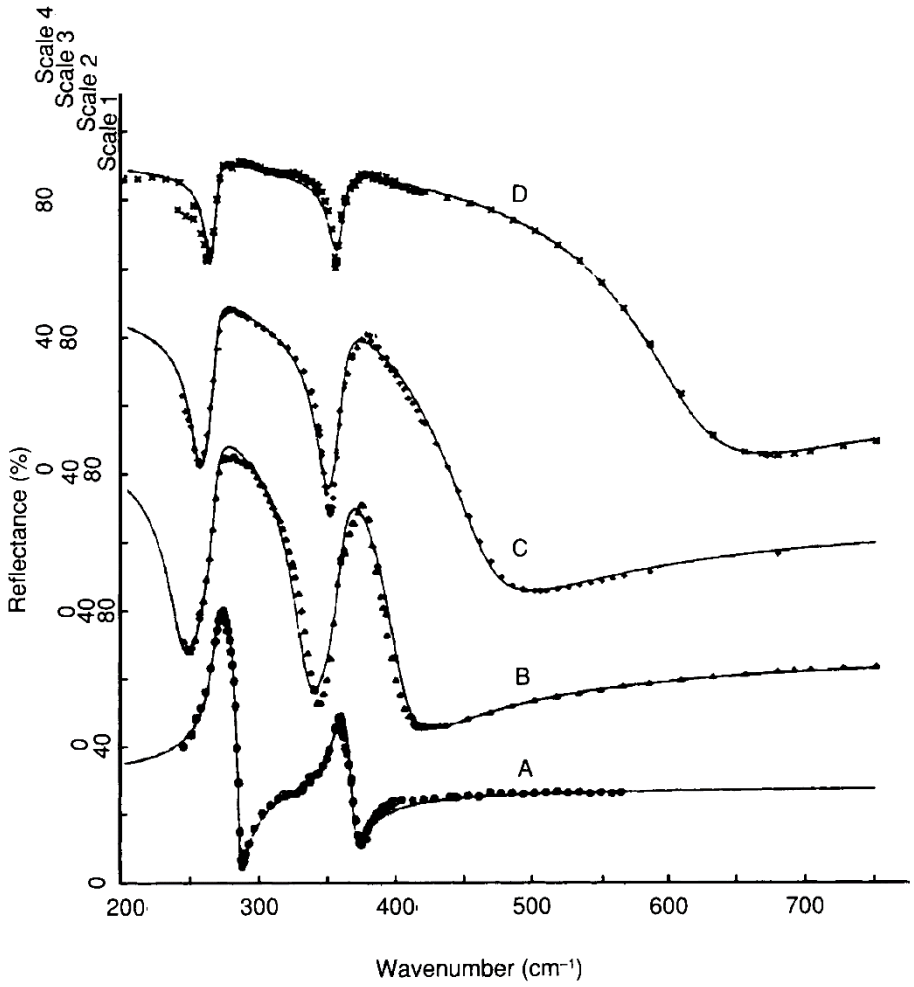

Figure 1.10 *Infrared reflectance for a ternary semiconductor, $Al_{0.14}Ga_{0.80}As$. Carrier concentration n in cm^{-3}: curve A, 3.2 x 10^{16}; curve B, 1.8 x 10^{18}; curve C, 2.8 x 10^{18}; curve D, 4.8 x 10^{18}. Curve A shows nearly pure lattice response, with peaks at 270 cm^{-1} and 370 cm^{-1} from the GaAs-like and AlAs-like TO modes, respectively. Curves B, C, and D show increased low wavenumber reflectance, and plasmon-phonon minima related to free carriers.* [28]

The Drude model with a constant scattering time τ is the most basic classical theory for electrons in semiconductors. The accuracy of this model was verified for GaAs and InP at long infrared wavelengths [29,30]. Some researchers, have added semi-classical features to the Drude model [27,31], while others, have introduced a frequency-dependent $\tau(\omega)$ [32,33]. These improvements illuminate the underlying physics while complicating the analysis without significantly improving its accuracy.

The Drude model works well in conjunction with the effective-mass approximation (m^*) to produce the a.c. conductivity $\sigma(\omega)$ required for the total dielectric function $\varepsilon(\omega)$. The electromagnetic field can be treated in the limit q

$\rightarrow$ 0 because the momentum of an infrared photon is much less than the electronic momentum. The equation of motion of electrons (a similar development can be followed for a hole) can be written in a more suitable form as [17–26]:

$$m^* \left[\frac{dv}{dt} + \frac{v}{\tau}\right] = eE_0 e^{-i\omega t} \qquad \textit{Eq. 1.56}$$

where v is the electron velocity. The term $m^* v/\tau$ is a frictional force, assumed proportional to v and containing the constant scattering time τ. Similarly to ***Eq. 1.50*** , and from the solution to ***Eq. 1.56,*** and the relations $\mathbf{j} = \boldsymbol{ne}\mathbf{v} = \boldsymbol{\sigma}\mathbf{E}$ ($\mathbf{j}$ is current density), the a.c. conductivity can be written as [17–26]:

$$\sigma(\omega) = \frac{ne^2\tau}{m^*(1 - i\omega\tau)} \qquad \textit{Eq. 1.57}$$

which becomes the d.c. result $\sigma_0 = \mathrm{ne}^2\tau/m^*$ when $\omega = 0$.

We now have all the information required to construct a complete infrared dielectric response function $\varepsilon(\omega)$ for a semiconductor. Substituting $\sigma(\omega)$ and $\varepsilon_{lat}(\omega)$ from ***Eq. 1.57*** and from ***Eq. 1.47*** into ***Eq. 1.16*** yields the total dielectric response [17–26]:

$$\varepsilon(\omega) = (n + ik)^2 = \varepsilon(\infty) + \sum_{j=1}^{J} \frac{S_j \omega_{TOj}^2}{\omega_{TOj}^2 - \omega^2 - i\Gamma_j \omega} - \frac{\omega_p^2}{\omega\left(\omega + \frac{i}{\tau}\right)} \qquad \textit{Eq. 1.58}$$

where the last term denotes the free carrier contribution and is written to emphasize the free carriers' characteristic plasma frequency [17–26]:

$$\omega_p^2 = \frac{ne^2}{\varepsilon_0 m^*} \qquad \textit{Eq. 1.59}$$

which is the natural frequency of their collective longitudinal oscillations and contains n *and* m^*. ***Eq. 1.58*** also depends on τ . If ω_p and τ are measured from infrared data, and m^* is known, then carrier density n and mobility $\mu = er/m^*$ can be calculated. On the other hand, if n is known, the determining of ω_p yields m^* , giving infrared measurements an important role in exploring band structure. However, even if m^* is unknown, an infrared determination of ω_p and

τ directly gives the d.c. resistivity, which is given by $\rho = m^*/ne^2r = 1/(\varepsilon_0\omega_p^2\tau)$ [17–26].

To better understand how ω_p and τ influence infrared spectra, let us consider a non-polar semiconductor like silicon, without a resonant TO term. The dielectric function transforms into:

$$\varepsilon(\omega) = (n + ik)^2 = \varepsilon(\infty) - \frac{\omega_p^2}{\omega\left(\omega + \frac{i}{\tau}\right)} \qquad \textbf{\textit{Eq. 1.60}}$$

This allows us to calculate the portion of the absorption α_{fc} due to free carriers. At moderate carrier densities in the very far-infrared, it is [17–26]:

$$\alpha_{fc} = \frac{\omega_p^2\tau}{c\sqrt{\varepsilon(\infty)}(1 + \omega^2\tau^2)} \qquad \textbf{\textit{Eq. 1.61}}$$

which is proportional to free carrier density and is affected by τ. When $\omega\tau \gg 1$, which is true for materials with relatively high mobility, the absorption increases as λ^2, implying that carriers become increasingly important at longer wavelengths.

Transmission data can be used to detect free-carrier absorption, which also affects reflectance spectra. **Figure 1.10** and

Figure 1.9 show that as the extinction coefficient k dominates the reflectance expression, reflectance increases with wavelength and carrier concentration (***Eq. 1.26***). Other characteristics of reflectance spectra are related to ω_p and τ. Consider ***Eq. 1.60*** with undamped electrons $\omega_p/\sqrt{\varepsilon_\infty}$. For simplicity take($\tau \to \infty$). ε(ω) is zero at a frequency commonly known by 'plasma-edge frequency' ω_{pe} which from ***Eq. 1.60*** is $\omega_p/\sqrt{\varepsilon_\infty}$. For $\omega > \omega_{pe}$, *n* is positive and k is 0; infrared waves propagate in the solid. There is no wave propagation for $\omega < \omega_{pe}$, because n is negative, and k is non-zero. The reflectance is high for $< \omega_{pe}$, and drops dramatically at ω_{pe}. This plasma edge provides a direct method for calculating carrier concentration from reflectance spectra. **Figure 1.11** depicts its appearance in silicon spectra, where it is visible due to the lack of features related to phonons. **Table 1.1** shows typical ω_{pe} values for various semiconductors [17–26].

The longitudinal plasma mode is also useful and informative in binary and ternary semiconductors that support resonant TO modes. The carriers do not shift the transverse optical modes, but the LO mode is shifted because

mobile carriers screen its associated macroscopic field. Instead of distinct plasmon and phonon modes, the carriers and phonons interact to produce longitudinal coupled modes with two new characteristic frequencies, ω_+ and ω_-, defined by setting $\varepsilon(\omega) = 0$ in ***Eq. 1.58***. These are, in the simplified limit of no phonon or plasmon damping [17–26]:

$$2\omega_{\pm}^2 = (\omega_{LO}^2 + \omega_{pe}^2) \pm \sqrt{(\omega_{LO}^2 - \omega_{pe}^2)^2 + \frac{4\varepsilon(\infty)\omega_{LO}^2\omega_{pe}^2}{\varepsilon(0)}} \qquad \textit{Eq. 1.62}$$

Because the reflectance has a minimum near $\varepsilon(\omega) = 0$, the frequencies are identified with two reflectance minima, which Olson and Lynch first observed in the infrared. Most semiconductors with typical carrier densities have ω_+ and ω_- in the mid-to-far-infrared range. When damping is factored into these calculations, the main effect is to shift the reflectance minima from zero to finite values that depend on free carrier scattering. As an example, **Figure 1.10** shows plasmon-phonon minima in a ternary semiconductor. Raman spectra also show the plasmon and coupled plasmon-phonon modes [17–26].

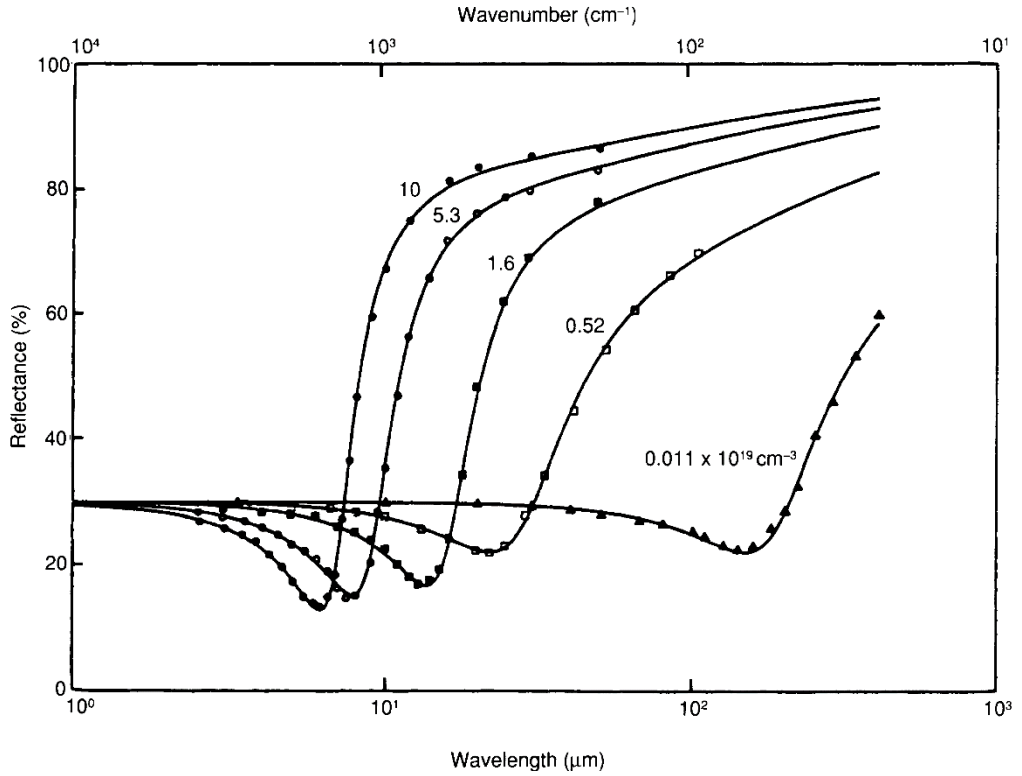

Figure 1.11 *Reflectance spectra for η-silicon, showing the plasma edge as a function of carrier concentration, for η = 1.1 x 10^{17} to 1.0 x 10^{30} cm^{-3}* [34]

1.6.3 Kramers-Kronig Method and Relations

Another powerful method devised by scientists is the Kramers-Kronig method or relation, which is a linearized simple way of estimating the dielectric response function of various structured materials, including amorphous, polycrystalline, single crystalline, and many others. This method allows one to convert complex relations into linear response functions with real and imaginary parts that can be calculated and related to each other using Cauchy integrals. This method was used in recent studies by FTIR spectroscopic analysis, which produced acceptable and accurate results when compared to other techniques. One limitation of this method or analysis is the evaluation of Cauchy integrals or the difficulty in developing programs that can estimate such integrals. The Kramers-Kronig analysis is discussed in this section [17–26].

The Fresnel coefficient of reflectivity is a complex entity, just like the dielectric function defined in the Lorentz method discussed above. It can be expressed as [17–26]:

$$r(\omega) = A(\omega)e^{i\theta(\omega)} \qquad \textbf{Eq. 1.63}$$

Where A is an amplitude and θ is a phase.

The Fresnel coefficient of reflectivity can be linearized in the following way:

$$ln\big(r(\omega)\big) = ln\left(\sqrt{A(\omega)}\right) + i\theta(\omega) \qquad \textbf{Eq. 1.64}$$

What is measured in experiment is the reflectivity defined as $r \times r^*$ where $r^*$is the complex conjugate of r. Thus, a reflectivity measurement yields A^2.
Let us now introduce the Kramers-Kronig theorem, which will be used to calculate the real and imaginary parts of $\ln(r)$ given in ***Eq. 1.64***. The Kramers-Kronig relation states that the response function of a damped harmonic oscillating system is represented by $\boldsymbol{\alpha(\omega) = \alpha 1(\omega) + i\alpha 2(\omega)}$, where α1 and α2 are the real and imaginary parts of the response function, defined as:

$$x(\omega) = \alpha(\omega)F(\omega) \qquad \textbf{Eq. 1.65}$$

Where F(ω) is the total force of the harmonic system given by:

$$m_j \frac{d}{dt}\left(\frac{dx}{dt}\right) + \gamma_j \frac{dx}{dt} + \omega_j{}^2 x = F(\omega) \qquad \textbf{Eq. 1.66}$$

where j denotes the number of oscillators in the system, and m and γ are the mass and damping coefficients, respectively. As a result, the response function, as in Drude and Lorentz oscillators, can be written as:

$$\alpha(\omega) = \sum_{j=1}^{N} \frac{f_j}{\omega_j{}^2 - i\gamma_j\omega - \omega^2} = \sum \frac{f_j\,(\omega_j{}^2 + i\gamma_j\omega - \omega^2)}{(\omega_j{}^2 - \omega^2)^2 + (\gamma_j\omega)^2} \qquad \textbf{Eq. 1.67}$$

Where $f_j = \frac{1}{m_j}$ is a constant and j runs over the number of oscillators or atoms, assuming there are N atoms represented as oscillators within the given system.

To apply the Kramers-Kronig relation, the function has to satisfy the following conditions:

1- The poles of the response function should be located entirely below the real axis.

2- The integral of $\frac{\alpha(\omega)}{\omega}$ should vanish as ω approaches to ∞ in the upper semi-infinite complex ω-plane, with α(ω)→0 as ω→± ∞
3- The real and imaginary parts of the response function (namely α1(ω) and α2 (ω)) should be even and odd to ω respectively.

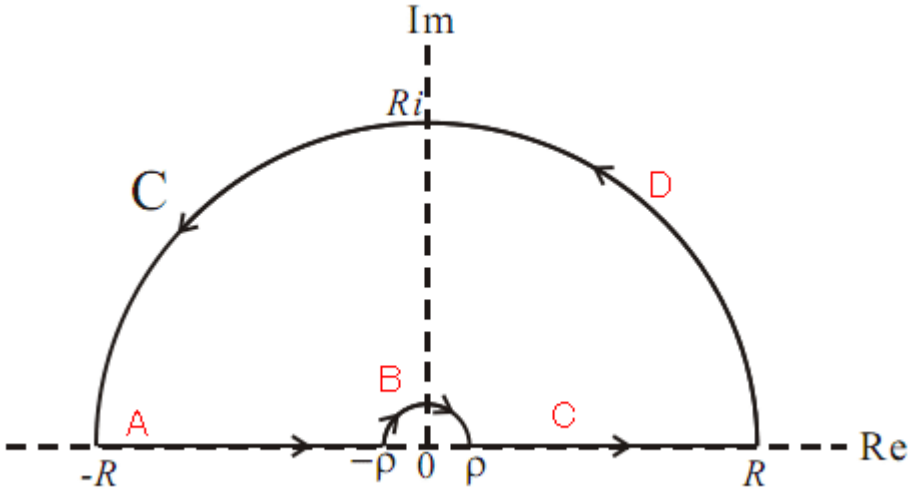

Figure 1.12 *the segments and the upper semi-infinite complex plane for Cauchy integral.*

Having satisfied the above condition, the response function can be evaluated using the Cauchy Integral expressed below:

$$\alpha(\omega) = \frac{P}{i\pi}\int_{-\infty}^{\infty}\frac{\alpha(s)}{s-\omega}\,ds \qquad \textit{Eq. 1.68}$$

where P denotes the principal value of the integral. Integrating over the segment A, then arc B, then Segment C (**Figure 1.12**), the Cauchy integral transforms to:

$$\int_{-\infty}^{\infty}\frac{\alpha(s)}{s-\omega}\,ds \;\rightarrow\; \alpha(\omega)\int_{\pi}^{0}\frac{iue^{i\theta}}{ue^{i\theta}}\,d\theta = -i\pi\alpha(\omega) \qquad \textit{Eq. 1.69}$$

with:

$$s = w + ue^{i\theta} \qquad \textit{Eq. 1.70}$$

Using the even and odd properties of the real and imaginary part of the response function in ***Eq. 1.67***, the above integral can be separated into 2 parts:

$$\alpha 1(\omega) = \frac{P}{\pi}\left(\int_0^{\infty} \frac{\alpha 2(s)}{s-\omega}\, ds + \int_0^{\infty} \frac{\alpha 2(p)}{p-\omega}\, dp \right) \quad \textit{Eq. 1.71}$$

$$\alpha 2(\omega) = -\frac{P}{\pi}\left(\int_0^{\infty} \frac{\alpha 1(s)}{s-\omega}\, ds - \int_0^{\infty} \frac{\alpha 1(p)}{p-\omega}\, dp \right) \quad \textit{Eq. 1.72}$$

In the above equations ***Eq. 1.71*** and ***Eq. 1.72***, p is a dummy variable and can be replaced by s, further reducing to:

$$\frac{1}{s-\omega} + \frac{1}{s+\omega} = \frac{2s}{s^2-\omega^2} \quad \textit{Eq. 1.73}$$

$$\frac{1}{s-\omega} + \frac{1}{s+\omega} = \frac{2s}{s^2-\omega^2} \quad \textit{Eq. 1.74}$$

$$\alpha 1(\omega) = \frac{2P}{\pi}\left(\int_0^{\infty} \frac{s\alpha 2(s)}{s-\omega}\, ds \right) \quad \textit{Eq. 1.75}$$

$$\alpha 2(\omega) = -2\omega\frac{P}{\pi}\left(\int_0^{\infty} \frac{\alpha 1(s)}{s-\omega}\, ds \right) \quad \textit{Eq. 1.76}$$

The Kramers-Kronig relations can be applied to reflectivity measurement to measure the phase of the Fresnel coefficient of reflectivity from the amplitude which is usually measured experimentally. Applying Kramers-Kronig relation, the phase of r takes the form:

$$\theta(\omega) = -\omega\frac{P}{\pi}\left(\int_0^{\infty} \frac{ln(R)}{s-\omega}\, ds \right) \quad \textit{Eq. 1.77}$$

$$\theta(\omega) = -\frac{1}{2\pi}\left(\int_0^{\infty} ln\left(\left|\frac{s+\omega}{s-\omega}\right|\right) \frac{dln\big(R(s)\big)}{ds} ds \right) \quad \textit{Eq. 1.78}$$

The measured amplitude and the calculated phase allow obtaining the Fresnel coefficient of reflectivity r(ω) in the measured spectral range. From the knowledge of r(ω), the complex dielectric function ε(ω) can be obtained from the relation $r(\omega) = \frac{\sqrt{\varepsilon(\omega)}-1}{\sqrt{\varepsilon(\omega)}+1}$.

After presenting the basic physics and optical properties of semiconductors in this chapter, we present in the following chapter the most widely used experimental techniques that take advantage of these properties to measure the thermal properties of semiconductors.

2 Commonly used optical techniques for thermal characterization

The widespread usage of nanostructures and nanomaterials has created a fresh set of problems in thermal management, but it has also opened up new avenues for energy conversion, storage, and generation, as well as a slew of other technical possibilities. Normal thermal calculation techniques hit their limits at the microscale and below, and many innovative approaches have been created to address these limitations. Contactless photothermal approaches have been extensively used in recent years and have shown their benefits in terms of flexibility, temporal and spatial resolution, and even sensitivity in some cases. The thermal properties of bulk materials, thin films, multilayers, suspended structures, and nanomaterials have all been measured using optothermal Raman, Thermo-reflectance, and photothermal beam deflection method. An attempt to briefly cover the fundamentals of these methods with some typical applications is made in this chapter.

For certain technical advancements, a material's ability to conduct heat is of vital importance. Joule heating in microelectronic components is one of the most prominent problems, which limits system efficiency due to inadequate heat dissipation. Thermal conductivity determines a material's ability to dissipate heat; Fourier's law of heat conduction states that the heat flux density over a temperature gradient is the product of thermal conductivity and temperature gradient.

While methods for measuring the thermal conductivity of bulk materials have long been developed, characterizing thin films and interfaces, as well as micro- and nanostructures, which are all extremely common in modern applications, is much more difficult [35,36].

Size effects begin to occur when the structure's characteristic dimensions, such as the thickness of a thin layer, are close to or smaller than the mean free path or wavelength of the heat carriers in the structure, i.e., electrons or phonons, and the thermal behavior is significantly altered relative to the bulk content. This can be seen in thin films by a decrease in thermal conductivity, (also in-plane), below a certain thickness that varies depending on the substrate. Many aspects, from planning to functionalization and design, may affect thermal conductivity at the micro- and nanoscale, and are of considerable importance not only to the scientific/academic community but also to technical applications, as evidenced by various publications, including many review papers [35,37–40].

2.1 Transient Thermoreflectance

2.1.1 Theory

There are two types of thermal characterization techniques: steady state and transient measurements. The Fourier law of heat conduction in its differential form:

$$q = -\kappa \nabla T \qquad \textit{Eq. 2.1}$$

is the basis for steady state measurements. Here, q is the heat flux density, ∇T is the temperature gradient, and κ is the thermal conductivity. The local heat flux and temperature gradient are measured in steady state calculations, and the thermal conductivity can be estimated. Temperature sensors are used to determine the temperature gradient for a spatial difference, and the heat flux is known and is constant over time, i.e., $\delta q/\delta t = 0$.

The steady state techniques have some disadvantages, including parasitic heat loss, temperature sensors contact resistance, lengthy waiting times to achieve steady state. Also, samples must typically be larger than a few millimeters. Transient approaches are often preferred for nanoscale measurements due to these disadvantages.

A time-dependent heat source and a localized temperature probe laser are used in transient measurements. Paddock and Eesley, who used picosecond thermoreflectance to calculate the thermal diffusivity of thin metal films, introduced the time-domain thermoreflectance technique in 1986 [41]. The procedure has also been used to determine the thermal and acoustic properties of bulk samples [42], thin films [43,44], interfaces [45–48] and liquids [49–51] etc. It has also been used to investigate heat transfer fundamentals including phonon scattering processes [52] and non-equilibrium electron–phonon interactions [53,54]. It has also seen widespread use in the field of picosecond ultrasonics. [55] The temperature of the sample is modulated using a pulsed or frequency-modulated laser (the pump beam) in the thermoreflectance technique, and the temperature change is detected by measuring the reflectance of a second laser (the probe beam). The energy of the pump beam pulse is absorbed optically at the sample surface, causing a local temperature rise. The temperature-induced stress at the surface changes its optical properties, resulting in a variation in reflectivity ΔR. This is the thermoreflectance effect [56].

The sample surface is usually coated with a thin metal layer called the transducer to ensure that the pump laser is absorbed at the sample surface. Over a temperature range of a few degrees, the reflectivity change $\Delta R/R$ caused by a temperature change ΔT is linear in the transducer.

$$\frac{\Delta R}{R} = \left(\frac{1}{R}\frac{\delta R}{\delta T}\right)\Delta T = C_{TR}\Delta T \qquad \textit{Eq. 2.2}$$

where C_{TR} is the proportionality constant or thermoreflectance coefficient. C_{TR} is usually in the range of 10^{-5} to 10^{-3} K^{-1}. Optical reflection, light polarization, the interplay of electrical bands and electronic transitions, and electron–phonon interactions all influence a sample's thermoreflectance. As a result, the effect is greatly influenced by the wavelength of the probe beam and the material of the transducer. The measured reflectivity change of the probe beam is an analog for the local temperature change when C_{TR} is known. Since thermoreflectance is a transient process, it does not require knowledge of the absolute temperature increase. However, the wavelength-transducer material couple must be selected in a way to maximize C_{TR} and thus obtain the maximum temperature resolution.

The thermoreflectance technique can be implemented in time-domain thermoreflectance (TDTR) or frequency-domain thermoreflectance (FDTR).

2.1.2 TDTR setup

The thermoreflectance response is measured by the TDTR method as a function of the time between the arrival of the pump and probe pulses on the sample surface, where the pump beam deposits a periodic heat flux on the sample surface and the probe beam detects the resulting temperature shift by reflectance change. **Figure 2.1** shows a schematic diagram of a standard TDTR setup [57].

Due to its excellent beam efficiency and ultrafast pulses, the current most popular TDTR implementation relies on a Ti:Sapphire mode locked laser with a wavelength about 800 nm, a repetition rate of 80 MHz, and laser pulses of 100 fs. An optical isolator is installed at the laser's output to shield the oscillator from back-reflections. The Laser power is modified with λ/2 waveplates along the optical path. to split the laser beam into two, namely the pump beam and the probe beam, a polarizing beam splitter (PBS) change the quantities heading to the pump and probe beam directions, as the probe beam strength centered on the sample should be weak enough in contrast to the pump

beam to prevent the sample self-heating. This solution cross-polarizes the pump and probe beams at the same time, simplifying detection as discussed below.

The pump beam is modulated using an electro-optic modulator (EOM) attached to a function generator. Modulating the beam at frequencies ranging from 0.2 MHz to 20 MHz, is the most general implementation. The susceptibility to basic thermal parameters, specifically thermal conductivity and thermal boundary conductance (TBC), is increased or decreased by using various modulation frequencies [58]. The lock-in amplifier used for signal acquisition uses this frequency generated by the function generator as a reference. For cost-effectiveness, acousto-optic modulators (AOM) may be used instead of EOM [59–62]. However, An AOM runs at lower frequencies (in general <1 MHz), thus it lacks the flexibility of EOMs in terms of studying a wider range of materials and structures. For greater spatial resolution, the pump beam is then centered on the sample using a microscope objective. A mechanical delay line is used to delay the probe beam relative to the pump beam. Because of the probe beam's long optical path, this approach necessitates careful adjustment of the delay stage to prevent signal variations caused by misalignment, which could lead to misinterpretations of the measured values.

After that, the probe beam is centered on the sample in the same way that the pump beam was. Due to the small value of the thermoreflectance coefficient, the reflected pump beam is around 10^4 times more powerful than the thermoreflectance signal. As such, the pump signal should be entirely filtered out, leaving only the probe beam to enter the photodetector, to ensure proper data analysis. Placing a PBS between the objective and the detector will achieve a first stage of filtering with >99 percent efficiency with cross-polarized beams. To gain still more filtering, a second stage is normally paired with the first. There are three different configurations that can be used to do this: 1- Spatial filtering: the pump beam is held parallel to the probe beam but slightly shifted before the focusing objective so that its reflection can be filtered out with an aperture behind which the probe beam is detected by a fast photodetector; 2- the two-tint configuration [63], in which two beams slightly shifted in wavelength, usually at 785 ± 5 nm, are separated with a sharp-edged wavelength filter before the focusing objective; 3- the two-color separation [49,64], with non-linear optical crystals like barium borate (BBO), second harmonic generation will transform any beam—usually the

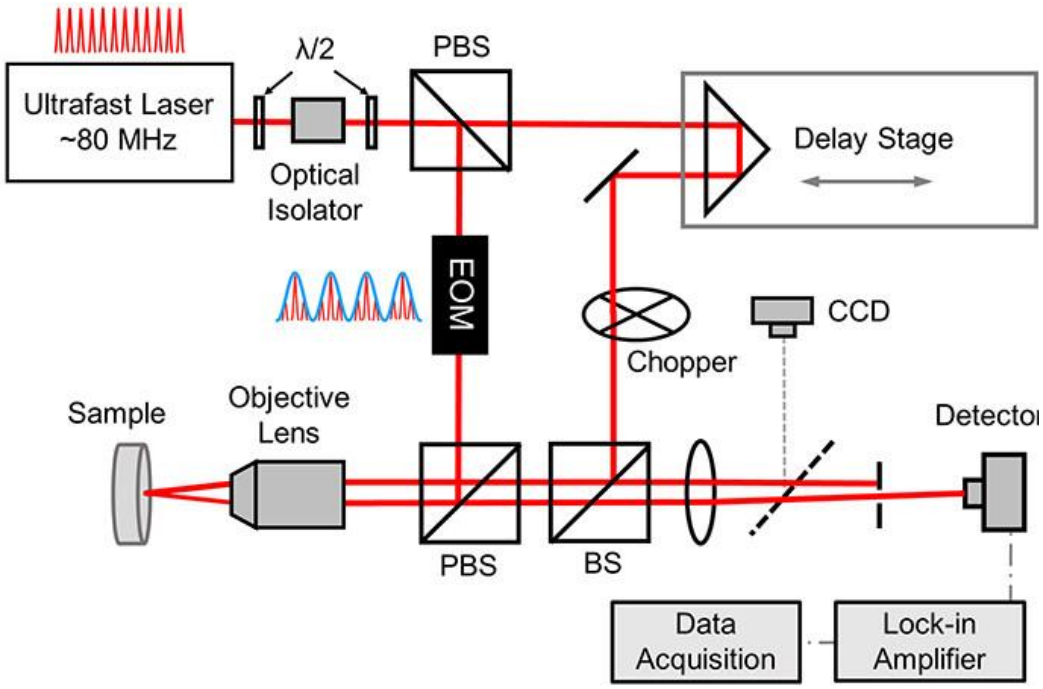

Figure 2.1 *Schematic of a typical transient thermoreflectance setup. The acronyms PBS, BS, EOM, and λ/2 stand for polarizing beam splitter, beam splitter, electro-optic modulator, and half-wave plate, respectively* [57].

pump to maintain an optimum thermoreflectance coefficient—to 400 nm, allowing for simple color separation and filtering. The first design is simpler to apply but only works with optically flat samples (surface roughness < 15nm), while the other two work for optically rough samples, but also limit the available laser power, which might make it difficult to test certain high thermal conductivity materials like diamond, depending on the initial power and efficiency of the second harmonic generation.

A fast-response photodiode detector collects the reflected probe beam and converts the optical signals into electrical signals. The photodetector's RF electrical signal is then fed into a lock-in amplifier that is synced to the EOM modulation frequency. At the modulation frequency, the RF lock-in amplifier produces an in-phase (Vin) and an out-of-phase ($Vout$) signal. The selection of a lock-in amplifier should be done with caution. While higher harmonics can be used to calculate thermal properties [58], using the fundamental frequency eliminates data processing complications. In fact, if the EOM modulation output is a square wave, a lock-in amplifier with sine wave multipliers is desired to prevent signal interference with higher square wave harmonics. If the pump beam modulation is a sine wave, a more cost-effective alternative may be chosen. By adding modulation to the probe signal, (by means of a chopper for

example as shown in **Figure 2.1**) a double lock-in scheme may be implemented to prevent coherent signal pick-up at the detector frequency [65].

A reversible flip-mirror in front of the aperture or the filter accompanying the detector is typically used to allow a complementary metal–oxide–semiconductor (CMOS)/charge–coupled device (CCD) camera to monitor the sample surface and pump and probe beams. This ensures that the pump and probe beams are aligned and focused on the sample surface. To obtain the thermal properties of the sample in most TDTR experiments, the signals are taken as the phase of the observed temperature response as conveyed by the reflected probe beam, computed as $\varphi = tan^{-1}(Vout/Vin)$, or equivalently the ratio $R = -Vin/Vout$. The benefit of using the phase signal for data reduction over the amplitude signal is that it does not require normalization. Furthermore, when the $Vout$ signal is weak, the normalized amplitude signal loses sensitivity to the sample's thermal properties. However, care must be taken to account for the additional phase shift induced into the measured signals by wires, electronic devices, and optical components. The fact that the $Vout$ signal in TDTR experiments should be constant over the zero-delay period can usually be used to cancel this phase shift caused by the instrumentation.

Due to its high absorption (the 99% absorption depth is 60 nm) and an unusually large thermoreflectance coefficient $dR/dT \sim 10^{-4}\,K^{-1}$ at the 800nm wavelength, an Al thin layer with a thickness of ~100 nm is a typical option for the transducer layer for a Ti:sapphire oscillator whose wavelength is centered around 800 nm. Because of this high thermoreflectance coefficient, the thin metallic transducer layer not only allows for the assumption of a surface heat flux boundary condition, simplifying the analysis, but it also increases the overall SNR.

Aside from the unknown thermal properties of the sample layer to be calculated, there are several other input parameters that influence the signals in TDTR experiments that must be pre-determined as precisely as possible (such as the laser spot size, thermal conductivity of the transducer layer, thickness and heat capacity of each layer in the sample stack). The most popular methods for determining these input parameters are briefly listed below:

While several methods, such as the knife-edge method and patterned sample image method, can be used to characterize the laser spot size, measuring the spatial correlation between the pump and probe focal spots is a precise and simple-to-use methodology for TDTR. With a positive delay time of ~100 ps and a high modulation frequency of 10 MHz, the pump beam spot is swept across the probe beam spot in this process. Fitting the Vin profile to a Gaussian function $Vin \sim exp(-x_c^2/w_0^2)$, where x_c is the offset distance, yields the root-mean-square (RMS) average of the pump and probe spots w_0. Since the TDTR signals are influenced by the RMS average of the pump and probe spot sizes

rather than their individual sizes, this basic approach works well for TDTR studies (see Section 2.1.3 for more information on thermal modeling).

The thermal conductivity of the metal transducer layer can be determined using a four-point probe electrical resistance measurement and the Wiedemann-Franz law, $K_m = L_m T/RC'h_m$,where L_m is the Lorenz number for the metal film, T is the temperature, R is the electrical resistance measured using a four-point probe, and C' is a constant related to the sample lateral size and the spacing between the probe needles. Picosecond acoustics may be used to calculate the metal transducer thickness h_m. As metal film is deposited on the sample, a wide and clean glass slide is normally placed next to the sample, and the four-point probe measurement is done on the metal film deposited on the glass slide instead. The four-point probe measurements are usually only done at room temperature. The additional electrical resistivity of the metal film relative to its pure bulk equivalent is thought to be primarily caused by temperature-independent impurity scattering, in order to be able to evaluate the thermal conductivity of the metal film at other temperatures. The four-point probe at room temperature will thus estimate the additional electrical resistivity of the metal film, which, when added with the temperature-dependent thermal conductivity of its bulk equivalent from the literature, provides the temperature-dependent thermal conductivity of the metal film.

The heat capacities of the metal transducer film and sub-layers are usually considered to be the same as those of their bulk form and can be found in the literature. Frequency-dependent TDTR tests will concurrently assess the thermal conductivity and heat capacity of samples whose heat capacities are not commonly available in the literature or are not observable using standard techniques such as differential scanning calorimetry.

For TDTR experiments, an estimate of the steady-state temperature rise is also necessary, as the temperature rise must be minimal (usually less than 10 K) to ensure that the reflectance variation is linearly proportional to the temperature change. $\Delta T = \frac{A_0}{2\sqrt{\pi} w_0} \frac{1}{K}$, (where A_0 is the laser power absorbed by the sample), is Cahill's [66] term for steady-state temperature increase for a semi-infinite solid. The temperature increase for thin layers and interfaces can be calculated as $\Delta T = \frac{A_0}{\pi w_0^2} \frac{h}{K}$ and $T = \frac{A_0}{\pi w_0^2} \frac{1}{G}$, respectively. Please keep in mind that these formulas are only meant to be used as a rough estimate. More elaborate derivations can be found in reference [67]. Thermal properties are normally extracted using a multilayer model. Details are given in the next section.

2.1.3 Thermal model and signal analysis

TDTR is used to determine thermal transport properties by modifying free parameters (unknown thermal properties) in a thermal transport model to achieve the best fit between the model prediction and the experimental results. Despite considerable progress in observing fascinating or even counter-intuitive phenomena in nanoscale thermal transport, most studies still use the effective thermal conductivity of nanostructured materials as a shared language to understand observations and interact through communities in physics, materials, and engineering. The bulk of the theoretical work in the literature used Fourier's law of heat conduction with an effective thermal conductivity to derive thermal properties. When applying a diffusive thermal transport model to systems where phonons with long mean-free paths (MFPs) carry a large fraction of the heat, caution is advised [68–71] .

Early TDTR data reduction methods may only be extended to a few simple situations with a lot of assumptions. Cahill [66] made a significant contribution to the data interpretation of TDTR studies in 2004. The so-called "pulse accumulation" effect was taken into account when solving the three-dimensional heat diffusion equation via multi-layered structures, i.e., the contribution of a new pulse must account for the previous pulse that has not dropped to a negligible value. Schmidt's model [72] for anisotropic heat conduction was expanded to include thin films, which are most likely anisotropic due to the size effect of energy carriers. Though further simulation work is required for TDTR calculations in different complex contexts, the thermal model for the most common case in TDTR experiments is highlighted here.

Figure 2.2 depicts a diagram of the sample structure used in TDTR studies. Both the laser profile and the thermal properties of the sample are presumed to be axisymmetric rather than in-plane anisotropic in this simple model; both heating and sensing take place on the sample's top surface; and the different phonon modes are assumed to be in thermal equilibrium, resulting in effective thermal properties Kr, Kz, C, and G can be considered for each layer. The thermal modeling of TDTR experiments consists of two steps: the first is to solve heat diffusion in a multilayer stack, and the second is to model the data collected from the experiments.

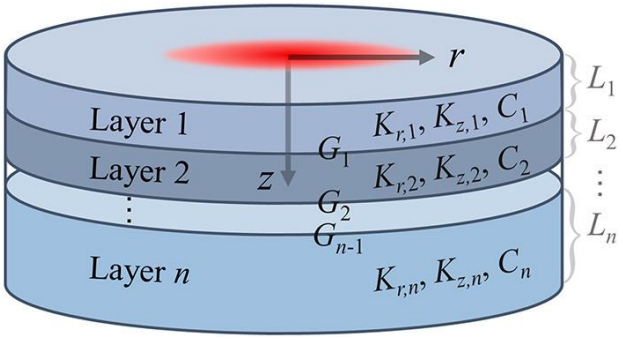

Figure 2.2 *Schematic of a typical Multi-layered sample in thermoreflectance measurements. The acronyms K_r, K_z, stand for Thermal Conductivities in the radial and through-plane direction respectively. C is the volumetric heat capacity. G is the interfacial thermal conductance between 2 layers* [57].

2.1.3.1 Solution of multi-layered sample heat diffusion equation

Several papers have been published on the use of layered structures to solve the one-dimensional heat diffusion equation [73–75]. Feldman's algorithm [74,75] was expanded to three-dimensional heat conduction by Cahill [66], who used it to measure thermal responses in TDTR. Schmidt [76], on the other hand, took Carslaw and Jaegar's [73] solution to heat conduction in solids and generalized it to account for three-dimensional and anisotropic heat conduction. Using a quadrupole method [77], we summarize the solution of the anisotropic heat diffusion equations in cylindrical coordinates for a multilayered structure. The governing equation based on Fourier's law of heat conduction is written as:

$$C\frac{\partial T}{\partial t} = \frac{\eta K_z}{r}\frac{\partial}{\partial r}\left(r\frac{\partial T}{\partial r}\right) + K_z\frac{\partial^2 T}{\partial z^2} \qquad \textbf{Eq. 2.3}$$

where Kr and Kz are the sample's thermal conductivities in the radial and through-plane directions, respectively, $\eta = K_r/K_z$ is the anisotropic thermal conductivity parameter, and C is the volumetric heat capacity. This parabolic partial differential equation can be simplified into an ordinary differential equation by applying the Fourier transform to the time variable t and the Hankel transform to the radial coordinate r [25]:

$$\frac{\partial^2 \Theta}{\partial z^2} = \lambda^2 \Theta \qquad \textbf{Eq. 2.4}$$

Where Θ is the Frequency domain temperature, $\lambda^2 = 4\pi^2 k^2 \eta + i\omega C/K_z$. k is the Hankel transform variable, and ω is the angular frequency [25]. The solution for this differential equation can be expressed as follows:

$$\Theta = e^{\lambda z} B^+ + e^{-\lambda z} B^- \qquad \textbf{Eq. 2.5}$$

B^+, B^- are 2 complex constants to be determined upon the boundary conditions.

Eq. 2.1 and ***Eq. 2.5*** lead to the heat flux $Q = -K_z(\frac{d\Theta}{dz})$, and can be written as:

$$Q = \gamma(-e^{\lambda z} B^+ + e^{-\lambda z} B^-) \qquad \textbf{Eq. 2.6}$$

where $\gamma = K_z \lambda$.

Eq. 2.5 and ***Eq. 2.6*** can be written as matrices to simplify the derivations:

$$\begin{bmatrix} \Theta \\ Q \end{bmatrix}_{i,z=L} = \begin{bmatrix} 1 & 1 \\ -\gamma_i & \gamma_i \end{bmatrix} \begin{bmatrix} e^{\lambda L} & 0 \\ 0 & e^{-\lambda L} \end{bmatrix}_i \begin{bmatrix} B^+ \\ B^- \end{bmatrix}_i = [N]_i \begin{bmatrix} B^+ \\ B^- \end{bmatrix}_i \qquad \textbf{Eq. 2.7}$$

B^+, B^- are the properties of layer i. By matrix inversion of ***Eq. 2.7***, and substituting L=0, we obtain:

$$\begin{bmatrix} B^+ \\ B^- \end{bmatrix}_i = \frac{1}{2\gamma_i} \begin{bmatrix} \gamma_i & -1 \\ \gamma_i & 1 \end{bmatrix} \begin{bmatrix} \Theta \\ Q \end{bmatrix}_{i,z=0} = [M]_i \begin{bmatrix} \Theta \\ Q \end{bmatrix}_{i,z=0} \qquad \textbf{Eq. 2.8}$$

Another matrix is used as the relation between the heat flux and the temperature at the top of a lower layer (i+1, z=0) to those at the bottom of an upper layer (i, z=L), where heat is transferred through the interface:

$$\begin{bmatrix} \Theta \\ Q \end{bmatrix}_{i+1,z=0} = \begin{bmatrix} 1 & -1/G \\ 0 & 1 \end{bmatrix}_i \begin{bmatrix} \Theta \\ Q \end{bmatrix}_{i,z=L} = [R]_i \begin{bmatrix} \Theta \\ Q \end{bmatrix}_{i,z=L} \qquad \textbf{Eq. 2.9}$$

G is the interface conductance between the 2 consecutive layers. The temperature and the heat flux relation between the bottom of the layered sample with respect to those on the top sample surface would become:

$$\begin{bmatrix}\Theta\\Q\end{bmatrix}_{i=n,z=L_n} = [N]_n[M]_n \dots [R]_1[N]_1[M]_1 \begin{bmatrix}\Theta\\Q\end{bmatrix}_{i=1,z=0} = \begin{bmatrix}A & B\\C & D\end{bmatrix}\begin{bmatrix}\Theta\\Q\end{bmatrix}_{i=1,z=0} \quad \textbf{Eq. 2.10}$$

The boundary conditions at the bottom of the substrate allows us to consider $Q_{z\to\infty} = 0$. Substituting in ***Eq. 2.10***: $0 = \mathrm{C}\Theta_{i=1,z=0} + \mathrm{D}Q_{i=1,z=0}$.

The temperature response versus the applied heat flux of unit (which is essentially Green's function $\hat{G}$ [66]) can be written as:

$$\hat{G}(k,\omega) = \frac{\Theta_{i=1,z=0}}{Q_{i=1,z=0}} = -\frac{D}{C} \quad \textbf{Eq. 2.11}$$

Now with $\hat{G}$ known, the temperature response is simply the product of this function with the heat source flux at the surface (in the frequency domain).

2.1.3.2 Model of the different acquired signals

To model the different signals, we start by considering the laser pulses as Dirac delta function (δ), since the pulse duration is quite short (< 0.5 ns) compared to the pulsing rate at 80 MHz (12.5 ns). The pump laser intensity can be written in real space as:

$$p_1(r,t) = \frac{2A_1}{\pi w_1^2} exp\left(-\frac{2r^2}{w_1^2}\right) e^{i\omega_0 t} \sum_{n=-\infty}^{\infty} \delta(t - nT_s - t_0) \quad \textbf{Eq. 2.12}$$

Representing a train of pump beam pulses modulated by a sinusoidal wave of frequency ω_0. T_s is the period of the laser pulsing repetition rate. $T_s = \frac{1}{f_{rep}} = 2\pi/\omega_s$. A_1 is the average laser power. w_1 is the laser radius. t_0 is an arbitrary time shift for the laser pulses.

By applying Hankel space transform and Fourier time transform, on ***Eq. 2.12***, we obtain the following:

$$P_1(k,\omega) = A_1\, exp(-\pi^2 k^2 w_1^2/2)\omega_s \sum_{n=-\infty}^{\infty} \delta(\omega - \omega_0 - n\omega_s)\, e^{-in\omega_s t_0} \quad \textbf{Eq. 2.13}$$

Substituting ***Eq. 2.13*** in ***Eq. 2.11***, leads to the following:

$$\Theta(k,\omega) = P_1(k,\omega)\hat{G}(k,\omega) \qquad \textit{Eq. 2.14}$$

The temperature distribution on the surface due to the modulated pump beam, can be derived by applying inverse Hankel transform to the previous equation, leading to:

$$\Theta(r,\omega) = \int_0^\infty P_1(k,\omega)\hat{G}(k,\omega)\, J_0(2k\pi r)2\pi k dk \qquad \textit{Eq. 2.15}$$

The inverse Fourier transform would give the temperature distribution with respect to time $\theta(r,t)$.

Similarly, the probe beam, that detects the temperature variation due to the pump beam pulses, has the following intensity form:

$$p_2(r,t) = \frac{2A_2}{\pi w_2^2} exp\left(-\frac{2r^2}{w_2^2}\right) e^{i\omega_0 t} \sum_{m=-\infty}^{\infty} \delta(t - mT_s - t_0 - t_d) \qquad \textit{Eq. 2.16}$$

And in frequency domain through Fourier transform, it takes the following expression:

$$p_2(r,\omega) = \frac{2A_2}{\pi w_2^2} exp\left(-\frac{2r^2}{w_2^2}\right) \sum_{m=-\infty}^{\infty} \delta(\omega - m\omega_s) e^{-im\omega_s(t_0+t_d)} \qquad \textit{Eq. 2.17}$$

A convolution between the sample surface temperature profile and the probe profile, would lead after some derivations to the following form [76]:

$$\Delta\Theta(\omega) = A_1 \int_0^\infty \sum_{n=-\infty}^{\infty} \delta(\omega - \omega_0)\hat{G}(k,\omega_0 + n\omega_s) e^{in\omega_s t_d} \times exp[-\pi^2 k^2 (w_1^2 + w_2^2)/2] 2\pi k dk \qquad \textit{Eq. 2.18}$$

Let $w_0 = \sqrt{(w_1^2 + w_2^2)/2}$ (the RMS average of the probe and pump beam radii). We can express the temperature response due to harmonic heating as follows:

$$\Delta T(\omega) = A_1 \int_0^\infty \hat{G}(k,\omega) exp(-\pi^2 k^2 w_0^2) 2\pi k dk \qquad \textit{Eq. 2.19}$$

Substituting the above in ***Eq. 2.18*** leads to the following:

$$\Delta\Theta(\omega) = \delta(\omega - \omega_0) \sum_{n=-\infty}^{\infty} \Delta T(\omega_0 + n\omega_s) e^{in\omega_s t_d} \qquad \textit{Eq. 2.20}$$

By inverse Fourier transform, we obtain the signal that is measured by the detector, expressed in the time domain.

$$\Delta R(t) = e^{i\omega_0 t} \sum_{n=-\infty}^{\infty} \Delta T(\omega_0 + n\omega_s) e^{in\omega_s t_d} \qquad \textit{Eq. 2.21}$$

The acquired signal is passed through the lock-in amplifier which multiplies it by a reference in-phase, and another reference out of phase (shifted by 90 degrees), both at frequency ω_0 [78]. We obtain the following two components,

$$V_{in} = Re[\Delta R(t)] = \frac{1}{2} \sum_{n=-\infty}^{\infty} [\Delta T(\omega_0 + n\omega_s) + \Delta T(-\omega_0 + n\omega_s)] e^{in\omega_s t} \qquad \textit{Eq. 2.22}$$

$$V_{out} = Im[\Delta R(t)] = \frac{1}{2} \sum_{n=-\infty}^{\infty} [\Delta T(\omega_0 + n\omega_s) - \Delta T(-\omega_0 + n\omega_s)] e^{in\omega_s t_d} \qquad \textit{Eq. 2.23}$$

The above signals emanating from the lock-in amplifier are measured for different values of time delay t_d. Fitting the ratio of $-V_{in}/V_{out}$ to the thermal model would allow measurement of the different sample thermal parameters (K_z, K_r, G) [66].

2.2 Opto-thermal Raman

As previously mentioned, Raman spectroscopy allows for the detection of infrared vibrational modes that would otherwise go undetected or inactive using Fourier or infrared spectroscopic analysis. From this point of view, Raman spectrometers became a part of a scientists' daily lives in the laboratory. Furthermore, the rapid advancement seen in thin film manufacturing and

property investigation necessitates ongoing adjustments and advancement to experimental measuring tools, and Raman spectroscopy is no exception. One such progress, as previously mentioned, is the introduction of opto-thermal Raman spectrometers, which are increasingly being used in thermal and optical analysis. To that end, the goal of this section is to introduce the reader to such systems, namely opto-thermal Raman spectrometers, by discussing their theoretical background and application.

Raman thermometry, also known as opto-thermal thermometry, is a type of thermometry, that uses light within Raman spectroscopy, is a straightforward, steady-state, destruction less (damage less) technique for measuring the thermal properties of any material, specifically its thermal conductivity, by using the Raman signal as thermometer [79,80]. The Raman Signal is studied in order to estimate local temperature and visualize temperature-related phonon properties. The determination of the temperature ratio between Stokes and Anti-Stokes intensities, as expressed below, is one of the widely used methods.

$$\frac{I_A}{I_S} = A\frac{n}{n+1} = Ae^{-\frac{\hbar\omega}{K_B T}} \qquad \textit{Eq. 2.24}$$

Where $\hbar$, ω, K_B, and T, denotes the reduced Planck constant, angular frequency of phonons, Boltzmann constant and the temperature respectively. A is a normalization or calibration constant experimentally determined and n is the phonon population, or phonon volumetric-density of state in energy levels involved in anti-stokes and stokes processes.

Another method for estimating temperature from Raman spectra is to use the peak position and FWHM, both of which are temperature sensitive and dependent. Because of the anharmonicity of the lattice potential, an increase (decrease) in temperature causes thermal expansion (contraction) and hence a change in interatomic forces. The position of the Raman peak changes as the aforementioned changes at the level of interatomic forces, results in a redshift to lower wave numbers as the temperature rises. It is worth to mention that the broadening of the linewidth determined by Raman spectroscopy, is due to the temperature dependence of phonon lifetime, originated from an-harmonic terms with the interacting potential. As a result, spectral position peaks and FWHM of the desired sample, are thoroughly analyzed as the sample is replaced under the laser spot within the mentioned spectrometer, as a mean of determining its temperature change and determining that desired thermal properties.

The Raman peaks and their positions are highly dependent and sensitive to experimental conditions, which is one of the method's drawbacks. The normalizing or calibration constant may also play a role in peak position,

but the dependence of these peaks on sample structure and purity is a well-known issue. As a result, impurities, defects, and voids play a role at the level of these peaks, resulting high uncertainty in estimating properties. However, these are technical issues that can be resolved during the experimental or deposition phases. As a result, the method has been widely used in crystallized semiconductors, insulators and metals, thin films, and especially two-dimensional samples, yielding fairly accurate results. It is critical to draw the reader's attention to the fact that the method fails for amorphous samples or systems due to a lack of symmetry and crystalline structure or shape.

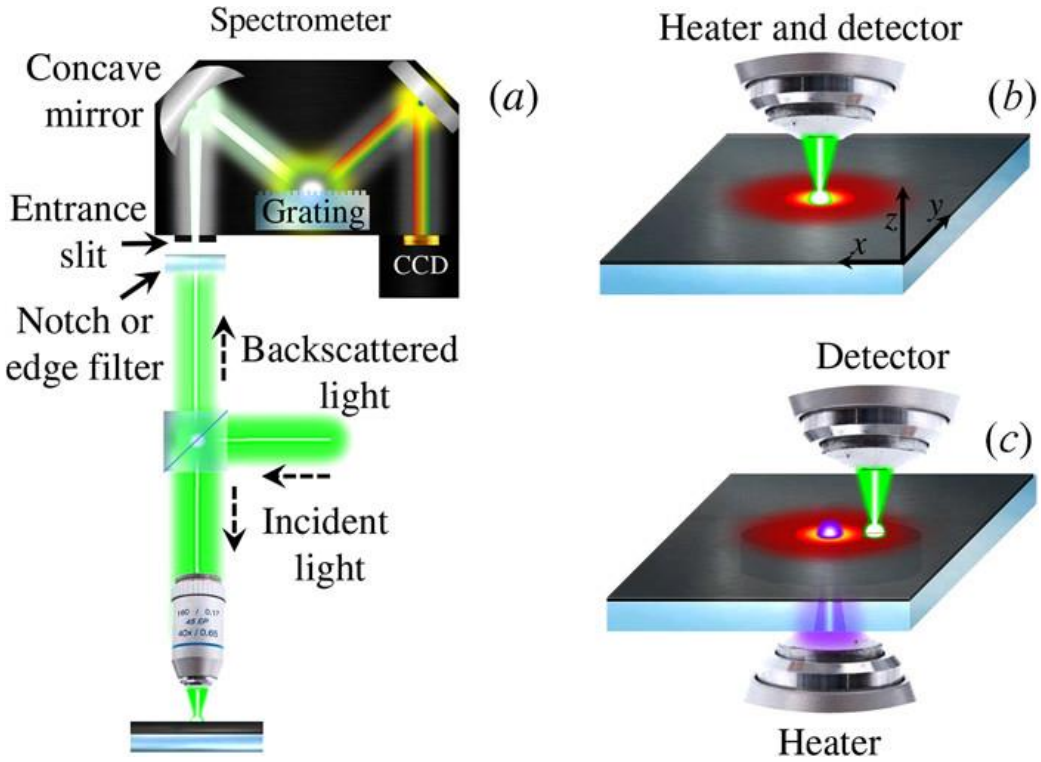

Figure 2.3: *Figure showing a Raman spectrometry (a) and Raman thermometry or opto-thermal Raman spectroscopy (b & c)* [79].

2.2.1 Raman Thermometry: single laser configuration

Raman spectrometers or thermometers (with a single laser source), use laser excitation as a heat source as well as a temperature monitor at the same time. A microscope objective focuses the excited laser on the sample surface. Varying the power of the incident laser beam affects the local temperature of the sample. It's worth noting that the temperature variation on the sample is strongly dependent on the sample's optical and thermal properties. As a result, thermal conductivity can be estimated using measurements of thermal diffusivity taken by this method, by using a certain thermal model. We assume that the absorbed laser light is equal to the power density for heating the sample, expressed as:

$$P(x,y,z) = \alpha_0 \frac{2P_a}{\pi\sigma^2}\, e^{-2\left(\frac{x^2+y^2}{\sigma^2}\right)} e^{-a_o z} \qquad \textit{Eq. 2.25}$$

The above equation can be modified by transferring from cartesian to cylindrical coordinates as follows:

$$P(r,z) = \alpha_0 \frac{2P_a}{\pi\sigma^2}\, e^{-2\left(\frac{r^2}{\sigma^2}\right)} e^{-a_o z} = P(r)f(z) \qquad \textit{Eq. 2.26}$$

Where P(r) denotes the radial component of the power density and f(z) the z-plane or out of plane component. Furthermore, P_a, α_o, and σ denote the absorbed power, optical absorption coefficient, and the laser beam's spot radius, respectively. Each material's thermal conductivity can be measured, by suffixing to isotropic and semi-infinite material:

$$K = \frac{P_a}{4\,\Delta T\,\sigma\sqrt{\pi}} \qquad \textit{Eq. 2.27}$$

Where $\Delta T = T_{measured} - T_{sink}$ is the temperature difference between the warmed sample and the surrounding atmosphere, which serves as a heat sink; this value represents the sum of temperature increase. Since the laser is heating and probing the sample at the same time, the temperature measured should be calculated and believed to be spatially distributed similarly to that of power density, as stated explicitly below:

$$T_{measured} = \frac{\int_0^\infty T(r) e^{-(\frac{r^2}{\sigma^2})} r dr}{\int_0^\infty e^{-(\frac{r^2}{\sigma^2})} r dr} \qquad \textit{Eq. 2.28}$$

Where T(r) is the temperature distribution, which follows the same trend as the laser density distribution, as seen below:

$$T(r) = \frac{2P_a}{K\sigma\sqrt{\pi}} e^{-2(\frac{r^2}{\sigma^2})} I_O(2\left(\frac{r^2}{\sigma^2}\right)) \qquad \textit{Eq. 2.29}$$

Where I_o denotes the modified Bessel function of zeroth order. One should be careful when using materials with low absorbance, since these materials can repel a considerable portion of the laser light, recommending, for such cases, semi-analytical and simulation research.

Raman thermometry has the advantage of being able to achieve sub-micrometer and, in some cases, nanometer resolution, which allows for the analysis of thermal properties at these ranges of resolution or depth. Such credentials in Raman Spectroscopy and thermometry have been greatly improved, and they are being further demonstrated in experimental sectors and facilities. One such advancement was the introduction of Tip Enhanced Raman Spectroscopy or thermometry, which allowed the study of optical and thermal properties at nanometer even reaching 10 nm resolutions.

Another breakthrough for measuring thermal properties using Raman thermometry is the use of Finite Element schemes (FEM), as such simulations provide for greater flexibility in adjusting the laser heating capacity and visualizing its impact on the thermal properties under investigation. Furthermore, such simulation can be extended to any substance, even complicated materials that can be difficult to produce at times. It may also expand the field of study that affects thermal properties within the studied samples by adding boundary conditions, grain-size, and limits, extending the finite size of the sample, structures, impurities, and several heating sources or processes such as heat conduction or convection from the atmosphere.

The calculation of absolute absorbed power results in a typical source of error and confusion in such approaches. Since the temperature increase is directly proportional to the spread of laser power, any change in laser power would influence thermal conductivity or the measured thermal property. To avoid such errors, the calculation power absorption should include or pass through the steps shown in the figure below:

1. Calibration of incident laser power with secondary sensors

2. Calibration of reflected power with secondary sensors using highly reflective mirrors and optical devices.
3. Finally simultaneous measurement of incident reflected and transmitted powers using the sample.

These calibrations consider all potential losses, such as absorption and reflection from the microscope's various components and instruments. To mitigate or even prevent nonlinear responses from optical devices, it is best to calculate the power in relation to incident capacity. As a result, after properly adjusting the laser light on the sample surface, the reflectance, absorbance, and transmittance are determined from incident, reflected, and transmitted powers. The absorbance for instance is calculated as follows:

$$A = 1 - R - T = 1 - \frac{P_r}{P_i} - \frac{P_t}{P_i} \qquad \textbf{Eq. 2.30}$$

Where A, R and T are the relative absorptivity, reflectivity and transmittivity respectively and P_i, P_r, and P_t denote the incident, reflected and transmitted power.

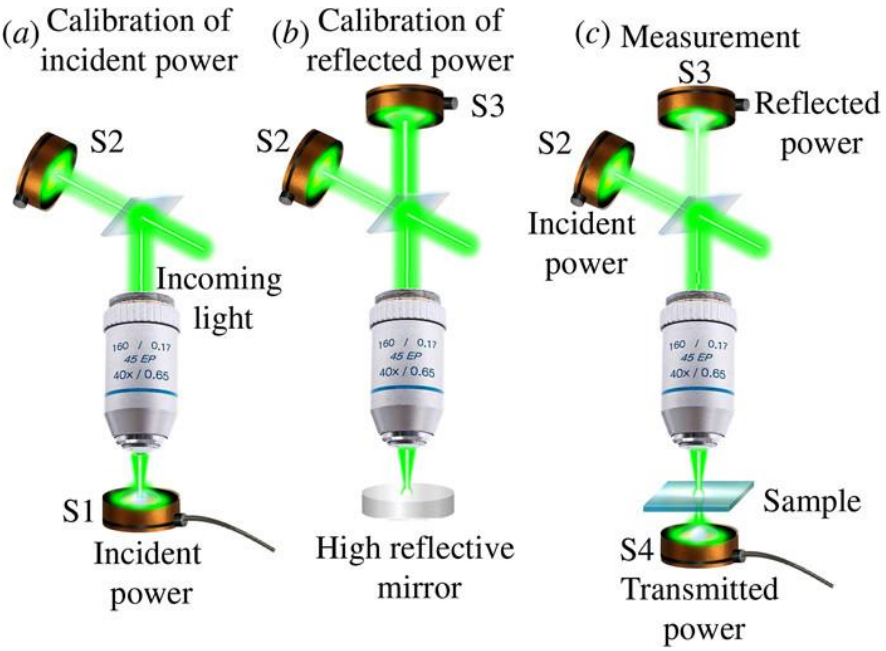

Figure 2.4: *Schematic representation of the Raman thermometry and the calibration steps followed* [79]

2.2.2 Two-laser Raman thermometry

The heating and low power density dispersed laser are segregated in this process, which is close to that of single laser Raman thermometry. It is worth noting that the heating laser is centered on the lower section of the examined sample, while the low powered laser is focused on the upper section of the above samples. The benefit of a two-laser device over a single laser process is that thermal conductivity or thermal property calculation is independent of weight distribution. As a result, this method does not take into account the absorbing strength of the sample, particularly when the sample is 2-D, and instead provides a thermal map, facilitating thermal property analysis.

This method is similar to that of a single laser Raman thermometry with the following minor difference: the heating laser and low power probe laser are separated. The heating laser is focused on the lower section of the investigated sample, whereas the low power laser on the upper section of the mentioned samples as shown in **Figure 2.4**(c). The advantage of the two-laser system over that of single laser method, is the independence of thermal conductivity or thermal property measurement from the absorbed power distribution. Thus, the two-laser method does not need to make some assumptions about the power absorbed in the sample, especially when the sample is a 2-D one, it directly provides the thermal map, thus facilitating thermal property analysis.

In the case of two-dimensional samples, there is no temperature variation along the third dimension, which is also assumed to be purely diffusive, with an analytical model that follows Fourier's law, as expressed below:

$$\frac{P_a}{A} = -K(T)\frac{dT}{dr} \qquad \textit{Eq. 2.31}$$

Where P_a represents absorbed power, A, K and T denote cross-sectional area, the thermal conductivity, and the temperature respectively. With the thickness of the sample t given the cross-sectional area can be reduced to:

$$A = 2\pi tr \qquad \textit{Eq. 2.32}$$

When the heat flux is enclosed in a hypothetical cylinder with radius r, the previous equation can be written as follows:

$$\frac{P_a}{2\pi t} = -K(T) r \frac{dT}{dr} \qquad \textit{Eq. 2.33}$$

$$\frac{P_a}{2\pi t} = -K(T) \frac{dT}{d(ln(r))} = -K(T)\theta(r) \qquad \textit{Eq. 2.34}$$

As a result, the thermal conductivity can be estimated as:

$$K(T) = -\frac{P_a}{2\pi t \theta(r)} \qquad \textit{Eq. 2.35}$$

In case the thermal conductivity is independent of temperature and radial position r, i.e. constant, the variation of the temperature within the sample can be obtained analytically and can be fitted linearly on a log-lin plot:

$$dT = \frac{-P_a}{2\pi t K r} dr \qquad \textit{Eq. 2.36}$$

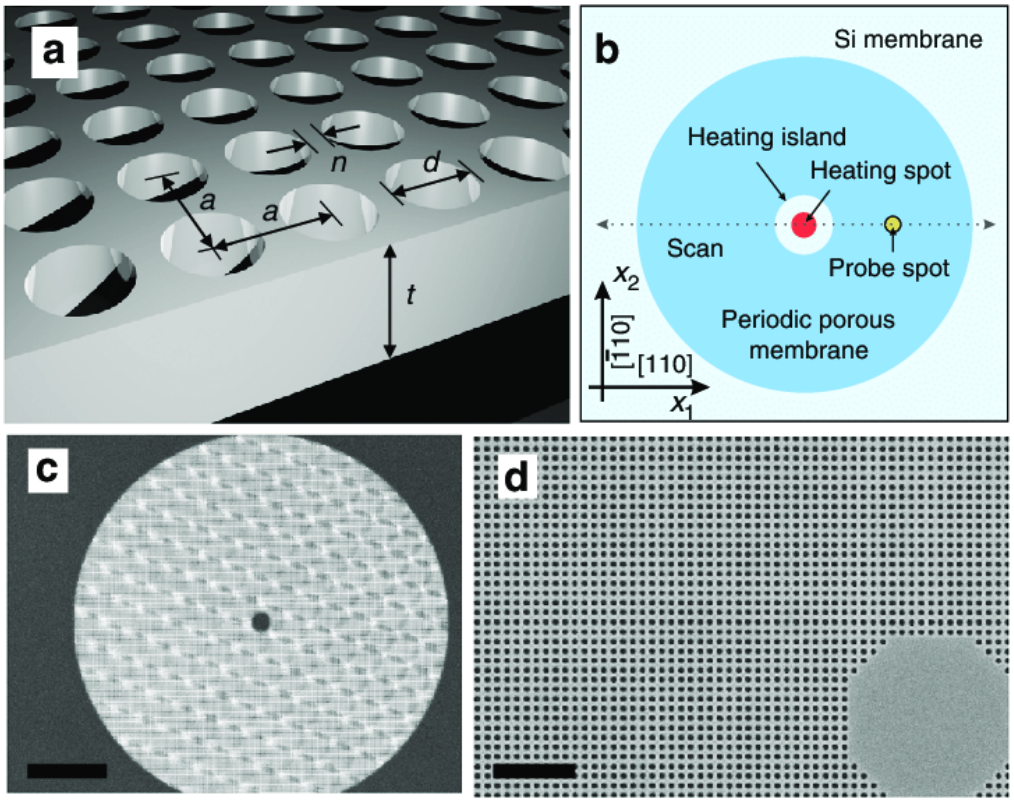

Figure 1.1: *Schematic representation of thermal conductivity calculation of 2-dimensional cylindrical sample using 2 laser Raman thermometer* [81].

Integrating we obtain:

$$\int_{T_O}^{T} dT = \int_{r_o}^{r} \frac{-P_a}{2\pi t K r}\, dr \qquad \textit{Eq. 2.37}$$

$$T = T_0 + \frac{P_a}{2\pi t K}\, ln(\frac{r_o}{r}) \qquad \textit{Eq. 2.38}$$

However, at elevated temperature, the thermal conductivity is not independent of temperature and should be considered in the above analysis, usually, for semiconductors, the thermal conductivity varies as $\frac{1}{T^x}$ where x is an integer.

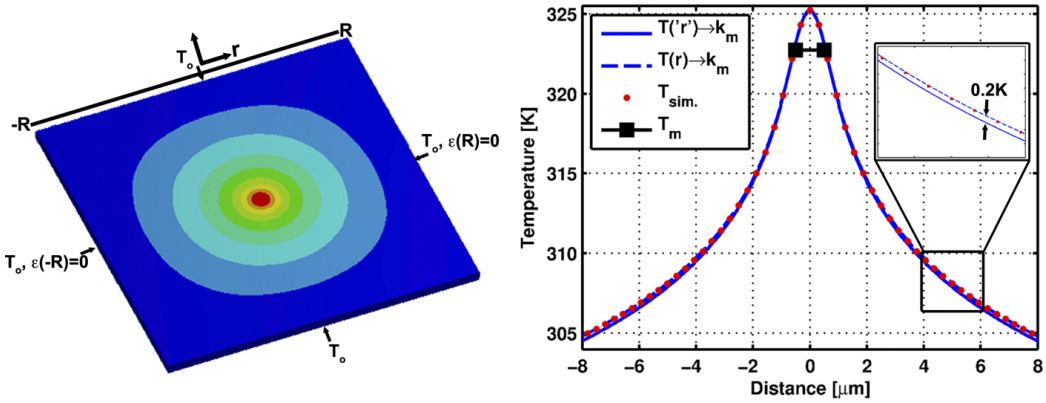

Figure 1.2: *figure showing the temperature variation within a sample measured using 2 – laser Raman thermometry* [82]

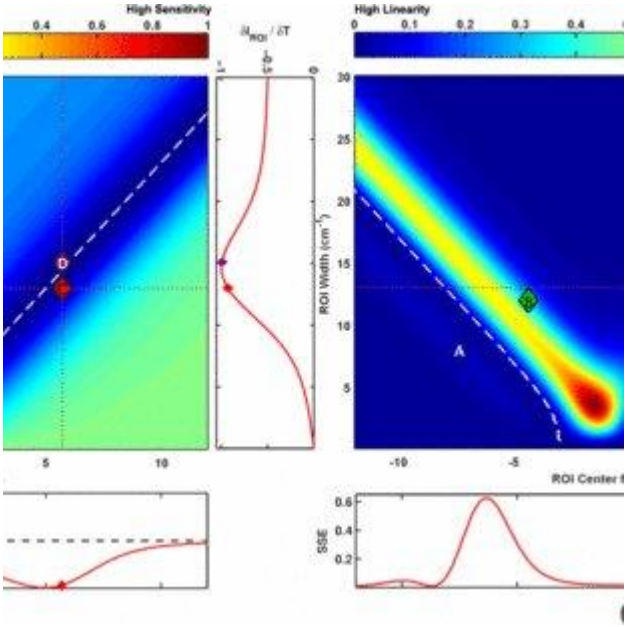

Figure 1.3: *figure showing the temperature variation within a silicon sample measured using 2 –laser Raman thermometry, linear and analytical maps respectively* [81].

As a result, when the absorbed power is uniform along with the thickness, the two-laser Raman technique, in conjunction with the analytical model described above, can be used. This is true for any material that exhibits a temperature-dependent phonon Raman scattering signal. When the temperature coefficient at a given temperature range can be determined, the Raman shift vs temperature must be pre-calibrated.

The temperature resolution is determined by the material under consideration and can be estimated using the spectral resolution.

Diffraction limits the spatial resolution, which can be as low as 300 nm. This technique has been used to measure the thermal conductivity of suspended quasi-2D structures such as Si membranes of various thicknesses, porous membranes, phononic crystals (PnCs), and 2D materials, and it is especially useful for studying the temperature dependence of thermal conductivity in the most unexplored temperature range (400–1000 K).

As previously stated, Raman Thermometry has become a part of a scientist's life in the laboratory, where they study a variety of different properties of various materials. As technology advances and the demand for materials, particularly low-dimensional materials, grows, a thorough understanding of their thermal properties becomes increasingly important. This will lead to further advancements in Raman spectroscopy and thermometry, such as Laser flash Raman thermometry or spectroscopy, Energy transport-state

resolved Raman and frequency-domain ET-Raman, Time-domain differential Raman, Frequency-resolved Raman, and others.

2.3 Photothermal beam deflection Technique

2.3.1 Background

The previously discussed thermoreflectance technique is one of the many optical heating methods that use lasers as heating sources. The **Figure 2.5** shows different measurement methods.

In the presence of a pulsed heating pump Laser beam alone, represented in Green in the **Figure 2.5**, (i.e. absence of a probe beam), acoustic emission and thermal emission techniques can be used.

In addition to a pump beam, if a probe laser beam is used with relatively high incidence angles, photothermal displacement (due to surface bump effect) and photothermal reflection techniques can be probed.

If the probe Laser beam is grazing or glancing the surface of the sample, the mirage technique (photothermal beam deflection) can be investigated.

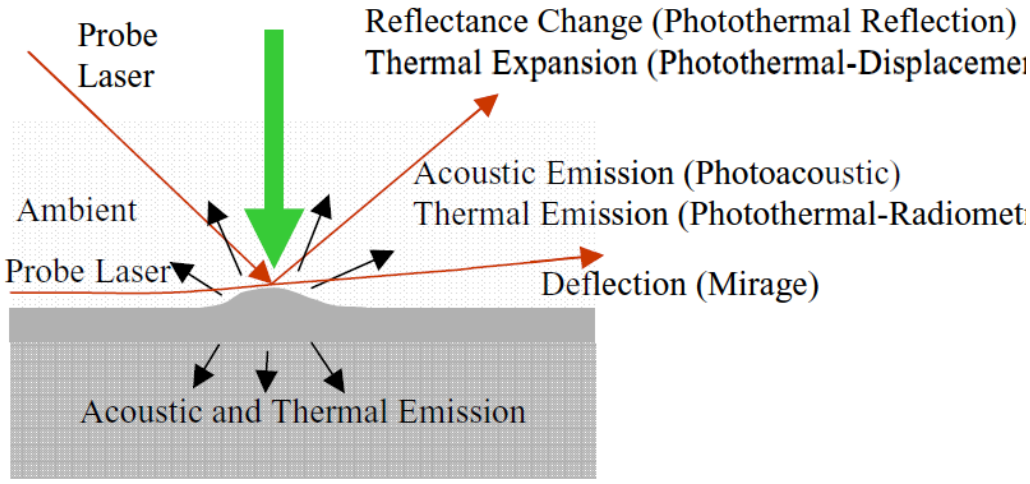

Figure 2.5: *Figure showing the different configurations for a pump – probe beam optical heating methods. Depending on the probe Laser presence and direction, different methods can be used of detection can be used* [83].

In this section the theory of the Mirage photothermal beam deflection technique is reviewed. In the next chapter, special attention will be given to the description of the new configuration of a mid-infrared photothermal beam deflection developed in our thermal physics laboratory at The American University of Beirut.

2.3.2 Theory of the mirage signal *(J. Younes et al., 2020)* [5]

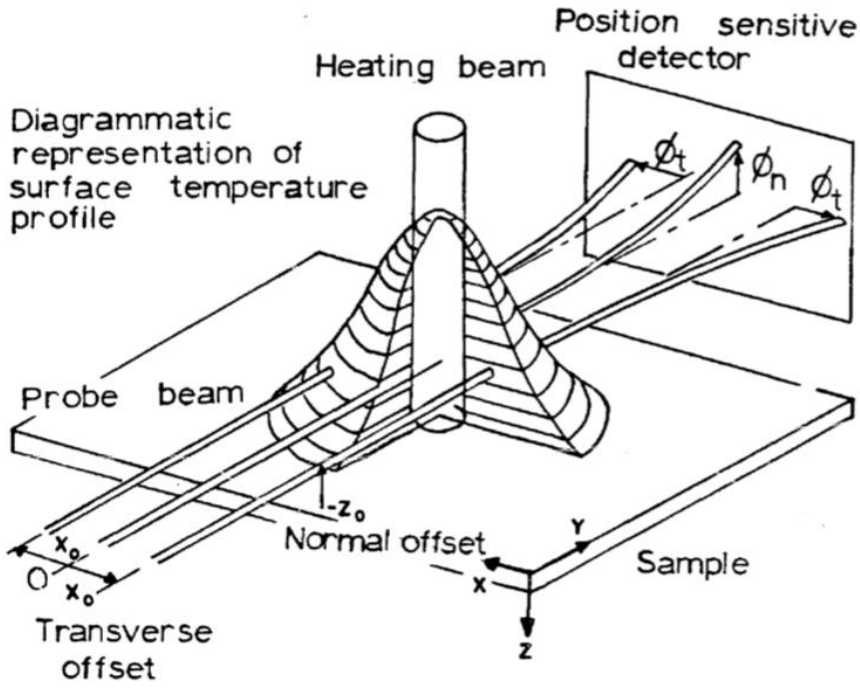

Figure 2.6: *Figure showing an illustration of the mirage effect, along with the temperature gradient in the air adjacent to the sample's surface. Deflection of the probe beam are shown for three offset distances between the pump and the probe beam* [84]

The mirage signal or the vector angular deflection of the probe beam, M, can be expressed as a function of the spatial variation of temperature in the air as:

$$\mathrm{M} = -\int_{-\infty}^{+\infty} \frac{1}{\mathrm{n}} \frac{\mathrm{dn}}{\mathrm{dT}} \nabla \mathrm{T_g}(\mathrm{r}) \times \mathrm{dr} \qquad \textit{Eq. 2.39}$$

where n is the air index of refraction and $T_g(r)$ is the temperature distribution in the air [5,85–88] Since in laser flash experiments the generated thermal waves are damped very fast, it is reasonable to assume that the term $\frac{1}{\mathrm{n}}\frac{\mathrm{dn}}{\mathrm{dT}}$ is a

constant over the thermal wave path. Moreover, it is normal practice to consider d**r** constant in one direction because the angular deflection is in the order of mrad. Assuming that the direction along which d**r** is constant is the y-direction, ***Eq. 2.39*** reduces to

$$M = -\frac{1}{n}\frac{dn}{dT}\nabla\overline{T}_g(x,z) \times \hat{y} \qquad \textit{Eq. 2.40}$$

where $\overline{T}_g(x,z)$ is a spatial-dependent temperature averaged over the y-direction. According to ***Eq. 2.40***, the angular deflection of the probe beam can be evaluated to a high degree of accuracy if the spatial distribution of temperature in the air is known.

Let us now consider that the air occupies the region $z < 0$ and the sample occupies the region $z \geq 0$. Since the IR radiations are absorbed in the surface layers of the measured sample, we can reasonably consider that the wave equation takes the form:

$$\nabla.\left[\kappa_g \nabla\overline{T}_g(x,z)\right] + \kappa_g q_g^2 \overline{T}_g(x,z) = 0 \qquad \textit{Eq. 2.41}$$

in the air (i.e. for $z < 0$) and the form

$$\frac{\partial}{\partial x}\left[\kappa_{s,x}\frac{\partial\overline{T}_s(x,z)}{\partial x}\right] + \frac{\partial}{\partial z}\left[\kappa_{s,z}\frac{\partial\overline{T}_s(x,z)}{\partial z}\right] + \kappa_{s,z} q_s^2 \overline{T}_s(x,z) = -\delta(x)\delta(z) \qquad \textit{Eq. 2.42}$$

below the surface of the measured sample (i.e. for $z \geq 0$), where we have assumed that the heating beam induces a point-like source of unit strength localized at x=0 and z=0. We have also defined a thermal wavenumber in the air as

$$q_g = (1+i)\left(\frac{\omega}{2\alpha_g}\right)^{1/2} \qquad \textit{Eq. 2.43}$$

and a thermal wavenumber in the sample as

$$q_s = (1+i)\left(\frac{\omega}{2\alpha_{s,z}}\right)^{1/2} \qquad \textit{Eq. 2.44}$$

In Equations ***Eq. 2.41*** - ***Eq. 2.44***, α is the thermal diffusivity, κ is the thermal conductivity, and ω is the frequency of modulation of the heating beam. The parameters of the air above the sample are indicated by the subscript ‘g’ (for

gas), the parameters of the sample in the x-direction are indicated by the subscripts 's,x'(for sample along the x-direction), and the parameters of the sample in the z-direction are indicated by the subscripts 's,z'(for sample along the z-direction). To reduce further the dimensionality of the problem, we write $\bar{T}(x,z)$ as a Fourier transform in x. Then, upon introducing the Fourier transform of $\bar{T}(x,z)$ in Equations ***Eq. 2.41*** and ***Eq. 2.42*** and taking the x derivative of the resulting equations, the wave equation takes the form

$$\frac{\partial}{\partial z}\left[\kappa_g \frac{\partial t_g(k,z)}{\partial z}\right] + \kappa_g k_g^2 t_g(k,z) = 0;\ \boldsymbol{z < 0} \qquad \textit{Eq. 2.45}$$

in the air and the form

$$\frac{\partial}{\partial z}\left[\kappa_{s,z} \frac{\partial t_s(k,z)}{\partial z}\right] + \kappa_{s,z} k_s^2 t_s(k,z) = -\frac{1}{2\pi}\delta(z); \boldsymbol{z \geq 0} \qquad \textit{Eq. 2.46}$$

in the sample, where

$$k_g = \left(q_g^2 - k^2\right)^{1/2} \qquad \textit{Eq. 2.47}$$

and

$$k_s = \left(q_s^2 - \frac{\alpha_{s,x}}{\alpha_{s,z}} k^2\right)^{1/2} \qquad \textit{Eq. 2.48}$$

The solution of the wave equations in the air (***Eq. 2.45***) and in the sample (***Eq. 2.46***) are of the form

$$t_g(k,z) = C_g e^{-ik_g z} \qquad \textit{Eq. 2.49}$$

with $z < 0$ and

$$t_s(k,z) = C_s e^{ik_s z} \qquad \textit{Eq. 2.50}$$

with $z \geq 0$, repectively. Given that the temperature must be continuous across the plane defined by $z = 0$, and the heat flux must have a discontinuity corresponding to the source strength on the same plane, the boundary conditions of the problem become:

$$t_g(k,0) = t_s(k,0) \qquad \textit{Eq. 2.51}$$

And

$$\kappa_{s,z}\frac{\partial t_s(k,z)}{\partial z}\bigg|_{z=0} - \kappa_g\frac{\partial t_g(k,z)}{\partial z}\bigg|_{z=0} = \frac{-1}{2\pi} \qquad \textbf{Eq. 2.52}$$

Upon solving Equations ***Eq. 2.51*** and ***Eq. 2.52*** for the constant C_g, we find

$$C_g = \frac{i}{2\pi\left(\kappa_{s,z}k_s + \kappa_g k_g\right)} \qquad \textbf{Eq. 2.53}$$

The angular deflection of the probe beam, thus, can be written as

$$M = \frac{i}{2\pi}\frac{1}{n}\frac{dn}{dT}\hat{y}\times\nabla\int_{-\infty}^{+\infty}dk\frac{e^{i(kx-k_g z)}}{\left(\kappa_{s,z}k_s + \kappa_g k_g\right)} \qquad \textbf{Eq. 2.54}$$

To take into account the finite sizes of the heating and probe spots, we assume that both beams have Gaussian profiles. Upon considering that the heating beam is centered at x = 0 and the probe beam is centered at a distance x from the origin and at a height h above the surface, the transverse component of the angular deflection of the probe beam (i.e. the component in the x-direction) takes the form

$$M_{trans} = \frac{-1}{\pi}\frac{1}{n}\frac{dn}{dT}e^{-q_g^2R_2^2/4}\int_0^{+\infty}dk\frac{k_g cos(kx)e^{ik_g h}e^{-k^2R_1^2/4}}{\left(\kappa_{s,z}k_s + \kappa_g k_g\right)} \qquad \textbf{Eq. 2.55}$$

and the longitudinal component of the angular deflection of the probe beam (i.e. the component in the z-direction) takes the form

$$M_{long} = \frac{-i}{\pi}\frac{1}{n}\frac{dn}{dT}e^{-q_g^2R_2^2/4}\int_0^{+\infty}dk\frac{ksin(kx)e^{ik_g h}e^{-k^2R_1^2/4}}{\left(\kappa_{s,z}k_s + \kappa_g k_g\right)} \qquad \textbf{Eq. 2.56}$$

where R_1 and R_2 are the radii of the heating and probe beams, respectively. In Equations ***Eq. 2.55*** and ***Eq. 2.56***, we make use of the symmetries of the integrals to express the deflection components in terms of integrals from zero to infinity with trigonometric functions in x. In principle, in the limit of isotropic medium (i.e., $\kappa_{s,x} = \kappa_{s,z}$ and $\alpha_{s,x} = \alpha_{s,z}$), the thermal diffusivity of the measured sample can be deduced from the transverse and longitudinal deflection of the probe

beam through the dependence of q_s on the sample thermal diffusivity (see ***Eq. 2.44***).

3 Mid-IR photothermal beam deflection technique for fast measurement of thermal diffusivity and highly sensitive subsurface imaging *(J. Younes et al., 2020)* [5]

3.1 ABSTRACT

The resonances of phonon and plasmon modes make the absorbance coefficient of materials tremendously high in the mid-infrared spectral range, which allows for a mid-infrared excitation laser to heating the surface layers of these materials with high efficiency. Further, phonon scattering by defects and defect-induced localized vibrational modes affect the local infrared dielectric function and hence, the local infrared absorption coefficient. In this manuscript, I present a mid-infrared photothermal beam deflection technique that takes advantage of the strong interaction between infrared optical excitations and vibrational modes to measure the thermal diffusivity of materials without any sample preparation and takes advantage of the strong dependence of the infrared complex dielectric function on defects to detect subsurface defects with high sensitivity. I demonstrate the importance of the developed technique by measuring the thermal properties of highly transparent and reflective samples and detecting defects undetectable with any of the existing optical methods.

Namely, using the developed technique, I found that the thermal diffusivities of high-quality Si, crystalline AlN, and crystalline α-SiO_2 substrates are 1.00 ± 0.05, 0.67 ± 0.02, and 0.09 ± 0.01, respectively, and we record highly resolved images of structural subsurface defects, as well as defects produced by ion-implantations at a depth of 62 μm under the surfaces of 4H-SiC substrates.

3.2 INTRODUCTION

Recent developments in materials processing for high-efficiency electronic systems have been accompanied by an increase in the power density of the end electronic device. Thus, materials free of defects, which may accumulate a high amount of heat in a small volume [89], are essential requirements for fast heat dissipation and extending the device lifetime. It is, therefore, indispensable for device failure prevention to have a nondestructive technique for both accurate measurement of materials' thermal properties and highly sensitive detection of subsurface defects.

Thermoreflectance and optothermal Raman spectroscopy are widely used optical techniques for measuring the thermal properties of solids. The thermoreflectance technique is based on measuring the variation of the reflectance of a probe beam as a function of the variation of the temperature of the measured sample due to energy put in it at a given rate in the form of laser pulses [90,91]. The relation between the reflectance of the probe beam and the local temperature of the sample provides a measure of the thermal conductivity in the sample investigated. Although the thermoreflectance technique has proven to be successful in accurately measuring the thermal properties of materials, it requires sample preparation and is invasive as the classical scheme in this technique uses a metal thin film transducer heated by an optical pulse (pump) in the visible spectral range [90]. Optothermal Raman spectroscopy also has attracted much attention for the optical investigation of the thermal transport in solids [92,93]. It has emerged as a steady method that can reveal the thermal conductivity of the measured sample through the dependence of the Raman peak on the optical excitation power. The Raman peak position depends on the temperature of the sample in the region where the light is focused. Hence, it can be used as a thermometer to measure the variation of local temperature as a function of input power. Upon using Fourier law, such a relationship readily leads to an accurate evaluation of the thermal conductivity of the sample investigated. Optothermal Raman spectroscopy does not require any sample preparation to measure the thermal conductivity of solids. However, it is limited to two-dimensional materials and three-dimensional materials of low thermal properties [94–96]. This limitation is due to that fast heat dissipation in a three-dimensional material of high thermal properties prevents a local temperature rise and, consequently, a shift in the Raman peak as a function of the excitation laser power.

The photothermal beam deflection (PBD) technique, on the other hand, has emerged as a multi-purpose analysis method of a variety of solids, liquids, and gases. It consists of optically generating and detecting rapidly damped thermal waves in the measured solid or the surrounding medium. The thermal

wave generation is commonly achieved by employing short laser pulses focused on the surface of the sample, while the temporal and spatial distributions of temperature, which are the principal determinants of the thermal properties of the material, are detected by the mirage effect [97–104], or through the thermal radiation of the sample [105–110]. The advantage of the PBD technique on the thermoreflectance and optothermal Raman techniques is that it can be used to estimate the defect concentration level on the surface and in the volume of the measured material through the measurement of the optical absorption coefficient associated with these defects [111–122]. Such a simultaneous measurement of the thermal properties and defect level in materials is indeed strategic for in-line process control, as well as to optimize defect-free materials of high thermal properties for the manufacturing of high-performance electronic devices.

Among the various PBD techniques, the ones configured for pump-probe measurements have the advantage that can simultaneously measure thermal transport properties in the sample investigated and provide valuable information about defect concentrations on and beneath the measured surface. As will be described in the next section, for accurate analysis of the recorded signal, it is required that the pump laser light be absorbed in the surface layers of the measured sample. Hence, the measured sample should be optically thick. The reported pump-probe PBD experiments nevertheless use pump lights with wavelengths in the optical range from near-infrared (NIR) to near-ultraviolet (NUV). These wavelengths can be absorbed in the surface layers only when the measured material is opaque in this spectral range. Such a requirement limits the use of these experiments to the class of materials presenting electron resonances in the NIR-NUV spectral range [123–129]. Moreover, even when the material investigated is opaque due to electron resonances, the excitation of electronic structures often may generate an electron-hole plasma similar in many respects to the thermal wave, hindering the detection of intrinsic thermal properties of the measured material [130]. A PBD experiment with a mid-IR pump laser has been successfully used for the special case of skin spectroscopy and non-invasive glucose measurement [131]. It demonstrated the possibility of incorporating a mid-IR pump laser in a PBD experiment. In this contribution, I present a PBD technique with a mid-IR pump laser (IR-PBD) to extend the applicability of the conventional PBD methods. The advantage of a mid-IR pump laser is that it makes the technique more accurate and applicable for a wider range of materials, as the vast majority of materials are opaque in the mid-IR spectral range due to vibrations resonances. It would also present a unique capability to detect, directly and with high sensitivity, defects buried at large depths beneath the measured surface. Unlike the existing PBD experiments, which require the deposition of a metallic layer to create a heating

spot on the surface of an optically thin material [97], the proposed technique is capable of creating periodic heating on the surface without depositing of any metallic absorbing layer as most of the materials are optically thick in the mid-IR spectral range. Further, the complex dielectric function in the mid-IR is very sensitive to defects through their local and extended vibration modes [132,133], as well as through their contribution to the enhancement of anharmonic vibrations [134]. Hence, the local absorption of the IR heating beam strongly depends on the degree of defect concentration in the measured region. This highly sensitive response of defect to a mid-IR excitation makes the proposed technique suitable for highly sensitive and direct detection of subsurface defects. The technique uses the bending of a visible probe beam due to the mirage effect to monitor the damping of the optically generated thermal waves in the air and evaluate thermal properties of the material, whereas it uses the bending of the probe beam due to thermoelastic surface deformation for direct subsurface imaging of defects in the measured sample.

We use the developed technique to measure the thermal diffusivities of highly transparent and highly reflective materials in the visible spectral range. We demonstrate that the developed IR-PBD technique can measure the thermal diffusivities of these materials with accuracy and without any deposition. We present an approach to take into account the thermoelastic deformation of the surface in the analysis of the photothermal beam deflection due to the mirage effect. Another critical development we present is that we demonstrate the unprecedented subsurface imaging power of the proposed technique by imaging structural subsurface defects and damages induced at about 62 µm beneath the surface of a 4H-SiC substrate.

3.3 EXPERIMENTAL SETUP AND DATA ANALYSIS

In this section, the developed experimental setup and is presented. I highlight necessary experimental procedures to eliminate all sources of experimental errors.

3.3.1 Experimental setup (General simplified description)

A simplified diagram of the experimental setup is depicted in **Figure 3.1**. A 10.6 µm wavelength CO_2 laser beam is modulated at different frequencies using an acousto-optic modulator and focused on the sample surface using a 3 cm effective focal length lens. The CO2 laser beam is combined with a low power argon-ion laser beam for visualization and alignment purposes. An IR camera

and a single axis positioning stage are used to drive the sample surface to the exact focal point of the heating beam. The IR camera is also used to monitor the variation of the local absorbance of the surface during data acquisition, through the measurement of the back-reflected IR beam. The mechanical and thermal responses of the region irradiated by the IR heating beam is monitored by using a He-Ne laser probe beam incident to the sample surface at very small angles.

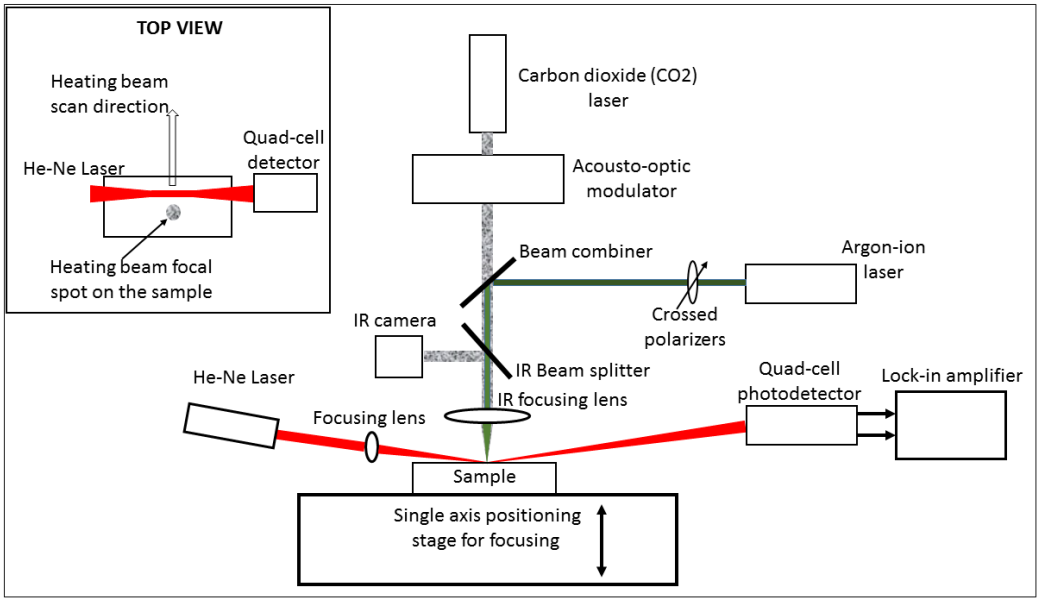

Figure 3.1 *Simplified diagram of the developed IR-PBD apparatus* [5].

The amplitudes and phases of the longitudinal component (parallel to the heating beam) and the transverse component (perpendicular to the heating beam) of the He-Ne probe beam after interacting with the sample and the air layer above the heated region are measured with a four-quadrant photodetector whose outputs are amplified with a two-channel lock-in amplifier. As depicted in **Figure 3.1**, the heating beam is moved across the sample surface perpendicularly to the probe beam using a single axis positioning stage. All the measurements are repeated for several different frequencies.

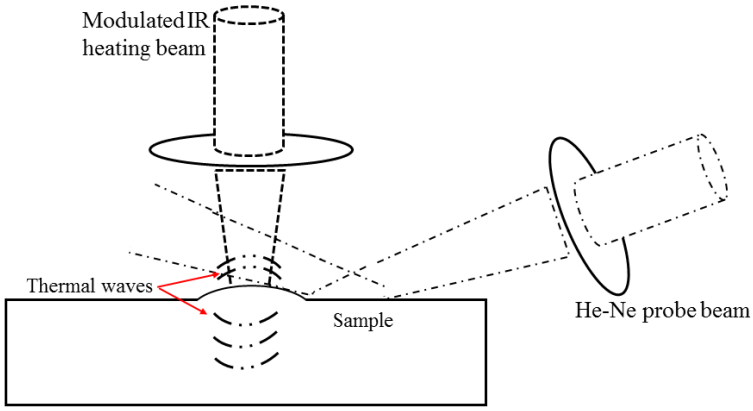

Figure 3.2 *Sketch of surface thermoelastic deformation and generation of thermal waves in the sample and the air upon heating by mid-infrared laser* [5].

The interactions of both the heating and probe beam with the measured sample, as well as the physical phenomena occurring in the heated region, are schematized in **Figure 3.2**. The periodic sample irradiation leads to the generation of thermal waves, which damp rapidly in the air layer in contact with the sample surface. The periodic temperature gradient in the air accompanying the thermal waves gives rise to a periodic gradient of refraction index capable of periodically deflecting the He-Ne laser probe beam passing very close to the sample surface, at the frequency of the modulation of the heating beam. However, besides the induced temperature gradient in the air, the thermoelastic deformation of the surface may significantly deflect the longitudinal component of the He-Ne probe beam. It is worth noting here that the important thermoelastic deformation of the surface due to the high absorbance of IR in the surface layers makes the largest contribution to the deflection of the longitudinal component of the probe beam. Thus, the transverse component of the probe beam is deflected due to only the mirage effect, whereas the longitudinal component of the probe beam is deflected primarily by the thermoelastic deformation of the surface.

3.3.2 Detailed experimental setup with components description.

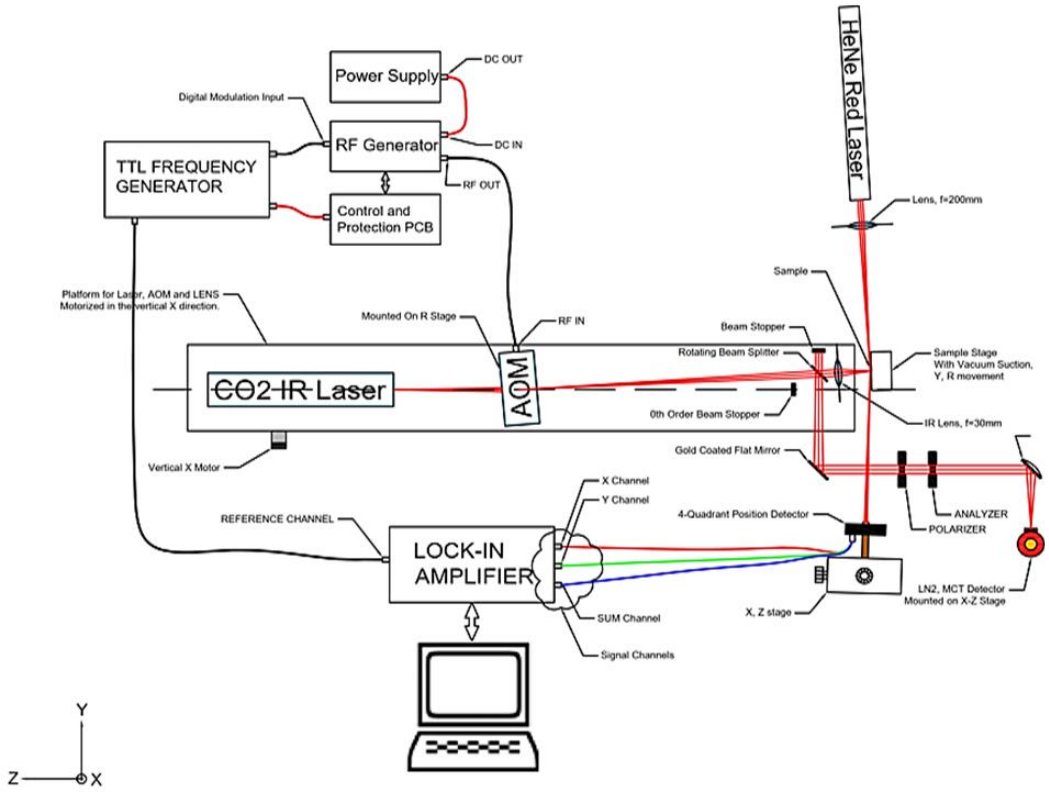

Figure 3.3 *Diagram with further details about the developed IR-PBD* [5].

I built the whole setup completely in-house at the Thermal Physics Lab of AUB. The whole setup is installed on a **pneumatic optical table**, to minimize vibrations and noise introduced in the system and surrounded by plexi-glass shielding for safety due to IR.

Below is a description of the main components of the developed IR-PBD setup:

- A platform whose height can be adjusted by means of a precise motor holds a CO2 IR Laser, and Acousto-Optic Modulator and a Focusing Lens.

- **Pump beam Laser:** the pump laser used in the system is a CO2 IR Laser that emits a continuous wave (CW). The wavelength of the Laser can be adjusted between 10.3 μm and 10.8 μm, with an output power of 1 Watt. Since the wavelength of the Laser and its power output depends on the Temperature of the CO2, a heating controller combined with a water- and air-cooling system (precise temperature chiller) is used to maintain the

Laser at a constant temperature around 81.5 °F , to stabilize both the wavelength at 10.6 μm and the power. The Laser beam diameter is 2.4 mm, with a divergence of 5.5 mrad, and an horizontal polarization.

- **Pump beam modulation**: The modulator chosen for the pump beam is an Acousto-Optic modulator (AOM) that is driven through a dedicated RF Generator. The RF Generator is controlled by a Square wave Function Generator. The AOM works by deflecting the Laser at a pulsed rate (set by the frequency generator). The AOM has been chosen with specific rise time, with Germanium window, with an aperture of 9.4 mm. The operational wavelength is 10.6 μm . Two beams are exiting the AOM: the zeroth order beam that is not deflected and varies in our case between 100 mW and 700 mW and is stopped by a beam stopper. The first order beam exiting the AOM is used as the actual heating pump beam which is pulsed at the frequency set by the function generator, and the intensity of this heating beam is set by the amplitude of the square wave and varies between 0 and 700 mW. As such we can control both the intensity and the pulsing rate of the heating. Both the AOM and its RF Generator are cooled by a dedicated stable water cooler/re-circulator to maintain a temperature of around 292K.

- The intensity of the pump beam Laser is constantly monitored at the output of the AOM, by a high-speed Power meter, that is used to compensate for any potential fluctuation in the pump beam power.

- An argon Laser is superimposed (through a beam combiner), with the IR pump beam emanating from the AOM, as an aid to facilitate the proper alignment of the IR laser beam on the sample.

- **The Focusing lens** is a special mid-IR focusing lens of 3 cm focal distance.

- **Probe beam Laser:** the used probe beam Laser is a He-Ne red Laser having a wavelength of 632.8 nm, with a power of 5 mW CW, a beam diameter of 0.81 mm, and a divergence of 1 mrad. A focusing lens with focal distance of 20 cm is mounted on the output of the Laser to focus the Laser on the sample surface. The Laser beam incident towards the sample is grazing the surface of the sample, and the reflected beam continues towards the center of the photodetector.

- **Position Sensitive Detector:** to measure the deflection of the Probe beam, we employ a 4-quadrant sensitive photodetector. The detector has a built-in amplifier circuitry with response up to 250 KHz. The detector works

between 400 nm and 1100 nm. The diameter of the beam incident on the detector should be less than 3.0 mm, in order to work properly. The detector has 3 output channels: H, V and SUM, that determine the transverse deflection of the Laser spot, the longitudinal deflection and the SUM of all Quadrants (used to compensate for fluctuation in the probe beam). The detector is also mounted on a 2 -axis translation stage combined with rotation to allow horizontal and vertical positioning of the probe beam in the center of the 4-quadrants.

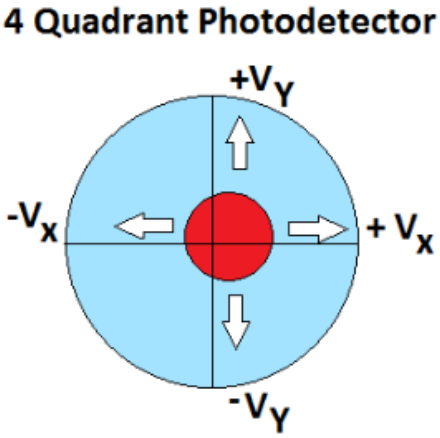

Figure 3.4: *Diagram of the four-quadrant position sensitive photodetector.*

- The deflection outputs of the detector are connected to a dual channel **Lock-in amplifier**, whose reference channel is taken from the same function generator controlling the pulse rate.

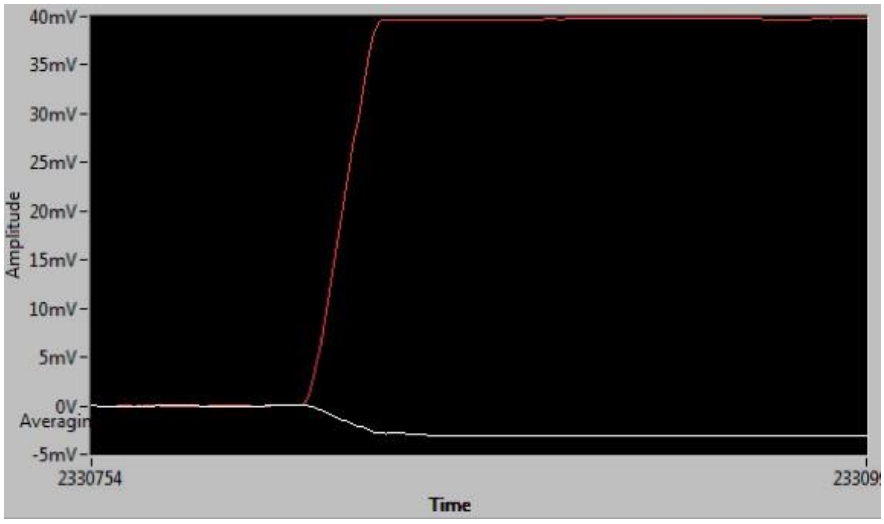

Figure 3.5: *Transverse deflection (white) and Longitudinal deflection (red) of the probe beam as shown in an extract of one of the windows of the control software. The amplitude of the longitudinal deflection is much larger than the transverse deflection, due a contribution from the surface photothermal displacement effect (the surface bump induced by the heating beam).*

- The other detector channel (SUM), and the output of the power meter are connected to an in-house developed acquisition system (comprising of a National Instruments sbRIO Board with built-in FPGA and 4 channel Analog inputs PCB). I have programmed the acquisition system to act as a 2-channel software defined Lock-in Amplifier specifically for the correction of the fluctuations of the Pump and probe beams. This lock-in is also referenced to the same function generator. The usage of the FPGA allows for fast and accurate lock-in amplification. I have also completely developed the FPGA software in-house to allow for any needed modification or optimization.

- The sample is mounted on a moving stage that can move the sample in X, Y and Z direction, that allows positioning of the sample and also focusing the pump beam on the sample surface.

- The part of the heating pump beam that is reflected off the sample surface is directed towards an IR camera through a set of polarizer-analyzer to minimize the intensity of the heating beam to a level safe for the IR camera. The image given by the IR camera would allow adjusting the sample position to put it in focus in front of the focusing lens (during the alignment procedure), by minimizing the pump beam spot size as seen on the IR

camera, when moving the sample stage in the Z direction. Furthermore, it would allow to monitor the sample surface absorption (actually the back reflectivity) and normalize the mirage signals against this measured reflectivity (cf. section 3.4.1).

- A PC is connected to the 2 lock-in amplifiers and the motorized stages. The control software runs on this PC. I have written the control software on Labview platform. The software controls the whole setup, acquisition, lock-in amplifiers, power meter, etc. and allows for signals visualization, data acquisition and recording in excel format. This data is then analyzed by a Matlab code developed in-house that performs the fitting procedure and allows the extraction of the thermal diffusivity as per the thermal model detailed in the Theory of the Mirage technique (cf. section 2.3.2 and section 3.3.3)

Note 1: the CO2 Laser (pump heating beam) is horizontal and perpendicular to the sample that is held vertical.
Note 2: the probe beam Laser is horizontal and perpendicular to the 4-quadrant photodetector.
Note 3: the sample, probe beam and detector are held in the same position, however the heating pump beam (along with the AOM and the focusing lens) is moved to vary the distance between the Pump and probe beam.

3.3.3 Signal analysis *(J. Younes et al., 2020)* [5]

The Theory of the mirage signal has already been established previously in section 2.3.2, where the transverse and longitudinal deflection components have been modelled and derived.

Nevertheless, due to the strong contribution of the thermoelastic deformation of the surface to the deflection of the longitudinal component of the probe beam, taking into account both the longitudinal and transverse components of the probe beam would overestimate the thermal diffusivity of the measured sample. Therefore, to evaluate the thermal diffusivity of the measured sample accurately, we take into account the amplitude and phase of only the transverse component of the probe beam, which is deflected due to the mirage effect. Yet, while the longitudinal component of the probe beam cannot be used to analyze the thermal transport in the measured sample, it is of utmost importance for highly sensitive detection of subsurface defects, because the IR absorbance, and consequently the thermoelastic deformation of the surface, is strongly affected by the presence of defects beneath the absorbing surface. In

Section 3.4, we illustrate how the thermoelastic deformation of the surface may lead to a significant overestimation of the thermal diffusivity, and how it is of great use in subsurface imaging.

3.4 RESULTS AND DISCUSSION [5]

The analysis model presented previously considers that incident energy is absorbed in the surface layers of the measured sample, or more precisely, in a layer substantially thinner than the wavelength of the generated thermal wave. Hence, the validity of the model assumption, and consequently, the ability of the analysis model to extract from the measured vector angular deflection of the probe beam accurate value of thermal diffusivity increases as the optical absorption coefficient of the measured material increases.

As mentioned previously, the strong interaction between infrared optical excitation and lattice or plasma vibration modes strikingly enhances the optical absorption coefficient of a wide class of materials in the mid-IR spectral range. Therefore, the IR-PBD measurement technique with detection by the mirage effect presented in this contribution has the advantage, compared to similar experimental setups with visible pump laser, of highly accurate measurement of thermal diffusivity and broader applicability.

To demonstrate the advantage of using a mid-IR pump laser in a PBD experiment, we present below thermal diffusivity measurements on samples unmeasurable by using similar setups with a visible pump laser (because of their high reflectivity and transmissivity in the visible spectral range). We also show that the use of a mid-IR pump laser adds a new dimension to the applicability of the PBD experiment by allowing for highly sensitive subsurface imaging with a good spatial resolution.

3.4.1 Measurement of materials thermal diffusivities (α) using IR-PBD [5]

Irrespective of the wavelength of the heating source, the principal difficulty in determining the thermal diffusivity of the measured sample using photothermal beam deflection by the mirage effect stems in that the theory of the mirage signal involves, in addition to the sample thermal diffusivity α, a large number of unknown experiment parameters. These parameters are the thermal properties of the air, the radius of the heating beam R_1, the radius of the probe beam R_2, and the height of the probe beam above the surface h. Indeed, separate experiments have to be carried out to reduce the number of free adjustable

parameters, and consequently, make the data fitting procedure faster and more accurate. Accordingly, we have first performed measurements with different heating beam powers to determine whether the induced temperature gradient in the air deviates the average thermal conductivity and diffusivity of the air from their known values at room temperature. We noticed that the laser power has no noticeable effects on the shapes of the transverse and longitudinal signals, and thus the local temperature rise has no effect on the parameters of the air determining the deflection of the probe beam. This result allowed us to consider α_g and κ_g as the room temperature thermal diffusivity and thermal conductivity of the air. We obtained the radius of the heating beam R_1 from the measured transverse component of the deflected probe beam whose maximum is situated one beam radius from the axis of the excitation beam, and we determined the radius of the probe beam R_2 by using the knife-edge method. At that point, the unknown parameters in the analysis model are only the thermal diffusivity of the measured sample and the height of the probe beam above the surface h.

The theory of the mirage signal accounts for the transverse and longitudinal deflection of the probe beam due to the mirage effect. However, the probe beam can also deflect due to some thermoelastic mechanisms not accounted for in the theory of the mirage signal, causing some systematic measurement errors. The principal measurement error may result from the deflection of the probe beam by the thermal bump or the thermoelastic surface deformation. This deflection mechanism primarily affects the longitudinal component of the vector angular deflection of the probe beam **M** [97]. To reduce such a measurement error, we consider in the fitting procedure only the transverse component of **M**, which is very slightly affected by the thermoelastic surface deformation. We demonstrate below the strong effect of the thermoelastic surface deformation on the longitudinal signal.

Another possible source of systematic error is the local variation in the absorbance of the measured surface. To avoid such a potential error in the measurement, we monitor the sample surface absorption through the back reflectivity of the heating beam using an IR camera. Then, we normalize the mirage signals using the obtained results.

An additional error may arise from the procedure adopted to fit the recorded signal to the theory of the mirage signal. The usual approach to deduce the unknown parameters from a PBD experiment with detection by the mirage effect is to fit simultaneously all the data recorded at different heating beam modulation frequencies to the analysis model using the multivariable least-squares fitting methods [135]. However, this fitting procedure implies that the parameter h, which describes the height of the probe beam above the surface, is independent of the modulation frequency of the heating beam. Such an

assumption may lead to a large error in evaluating the thermal diffusivity of the measured sample because

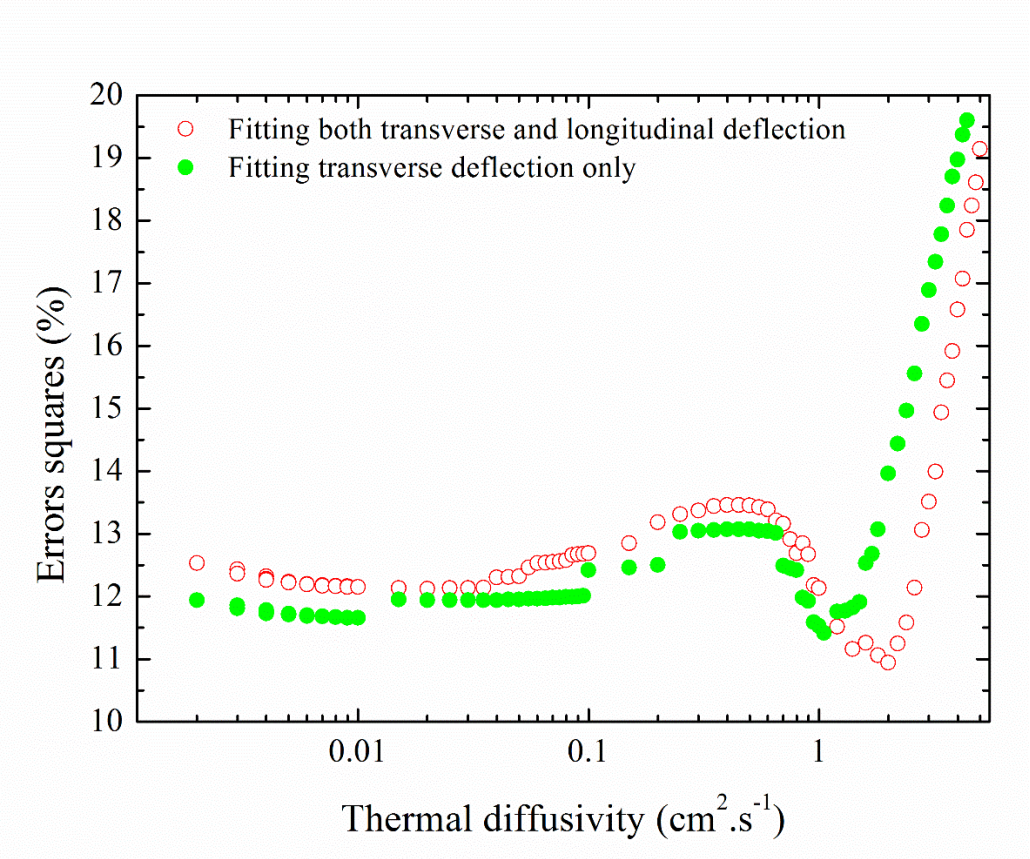

Figure 3.6 *The squares of the fitting errors when both the longitudinal and transverse signals from silicon are considered, and when only the transverse signal from silicon is considered.*

the perpendicular distance between the surface and probe beam (h) strongly depends on the modulation frequency of the heating beam. The dependence of h on the heating beam modulation frequency can be seen if we realize that $h = h_0 - a_{th}\Delta T L_{eff}$, where h_0 is the height of the probe beam above the surface when the pump laser is off, $a_{th}$is the coefficient of linear thermal expansion, ΔT is the change in temperature over an average effective length L_{eff}. Now, if we replace ΔT by the absorbed energy per volume divided by the sample heat capacity, and consider that the energy absorbed per cycle is $\beta P / 2f$, where β is the optical absorption coefficient, P is the power incident on the sample, and f is the heating beam modulation frequency, we obtain the expression $h = h_0 - a_{th}\beta P L_{eff} / 2AL_h \pi f \rho C$. This expression demonstrates the dependence of h on

the heating beam modulation frequency. Here, L_h is the heated length, A is the heated area, ρ is the mass density, C is the heat capacity per unit mass. Therefore, to obtain an accurate value for the thermal diffusivity of the measured sample, we fit each of the spectra measured at different modulation frequencies separately with setting h and the thermal diffusivity α as free adjustable parameters and plot, for each modulation frequency, the squares of the errors versus thermal diffusivity. Then, we consider the thermal diffusivity of the measured sample to be the value corresponding to the minimum of the curve acquired by summing all the obtained curves of the squares of the errors versus thermal diffusivity.

We also note here that if the heated length, which is given by $L_{th} = \sqrt{\alpha/\pi f}$, is greater than the radius of the heating beam, the heated area or the radius of the effective hot spot radius on the sample depends on the modulation frequency. To avoid such an effect yielding an additional dependence of the signal on the modulation frequency, we make experimental arrangements to keep L_{th} smaller than R_1 for all the measured modulation frequencies. As will be shown below, this fitting procedure allows evaluating the thermal diffusivity of all the measured samples accurately.

We first performed measurements on high-quality silicon (Si) substrate. We recorded the magnitudes and phases of the transverse and longitudinal components of the vector angular deflection of the probe beam and fitted the recorded data twice, one time with considering both the transverse and longitudinal signals and another time with considering only the transverse signal. In both trials, we considered that the parameter h, which measures the height of the probe beam from the surface, depends on the heating beam modulation frequency. In **Figure 3.6**, we show the minima of the squares of the fitting errors in the two-dimensional space of α and h obtained from fitting both the transverse and longitudinal signals. We also show the minima of the squares of the fitting errors obtained from fitting only the transverse signal. As can be noticed, the best fit of both the transverse and longitudinal signals leads to a value of 2.0 $cm^2.s^{-1}$ for the thermal diffusivity of Si. This value is about twice the reported thermal diffusivity of Si [98,136,137]. However, when we fit only the transverse signal, we obtain a thermal diffusivity value of 1.00 $cm^2.s^{-1}$, which is in good agreement with reported thermal diffusivity values of pure crystalline Si. Indeed, the thermoelastic deformation of the sample surface caused by the local heating unavoidably enhances the longitudinal signal, and hence leads to an overestimation of the thermal diffusivity when the longitudinal signal is considered in the fitting procedures. One can better visualize how the thermal diffusivity is overestimated when the longitudinal signal is taken into account by comparing the recorded longitudinal and transverse signals with the calculated ones when both longitudinal and

transverse signals are considered (in **Figure 3.7**), and when only the transverse signal is considered in

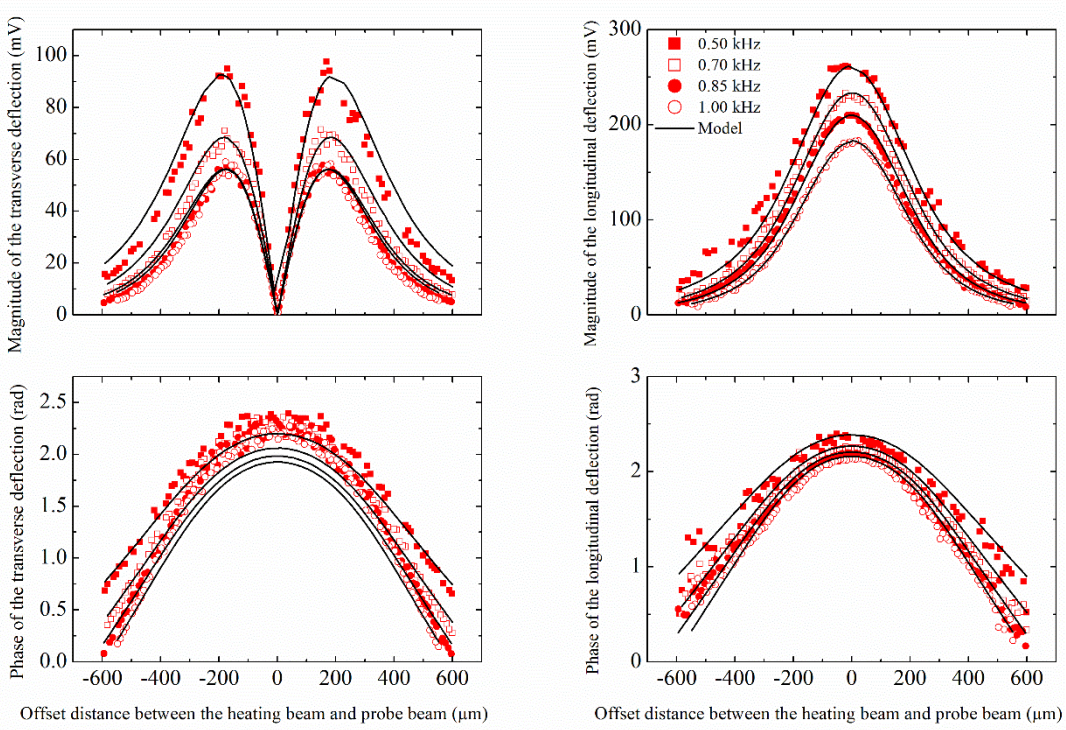

Figure 3.7 *Magnitudes and phases of the transverse and longitudinal components of the vector angular deflection as a function of the offset distance between the heating and probe beam for four different frequencies for a silicon substrate. The experimental data are shown using symbols. The theoretical spectra are represented by solid lines. The theoretical curves are obtained by fitting both the longitudinal and transverse signals using the multivariable least squares fitting methods.*

the fitting procedure (in **Figure 3.8**). **Figure 3.7** shows that when both the transverse and longitudinal signals are taken into account, the magnitude and phase of the longitudinal signals are well described, whereas the magnitude and phase of the transverse signal are poorly described at all the modulation frequencies, and the thermal diffusivity is overestimated. However, **Figure 3.8** shows that considering only the transverse signal in the fitting procedure gives a precise value for the thermal diffusivity, although the magnitude and phase of the longitudinal signal are poorly described. These results add support to that the effect of thermoelastic surface deformation on the longitudinal signal leads to a significant overestimation of the thermal diffusivity.

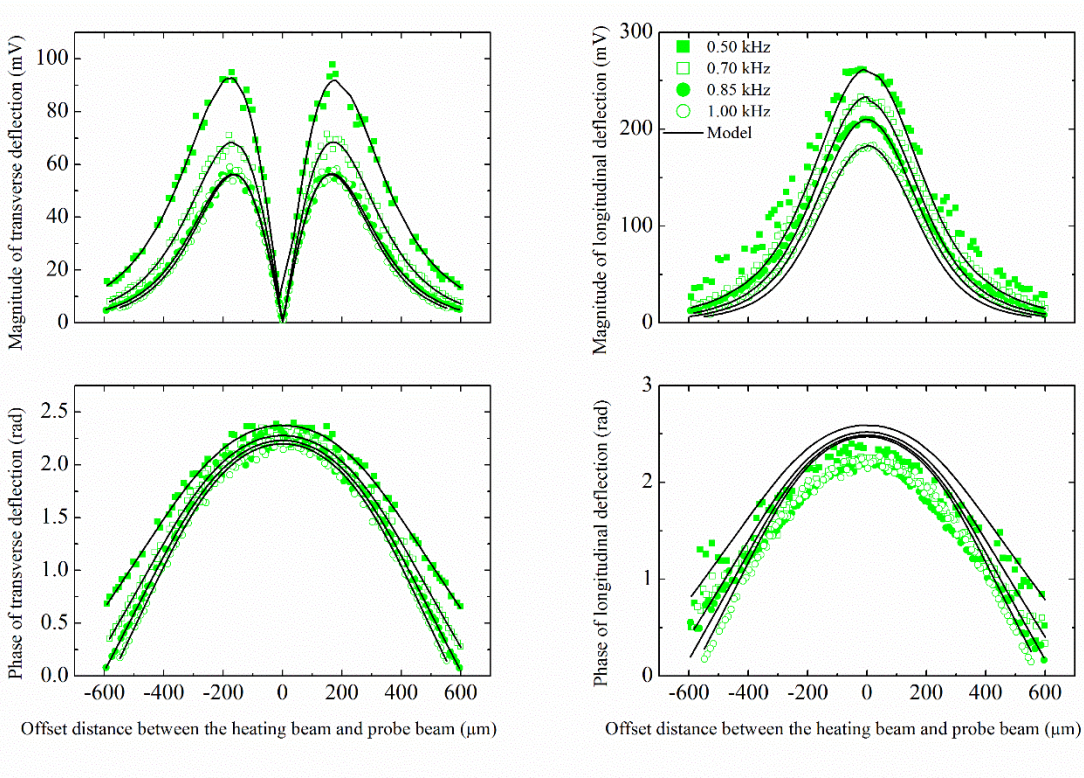

Figure 3.8 *Magnitudes and phases of the transverse and longitudinal components of the vector angular deflection as a function of the offset distance between the heating and probe beam for four different frequencies for a bare silicon substrate. The experimental data are shown using symbols. The theoretical spectra are represented by solid lines. The theoretical curves are obtained by fitting only the transverse signal using the multivariable least-squares fitting methods.*

Since it is difficult to account for the sample curvature and correct the longitudinal signal, the best convenient way to obtain a reliable value for the thermal diffusivity of the measured sample is to omit the longitudinal signal in the fitting procedure.

For further assessment of the reliability of the developed IR-PBD technique, we have also used it to measure the thermal diffusivity of polycrystalline quartz (α-SiO_2) and sintered aluminum nitride (AlN) substrates. The minima of the squares of the fitting errors in the two-dimensional space of α and h obtained from fitting the transverse signals of α-SiO_2, poly-AlN, and Si to ***Eq. 2.55*** are shown together in **Figure 3.9**.

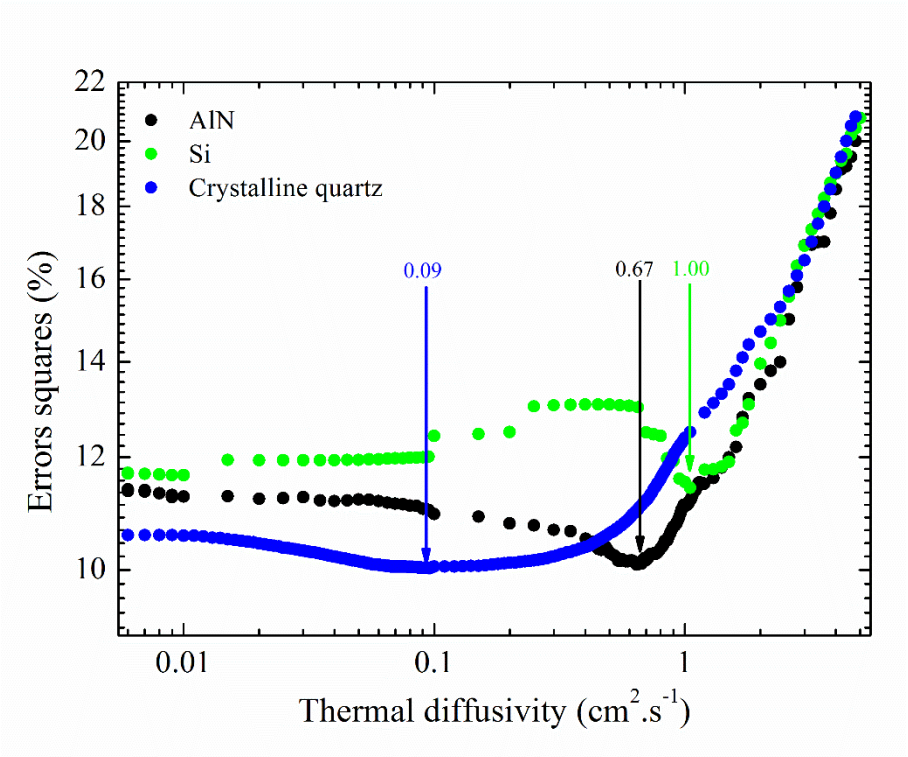

Figure 3.9 *The errors squares of the fitting of the magnitude and phase of the transverse signals from substrates of silicon, polycrystalline quartz, and polycrystalline sintered aluminum nitride.*

Table 3.1

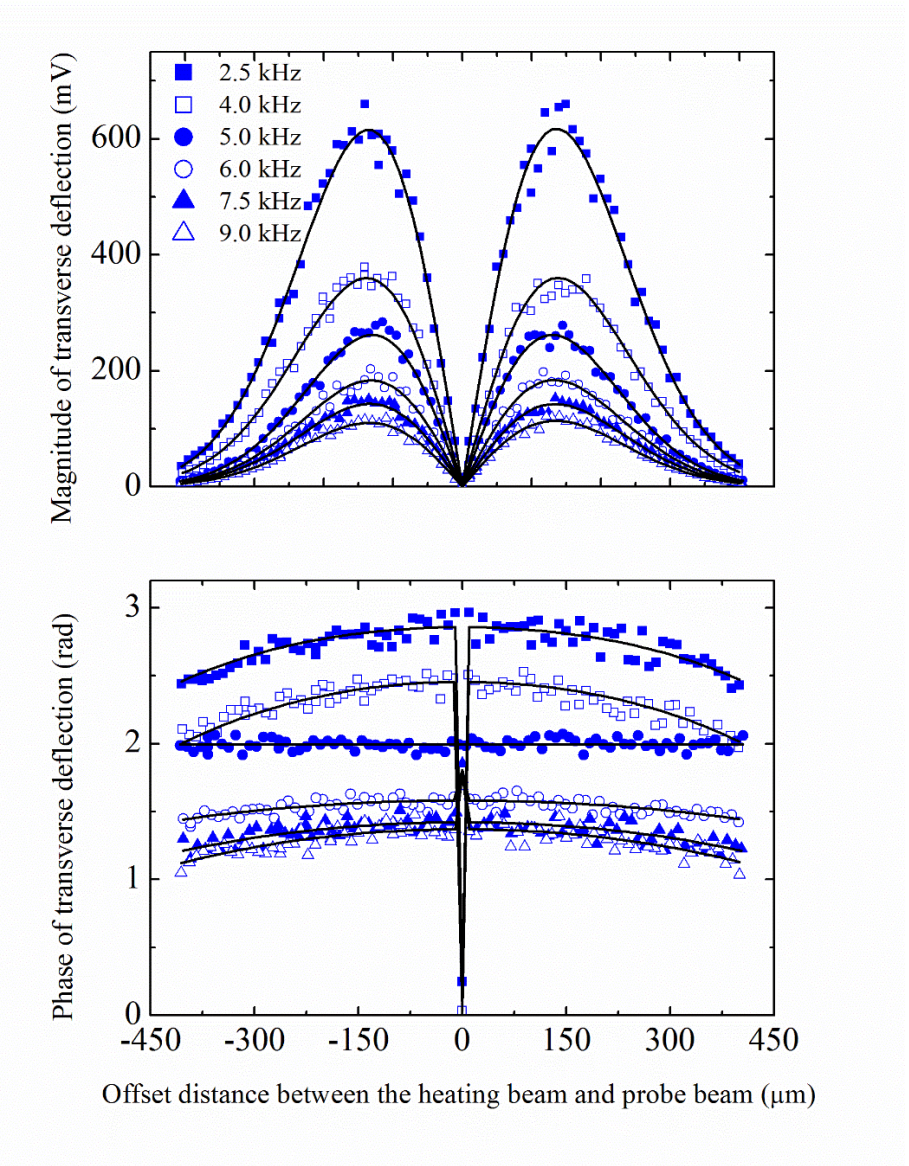

Figure 3.10 *Magnitude and phase of the transverse component of the vector angular deflection as a function of the offset distance between the heating and probe beam for six different frequencies for an α-SiO2 substrate. The experimental data are shown using symbols. The theoretical spectra are represented by solid lines. The theoretical curves are obtained by fitting the transverse component of the signal using the multivariable least-squares fitting methods.*

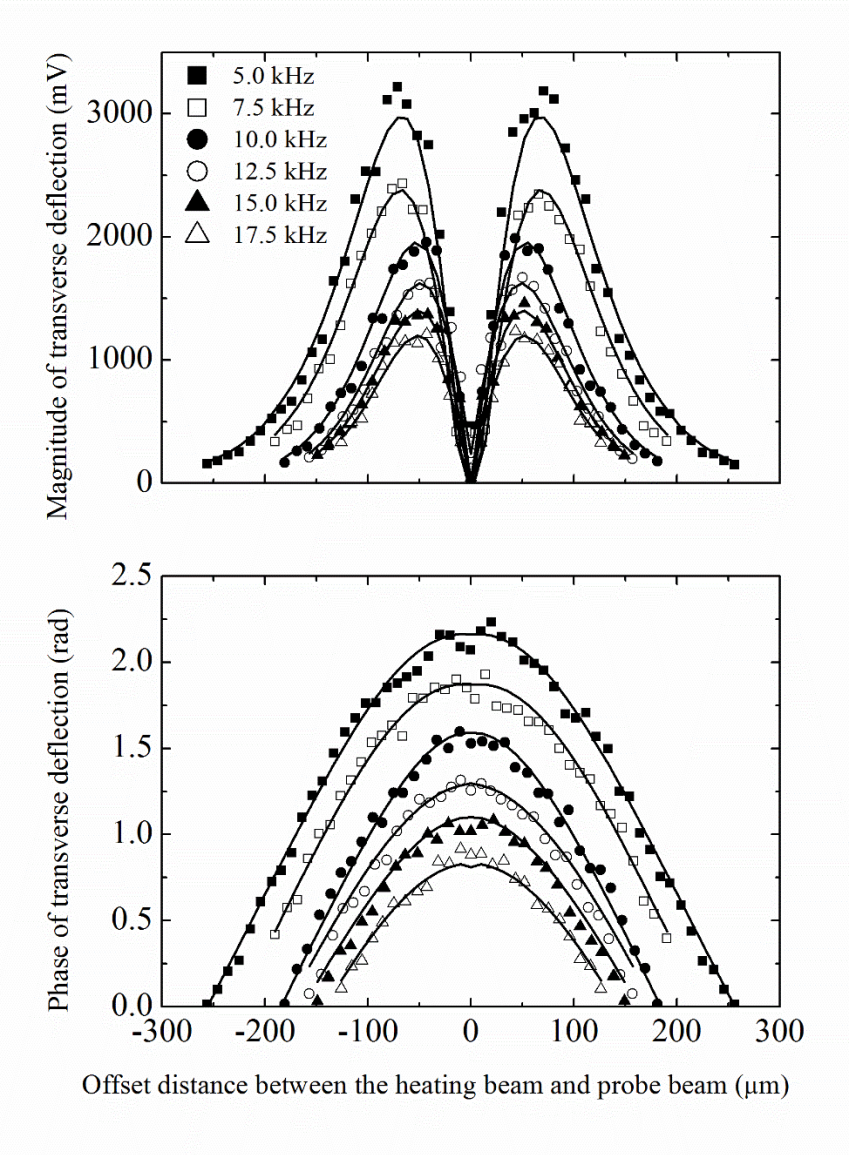

Figure 3.11 *Magnitude and phase of the transverse component of the vector angular deflection as a function of the offset distance between the heating and probe beam for six different frequencies for a sintered AlN substrate. The experimental data are shown using symbols. The theoretical spectra are represented by solid lines. The theoretical curves are obtained by fitting the transverse component of the signal using the multivariable least-squares fitting methods.*

Table 3.1 *Thermal properties of substrates of Si, α-SiO_2, and sintered AlN determined from the IR-PBD technique described in this work and from previous*

investigations. The mass density and specific heat capacity of Si are obtained from Refs. [138,139] *respectively. The mass density and specific heat capacity of α-SiO_2 are obtained from Refs.* [140,141]*, respectively. The mass density and specific heat capacity of AlN are obtained from Refs.* [142,143] *respectively.*

Material	*Present work*		*Previous investigations*			
	Thermal diffusivity (cm2.s-1)	*Thermal conductivity (W.K-1.m-1)*	*Thermal diffusivity (cm2.s-1)*	*Ref.*	*Thermal conductivity (W.K-1.m-1)*	*Ref.*
Si	*1.00 ± 0.05*	*160 ± 8*	*0.8-1.00*	[98,136,137	*142-160*	[139,144,145]
α-SiO2	*0.09 ± 0.01*	*15 ± 0.7*	*0.03-0.07*	[146]	*7-14*	[146]
poly-AlN	*0.67 ± 0.02*	*164 ± 5*	*0.12-0.98*	[147–150]	*100-272*	[147,151,152]

3.4.2 Highly sensitive subsurface defects imaging using mid-IR-PBD

In this part of Section 3.4, we demonstrate the high subsurface imaging power of the proposed technique by imaging subsurface structural defects and defects induced by implanting a low dose of H^+ ions at about 62 µm beneath the surface of a 4H-SiC substrate. By using mid-IR spectroscopic measurements, we show that the use of a mid-IR pump laser has the advantage of highly sensitive detection of subsurface defects. We also provide a detailed analysis of the spatial resolution of the proposed subsurface imaging technique.

Let us start first with the principle of PBD imaging. In a PBD experiment, the energy of the pump laser light absorbed in the irradiated region converts into heat. As the pump beam intensity is modulated, the heat is generated repeatedly at the modulation frequency. This mechanism results in the generation and propagation of thermal and elastic waves, which induce localized surface bumping occurring at the modulation frequency, leading to a periodic longitudinal deflection of a probe beam incident on the irradiated region. The presence of subsurface defects may scatter the generated thermal and elastic waves. It may also affect the absorption of the incident light. These processes may change the size and shape of the thermoelastic deformation of the heated region, and consequently, change the direction along which the probe beam deflects. Since the use of a four-quadrant photodetector permits the detection of such a change in deflection caused by subsurface defects, it appears that by fixing both the pump and probe lasers, moving the sample

perpendicularly to the heating beam, and measuring the deflection from the thermally deformed surface, images from subsurface defects can be recorded.

The signal of the beam deflection at the detector is given by:

$$S = \gamma \left\{ 2D \left[{du_z}/{dr(r_0)} \right] + 2u_z(r_0) \sin\theta + smaller\ terms \right\} \qquad \textbf{\textit{Eq. 3.1}}$$

where D denotes the distance from the sample to the detector, u_z is the surface displacement, θ is the angle of incidence of the probe beam, r_0 is the probe beam spot position relative to the pump beam spot, and γ is the sensitivity of the detector [153]. The first term in ***Eq. 3.1*** describes the contribution to the signal from a deflection by the slope of the thermoelastic surface displacement, while the second term is a measurement of the contribution to the signal from a small deflection of the probe beam by the vertical surface displacement. The second term is smaller than the first term by a factor in the order of the ratio of the sample-detector distance to the pump beam radius (around 10^4 in our experimental setup). The smaller terms are related to a minimal contribution to the signal from a slight displacement of r_0 during laser pumping. Thus, one can reasonably assume that the signal is due only to the first term in ***Eq. 3.1***, and therefore is directly proportional to the slope of the thermoelastic surface displacement [153]. To derive an expression for the slope of the thermoelastic surface displacement $\frac{\partial u_z}{\partial r}$ and predict the signal intensity on the detector, the equation for thermal diffusion:

$$\frac{\partial T}{\partial t} = \kappa \nabla^2 T + \frac{\bar{W}}{\rho C} \qquad \textbf{\textit{Eq. 3.2}}$$

and the thermoelastic Navier-Stokes equation for the displacement u_q

$$\nabla^2 u_q + \frac{1}{1-2\nu}\frac{\partial e}{\partial q} - \frac{2(1+\nu)}{1-2\nu}\alpha_{th}\frac{\partial Z}{\partial q} + \frac{X_q}{G} = 0 \qquad \textbf{\textit{Eq. 3.3}}$$

where:

$$2G = \frac{E}{1+\nu}\ ;\ e = \varepsilon_x + \varepsilon_y + \varepsilon_z \qquad \textbf{\textit{Eq. 3.4}}$$

have to be solved with appropriate initial and boundary conditions [153]. In Equations ***Eq. 3.2*** **-** ***Eq. 3.4***, $\bar{W}$ is the heat generated per unit time and per unit area, q is a Cartesian coordinate (x, y, or z), Z indicates differences of

temperature, E is Young's modulus, ν is Poisson's ratio, α_{th} is the coefficient of linear thermal expansion, $\varepsilon_q$denotes a displacement gradient in the q-direction, and $X_q$stands for a strain gradient in the q-direction. As demonstrated in Ref. [153], by using Green's functions for a slab pumped with a Gaussian beam, the solution to ***Eq. 3.2*** and ***Eq. 3.3*** providing the slope of the thermoelastic surface deformation in cylindrical coordinates takes the form

$$\frac{\partial U_z}{\partial r}(r,0) = f(\beta_{local}, R, D) \qquad \textit{Eq. 3.5}$$

where β_{local} is the local optical absorption coefficient, R stands for the local thermal properties, and D is a parameter related to the power and radius of the pump beam. The slope of the thermoelastic surface displacement was found to be insensitive to elastic properties. One can readily notice from **Eq. 3.5** that the contrast in a subsurface image recorded in a PBD experiment depends on local variations in the thermal properties within the heat-reaching depth, i.e., within a depth of $\mu_s = \sqrt{2\alpha/\omega}$, and local variations in the optical absorption coefficient within the light-reaching depth, i.e., within a depth of $\mu_\beta = 1/\beta$. Here, β is the macroscopic optical absorption coefficient of the measured sample. It follows from the above that either the thermal diffusion length or the wavelength of the pump laser beam determines the spatial resolution of a PBD subsurface imaging technique. It is in the order of the thermal diffusion length if the subsurface defect presents thermal properties different from those of the host material. However, it can be significantly enhanced to the order of the wavelength of the pump laser light in the material (which is smaller than that in the air) if the defect has an optical absorption coefficient different from that of the host material.

For direct assessment of the sensitivity of the developed technique to detect deep subsurface defects, we focused an H^+ ion beam on a small area at the surface of a commercial c-oriented 4H-SiC substrate. We set the dose and energy at 10^{14} H^+ ions/cm^2 and 10 keV, respectively, to create a defective area of about 250 x 250 μm^2 at a depth of 62 ± 2 μm. Then, we scanned the sample surface with measuring both the amplitude and phase of the longitudinal component of the probe beam deflected from the periodically deformed surface.

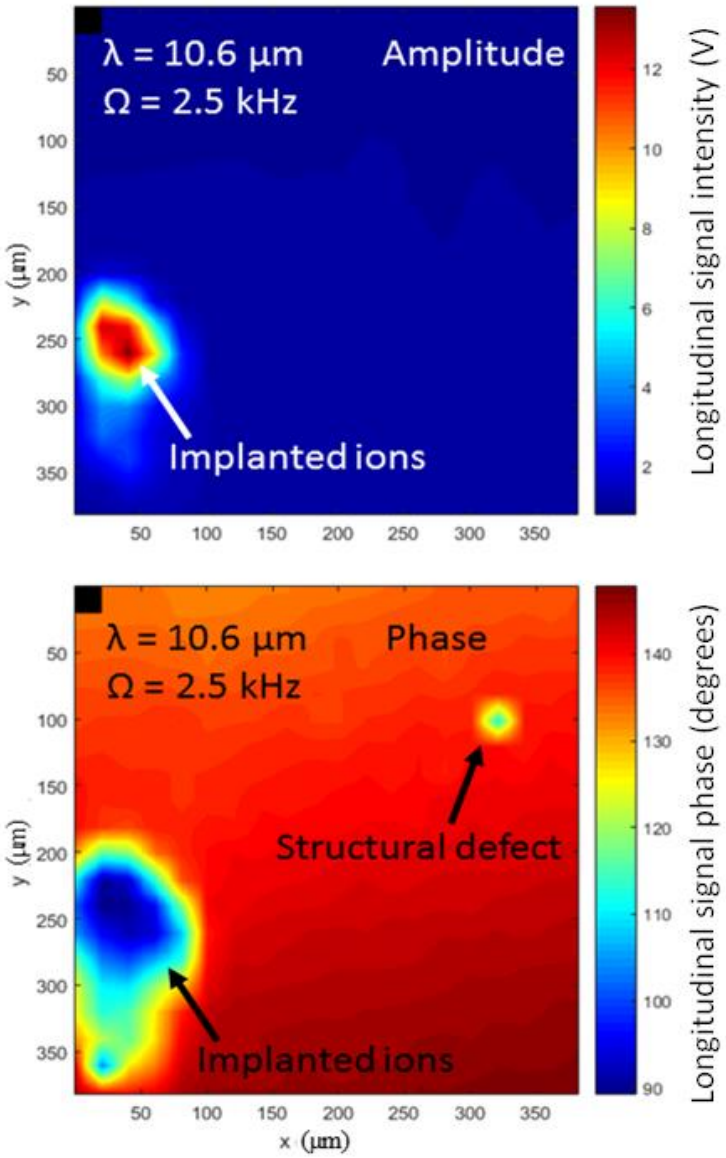

Figure 3.12 *Amplitude and phase images of a defective subsurface region induced by ions implantation. A structural defect could be detected in the phase image* [5].

The modulation frequency in these measurements was set at 2.5 kHz. We obtained extremely reproducible and well-contrasted amplitude and phase images of the defective subsurface region induced by the ions implantation. These images are shown in **Figure 3.12**. The obtained results show that the phase image is more sensitive than the amplitude image to the borders of the defective region. We attribute this difference in sensitivity between the amplitude and phase images to that the limitation of the efficiency of the four-

quadrant photodetector affects mainly the amplitude of the signal. Besides the precise imaging of such a deep defective region in the sample investigated, we could detect a well-resolved structural defect with regular geometric shape in the phase image. Based on the principle of PBD subsurface imaging presented above, we present in the rest of this section a detailed analysis of the high sensitivity and good spatial resolution achieved by using a pump laser in the mid-IR spectral range.

Let us investigate first the advantage of a mid-IR pump beam in terms of sensitivity. In **Figure 3.13**, we present mid-IR reflectivity spectra of three samples of 4H-SiC cut from the same substrate, but two of them uniformly irradiated by H+ ions at different doses to have samples with various defect concentrations. The energy of the incident ions was set at 10 keV to create defects distributed uniformly at a depth of 62 ± 2 µm from the surface. We also present in **Figure 3.13** the extinction coefficient curves obtained from the Kramers-Kronig conversion of the IR reflectivity spectra of the three measured samples [154]. It is clear that the presence of defects significantly alters the reflectivity and extinction coefficient, and consequently, the absorption coefficient in the mid-IR spectral range. However, the effect of defects on the extinction coefficient weakens rapidly as the wavelength shifts towards the visible spectral range. These results demonstrate that pumping with a mid-IR laser provides efficient optical sensing of defects embedded beneath the surface, which explains the observed high sensitivity of the developed technique to subsurface defects. The effect of defects on the absorption coefficient only in the mid-IR is understandable if we realize that the presence of a subsurface defect induces local vibrational modes and damps the normal vibrational modes, whose frequencies are in the mid-IR spectral range. Hence, it alters the local complex dielectric function and absorption coefficient only in the mid-IR spectral range [155]. It results that due to the strong effect of defects on the local optical absorption coefficient in the mid-IR spectral range, the use of a mid-IR pump laser in a PBD subsurface defects imaging has the advantage of greater sensitivity to defects situated at a depth μ_β from the surface.

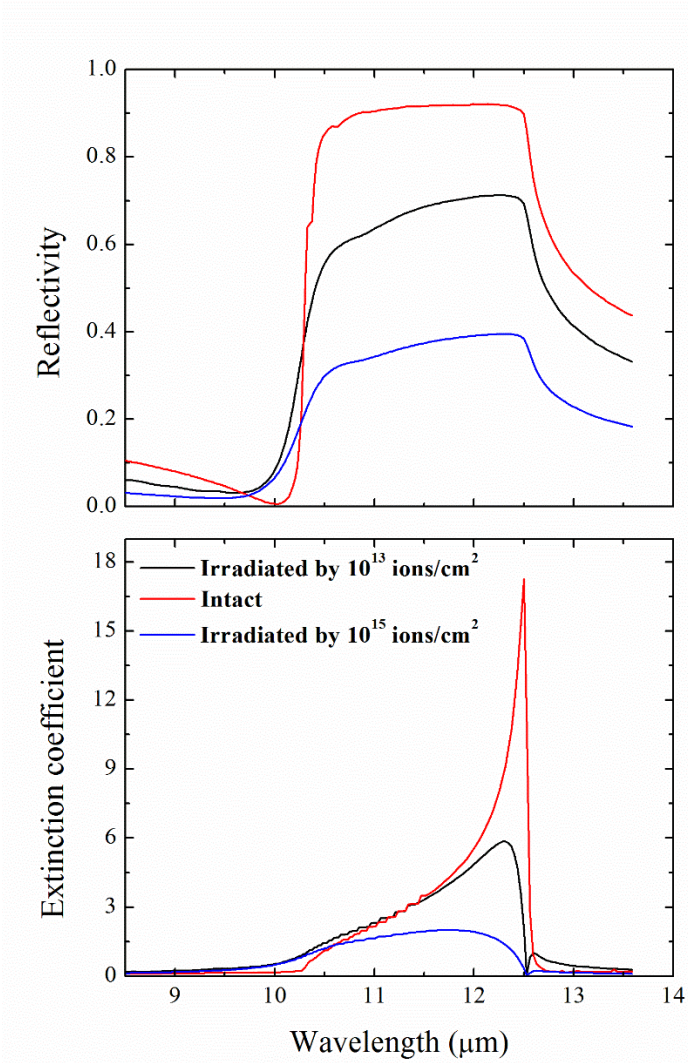

Figure 3.13 *Reflectivity and extinction coefficient spectra of intact and ion-irradiated silicon carbide substrates showing the strong dependence of the absorption of a polar material on the defect level in the mid-infrared spectral range.*

Let us now investigate the spatial resolution that can be achieved when a mid-IR pump laser is used in a PBD subsurface imaging technique. As mentioned earlier, when the sample is heated with a mid-IR laser, the spatial resolution is determined by the wavelength of the electromagnetic wave propagating inside the material. However, the coupling of the electric field of the mid-IR pump beam with the electric field associated with a longitudinal zone-center optical phonon mode gives rise to a phonon-polariton electromagnetic wave propagating in the sample [156]. In general, the phonon-polariton dispersion relation is given by

$$(ck)^2 = \varepsilon(\omega)\omega^2 \qquad \textit{Eq. 3.6}$$

where c is the speed of light in vacuum, and $\varepsilon(\omega)$is the complex dielectric function of the measured sample. The phonon-polariton dispersion relation associated with the intact SiC sample is plotted in **Figure 3.14** assuming real wavenumber ω and complex wavevector k. The real and imaginary parts of $\varepsilon(\omega)$ are derived from the reflectivity spectrum of the measured sample using the Kramers-Kronig conversion technique. The phonon-polariton dispersion in **Figure 3.14** clearly shows that for the wavenumber of the used pump laser beam, the slope of the phonon-polariton dispersion curve is very small. Such a small slope indicates that the group velocity of the phonon-polariton wave generated by the mid-IR pump laser beam is significantly lower than the group velocity of light in vacuum and the group velocity of visible light in the measured sample. This low speed of the phonon-polariton wave can be understood if we realize that the phonon-polariton wave, as it results from the coupling between photon and phonon, has a photon-phonon mixed character, which makes its velocity near phonon resonances closer to the phonon speed. As a result, the wavelength of the phonon-polariton electromagnetic wave propagating in the sample is significantly smaller than the wavelength of the pump laser beam (10.6 μm). Consequently, the slope of the thermoelastic surface deformation in an IR-PBD subsurface imaging experiment is sensitive to defects significantly smaller than the wavelength of the pump laser. The detector nevertheless integrates the deflection of the entire probe beam, then weights by the overall detected intensity. This detector function makes the spatial resolution of the IR-PBD subsurface imaging technique determined mainly by the size of the probe beam spot. Thus, the use of a mid-IR pump beam in a PBD subsurface imaging experiment has the advantage of greater sensitivity to subsurface defects and spatial resolution determined by the diffraction limit of the probe beam.

The high sensitivity and good spatial resolution of the developed IR-PBD subsurface imaging technique are not restricted to polar materials supporting phonon-polariton electromagnetic waves. The electric field of a mid-IR heating source can also couple to the electric field caused by the collective oscillations of free charges in metals or doped crystals to give rise to a plasmon-polariton propagative electromagnetic wave [157], whose dispersion relation is very similar to that of a phonon-polariton electromagnetic wave. In that case, subsurface defects remain detectable through induced local variations in the optical absorption coefficient with a resolution in the order of the wavelength of the probe beam. However, in the case of nonpolar undoped

insulators, the spatial resolution degrades to the order of the Pythagorean sum of the pump and probe laser radii $(R_1^2 + R_2^2)^{1/2}$ [153].

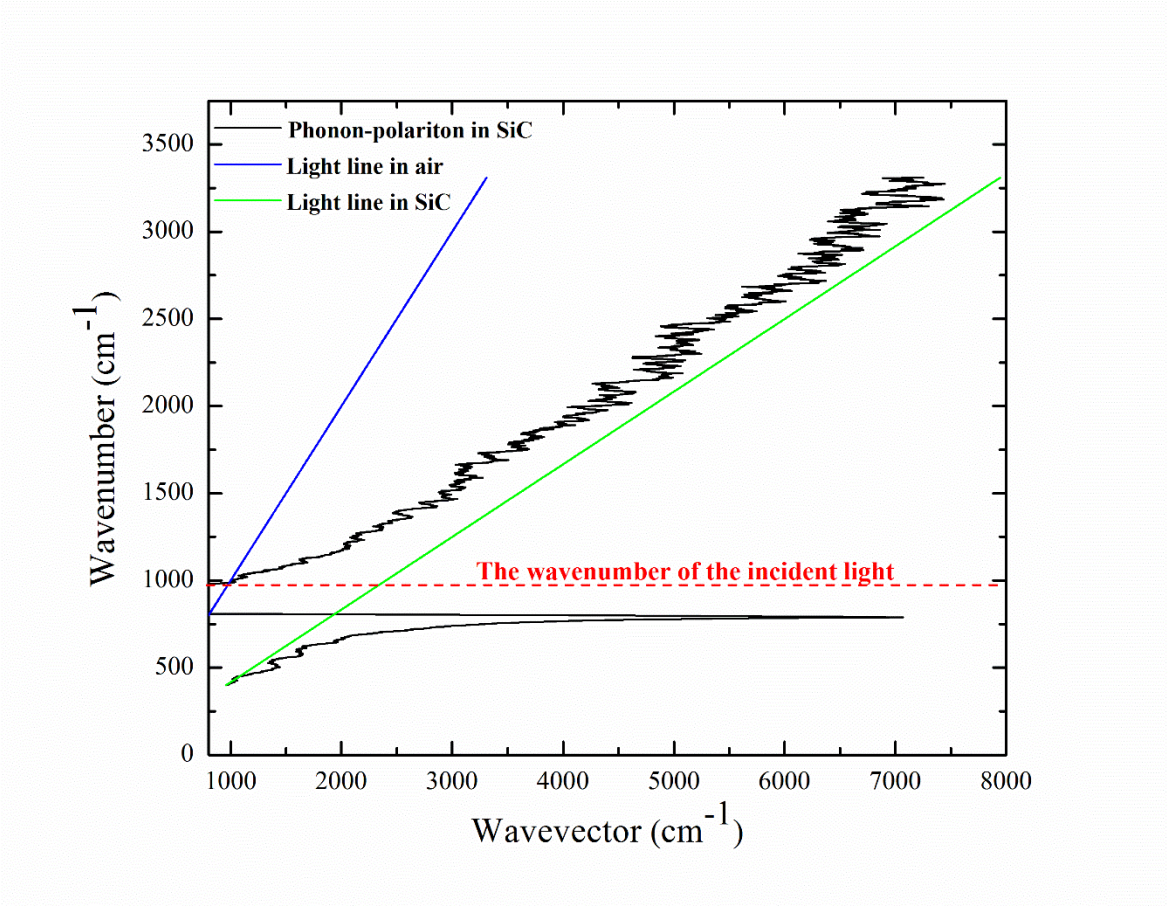

Figure 3.14 *Dispersion relation of the phonon-polariton electromagnetic wave in 4H-SiC crystal. The IR complex dielectric properties for the calculation of the dispersion relation are obtained from Kramers-Kronig conversion of the reflectivity spectrum.*

3.5 Conclusion

We presented a mid-IR photothermal beam deflection setup for fast measurement of thermal diffusivities of a broad class of materials and highly sensitive subsurface imaging. The developed setup uses the mirage effect to detect heat waves generated by the mid-IR source. We chose the excitation wavelength to be in the mid-infrared spectral range to ensure maximum absorption of light energy by phonon and plasmon modes in the surface layers of the sample, and consequently allow for thermal diffusivity measurement

without the need of any sample preparation. We demonstrated the importance of the mid-IR pump laser in a PBD experiment by measuring materials of extreme transmissivity and reflectivity in the visible spectral range without any metallic coating, which is unavoidably needed for measurement with a visible pump laser. We also emphasized the suitability of the proposed technique for highly sensitive imaging of subsurface defects in materials. We demonstrated the high subsurface detection power of the proposed technique by detecting damages induced by ions implanted at a depth of 62 ± 2 µm below the surface, and subsurface structural defects in a 4H-SiC substrate. We showed that the developed mid-IR setup takes advantage of the strong dependence of materials absorption coefficients in the mid-IR on defects to image defects buried at a large depth below the surface with high sensitivity. We provided a detailed analysis of the spatial resolution that could be achieved. We demonstrated that due to the low velocity of the phonon-polariton or plasmon-polariton near resonances in the mid-IR spectral range, the spatial resolution of an IR-PBD imaging technique could be in the order of the wavelength of the probe beam for materials supporting these electromagnetic waves. As the proposed technique simultaneously measures the thermal diffusivity and images subsurface defects with high sensitivity and good spatial resolution, it is expected to respond to important industrial needs for enhancing the performance of novel electronic devices.

4 Thermal and infrared analysis of the directional dependence of heat transport and defect formation in proton-irradiated 4H-SiC [158]

4.1 Introduction

The effect of the proton irradiation dose on the thermal transport anisotropy, free carrier density, and directional dependence of defect formation in 4H-SiC is studied using thermal wave scattering and infrared spectroscopy. Thermal waves are generated by infrared laser pulses, and the thermal diffusion length is measured along and perpendicular to the sample surface by using the deflection of a laser probe beam due to the mirage effect. The effect of the proton irradiation dose on the in-plane and cross-plane thermal diffusivity is measured as a function of depth. It is demonstrated that proton irradiation causes significant damage mainly in the direction perpendicular to the sample surface. Irradiation-induced free carriers contributing to heat transport in the sample plane are revealed by the Kramers-Kronig analysis of infrared reflectivity spectra of the studied samples. Measurements of cross-plane thermal diffusion lengths in the irradiated samples are converted into depth profiles of defect density. It is shown that the highly damaged zone in irradiated 4H-SiC thickens and approaches the proton reaching depth as the irradiation dose increases. Thermal wave scattering complemented by infrared spectroscopy is proposed as an efficient approach for the directional analysis of irradiation-induced modification of physical and structural properties of materials.

Silicon carbide (SiC) crystallizes in many structures called polytypes. The 4H-SiC polytype, which consists of four atomic layers stacked in a hexagonal Bravais lattice, has attracted increased attention because it corresponds to a wide-bandgap semiconductor with electrical, mechanical, and thermal properties suitable for high-power devices operating in harsh environments [159–165], such as nuclear reactors [166–168]. Extensive research has therefore been conducted on the effects of many types of nuclear irradiation on 4H-SiC [169–182]. However, the irradiation of 4H-SiC by protons has gained particular interest since it was discovered that the proton slicing technology allows obtaining ultrathin freestanding single-crystalline

4H-SiC substrates. This technology consists in irradiating a bulk crystal with protons to produce a highly damaged and fragile zone at a depth close to the end of the trajectory of the protons. Then, thin layers and flakes are detached from the irradiated bulk crystal by supplying additional energy, often in the form of heat [183,184].

Lattice damages due to proton irradiation of 4H-SiC have been detected experimentally [185–190], and it is now well known that a highly damaged zone forms close to the end of the trajectory of the protons. However, the structure of the irradiation-damaged 4H-SiC lattice and the extent to which proton irradiation alters the physical properties of 4H-SiC remain unclear. Unveiling these properties of proton-irradiated 4H-SiC is certainly crucial to predict the performance and lifetime of devices based on 4H-SiC material exposed to a given proton irradiation dose. The experimental techniques commonly used to characterize proton-irradiated materials are secondary ion mass spectroscopy (SIMS), Rutherford backscattering spectroscopy (RBS), and cross-sectional Raman spectroscopy. SIMS and RBS are accurate in measuring the depth profiles of ions concentrations in proton-irradiated samples [191]. Channeling RBS and cross-sectional Raman spectroscopy, on the other hand, have been widely used to provide a depth profile of the defect density in irradiated materials [186–188]. Nevertheless, none of these techniques is suitable for revealing the crystallographic directions along which defects form and measuring the effect of proton irradiation on the anisotropy of physical properties of the irradiated material.

In this section, we tackle this issue and perform a directional analysis of thermal diffusivity and depth profiles of defect density in 4H-SiC substrates irradiated with protons at 3MeV with different irradiation doses using the interaction of in-plane and cross-plane thermal waves with irradiation induced defects. Thermal waves are generated by a modulated infrared (IR) pumping laser beam, and the temperature gradient on the surface is detected using the deflection of a He-Ne probe beam due to the mirage effect. Then, the photothermal spectrum analysis, comparatively rare for the techniques commonly used to characterize irradiated materials, is performed based on a simple model to obtain directional-dependent thermal transport properties and depth profiles of defect density in the measured samples. The IR reflectivity spectra of the studied samples were analyzed using the Kramers-Kronig theorem to complement the IR photothermal measurements and obtain a full picture of the effect of the irradiation dose on structural and electronic properties of 4H-SiC. The advantage of using an IR pumping beam comes from the fact that 4H-SiC has a high absorption coefficient for IR excitations, allowing the absorption of a significant amount of the incident IR light in the surface layers, which is essential for locating the depths of the scattering centers. The

advantage of IR spectroscopy, on the other hand, stems from the fact that defects in polar materials can be detected through their marked signatures in the IR spectrum and that the density of free carriers can be revealed through the coupling between plasmon modes and infrared active longitudinal phonon modes.

4.2 METHODS

Five samples were cut from a commercial n-type c-oriented 4H-SiC wafer of electrical resistivity equal to 0.021 Ω.cm. Four of them were irradiated with 3 MeV protons (H^+ ions) at different doses, and one sample was left intact. The irradiation doses were set at 2.5 x 10^{15}, 5.0 x 10^{15}, 1.0 x 10^{16}, and 2 x 10^{16} ions/cm^2. The implantation of the H^+ ions was carried out at room temperature and the irradiated samples were tilted about 7° relative to the axis of the ion beam to avoid ion channeling effect. Classical Monte Carlo simulations performed using the SRIM code [192] showed that the concentration depth profiles of hydrogen in the irradiated samples exhibit narrow peaks centered at a depth of 60 ± 5 µm. Thus, as shown schematically in **Figure 4.1**, each of the irradiated samples studied in this work consists of an irradiated layer with a thickness a_1= 60 ± 5 µm separated from an intact 4H-SiC substrate by a zone of high concentration of H^+ ions. The only difference between the samples is the irradiation dose.

The cross-plane and in-plane thermal diffusion length in the samples were studied using an IR photothermal beam-deflection technique. The schematic diagram describing the IR photothermal experiment used is illustrated in **Figure 4.1**. This was discussed extensively in Sections (3.3.1 and 3.3.2), but I will briefly describe it as well: an acousto-optic modulator modulates a 10.6 µm wavelength CO_2 laser focused on the sample surface. The absorption of the incident IR beam by the infrared-active phonon and plasmon modes causes periodic local heating and periodic displacement of the surface, as well as the generation of rapidly damped thermal waves in the air above the heated surface. An incident He-Ne laser probe beam with a grazing angle (∼1° from the sample surface) is reflected off the heated surface. Since the heating beam, the probe beam, and the surface normal lie in the same plane, the surface displacement deflects only the longitudinal component (parallel to the heating beam) of the probe beam. Thermal waves generated in the air, on the other hand, give rise to periodic temperature and refractive index gradients capable of periodically deflecting the longitudinal and transverse components of the probe beam at the modulation frequency of the infrared heating beam. The deflection of the transverse component of the probe beam is thus due solely to the mirage

effect. The angular deflections of both components are recorded with a four-quadrant photodetector whose outputs are amplified with a two-channel lock-in amplifier. More details about the experimental setup can be found in Section 3.3.1 and 3.3.2 and in Ref. [5,193]. Then, the in-plane and cross-plane thermal diffusion length in the measured sample are obtained as a function of the modulation frequency by fitting the measured angular deflection of the transverse component vs. the offset distance between the heating beam and probe beam to a formalism for the mirage effect assuming a periodic and anisotropic heating of the sample (cf. Section 2.3.2 and Ref. [5]). For the intact sample (which can be considered as a semi-infinite material), it is assumed that periodic heating generates a single forward-going thermal wave in the sample. In that case, the formalism for the deflection of the transverse component of the probe beam is written as (cf. Section 2.3.2, Ref. [5]):

$$M_{trans} = \frac{-i}{\pi}\frac{1}{n}\frac{dn}{dT}e^{-q_g^2 R_2^2/4}\int_0^\infty dk \frac{k_g sin(kx)e^{ik_g h}e^{-k^2 R_1^2/4}}{\left(\kappa_{1,z}k_1 + \kappa_g k_g\right)} \qquad \textbf{\textit{Eq. 4.1}}$$

where x is the offset distance between the heating beam and probe beam. Here, n is the index of refraction of the air, R_1 is the radius of the heat spot on the sample surface, R_2 is the radius of the probe beam above the heated region, h is the height of the probe beam from the surface, $\kappa_{1,z}$ is the cross-plane thermal conductivity of the sample, and κ_g is the thermal conductivity of the air. The thermal wavevector in the sample is defined as

$$k_1 = \left(q_1^2 - \frac{L_{th}^2}{L_{th,z}^2}k^2\right)^{1/2} \qquad \textbf{\textit{Eq. 4.2}}$$

where L_{th} and $L_{th,z}$ are respectively the in-plane and cross-plane thermal diffusion length. The thermal wavenumber q_1 depends on $L_{th,z}$ according to

$$q_1 = (1+i)\left(\frac{1}{L_{th,z}}\right) \qquad \textbf{\textit{Eq. 4.3}}$$

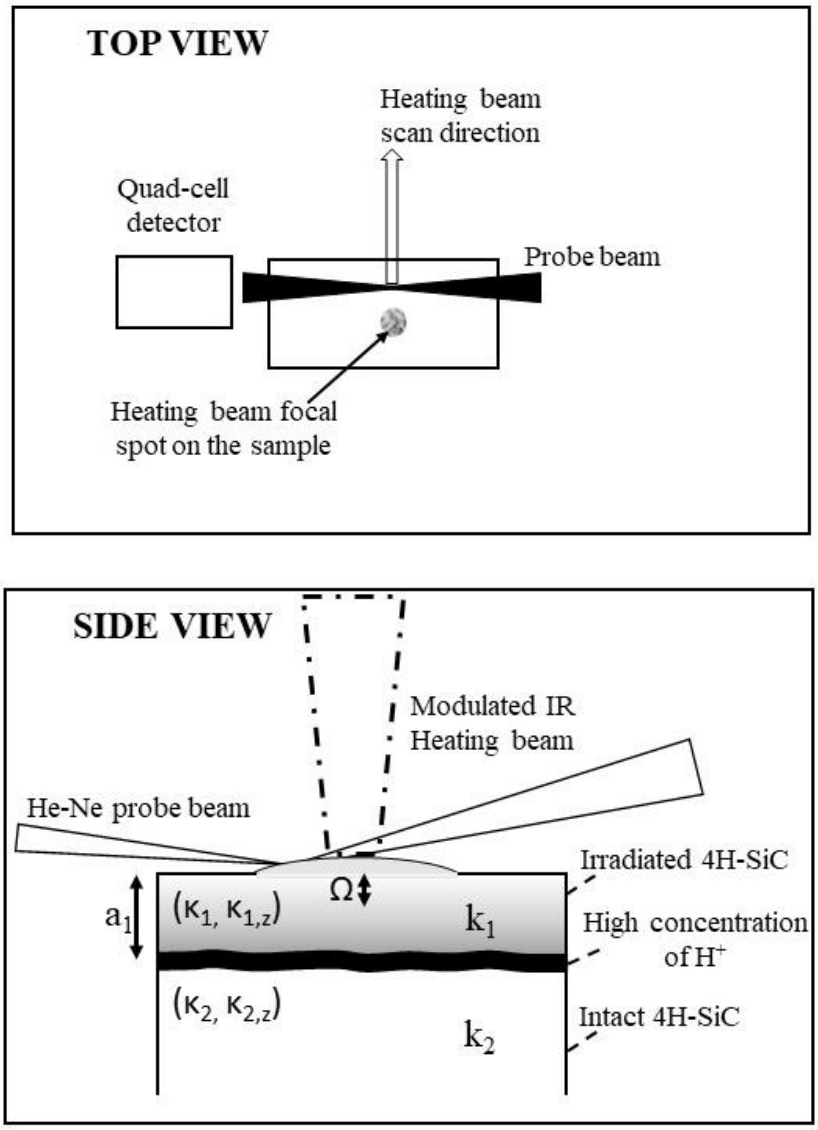

Figure 4.1 *Schematic representation of the proton-irradiated 4H-SiC samples investigated in this work and the infrared photothermal beam-deflection technique.*

The thermal wavevector in the air is given by $k_g = \left(q_g^2 - k^2\right)^{1/2}$, where $q_g = (1+i)\left(\Omega/2\alpha_g\right)^{1/2}$, Ω is the angular modulation frequency, and α_g is the thermal diffusivity of the air. The derivation of ***Eq. 4.1*** is detailed in Refs. [5,193] and in Section 2.3.2. To reduce the number of adjustable parameters, R_2 is measured using the knife-edge method and R_1 is estimated from the photothermal beam-deflection theory, which predicts that the maximum of the transverse signal amplitude occurs at $r = 1.1 \times R_1$ [194].

Moreover, we can notice from **Eq. 4.2** and ***Eq. 4.3*** that $L_{th,z}$ has almost the same effect on the real and imaginary part of the thermal wavevector k_1. In other words, $L_{th,z}$ affects in the same way the propagation term and damping term of the generated thermal wave and therefore has no significant influence on the amplitude and phase of the transverse signal. Consequently, for the case of semi-infinite materials, the photothermal beam-deflection technique is insensitive to $L_{th,z}$ and the only adjustable parameters are R_1, h, and the in-plane thermal diffusion length L_{th}.

For a given modulation frequency Ω, the in-plane thermal diffusivity $\alpha_{//}$ is related to L_{th} by

$$L_{th} = \sqrt{\frac{\alpha_{//}}{\pi\Omega}} \qquad \textbf{\textit{Eq. 4.4}}$$

Thus, the in-plane thermal diffusivity of the intact sample can be obtained by measuring $L_{th}$for several modulation frequencies and calculating the slope of the straight line passing through origin that best fits the measured L_{th}^2 vs. $1/\pi\Omega$.

As mentioned previously, the irradiated samples are considered to be formed by an irradiated layer with a thickness a_1= 60 ± 5 µm separated from an intact 4H-SiC substrate by a zone of high concentration of hydrogen. It is therefore assumed that in the case of irradiated samples, the thermal waves generated are backscattered at the interface between the irradiated and intact 4H-SiC. When forward-going and backward-going thermal waves are taken into account, the formalism for the angular deflection of the transverse component of the probe beam takes the form:

$$M'_{trans} = \frac{-i}{\pi}\frac{1}{n}\frac{dn}{dT}e^{-q_g^2R_2^2/4}\int_0^\infty dk\,\frac{k_g sin(kx)e^{ik_g h}e^{-k^2R_1^2/4}}{\left(\kappa_{1,z}k_1 coth(\theta_1)+\kappa_g k_g\right)} \qquad \textbf{\textit{Eq. 4.5}}$$

The complex constant θ_1 describing the relative amplitude and phase between the forward-going and the backward-going thermal waves in the irradiated region is given by:

$$\theta_1 = -ik_1a_1 + atanh\left(\frac{\kappa_{1,z}.k_1}{\kappa_{2,z}.k_2}\right) \qquad \textbf{\textit{Eq. 4.6}}$$

Here, k_1 and k_2 are the thermal wavevectors in the irradiated and intact 4H-SiC, respectively. These wavevectors depend on the in-plane and cross-plane thermal diffusion length, which in turn depend on the modulation frequency

(see ***Eq. 4.2*** and ***Eq. 4.3***). The parameters $\kappa_{1,z}$ and $\kappa_{2,z}$ are the cross-plane thermal conductivities of the irradiated and intact 4H-SiC, respectively. The derivation of ***Eq. 4.5*** is detailed in Ref. [195] and in Supplementary Information at the end of this chapter (Section 4.5.1). It is worth noting that the relative amplitude and phase between the forward-going and the backward-going thermal waves in the irradiated 4H-SiC makes the angular deflection of the transverse component of the probe beam dependent on both the in-plane and cross-plane thermal diffusion length. Consequently, in the case of multilayer systems, the adjustable parameters are R_1, h, as well as the in-plane thermal diffusion length L_{th} and the cross-plane thermal diffusion length $L_{th,z}$. The in-plane and cross-plane thermal diffusivity of the irradiated 4H-SiC can be obtained by following the procedure presented above for the case of a semi-infinite material.

To obtain information about the effect of the irradiation dose on structural and electrical properties of 4H-SiC, Fourier transform IR (FTIR) reflectivity measurements were performed on the samples described above. The measurements were carried out in the frequency range 400-4000 cm^{-1} with a spectral resolution better than 2 cm^{-1} using a deuterated triglycine sulfate (DTGS) detector and a potassium bromide (KBr) Beam-splitter. The IR beam was unpolarized and the angle of incidence was set at 45° to excite zone center optical phonon modes of different symmetries [196]. The reflectivity spectrum of each sample was normalized to the reflectivity spectrum of a gold mirror and the reproducibility of the measurements was verified by measuring the reflectivity spectra of the samples several times. The FTIR spectrometer was designed with the appropriate care to ensure that the reflected electromagnetic waves meet the plane wave approximation for accurate Kramers-Kronig conversion of the reflectivity spectra. It is worth noting that the resonance of the phonon and plasmon modes in the IR spectral range makes the absorption coefficient of 4H-SiC very high for an IR excitation. Furthermore, the irregularities at the hydrogen-enriched interface between the irradiated and intact 4H-SiC scatter the infrared light and prevent interference between the rays reflected from the irradiated 4H-SiC and the rays reflected from the intact 4H-SiC. Therefore, the recorded IR reflectivity spectra are essentially dictated by phonon and plasmon modes in the irradiated 4H-SiC, and their Kramers-Kronig conversions provide the real and imaginary parts of the infrared dielectric functions of the irradiated 4H-SiC layers only.

4.3 RESULTS AND DISCUSSION

The amplitudes and phases of the transverse signals obtained from the intact sample for nine different modulation frequencies are presented in **Figure 4.2** as a function of the offset distance between the heating beam and probe beam. The amplitude increases as the heating beam moves closer to the probe beam, then goes sharply to zero when the two beams overlap. At this point, the phase shifts by 2π and the amplitude repeats itself as a mirror image. When the phase of the signal reaches -2π or $+2\pi$, it changes sign. Beyond an offset distance of a few thermal diffusion lengths, mechanical coupling to the direct heated regions of the sample dominates, causing the phase to fluctuate. This part of the recorded spectra was omitted from consideration in the data analysis. As described in Section 4.2, while the angular deflection of the probe beam is insensitive to the cross-plane thermal diffusion length in the intact sample, the in-plane thermal diffusion length in that sample can be accurately obtained for each modulation frequency by fitting both the amplitude and phase of the transverse signals to ***Eq. 4.1***. The high quality of the multi-parameter least squares fits of the amplitudes and phases of the transverse signals from the intact sample is illustrated by solid lines in **Figure 4.2**. The in-plane thermal diffusivity of the intact sample is obtained, as shown in **Figure 4.3**, from the slope of the straight line passing through origin that best fits the measured L_{th}^2 with respect to $1/\pi\Omega$. An in-plane thermal diffusivity of 2.0±0.04 cm^2/s is obtained for intact 4H-SiC. This value corresponds to an in-plane thermal conductivity of 443 W/m.K, which is in agreement with previously reported results of thermal measurements and first-principles calculations on 4H-SiC [197,198].

The amplitudes and phases of the transverse signals obtained from the proton-irradiated 4H-SiC samples for nine different modulation frequencies are presented in Supplementary Information at the end of this chapter (Section 4.5.2) vs. the offset distance between the heating beam and probe beam. The shapes of these curves are similar to the shapes of the curves obtained from the intact sample. However, the best fit of the transverse signals from the irradiated samples to ***Eq. 4.1***, which considers

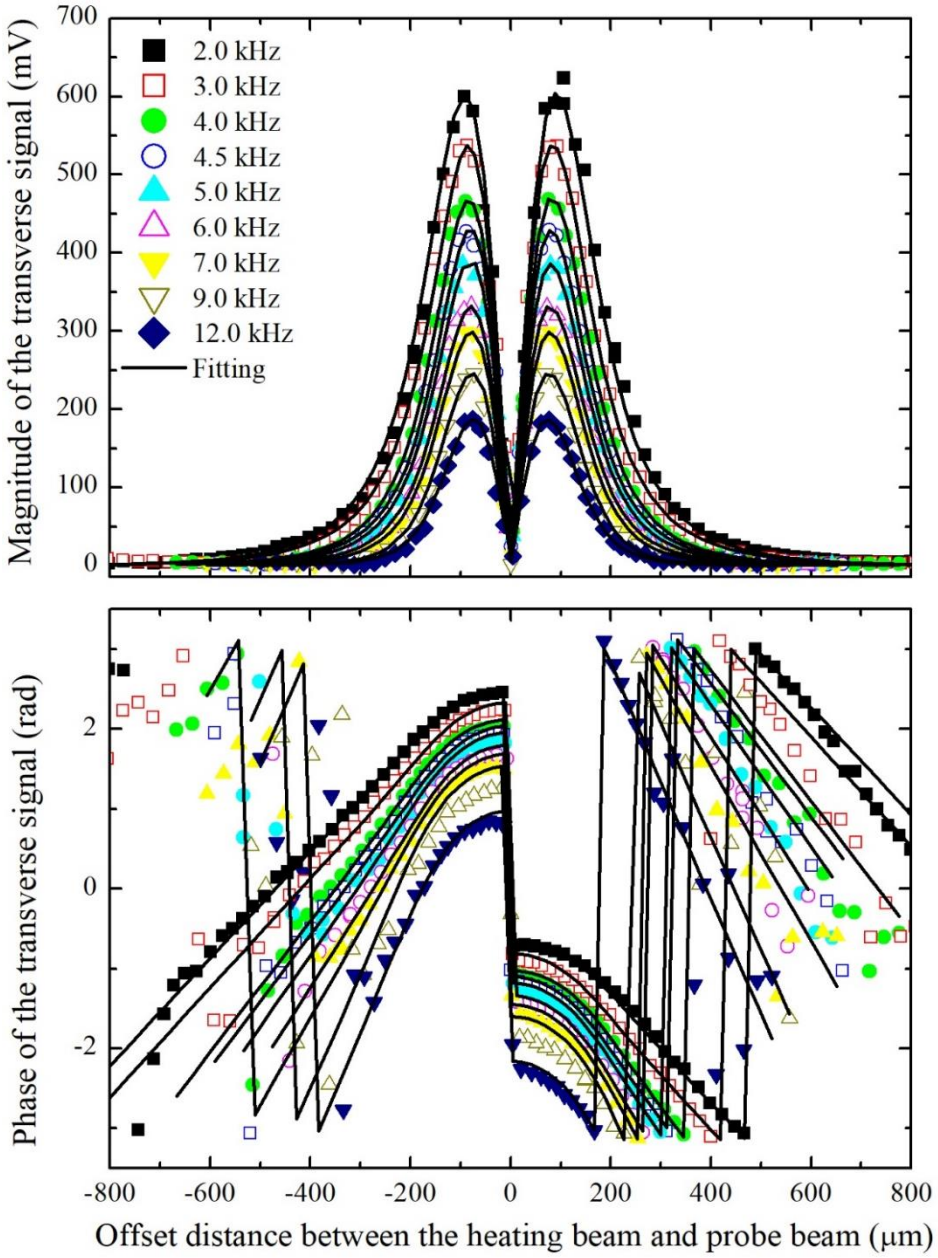

Figure 4.2 *Magnitudes and phases of transverse photothermal signals from an intact 4H-SiC substrate relative to the offset distance between the heating beam and probe beam for nine different heating beam modulation frequencies. The symbols represent the experimental data. The solid lines represent the fits of the experimental data to a formalism for the angular deflection of the probe beam due to the mirage effect with taking into account a single forward-going thermal wave.*

a single forward-going thermal wave, gave no reasonable result. Reasonable values for the thermal diffusion lengths in the implanted layers of these samples

were obtained only by fitting the measured transverse signals to ***Eq. 4.5***, which accounts for the backscattering of thermal waves at the hydrogen-enriched zone at the proton reaching depth. As demonstrated in Section 4.2, the backscattering of thermal waves at the interface between the irradiated and intact 4H-SiC makes both the in-plane and cross-plane thermal diffusion length measurable. The high quality of the multi-parameter least squares fits of the magnitudes and phases of the transverse signals from the irradiated samples is illustrated by solid lines in Supplementary Information at the end of this chapter (section 4.5.2).

The cross-plane thermal diffusion length $L_{th,z}$ in the 4H-SiC layer irradiated with a proton dose of 2.5 x 10^{15} ions/cm^2 is shown in **Figure 4.4**(a) vs. $1/\pi\Omega$. The cross-plane thermal diffusivity $\alpha_\perp$of that layer can be obtained from $L_{th,z}^2 \times \pi\Omega$. For high modulation frequencies, i.e., when the thermal wave dies out before reaching the irradiation-induced highly damaged zone, $\alpha_\perp$ turns out to be 0.81 cm^2/s. This value is about 38% lower than the cross-plane thermal diffusivity of defect-free 4H-SiC (as can be concluded from Refs. [197] and [198]), indicating irradiation-induced defects along the axis of the hexagonal unit cell of the irradiated 4H-SiC. For moderate modulation frequencies, the thermal diffusion becomes of the order of the irradiated layer. Thus, the thermal wave scatters at the highly damaged zone in the irradiated 4H-SiC layer, causing $\alpha_\perp$ to drop and $L_{th,z}^2$ to deviate from the linear dependence on $1/\pi\Omega$. For low modulation frequencies, the thermal wavelength becomes significantly larger than the thickness of the irradiated 4H-SiC layer, and thus the rate at which thermal waves scatter by irradiation-induced defects decreases with the modulation frequency. Therefore, $L_{th,z}^2$ increases again with $1/\pi\Omega$.

The in-plane thermal diffusion length L_{th} in the 4H-SiC layer irradiated with a proton dose of 2.5 x 10^{15} ions/cm^2 is shown in **Figure 4.4**(b) vs. $1/\pi\Omega$. As demonstrated in Section II, the slope of the straight line passing through origin that best fits the measured L_{th}^2 vs. $1/\pi\Omega$ gives the in-plane thermal diffusivity of the 4H-SiC layer whose thickness is determined by the thermal wave reaching depth. For high modulation frequencies, the thermal wave is extinguished before reaching the highly damaged zone, and hence, the measured 4H-SiC layer does not include that zone. In that case, the slope of the straight line passing through origin that best fits the measured L_{th}^2 vs. $1/\pi\Omega$ shows that the in-plane thermal diffusivity is 2.07 ± 0.04 cm^2/s. This value is comparable and even slightly higher than the in-plane thermal diffusivity of the intact sample, indicating that proton irradiation with a dose of 2.5 x 10^{15} ions/cm^2 causes no noticeable damage in the basal plane of the 4H-SiC hexagonal unit cell. The origin of the observed slight increase in in-plane

thermal diffusivity of the irradiated 4H-SiC will be discussed later. For lower modulation frequencies, the thermal wave generated at the surface reaches the severely damaged zone, and hence the measured 4H-SiC layer includes this zone.

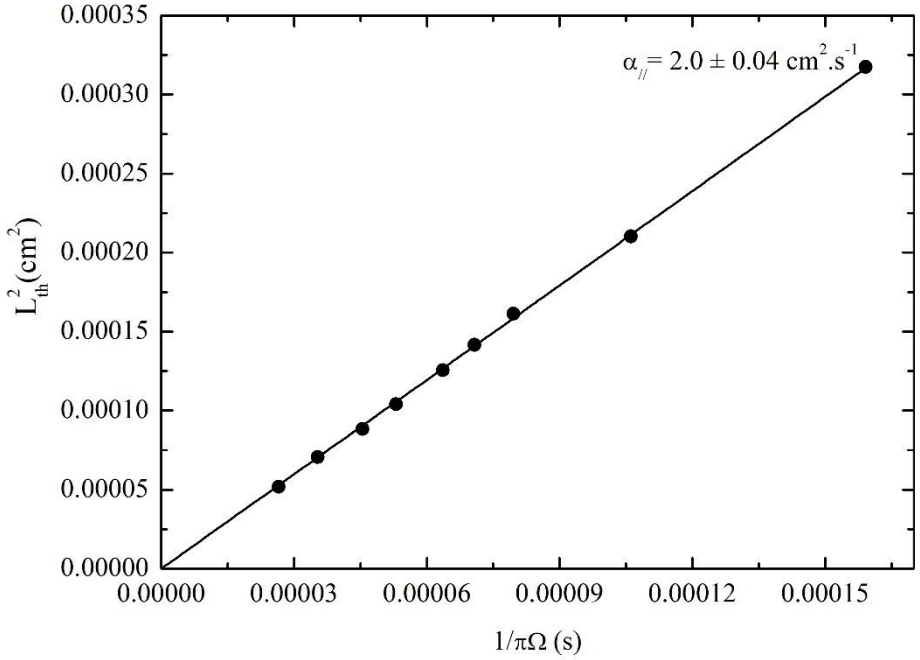

Figure 4.3 *Square of in-plane thermal diffusion length in intact 4H-SiC substrate vs.* $1/\pi\Omega$*, where* Ω *is the heating beam modulation frequency. The data set is fitted to a straight line passing through origin whose slope is equal to the in-plane thermal diffusivity of the measured sample. The uncertainties are determined by the experiment sensitivity and the scatter in the data points.*

As the thermal diffusivity of the highly damaged layer is low [199–203], the slope of the straight line passing through origin that best fits L_{th}^2 vs. $1/\pi\Omega$ decreases, indicating that the overall in-plane thermal diffusivity of the measured layer drops to 1.93 ± 0.04 cm^2/s. The relationship between the in-plane thermal diffusivity of the highly damaged zone and the overall in-plane thermal diffusivity of the measured 4H-SiC layer is provided in 4.5.3.

To complement the photothermal measurements, we performed FTIR reflectivity measurements on the intact and irradiated samples. The FTIR reflectivity spectra from the samples investigated are shown together

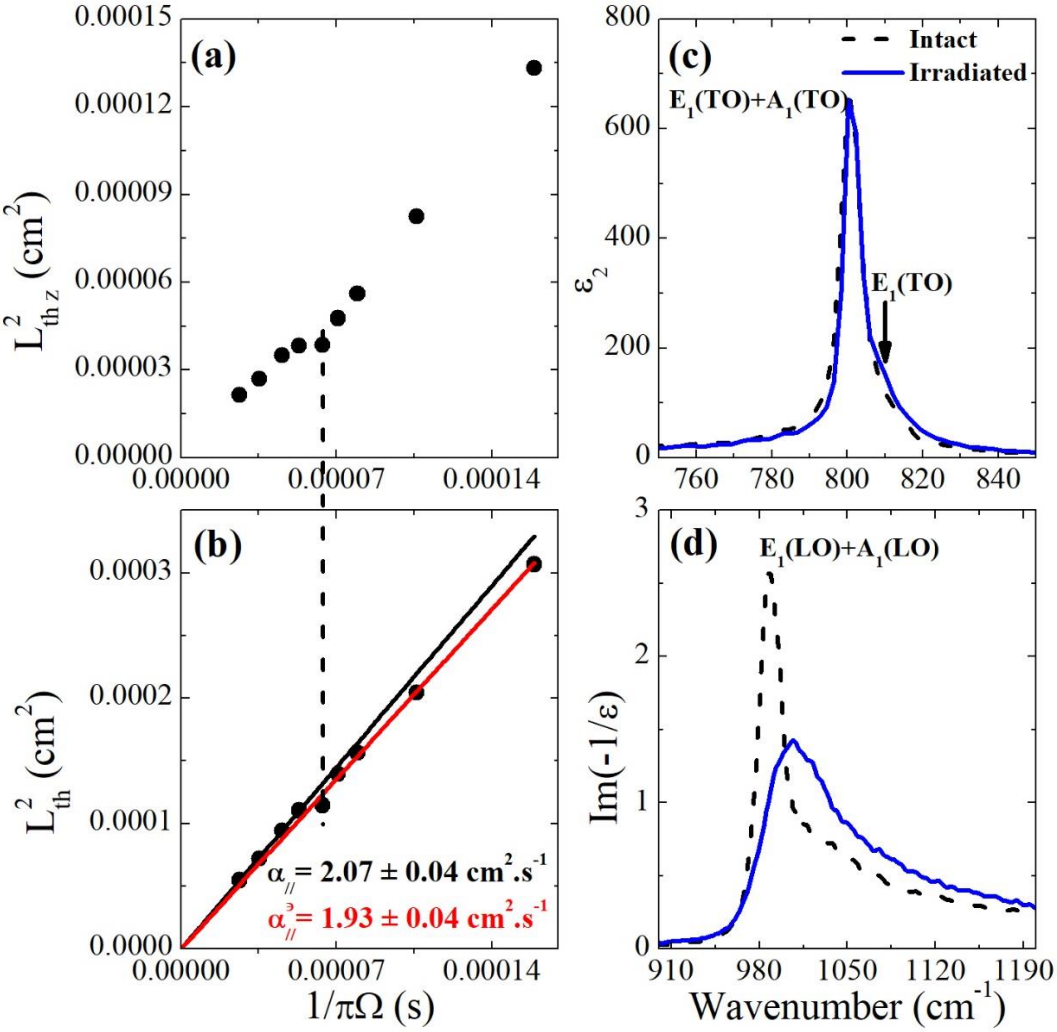

Figure 4.4 *Infrared analysis of 4H-SiC substrate irradiated with protons at 3MeV with a dose of 2.5 x 10^{15} H^+ ions/cm^2. (a) Square of cross-plane thermal diffusion length $L^2_{th,z}$ vs. the inverse of the heating beam modulation frequency. (b) Square of in-plane thermal diffusion length L^2_{th} vs. the inverse of the heating beam modulation frequency. The slopes of the straight line passing through origin that best fit the data points give the in-plane thermal diffusivity for high and low heating beam modulation frequencies. The uncertainties are determined by the experiment sensitivity and the scatter in the data points. The vertical dashed line is introduced to highlight the fact that $L^2_{th,z}$ and L^2_{th} undergo the strongest deviation from the linear behavior for the same modulation frequency. (c) Imaginary parts of the infrared dielectric functions of intact 4H-SiC and the irradiated sample. (d) Imaginary parts of the inverse of the negative of the dielectric functions of intact 4H-SiC and the irradiated sample.*

in **Figure 4.9**. The frequency-dependent infrared complex dielectric functions $\varepsilon(\omega)$ of the samples were obtained from the Kramers-Kronig (KK) conversion of the measured FTIR reflectivity spectra. The KK theorem was implemented with necessary precautions to minimize the error that can result from integration over a finite frequency range [154]. The resonances of the TO phonon modes are obtained from the imaginary part of the dielectric function and the resonances of the LO phonon modes are obtained from the imaginary part of the negative of the inverse of the dielectric function. The plasmon modes (i.e., the vibration modes corresponding to collective oscillations of free carriers) are also infrared-active and should show signatures in the IR spectrum. However, the frequencies of the LO phonon and plasmon modes usually occur very close to each other, and therefore, they couple through their associated electric fields to give rise to the so-called longitudinal plasmon-phonon mode [204–207]. The plasmon-phonon coupling manifests itself by a resonance frequency higher than that of the LO phonon mode and by a broad and asymmetric resonance line in the IR spectrum.

The resonance lines of the infrared-active transverse optical (TO) phonons in the intact sample and the sample irradiated with a dose of 2.5 x 10^{15} ions/cm^2 are shown in **Figure 4.4** (c), and the resonance lines of the infrared-active longitudinal optical (LO) phonon modes in these samples are shown in **Figure 4.4** (d). The detected phonons are of pure E_1 symmetry and mixed A_1 and E_1 symmetry. The identification of the symmetries of the infrared-active phonons in 4H-SiC is provided in section 4.5.4. No noticeable effect of proton irradiation at a dose of 2.5 x 10^{15} ions/cm^2 is observed on the imaginary part of the infrared dielectric function. This result indicates that the density of lattice damage induced by proton irradiation at a dose of 2.5 x 10^{15} ions/cm^2 is high enough to scatter cross-plane thermal waves, but low enough to be observed in vibrational spectroscopy. As the substrate used in this work is n-type, the resonance line of the LO phonon in the intact sample exhibits an asymmetric peak with a broad tail at high frequencies, indicating coupling between the mixed A_1 and E_1 symmetry LO phonon mode with a plasmon mode. The resonance line of the LO phonon in the sample irradiated with a proton dose of 2.5 x 10^{15} ions/cm^2, however, is shifted towards higher frequencies and is broader, indicating irradiation-induced additional free carriers in the implanted layer. As demonstrated above, proton irradiation of 4H-SiC with a dose of 2.5 x 10^{15} ions/cm^2 causes no noticeable damage in the basal plane of the 4H-SiC hexagonal unit cell. Hence, the additional free carriers generated by proton irradiation can contribute to heat transport in the plane of the sample and raise the in-plane thermal diffusivity of the irradiated layer over that of the intact

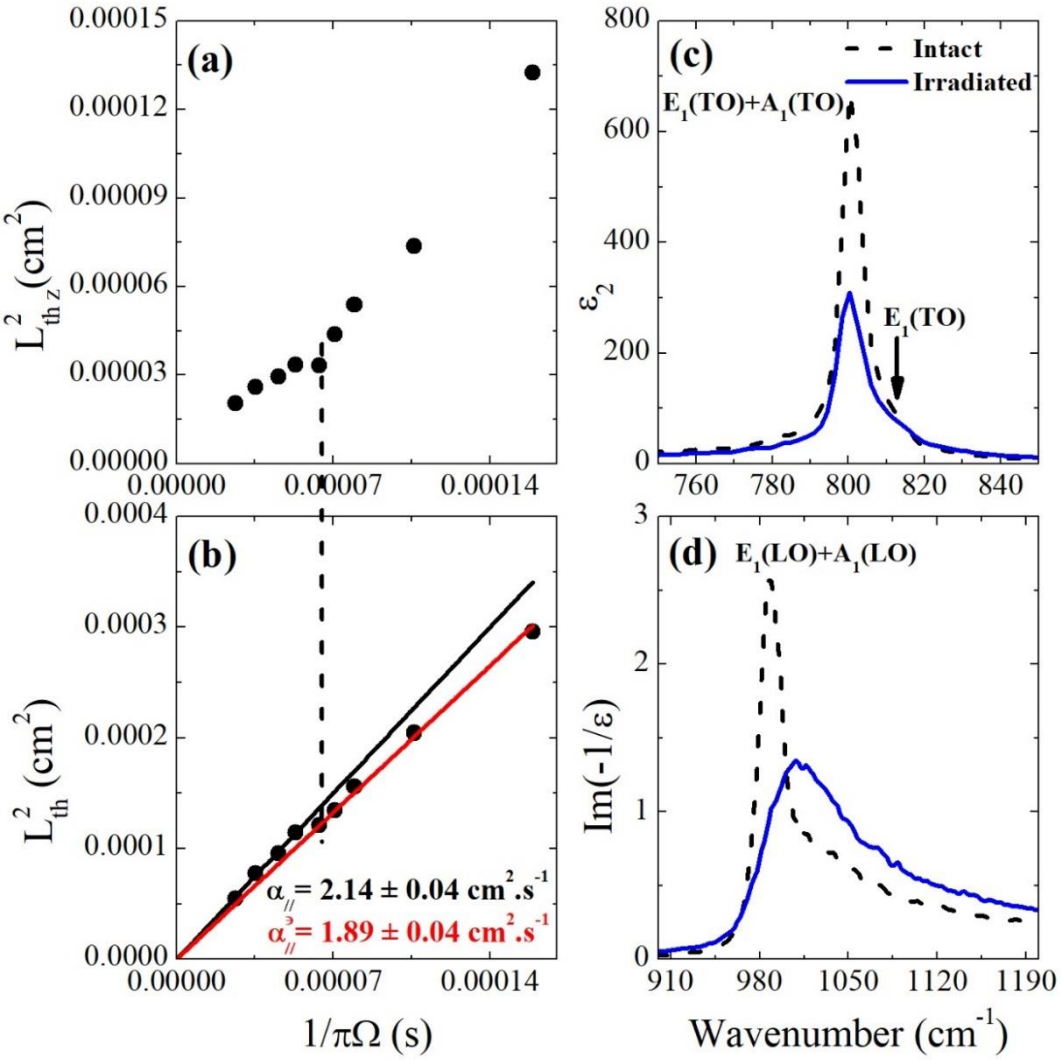

Figure 4.5 *Infrared analysis of 4H-SiC substrate irradiated with protons at 3MeV with a dose of 5.0 x 10^{15} H^+ ions/cm^2. (a) Square of cross-plane thermal diffusion length $L^2_{th,z}$ vs. the inverse of the heating beam modulation frequency. (b) Square of in-plane thermal diffusion length L^2_{th} vs. the inverse of the heating beam modulation frequency. The slopes of the straight line passing through origin that best fit the data points give the in-plane thermal diffusivity for high and low heating beam modulation frequencies. The uncertainties are determined by the experiment sensitivity and the scatter in the data points. The vertical dashed line is introduced to highlight the fact that $L^2_{th,z}$ and L^2_{th} undergo the strongest deviation from the linear behavior for the same modulation frequency. (c) Imaginary parts of the infrared dielectric functions of intact 4H-SiC and the irradiated sample. (d) Imaginary parts of the inverse of the negative of the dielectric functions of intact 4H-SiC and the irradiated sample.*

sample, which explains the fact that the in-plane thermal diffusivity of the implanted layer is slightly higher than that of the intact sample. Signature from

the E_1 symmetry LO phonon is not observed because the plasmon-phonon mode resonance line overwhelms it.

The cross-plane and in-plane thermal diffusion length in the sample irradiated with a proton dose of 5.0 x 10^{15} ions/cm^2 are shown in **Figure 4.5** (a) and **Figure 4.5** (b), respectively, for nine different modulation frequencies. For a modulation frequency of 12 kHz, the cross-plane thermal diffusivity $\alpha_{\perp}$is 0.77 ± 0.04 cm^2/s, which is about 41% lower than the cross-plane thermal diffusivity of defect-free 4H-SiC [197,198]. As the modulation frequency decreases (i.e., as the thermal wave generated at the surface reaches a greater depth), $\alpha_{\perp}$ decreases gradually, indicating that the density of the irradiation-induced defects along the axis of the hexagonal unit cell of 4H-SiC increases with depth. For the modulation frequency for which the cross-plane thermal diffusion length is of the order of the irradiated layer, the thermal wave scatters at the highly damaged zone, preventing $L_{th,z}^2$ from increasing with $1/\pi\Omega$ and causing $\alpha_{\perp}$to drop rapidly. For sufficiently low modulation frequencies, the thermal wavelength becomes significantly larger than the thickness of the irradiated 4H-SiC layer, so the rate at which thermal waves scatter by irradiation-induced defects decreases. Therefore, $L_{th,z}^2$ increases again with $1/\pi\Omega$.

The slope of the straight line passing through origin that best fits L_{th}^2 with respect to $1/\pi\Omega$ for the high modulation frequencies shows that the in-plane thermal diffusivity $\alpha_{//}$ of a 4H-SiC layer irradiated by protons at a dose of 5.0 x 10^{15} ions/cm^2 but not containing the highly damaged zone is 2.14 ± 0.04 cm^2/s. This value of $\alpha_{//}$, which is slightly higher than that of the in-plane thermal diffusivity of intact 4H-SiC, indicates that proton irradiation with a dose of 5.0 x 10^{15} ions/cm^2 causes no noticeable damage in the basal plane of the 4H-SiC unit cell and generates free carriers that contribute to heat transport. Evidence of irradiation-induced free carriers is demonstrated above for an irradiation dose of 2.5 x 10^{15} ions/cm^2 and will be demonstrated later for an irradiation dose of 5.0 x 10^{15} ions/cm^2. For lower modulation frequencies, i.e., when the measured 4H-SiC layer contains the heavily damaged zone, $\alpha_{//}$ drops to 1.89 ± 0.04 cm^2/s.

The resonances of the infrared-active TO and LO phonons in the intact sample and the sample irradiated with a dose of 5.0 x 10^{15} ions/cm^2 are shown in **Figure 4.5** (c) and **Figure 4.5** (d), respectively. As can be seen in **Figure 4.5** (c), the intensity of the resonance line of the TO phonon in the irradiated layer is lower than that of the resonance line of the TO phonon in the intact 4H-SiC, indicating that for a proton irradiation dose of 5.0 x 10^{15} ions/cm^2, the lattice deterioration reaches a level detectable in vibrational spectroscopy. The comparison between the resonance lines of the LO phonons in the irradiated layer and in the intact 4H-SiC, shown in **Figure 4.5** (d), clearly demonstrates

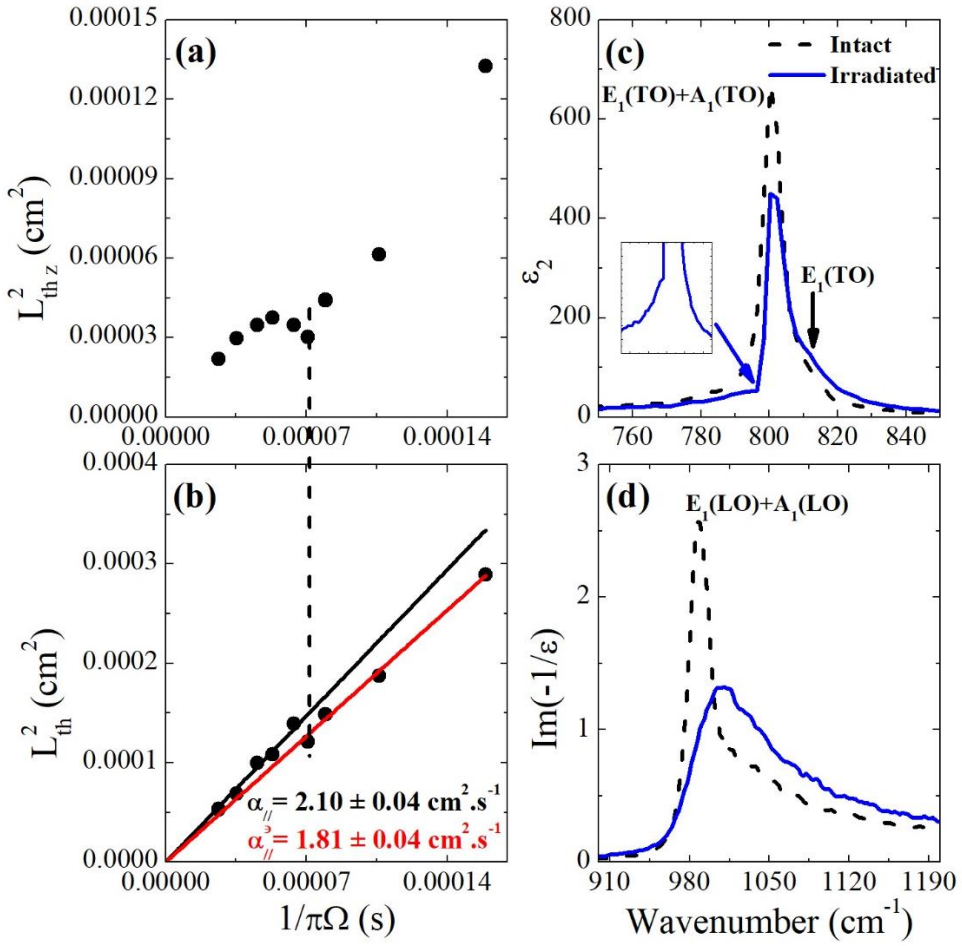

Figure 4.6 *Infrared analysis of 4H-SiC substrate irradiated with protons at 3MeV with a dose of 1.0 x 10^{16} H^+ ions/cm^2. (a) Square of cross-plane thermal diffusion length $L^2_{th,z}$ vs. the inverse of the heating beam modulation frequency. (b) Square of in-plane thermal diffusion length L^2_{th} vs. the inverse of the heating beam modulation frequency. The slopes of the straight line passing through origin that best fit the data points give the in-plane thermal diffusivity for high and low heating beam modulation frequencies. The uncertainties are determined by the experiment sensitivity and the scatter in the data points. The vertical dashed line is introduced to highlight the fact that $L^2_{th,z}$ and L^2_{th} undergo the strongest deviation from the linear behavior for the same modulation frequency. (c) Imaginary parts of the infrared dielectric functions of intact 4H-SiC and the irradiated sample. (d) Imaginary parts of the inverse of the negative of the dielectric functions of intact 4H-SiC and the irradiated sample.*

that a proton irradiation dose of 5.0 x 10^{15} ions/cm^2 generates additional free carriers whose collective vibrational mode couples with the LO phonon mode.

The cross-plane and in-plane thermal diffusion length in the sample irradiated with a proton dose of 1.0 x 10^{16} ions/cm^2 are shown in **Figure 4.6** (a) and **Figure 4.6** (b), respectively, for nine different modulation frequencies. For this irradiation dose, the curve corresponding to $L_{th,z}^2$ vs. $1/\pi\Omega$ gradually deviates from a straight line as the modulation frequency increases. Then, it decreases sharply for modulation frequencies for which the cross-plane thermal diffusion lengths are of the order of the thickness of the irradiated layer and increases again for frequencies for which the cross-plane thermal diffusion lengths are significantly larger than the thickness of the irradiated layer. However, the rate at which this curve increases at low frequencies is markedly lower than the rate at which it increases for lower irradiation doses. This behavior of the $L_{th,z}^2$ vs. $1/\pi\Omega$ curve indicates that the highly damaged zone in the layer irradiated with a proton dose of 1.0 x 10^{16} ions/cm^2 is significantly thicker than that in the layers irradiated at lower doses. The dependence of $\alpha_{//}$ on the modulation frequency shown in **Figure 4.6** (b) demonstrates, on the other hand, that even at such a high irradiation dose, the proton irradiation causes no noticeable damage in the basal plane of the 4H-SiC unit cell and the induced free carriers contribute to the heat transport in the plane of the irradiated layer. The fact that the drop in $\alpha_{//}$ when the thermal wave reaches the highly damaged region is now greater than that observed for lower irradiation doses also indicates that the highly damaged zone in the layer irradiated at a dose of 1.0 x 10^{16} ions/cm^2 is thicker than that in the layers irradiated at lower doses (see Section 4.5.3).

The resonance lines of the infrared-active TO and LO phonons in the intact sample and the sample irradiated with a dose of 1.0 x 10^{16} ions/cm^2 are shown in **Figure 4.6** (c) and **Figure 4.6** (d), respectively. As shown in **Figure 4.6** (c), at an irradiation dose of 1.0 x 10^{16} ions/cm^2, the mixed A_1 and E_1 symmetry TO phonon mode splits into two different modes. This phonon mode splitting is due to the effect of the stress field on the TO phonon resonance frequency in the highly damaged zone [208]. Thus, at an irradiation dose of 1.0 x 10^{16} ions/cm^2, the highly damaged zone becomes thick enough to be detected in IR spectroscopy. The comparison between the resonance lines of the LO phonon modes in the irradiated layer and the intact 4H-SiC substrate demonstrates, as for the layers irradiated at lower doses, irradiation-induced additional free carriers whose collective vibrational mode couples with the LO phonon mode. The cross-plane and in-plane thermal diffusion length in the sample irradiated with a proton dose of 2.0 x 10^{16} ions/cm^2 are shown in **Figure 4.7** (a) and **Figure 4.7** (b), respectively, for nine different modulation frequencies. The very pronounced drop of $L_{th,z}^2$ for moderate modulation frequencies and the strong decrease of $\alpha_{//}$ when the thermal wave reaches the

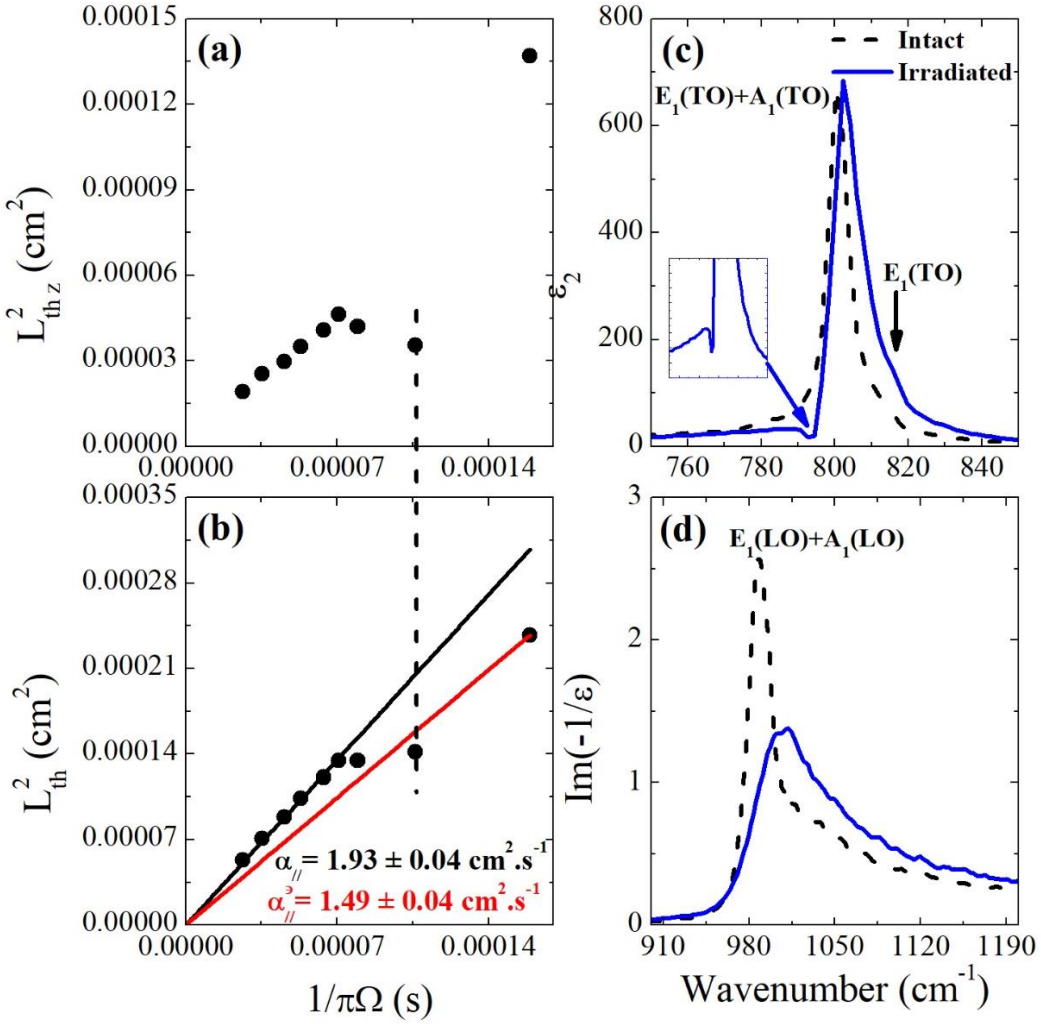

Figure 4.7 *Infrared analysis of 4H-SiC substrate irradiated with protons at 3MeV with a dose of 2.0 x 10^{16} H^+ ions/cm^2. (a) Square of cross-plane thermal diffusion length $L^2_{th,z}$ vs. the inverse of the heating beam modulation frequency. (b) Square of in-plane thermal diffusion length L^2_{th} vs. the inverse of the heating beam modulation frequency. The slopes of the straight line passing through origin that best fit the data points give the in-plane thermal diffusivity for high and low heating beam modulation frequencies. The uncertainties are determined by the experiment sensitivity and the scatter in the data points. The vertical dashed line is introduced to highlight the fact that $L^2_{th,z}$ and L^2_{th} undergo the strongest deviation from the linear behavior for the same modulation frequency. (c) Imaginary parts of the infrared dielectric functions of intact 4H-SiC and the irradiated sample. (d) Imaginary parts of the inverse of the negative of the dielectric functions of intact 4H-SiC and the irradiated sample.*

highly damaged region indicate that when the proton irradiation dose increases to 2.0 x 10^{16} ions/cm^2, the thickness of the highly damaged zone increases further. The value of $\alpha_{//}$ obtained for high modulation frequencies is very comparable to that of the intact 4H-SiC, indicating that even an extremely high irradiation dose (about one fifth of the dose at which 4H-SiC flakes are exfoliated [209]) does not cause any noticeable damage in the basal plane of the 4H-SiC unit cell. The resonance lines of the infrared-active TO and LO phonons in the intact sample and the sample irradiated with a dose of 2.0 x 10^{16} ions/cm^2 are shown in **Figure 4.7** (c) and **Figure 4.7** (d), respectively. As the irradiation dose increases to 2.0 x 10^{16} ions/cm^2, the splitting of the mixed symmetry TO phonon mode becomes more pronounced, indicating a further increase in the thickness of the highly damaged zone, while the resonance line of the LO phonon continues to reveal irradiation-induced free carriers.

According to the above discussion, proton irradiation induces defects mainly along the axis of the 4H-SiC unit cell. The depth profile of the axial defect density in the irradiated layer can be obtained from the cross-plane thermal diffusion length measured at different modulation frequencies. Let z be the depth of a scattering center (pint defect, dislocation, impurity, etc.). Due to the high damping of the thermal wave generated on the surface by the IR heating beam, it is reasonable to assume that the characteristic thermal wavelength λ_z is equal to the cross-plane thermal diffusion length [195]. The sensitivity of the thermal wave to the scattering center at depth z increases as λ_z increases. For instance, if $\lambda_z \leq z$, the thermal wave is insensitive to the defect as it vanishes before reaching depth z, and if λ_z is slightly larger than z, the thermal wave hardly interacts with the defect at depth z. Nevertheless, if $\lambda_z > 2z$, the thermal wave does not scatter at depth z because of the diffraction limit. Consequently, the most sensitive thermal wave to the scattering center at depth z is the one whose wavelength is equal to 2z. On the other hand, the strength of the thermal wave scattering can be determined from the relative difference between the cross-plane thermal diffusion length in the measured layer and intact 4H-SiC ($\Delta L_{th,z}/L_{th,z}$). Here, $L_{th,z}$ is the cross-plane thermal diffusion length in intact 4H-SiC and $\Delta L_{th,z}$ is the absolute difference between the cross-plane thermal diffusion length in the measured layer and intact 4H-SiC. Thus, the plot of $\Delta L_{th,z}/L_{th,z}$ vs. $L_{th,z}/2$ (which, as mentioned above, is equal to $\lambda_z/2$) provides a measure of the strength of thermal wave scattering as a function of the scattering center depth in the measured layer. In other words, such a plot provides a depth profile of the axial defect distribution in the measured layer.

The plots of $\Delta L_{th,z}/L_{th,z}$ vs. $L_{th,z}/2$ for the irradiated 4H-SiC layers are presented in **Figure 4.8**. These plots show that for low proton irradiation

doses, the highly damaged zone is at approximately 12 µm from the hydrogen-enriched interface between the irradiated and intact 4H-SiC. However, as the proton irradiation dose increases, the heavily damaged zone approaches the hydrogen-enriched interface, which is located at a depth of 60 ± 5 µm. The plots illustrated in **Figure 4.8** also show that, in accordance with the conclusion drawn from the behavior of $L_{th,z}^2$ in the irradiated 4H-SiC layers, the thickness of the highly damaged zone increases as the proton irradiation dose increases.

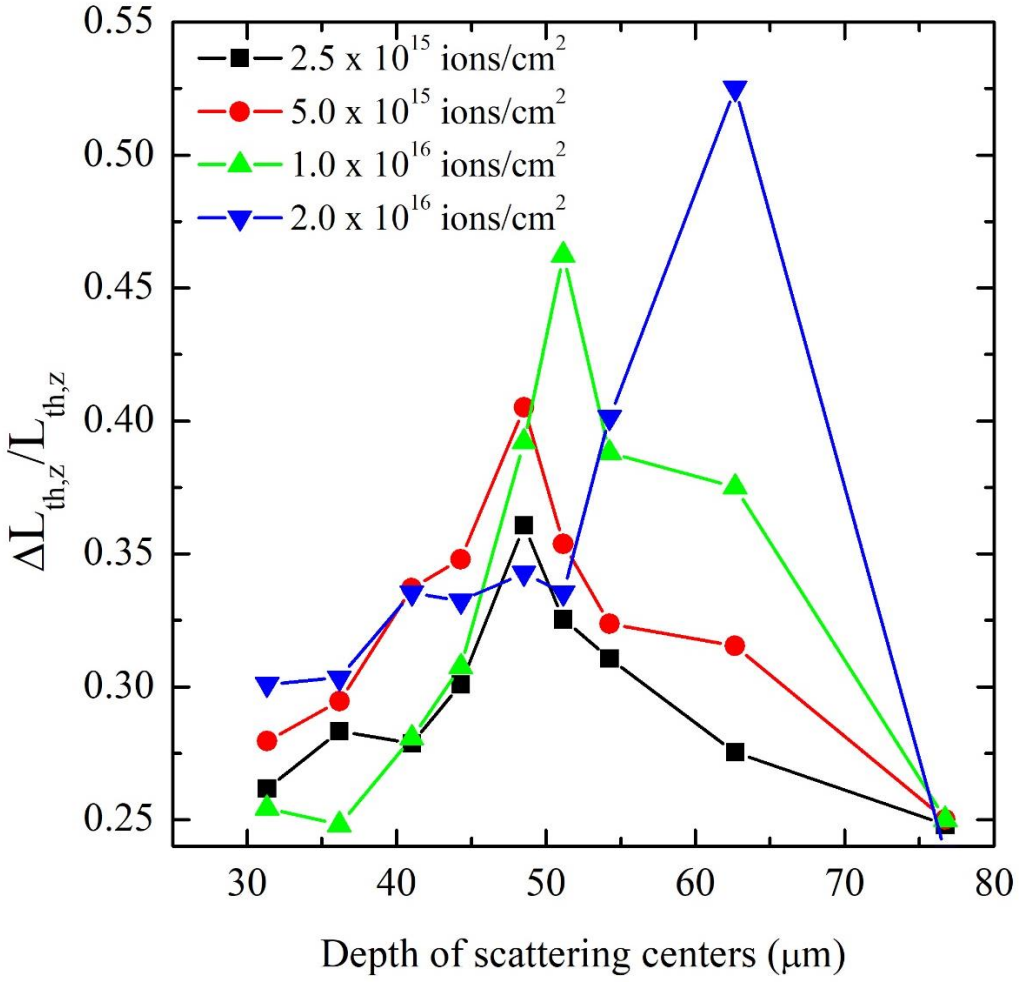

Figure 4.8 *Plots of the relative differences between the cross-plane thermal diffusion lengths in the irradiated 4H-SiC layers investigated in this work and in intact 4H-SiC vs. the half of the cross-plane thermal diffusion length in intact 4H-SiC revealing the depth profiles of the defect density in 4H-SiC substrates irradiated with protons at 3MeV with different irradiation doses.*

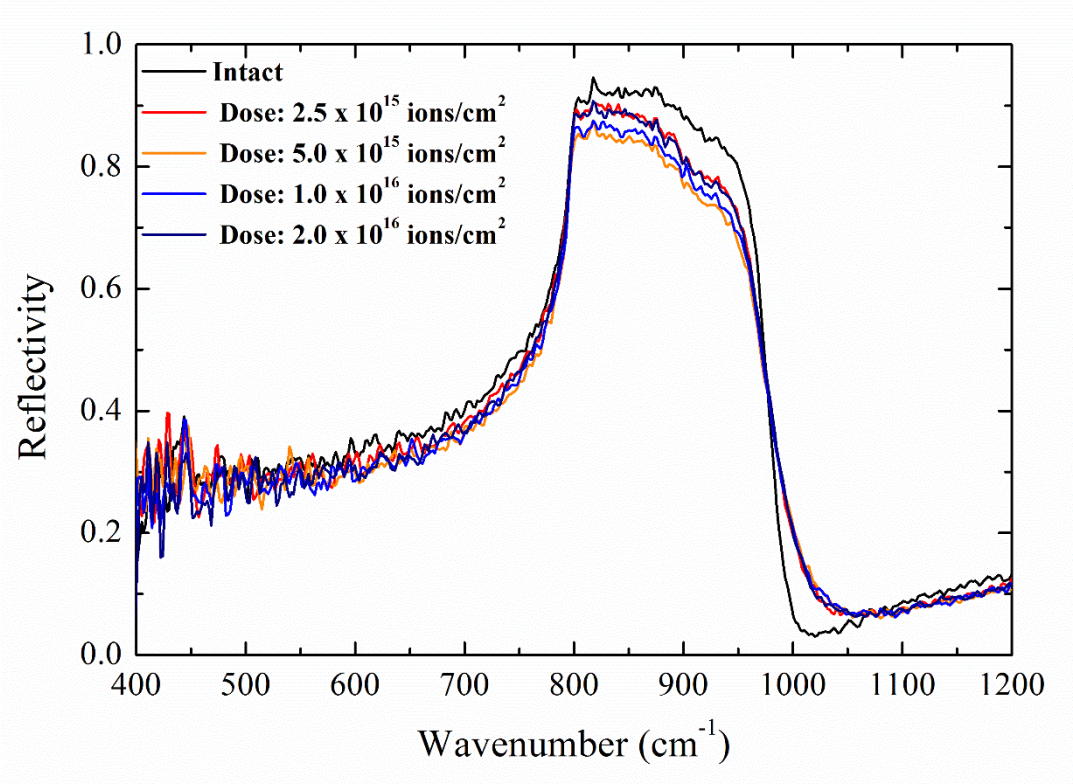

Figure 4.9: *Fourier transform infrared (FTIR) reflectivity spectra of the intact and proton-irradiated 4H-SiC samples. Due to the high absorption coefficient of 4H-SiC for an infrared excitation and the irregularities of the hydrogen-enriched interface between the irradiated and intact 4H-SiC, the interference between the rays reflected from the irradiated 4H-SiC and the rays reflected from the intact 4H-SiC is unlikely. As a result, the recorded IR reflectivity spectra are essentially dictated by phonon and plasmon modes in the irradiated 4H-SiC.*

4.4 CONCLUSION

Directional analysis of thermal diffusivity and depth profiles of defect density in proton-irradiated 4H-SiC substrates is performed using the interaction of thermal waves with irradiation-induced defects and IR spectroscopy. Pulses from a 10.6 µm wavelength CO_2 laser were used to generate thermal waves in 4H-SiC single crystal substrates irradiated with protons at 3MeV with different irradiation doses. The induced temperature gradients on the surfaces were measured using the deflection of a He-Ne laser probe beam due to the mirage effect. The cross-plane and in-plane thermal diffusion lengths in the irradiated

layers were obtained by fitting the measured angular deflection of the probe beam to a model for the mirage effect taking into account the anisotropic thermal properties of 4H-SiC. The variation of the square of the cross-plane thermal diffusion length relative to the inverse of the modulation frequency showed that proton irradiation causes significant damage along the axis of the hexagonal unit cell of 4H-SiC and that the highly damaged zone at which thermal waves scatter the most thickens as the irradiation dose increases. On the other hand, the variation of the square of the in-plane thermal diffusion length relative to the inverse of the modulation frequency showed that proton irradiation causes no noticeable damage in the basal plane of the 4H-SiC hexagonal unit cell and confirmed that the irradiation-induced highly damaged zone thickens as the irradiation dose increases. The effect of the proton irradiation dose on the cross-plane and in-plane thermal diffusivity of 4H-SiC was also deduced. The Kramers-Kronig conversion of the FTIR reflectivity spectra of the samples further confirmed that the thickness of the heavily damaged zone increases with the irradiation dose and showed that proton irradiation induces free carriers that can contribute to heat transport in the plane of the irradiated layer. Finally, the measurement of thermal wave scattering in the irradiated layers is used to generate the depth profile of the defect density in proton-irradiated 4H-SiC for different proton irradiation doses. The results showed that the highly damaged zone thickens and approaches the proton reaching depth as the irradiation dose increases.

4.5 Supplementary Information

4.5.1 Derivation of the probe beam angular deflection (particular case)

In the case where the generated thermal waves are backscattered at the interface between the irradiated and intact 4H-SiC(which is the zone of high concentration of H^+ ions) , the solution of ***Eq. 2.45*** takes the usual form, whereas the solution of ***Eq. 2.46*** takes the form

$$t_1(k,z) = C_1\ sinh(\theta_1 + ik_1 z) \qquad \textbf{\textit{Eq. 4.7}}$$

in the irradiated region (i.e., for $0 < z < a_1$, where a_1 is the thickness of the proton-reaching depth), and the form

$$t_2(k,z) = C_2\ sinh[\theta_2 + ik_2(z - a_1)] \qquad \textbf{\textit{Eq. 4.8}}$$

in the intact zone, where the subscripts 1 and 2 refer to the irradiated and intact 4H-SiC, respectively. The Equations ***Eq. 4.7*** and ***Eq. 4.8*** present solutions to ***Eq. 2.46*** taking into account thermal waves propagating in both the positive and negative z-direction. While the constant C_g in ***Eq. 2.49*** describes the amplitude and phase of the thermal waves propagating in the air and responsible for the deflection of the probe beam, the complex constant θ_1 describes the relative amplitude and phase between the forward-going and the backward-going thermal waves in the irradiated 4H-SiC. Given that the intact 4H-SiC beneath the irradiated 4H-SiC is thermally thick and there is no backward-going thermal waves in it, θ_2 must be infinite. The requirement that the temperature and heat flux be continuous at the interface between the air and the irradiated 4H-SiC results in

$$C_g = C_1 sinh(\theta_1) \qquad \textbf{Eq. 4.9}$$

and

$$\kappa_g k_g C_g + \kappa_{1,z} k_1 C_1 cosh(\theta_1) = 1/2\pi \qquad \textbf{Eq. 4.10}$$

which allows writing the constant C_g as

$$C_g = \frac{i}{2\pi[\kappa_g k_g + \kappa_{1,z} k_1 coth(\theta_1)]} \qquad \textbf{Eq. 4.11}$$

Using the requirement that the temperature and heat flux must be continuous at the interface between the irradiated and intact 4H-SiC, θ_1 in **Eq. 4.11** can be expressed as

$$\theta_1 = ik_1 a_1 - tanh^{-1}\left(\kappa_{1,z} k_1 / \kappa_2 k_2\right) \qquad \textbf{Eq. 4.12}$$

where $\kappa_{1,z}$ and $\kappa_{2,z}$ are the cross-plane thermal conductivities in the irradiated and intact 4H-SiC, respectively.

Using ***Eq. 4.11*** instead of ***Eq. 2.53*** in the theory of the mirage effect, the transverse angular deflection of the probe beam can be written as

$$M'_{trans} = \frac{-i}{\pi}\frac{1}{n}\frac{dn}{dT} e^{-q_g^2 R_2^2/4} \int_0^{+\infty} dk \frac{ksin(kx) e^{ik_g h} e^{-k^2 R_1^2/4}}{\left(\kappa_{1,z} k_1 coth(\theta_1) + \kappa_g k_g\right)} \qquad \textbf{Eq. 4.13}$$

4.5.2 Amplitudes and phases of the transverse photothermal signals obtained from the proton-irradiated samples.

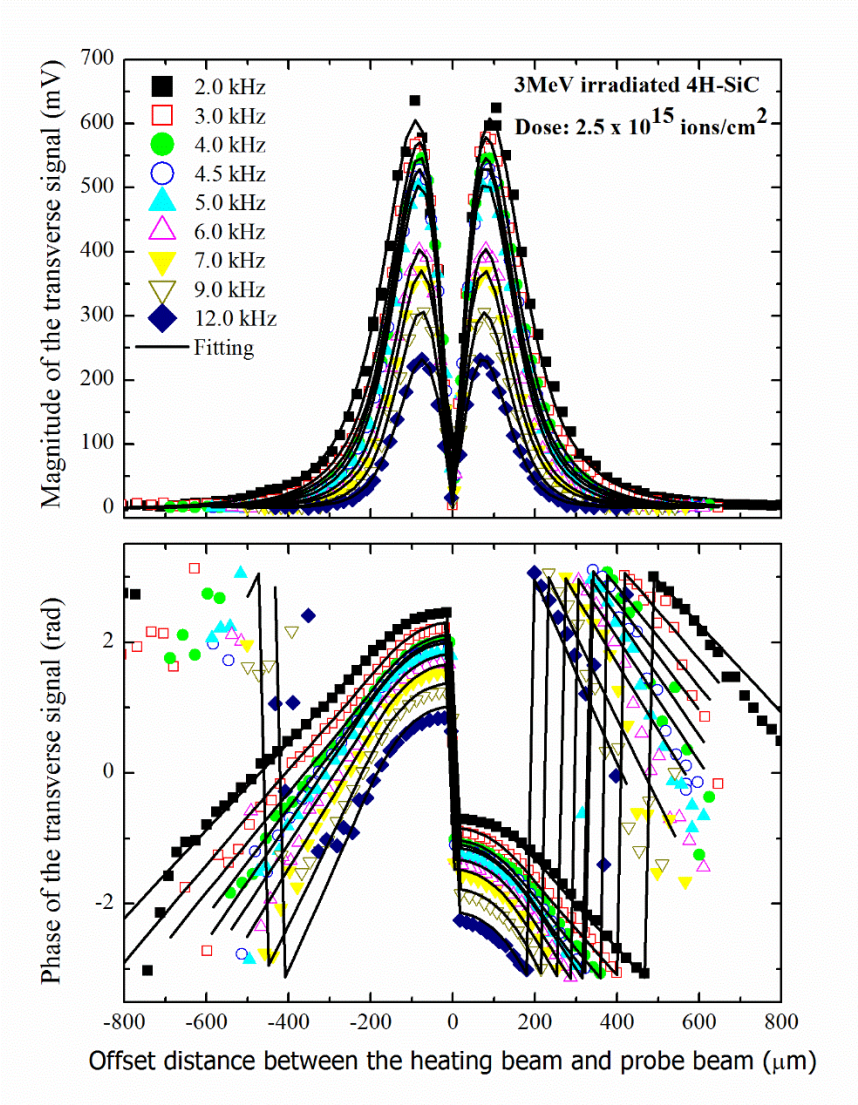

Figure 4.10 : *Magnitudes and phases of transverse photothermal signals from a 4H-SiC substrate irradiated with 3 MeV H^+ ions at a dose of 2.5 x 10^{15} ions/cm^3 relative to the offset distance between the heating beam and probe beam for nine different heating beam modulation frequencies. The experimental data are shown using symbols. The fits of the experimental data to a formalism for the angular deflection of the probe beam due to the mirage effect with taking into account forward-going and backward-going thermal waves are shown by solid lines.*

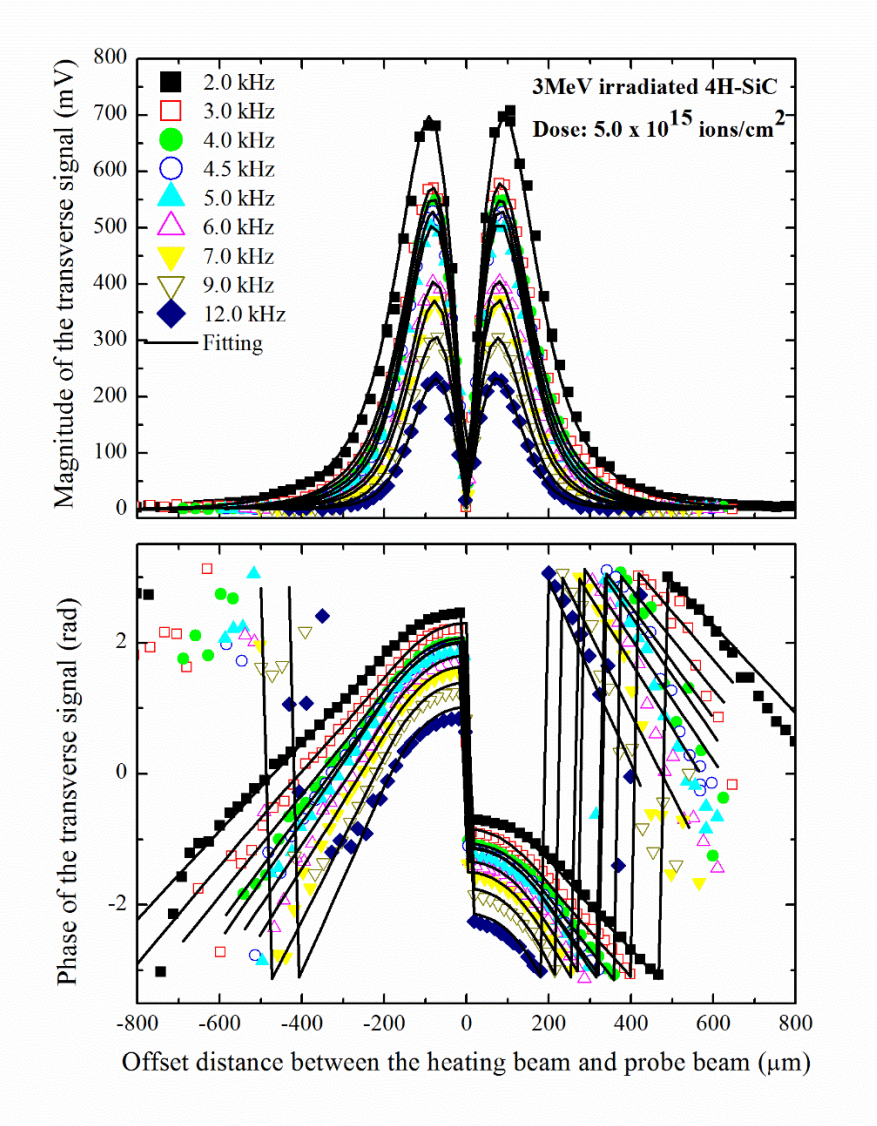

Figure 4.11: *Magnitudes and phases of transverse photothermal signals from a 4H-SiC substrate irradiated with 3 MeV H^+ ions at a dose of 5.0 x 10^{15} ions/cm^3 relative to the offset distance between the heating beam and probe beam for nine different heating beam modulation frequencies. The experimental data are shown using symbols. The fits of the experimental data to a formalism for the angular deflection of the probe beam due to the mirage effect with taking into account forward-going and backward-going thermal waves are shown by solid lines.*

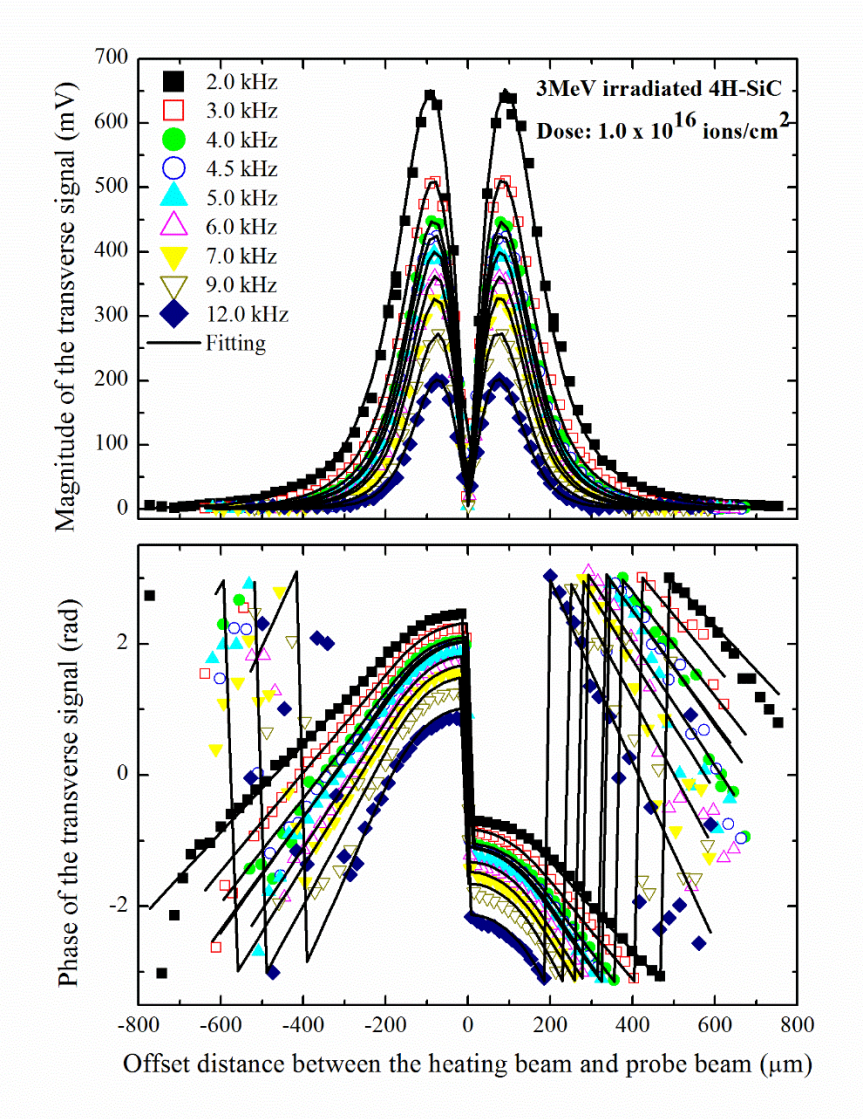

Figure 4.12: *Magnitudes and phases of transverse photothermal signals from a 4H-SiC substrate irradiated with 3 MeV H^+ ions at a dose of 1.0 x 10^{16} ions/cm^3 relative to the offset distance between the heating beam and probe beam for nine different heating beam modulation frequencies. The experimental data are shown using symbols. The fits of the experimental data to a formalism for the angular deflection of the probe beam due to the mirage effect with taking into account forward-going and backward-going thermal waves are shown by solid lines.*

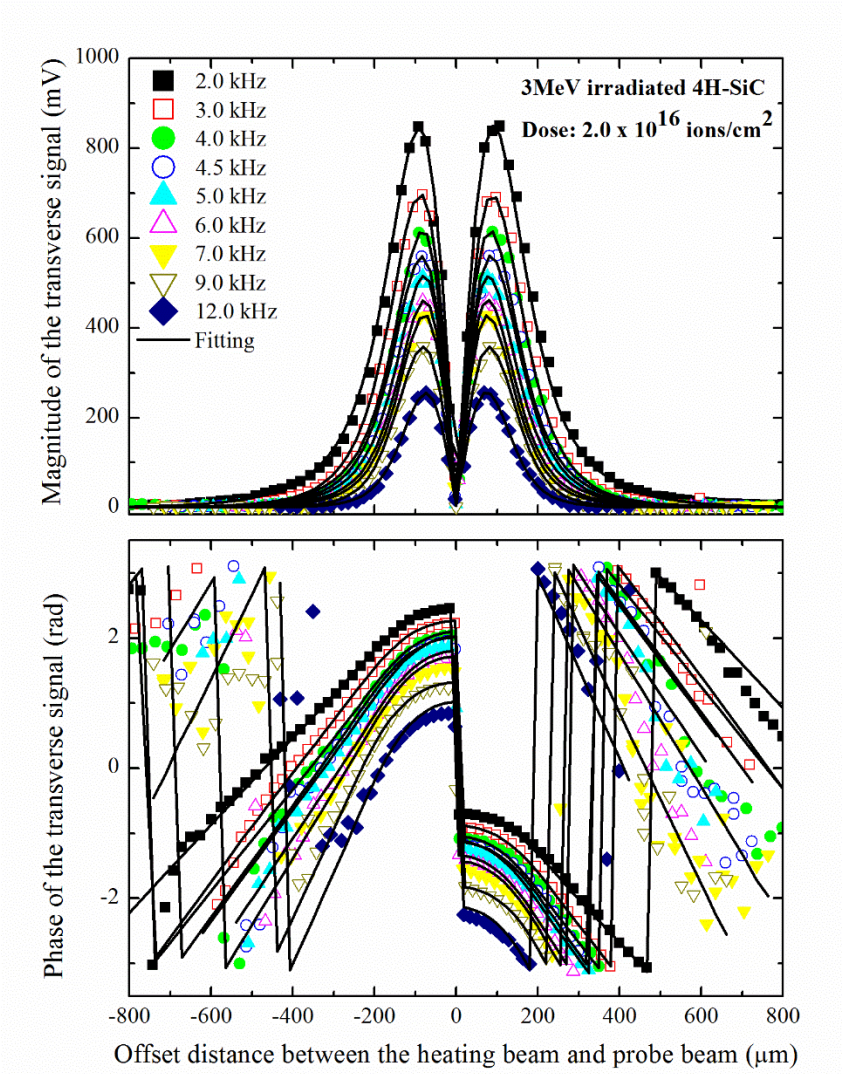

Figure 4.13: *Magnitudes and phases of transverse photothermal signals from a 4H-SiC substrate irradiated with 3 MeV H^+ ions at a dose of 2.0 x 10^{16} ions/cm^3 relative to the offset distance between the heating beam and probe beam for nine different heating beam modulation frequencies. The experimental data are shown using symbols. The fits of the experimental data to a formalism for the angular deflection of the probe beam due to the mirage effect with taking into account forward-going and backward-going thermal waves are shown by solid lines.*

4.5.3 Relationship between the in-plane thermal diffusivity of the highly damaged zone and the overall in-plane thermal diffusivity of the measured 4H-SiC layer

Let $\alpha_{//}$ be the in-plane thermal diffusivity of the 4H-SiC layer measured at high modulation frequencies, i.e., when the thermal wave is extinguished before reaching the highly damaged zone, and $\alpha'_{//}$ the in-plane thermal diffusivity of the 4H-SiC layer measured at low modulation frequencies, i.e., when the thermal wave reaches the highly damaged zone and the measured 4H-SiC layer includes that zone.

Now, consider that measurements are carried out at low modulation frequencies so that the measured 4H-SiC layer includes the highly damaged zone. The total in-plane heat flow rate in the measured layer is thus the sum of the in-plane heat flow rate in the highly damaged zone and the in-plane heat flow rate outside this zone. Since the in-plane heat flow rate is directly proportional to the in-plane thermal diffusivity times the layer thickness, the in-plane thermal diffusivity of the measured layer takes the form:

$$\alpha'_{//} L_{th} = \alpha''_{//} \Delta x + \alpha_{//} (L_{th} - \Delta x) \qquad \textit{Eq. 4.14}$$

where Δx and $\alpha''_{//}$ are the thickness and the in-plane thermal diffusivity of the highly damaged zone, respectively, and $\alpha_{//}$ is the in-plane thermal diffusivity outside the highly damaged zone. The thickness of the measured layer is assumed to be of the order of the thermal diffusion length. ***Eq. 4.14*** can be written in the form:

$$\alpha'_{//} = \alpha_{//} - \left(\alpha_{//} - \alpha''_{//}\right) \frac{\Delta x}{L_{th}} \qquad \textit{Eq. 4.15}$$

Since the thermal diffusivity decreases rapidly as the lattice damage increases [199–203], $\alpha_{//} > \alpha''_{//}$, and thus, according to ***Eq. 4.15***, the in-plane thermal diffusivity for low modulation frequencies $\alpha'_{//}$ is lower than the in-plane thermal diffusivity for high modulation frequencies $\alpha_{//}$. The deviation of $\alpha'_{//}$ from $\alpha_{//}$ increases as the defect density in the highly damaged zone increases and as the thickness of the highly damaged zone increases.

4.5.4 Identification of the symmetries of the 4H-SiC phonons observed in IR spectroscopy

The mode symmetries of the 4H-SiC phonon detected from IR spectroscopy can be identified by noting the following. Group theory predicts at the center of the Brillouin zone of 4H-SiC three Raman- and infrared-active axial optical phonon modes (A_1 symmetry optical phonon modes), three Raman- and infrared-active basal optical phonon modes (E_1 symmetry optical phonon modes), and four unpolarized E_2 symmetry optical phonon modes that are only Raman-active. This is in addition to B_1 symmetry optical phonon modes that are silent in both Raman and infrared spectroscopy [210]. The splitting of the phonon modes into A_1 and E_1 symmetry modes results from the anisotropy of the short-range interatomic forces. On the other hand, the long-range electrostatic forces split these polar phonon modes into transverse and longitudinal modes and raises the frequency of the LO phonon mode over that of the TO phonon mode [211]. In the case of 4H-SiC, the long-range electrostatic forces are the dominant forces. Therefore, at the center of the Brillouin zone, the TO phonon modes belonging to different symmetries group together and the LO phonon modes belonging to different symmetries group together at higher frequencies. Consequently, no interaction occurs between TO and LO phonon modes. However, under certain experimental conditions, phonon modes of mixed A_1 and E_1 symmetry type can be excited and observed in IR or Raman spectra [212]. In unpolarized IR spectroscopic measurements, the electric field splits into two individual components, one parallel and another perpendicular to the plane formed by the incident light and the material optical axis. The former interacts with phonon modes of mixed symmetry, whereas the latter interacts with phonon mode of pure E_1 symmetry [196]. However, in the particular case of SiC polytypes, the infrared-active zone center optical phonon modes are of two kinds, called strong and weak because of their very different IR strength [213]. The strong modes are common to all SiC polytypes, while the frequencies of the weak modes depend on the polytype [214]. Thus, the IR spectrum from 4H-SiC should exhibit signatures from mixed A_1 and E_1 symmetry TO and LO phonons and pure E_1 symmetry TO and LO phonons.

5 Measurement of Thermal diffusivity for thin layers by IR-PBD through SPP

As another application for the developed mid-IR photothermal beam deflection technique, we have measured Thermal diffusivity for thin Layers of amorphous Silicon Carbide (a-SiC) deposited on silicon (Si) substrate.
The reported thermal diffusivity values were quite considerable with respect to the value of the bulk material. The used mid-IR laser excites and launches electromagnetic surface waves, that are highly confined exactly on the surface of these amorphous thin layers.

The mid-IR photothermal beam deflection technique has been extensively described and established as per sections 3.3 and 2.3, and in ref. [5] The in-plane thermal diffusivity was measured by this technique. The experiments show that reducing the a-SiC thin film thickness enhances the interaction between the surface waves propagating on either side of the a-SiC film, leading to a substantial increase of the in-plane thermal diffusivity. The obtained results clearly show that the in-plane thermal diffusivity (due to these induced surface waves) of an a-SiC film of a thickness of a few nanometers is orders of magnitude larger than the thermal diffusivity by phonons in silicon. We think that the obtained results would allow further insights into the physics of electromagnetic waves confined on solid surfaces and provide an efficient way to counter the decrease of thermal transport by phonons due to the bigger rate of phonon-boundary scattering processes in low-dimensional structures.

5.1 INTRODUCTION

Due to technology advancement, there is a constant trend for the miniaturization of electronic component and devices such as lab-on-a-chip. Introduction of mobile devices, Internet of Things, has also contributed to the booming of Integrated nanoelectronics. The size of the electronic components and gates is being scaled down to a length of a few tens of nanometers. Technology industries are pushing for even smaller sizes for these compounds shortly down to a few nanometers. This continuous downsizing and the increase in their operating speeds and switching frequencies would certainly lead to hot spots localized over small areas. These hot spots can cause premature components

failure if left for a long time. Therefore, thermal management in electronic devices has become an increasingly important issue and a hot topic in microelectronics. Many research groups have demonstrated efficient phonon engineering methods for improving the thermal conductivity of dielectric materials for thermoelectric applications [215–218]. But there is still a lack of research tackling heat evacuation from low-dimensional dielectric materials, where classical heat carriers (phonons) suffer from high scattering rates.

Under certain conditions, the interaction of energy-carrying electromagnetic waves with optical phonons in a polar material produces p-polarized surface phonon-polariton (SPP) waves, which are highly confined electromagnetic waves at the material's surfaces [219–222]. In the near-field limit, tunneling of SPP modes between polar dielectrics separated by a vacuum gap of a few microns has showed orders of magnitude increase of thermal radiation [155,222–230]. SPP modes may theoretically transmit heat by conduction, which would answer the industrial demand for extremely efficient heat carriers in materials. SPP modes are insensitive to the classical center of scattering due to their long propagation length, long lifetime, shallow penetration depth, and electromagnetic nature, and hence may carry a high heat flux. Thermal conduction via SPP modes is particularly visible in an ultra-thin polar dielectric film, whereby surface modes on one surface interact with those on the other [231–234]. Furthermore, when the thickness of the polar dielectric layer decreases, the mean-free-path of tiny wave-vectors SPP antisymmetric modes increases dramatically, increasing further the SPP heat flux [231].

Theoretical predictions of efficient thermal conduction via SPP modes in suspended structures have been validated by experimental studies [235–238]. As a result, temperature measurements at surfaces of glass micro-tips provided evidence of SPP carrying energy [236], and thermal excitation of SPP modes followed by direct measurements of thermal conductivity in silicon dioxide (SiO2) nanoparticles beads in various surrounding materials clearly demonstrated significant thermal conduction via SPP modes at temperatures somewhat over room temperature [237]. In terms of planar geometries, recent tests have shown that heat conduction by SPP modes is equally efficient as thermal conduction by vibration modes in suspended silica films with 20 nm of thickness maintained at room temperature [238].

Near-field investigations, on the other hand, have shown that sandwiching a polar dielectric film between two nonpolar mediums with positive dielectric constants, leads to a remarkable confinement of SPP modes with substantial lifetimes at the film's surfaces [239–241]. These highly confined heat-carrying SPP modes with longer lifetime are more efficient in carrying more heat than the SPP modes of suspended polar films. The in-plane thermal diffusivity of such highly confined SPP modes at the surfaces of an

amorphous silicon carbide (a-SiC) film deposited on a silicon (Si) substrate is investigated in this study. We employ a photothermal-beam deflection technique with a mid-IR (MIR) heating source to excite and launch highly confined SPP modes at the surfaces of the a-SiC film, and we quantify the sample's in-plane thermal diffusivity as a function of the a-SiC film thickness at the same time. The thermal diffusivity by SPP modes is affected by the thickness of the a-SiC film (which controls the degree of the interaction between the waves propagating on either side of the a-SiC film).

The use of an amorphous polar dielectric film in this work is advantageous for two reasons. First, it allows for the elimination of thermal transport by phonons and electrons in the film, as well as the observation of SPP modes' contribution to in-plane thermal diffusivity. Second, the solution to the dispersion relations of the SPP modes in amorphous materials ranges from $k=0$ to $k\rightarrow\infty$ (where k is the wave-vector) due to the high damping factor, and unlike crystals, there is no physical reason to exclude any part of it [219]. As a result, despite the broad imaginary parts of the infrared dielectric functions of amorphous materials reducing the lifetimes and mean-free-paths of the SPP modes whose frequencies are close to the vibration resonance frequencies, the large number of SPP modes in amorphous materials allows for a considerable contribution of these modes to in-plane heat transfer.

5.2 EXPERIMENTS

The samples were prepared by pulsed Laser deposition (PLD) with the following conditions:

- A high power KrF excimer Laser operating @ 248nm focused on the target surface with energy = 400mJ.
- The laser pulses are around 20 nanoseconds.
- Repetition rate = 10 Hz.
- Substrate was a commercial Si(100) substrate.
- Vacuum Level around with pulses around 10^{-6} mbar.
- The target used was a high purity SiC polycrystalline target continuously rotating to ensure uniformity of target ablation.
- the Si substrate temperature was kept at 400 °C to ensure amorphous deposited films.

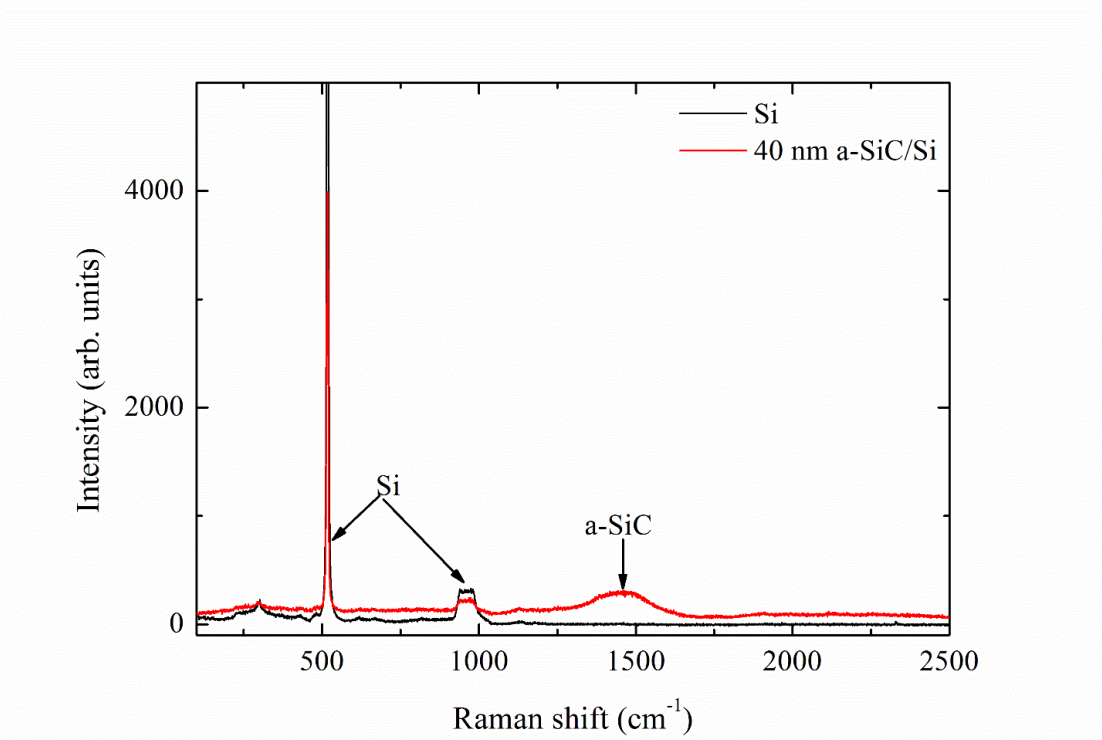

Figure 5.1: *Raman Spectra from a bare silicon substrate and a 40 nm thick amorphous silicon carbide film on a silicon substrate. According to Ref.* [242]*, the stoichiometry ratio in the deposited film is 1:1.*

Three different samples were prepared with deposition times of 5 minutes, 15 minutes, and 40 minutes to obtain a-SiC films on Si, with different thicknesses for the a-SiC Layer. Surface analysis by Atomic force microscopy (AFM) showed that the obtained films were 3 nm, 16 nm, and 40 nm thick. **Figure 5.1** shows the Raman spectrum of the 40 nm thick a-SiC film on Si. The broad peak at 1456 cm^{-1} is a clear signature of amorphous Si_xC_{1-x} with x=0.5 [242].

Using the IR-PBD technique described previously in sections 2.3 and 3.3 and Ref. [5], we measured the in-plane thermal diffusivity of the samples, in order to evaluate the contribution of the electromagnetic surface modes. **Figure 5.2** shows a schematic diagram of the measurement technique similar to ones previously found in **Figure 3.2**, but depicting also the mechanisms of the excitation and the generation of SPP modes on the surface of the measured sample. **Figure 5.2** also shows the deflection of the probe beam due to mirage effect, allowing the detection of the thermal waves generated in the air. As previously stated, a p-polarized 10.6 µm wavelength CO_2 laser beam is focused on the sample surface and modulated by an acousto-optic modulator. In amorphous materials, that correspond to short-correlation structures, the

requirement of total momentum conservation for the interaction between the IR radiations and the polar vibration modes breaks down [243–245]. As a result, regardless of their wave-vectors, vibration modes whose frequencies match those of the incident MIR radiations may absorb a significant portion of the heating beam. The high likelihood of optical absorption allows for significant heating in the a-SiC material, resulting in thermal activation of SPP, Zenneck, and guided modes [246]. The optical absorption of incoming MIR light in the a-SiC layer will be demonstrated later by experimental data. All of these thermally generated electromagnetic surface waves have the potential to contribute to thermal conduction in the measured sample's plane. Moreover, MIR radiations are highly absorbed by the sample surface, which causes a periodic vertical surface displacement in the heated zone [5]. Such a surface-induced localized defect has been shown to be effective in launching surface modes on the measured sample's surface [247].

The modulated heating beam is also used to create fast damped thermal waves in and above the measured sample, in addition to the stimulation and the launch of electromagnetic surface modes. These thermal waves cause periodic temperature and refraction index gradients in the air near the samples surface. At the frequency of the modulation of the heating beam, these gradients are capable of periodically deflecting the probe beam passing closely to the surface. In our experiment, the probe beam is incident at an angle of 1° with respect to the sample surface, and it focuses on the sample surface well before the heating spot. As a result, the angular deviation of the probe beam caused by the mirage effect occurs after the probe beam has been reflected off the sample surface. Consequently, the surface displacement may only contribute to the longitudinal component (along the z-axis) of the probe beam's angular deflection since the heating beam, probe beam, and sample normal are all in the same plane. To prevent contributions from surface movement, we exclude the longitudinal angular deflection and use a four-quadrant photodetector to only capture the transverse component (along the y-axis) of the angular deflection of the probe beam. The above explanation has already been tackled in section 3.4.1 and has demonstrated efficacy in suppressing the effect of surface displacement on the recorded signal [5]. As can be seen in the inset "TOP VIEW" of **Figure 5.2**, the heating beam is scanned along the sample surface in the

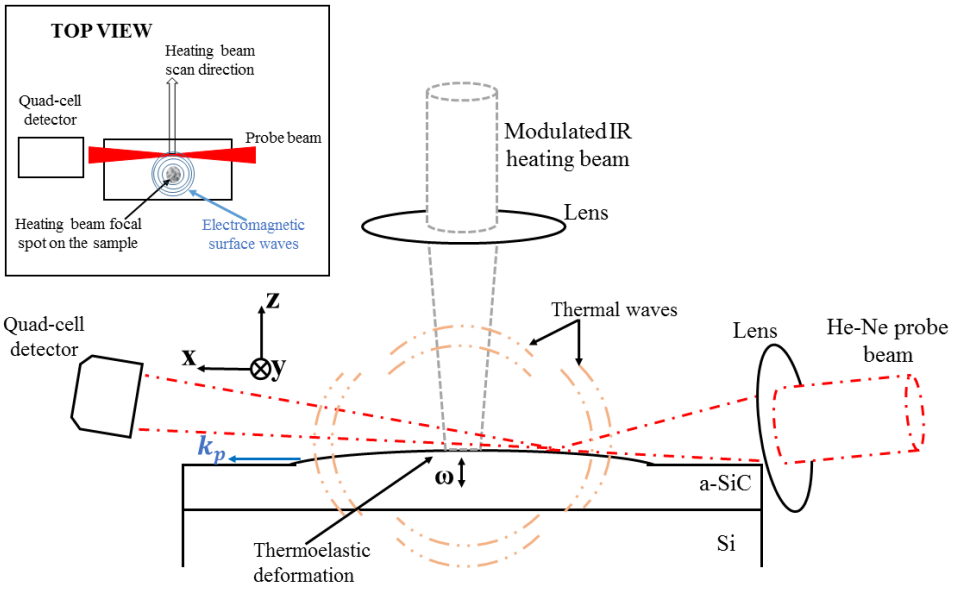

Figure 5.2: *Side view and top view of the experimental setup showing the scattering of electromagnetic surface waves at a thermoelastic deformation of the sample surface, the generation of thermal waves in the air and sample, and the detection of the generated thermal waves using the mirage effect.* k_p *is the wave-vector of the scattered electromagnetic surface modes.*

y-direction, perpendicularly to the probe and the angular deflection of the probe beam is recorded as a function of the offset distance between the heating beam and probe beam, in order to measure the thermal diffusivity. The measurement is repeated for different beam modulation frequencies thus increasing the accuracy of the analysis of the data. The experimental data are fitted to the anisotropic single-layer model for the mirage effect. The above model is accurate in this case as will be shown briefly below. Noting that the generated thermal wave in the air damps rapidly to zero [248]. As such, the thermal wave characteristic wavelength is almost equal to the thermal diffusion length, which is given by:

$$L_{th} = \sqrt{\frac{\alpha_{s,x}}{\pi f}} \qquad \textbf{Eq. 5.1}$$

where $\alpha_{s,x}$ is the in-plane thermal diffusivity of the measured sample, and f is the heating beam modulation frequency.

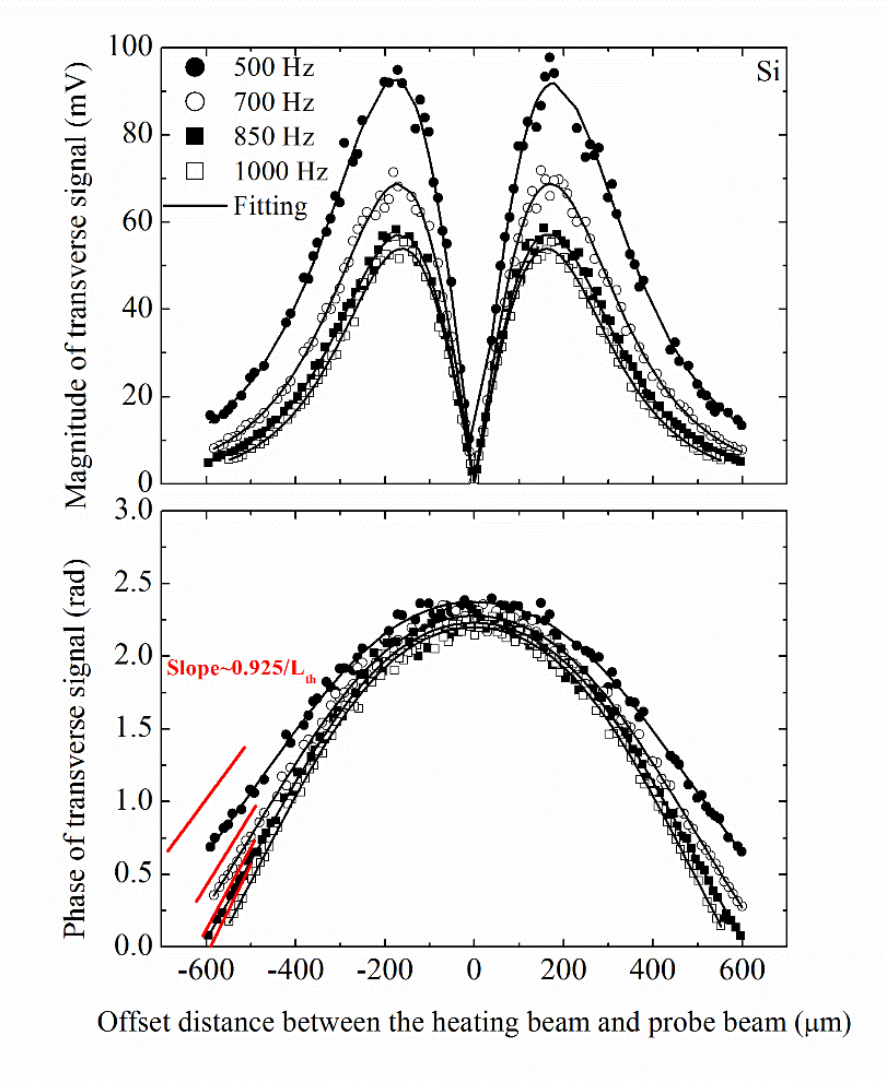

***Figure 5.3**: Magnitude and phase of the transverse signals from a bare silicon substrate relative to the offset distance between the heating beam and probe beam for four different heating beam modulation frequencies. The experimental data are shown using symbols. The fits of the experimental data to an anisotropic theory for the mirage effect are shown using solid lines.*

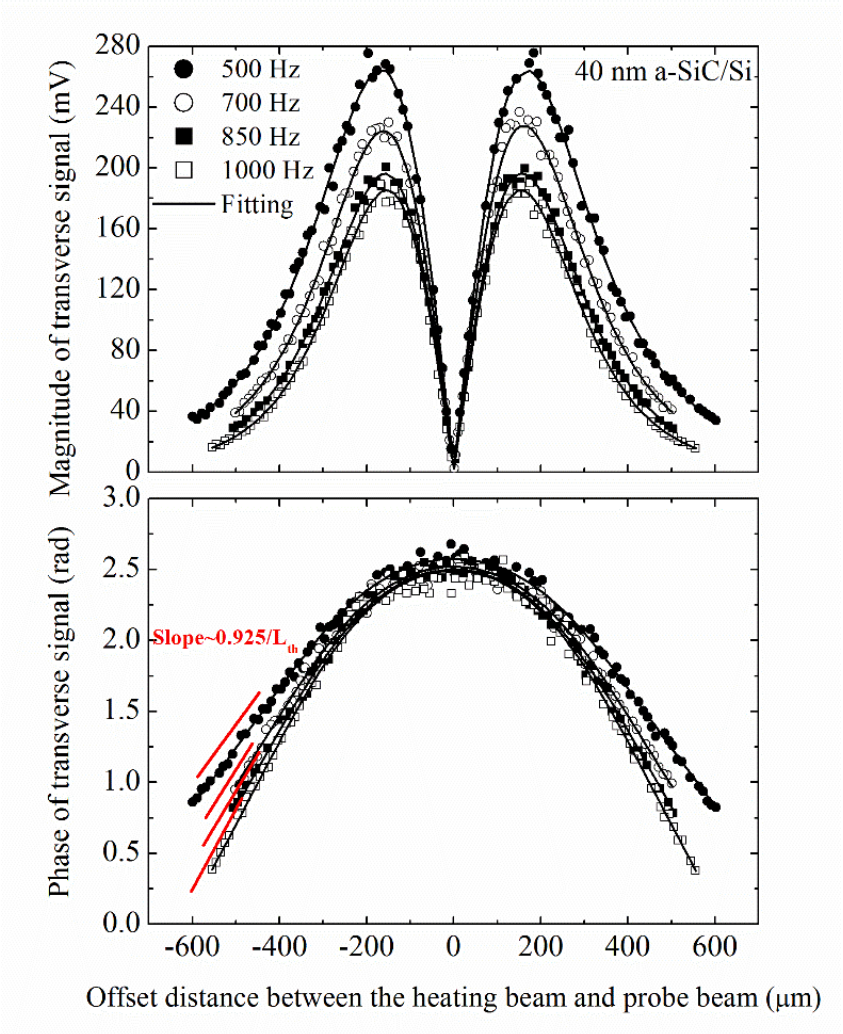

Figure 5.4: *Magnitude and phase of the transverse signals from a 40 nm a-SiC film on Si relative to the offset distance between the heating beam and probe beam for four different heating beam modulation frequencies. The experimental data are shown using symbols. The fits of the experimental data to an anisotropic theory for the mirage effect are shown using solid lines.*

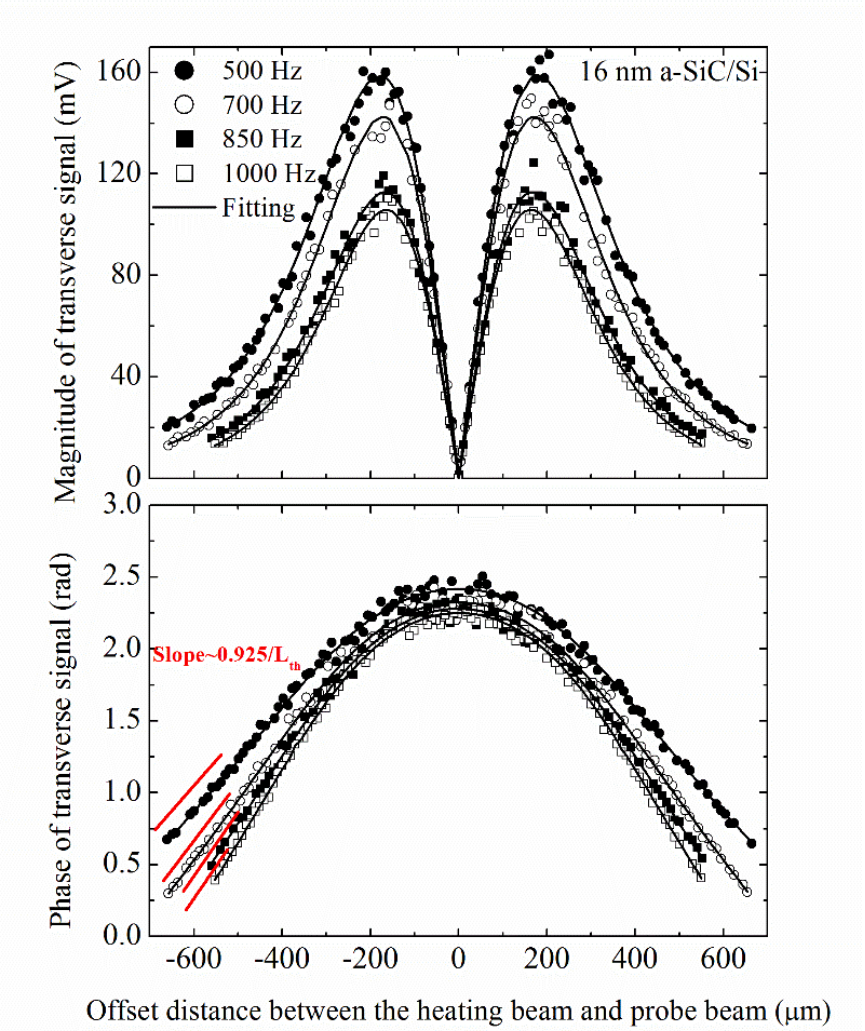

Figure 5.5: *Magnitude and phase of the transverse signals from a 16 nm a-SiC film on Si relative to the offset distance between the heating beam and probe beam for four different heating beam modulation frequencies. The experimental data are shown using symbols. The fits of the experimental data to an anisotropic theory for the mirage effect are shown using solid lines.*

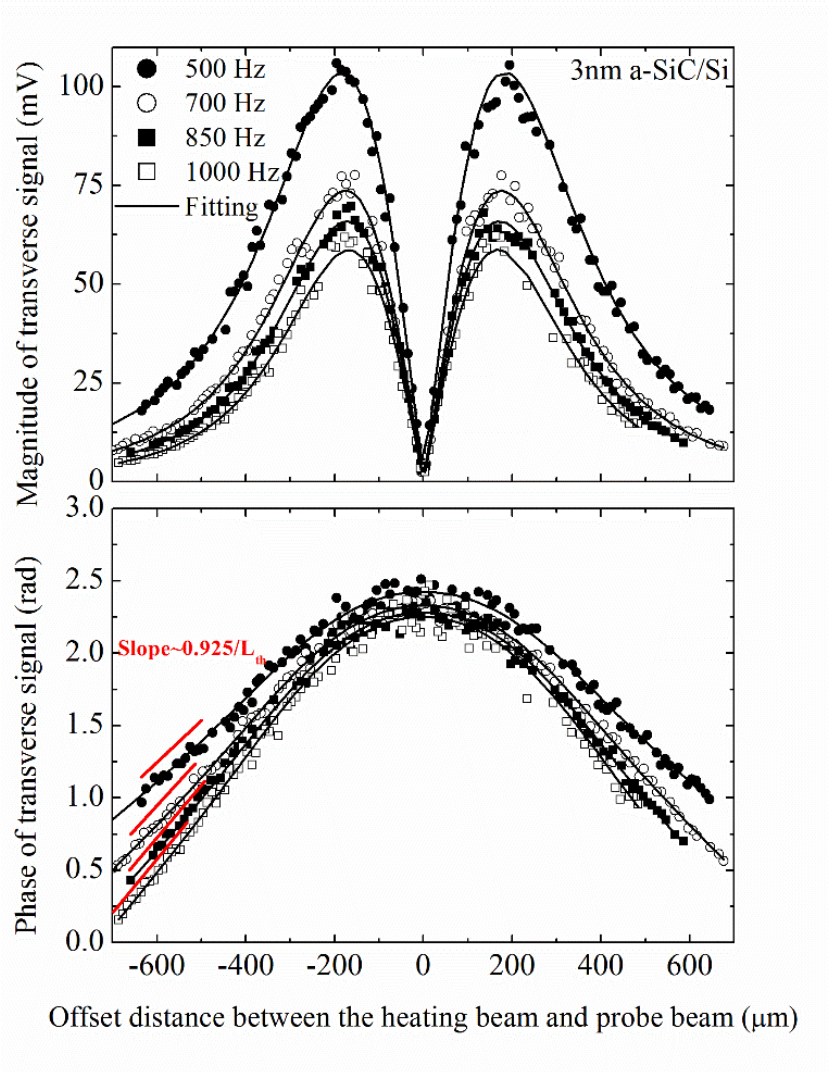

Figure 5.6: *Magnitude and phase of the transverse signals from a 3 nm a-SiC film on Si relative to the offset distance between the heating beam and probe beam for four different heating beam modulation frequencies. The experimental data are shown using symbols. The fits of the experimental data to an anisotropic theory for the mirage effect are shown using solid lines.*

Since, in this measurement, we only modulate the heating beam at frequencies on the order of 0.5 - 1 kHz and typically $\alpha_{s,x}$ is about 1 cm^2/s, the wavelength of the generated thermal wave is estimated to be approximately 150 µm. Given that the thicknesses of the deposited a-SiC films (nanometers) are orders of magnitude less than this value, the thermal wave created is consequently unaffected by the interface between the a-SiC layer and the Si substrate. As a result, the collected data may be described using a single layer model that

ignores thermal wave scattering at interfaces, proving that the above fitting is adequate.

5.3 RESULTS AND DISCUSSION

We present in **Figure 5.3**, **Figure 5.4**, **Figure 5.5**, **Figure 5.6**, the amplitudes and phases of the transverse signals obtained from a bare Si substrate, a 40 nm a-SiC film on Si, a 16 nm a-SiC film on Si, and a 3 nm a-SiC film on Si respectively. This transverse signal is plotted vs. the offset distance between the heating beam and probe beam. The fact that the magnitudes of the signals from the samples with a-SiC films are greater than the magnitudes of the signals from the bare Si substrate implies that a significant portion of the MIR radiations is absorbed and transformed into heat in the a-SiC films, thus proving that electromagnetic surface modes are thermally triggered in the a-SiC films.

The slope of the signal phase provides a precise estimate of the observed sample's in-plane thermal diffusivity. We deposit heat in the irradiated zone at a rate specified by the modulation frequency of the heating beam. The heat then diffuses out from the center, and the peak signal appears later (a more negative signal phase) as the offset distance between the heating beam and probing beam increases. As a result, the slope of the signal phase, the rate of heat transfer in the plane of the sample (i.e., the in-plane thermal diffusivity), and the modulation frequency of the heating beam must have a direct connection. Experiments carried out in reference [153] showed that beyond the heating beam waist, the slope of the signal phase is about $0.925\ \mathrm{rad}/L_{th}$ for optically thin materials, such as Si for optical excitation at a wavelength of 10.6 μm, where the in-plane thermal diffusion length

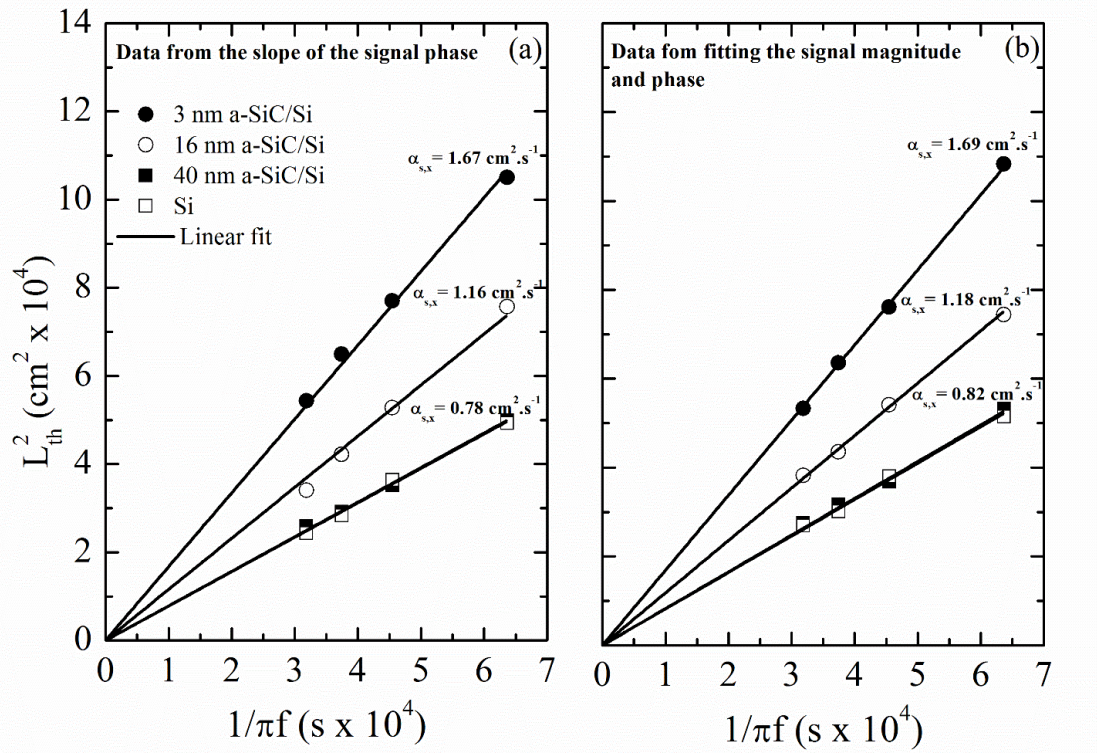

Figure 5.7: *The squares of the in-plane thermal diffusion length in the samples investigated versus* $1/\pi f$*, where f is the heating beam modulation frequency. Each set of data points is fitted to a straight line whose slope is equal to the in-plane thermal diffusivity of the corresponding sample. (a) Data points obtained from the analysis of the slopes of the phases of the measured signals. (b) Data points obtained from fitting the magnitudes and phases of the measured signals to a formalism for the mirage effect accounting for the anisotropy of thermal transport in the measured sample.*

L_{th} is related to the in-plane thermal diffusivity $\alpha_{s,x}$ and the heating beam modulation frequency f according to ***Eq. 5.1***. The slopes of the collected signals enabled us to estimate the in-plane thermal diffusion lengths of the samples measured at the four different modulation frequencies. As shown in **Figure 5.7**(a), we then plotted the squares of the determined thermal diffusion lengths vs $1/\pi f$ for each sample and fitted the data points with straight lines passing through the origin. According to ***Eq. 5.1***, the slopes of these straight lines provide the in-plane thermal diffusivities of the measured samples. The in-plane thermal diffusivity was the same for both the bare Si substrate and the 40 nm thick a-SiC layer on Si. As shown in **Figure 5.7**(a), the

obtained thermal diffusivity value for these two samples matches very well previously published values for Si thermal diffusivity. [137]. However, we noticed that when the thickness of the a-SiC layer is reduced, the in-plane thermal diffusivity of the a-SiC/Si structure increases significantly. In fact, the in-plane thermal diffusivity of the 3nm a-SiC layer on Si is roughly two times more than the thermal diffusivity of Si. These findings show significant enhancement of thermal diffusivity by surface electromagnetic waves and confirm the theoretical assumption that decreasing the thickness of the polar dielectric layer promotes the interaction between the surface electromagnetic waves (SPP) propagating on either side of it, thus enhancing significantly the in-plane thermal diffusivity.

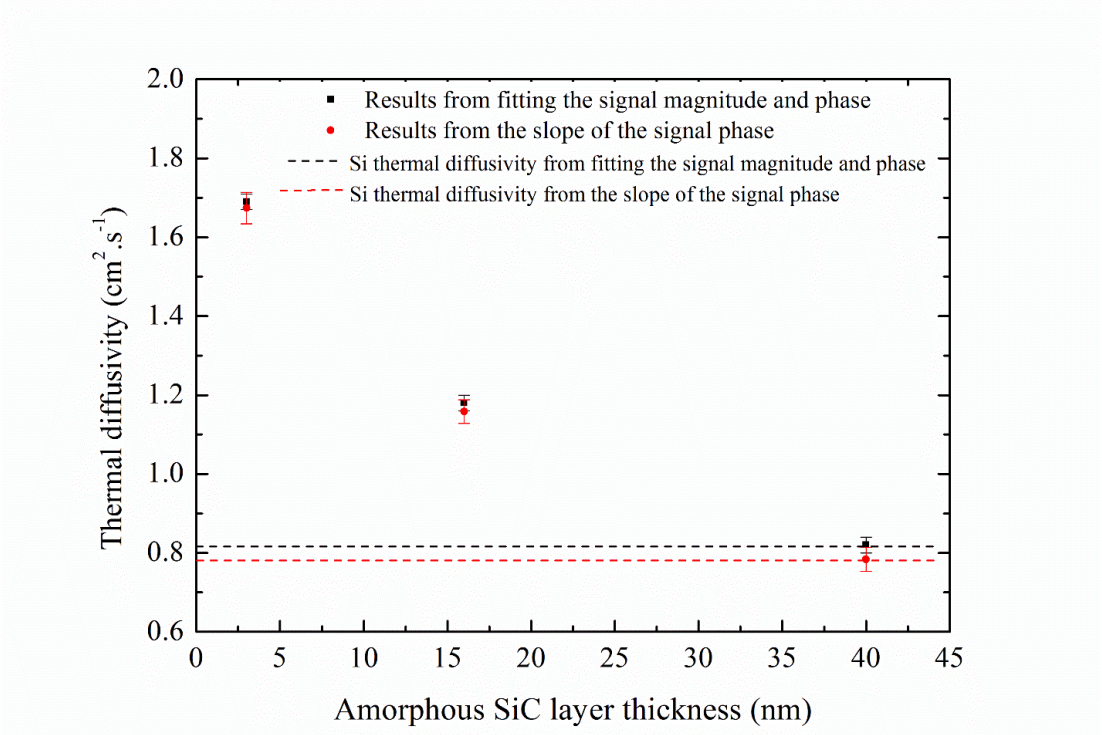

Figure 5.8: *In-plane thermal diffusivity versus the thickness of the a-SiC film as obtained from fitting the experimental data to an anisotropic formalism for the mirage effect and from the analysis of the slopes of the phases of the measured signals. The uncertainties are determined by the scatter in the data points.*

We also calculated the in-plane thermal diffusion lengths of the samples studied at the four modulation frequencies in a second way (besides the previous one employing the thermal diffusion length vs. frequency slope), by fitting the magnitudes and phases of the recorded transverse signals

to a mirage effect model that accounts for anisotropic thermal transport in the investigated medium. When we focus a probe beam at a grazing incidence angle (~1° with the sample surface) on the sample surface, the mirage effect dominates the transverse component of the vector angular deflection (the photo elastic effect due to the heat and the creation of a bump in the sample surface, can be conveniently omitted [5,222]), and we can express the transverse angular deflection as:

$$M_{trans} = \frac{-1}{\pi}\frac{1}{n}\frac{dn}{dT} e^{-q_g^2 R_2^2/4} \int_0^\infty dk \frac{k_g cos(kx) e^{ikgh} e^{-k^2 R_1^2/4}}{(\kappa_{s,z} k_s + \kappa_g k_g)} \qquad \textbf{Eq. 5.2}$$

where the subscript z relates to parameters defined in the cross-plane direction (i.e. perpendicular to the surface), n is the index of refraction of the air, R_1 being the radius of the heating beam spot on the sample surface, R_2 the radius of the probe beam directly above the heated region, h is the height (distance) of the probe beam with respect to the surface, $\kappa_{s,z}$ is the cross-plane thermal conductivity of the sample, and κ_g is the thermal conductivity of the air. The thermal wave-vector in the sample is defined as

$$k_s = \left(q_s^2 - \frac{L_{th}^2}{L_{th,z}^2} k^2\right)^{1/2} \qquad \textbf{Eq. 5.3}$$

It shows the dependence of the transverse deflection on both the cross-plane thermal diffusion length $L_{th,z}$ and the in-plane thermal diffusion length L_{th} [5]. The thermal wavenumber q_s is related the cross-plane thermal diffusion length according to:

$$q_s = (1+i)\left(\frac{1}{L_{th,z}}\right) \qquad \textbf{Eq. 5.4}$$

Similarly, the thermal wave-vector in the air is given by:

$$k_g = \left(q_g^2 - k^2\right)^{1/2} \qquad \textbf{Eq. 5.5}$$

where,

$$q_g = (1+i)\left(\frac{\omega}{2\alpha_g}\right)^{1/2} \qquad \textbf{Eq. 5.6}$$

Here, ω is the angular frequency of modulation, α_g is the thermal diffusivity of the air. In order to reduce the number of adjustable parameters of the model,

the radius of the probe beam R_2 was measured by using the knife-edge method. R_1 can be calculated by using the fact that for the measured heating beam modulation frequencies, the theory of photothermal-beam-deflection predicts that the maximum of the signal magnitude occurs at $r = 1.1 \times R_1$ [194]. Moreover, since electromagnetic surface modes do not contribute to heat transport in the direction perpendicular to the surface, we set the cross-plane thermal diffusion length $L_{th,z}$ equal to the thermal diffusion length of Si at the measured frequency for all of the studied samples. As such we have only 2 adjustable parameters: the height of the probe beam above the surface h, and the in-plane thermal diffusion length L_{th}.

Figure 5.3, **Figure 5.4**, **Figure 5.5**, and **Figure 5.6** show the high quality of the multi-parameter least-squares fits of the magnitudes and phases of the signals measured from the bare Si substrate and from the different samples exhibiting surface waves. **Figure 5.7**(b) shows the squares of the obtained diffusion lengths versus $1/\pi f$. To calculate the in-plane thermal diffusivities of the observed samples, we fitted the data points in **Figure 5.7**(b) with straight lines passing through the origin. We achieved results that were consistent with those obtained from analyzing the slopes of the phases of the measured signals. In **Figure 5.8**, we present the results for the in-plane thermal diffusivities of the measured samples obtained by fitting the experimental data to the mirage effect theory, as well as those obtained by analyzing the slopes of the signal phases. Although the results from the two alternative analytical approaches differed by ~5%, they both reveal a significant increase in the in-plane thermal diffusivity with the decrease of the thickness of the a-SiC layer deposited on Si.

According to the measurement analysis described above, the in-plane thermal diffusivity of the 3 nm thick a-SiC layer on Si is nearly twice that of Si. Because the total in-plane heat flow rate in this sample is the sum of the heat flow rate caused by electromagnetic waves propagating on the surfaces of the a-SiC film $\left(\frac{\Delta Q}{\Delta t}\right]_{EMSW}\right)$, and the heat flow rate caused by phonons in the Si substrate $\left(\frac{\Delta Q}{\Delta t}\right]_{Phonon}\right)$,

we can deduce:

$$\frac{\Delta Q}{\Delta t}\Big]_{EMSW} \approx \frac{\Delta Q}{\Delta t}\Big]_{Phonon} \qquad \textit{Eq. 5.7}$$

We know that the in-plane heat flow rate, is directly proportional to the in-plane thermal diffusivity multiplied by the material thickness. ***Eq. 5.7***

shows that the thermal diffusivity by electromagnetic surface waves in the 3nm thick a-SiC film is orders of magnitude greater than the thermal diffusivity by phonons in Si since the Si substrate is several orders of magnitude thicker. This finding draws a similarity between the tunneling of electromagnetic surface waves between polar dielectrics, which exhibited orders of magnitude increase in thermal radiation in the near-field limit, and the interaction of electromagnetic surface waves propagating on either side of a polar dielectric, which results also in orders of magnitude enhancement in thermal conduction.

5.4 CONCLUSION

We employed a photothermal-beam-deflection approach with a mid-IR source to stimulate and launch highly confined electromagnetic surface modes on the surfaces of a thin a-SiC film deposited on Si, while concurrently measuring the total thermal diffusivity in the structure's plane. Using two distinct methodologies, we examined the experimental data acquired from samples with a-SiC films of varying thicknesses. We discovered that for ultra-thin a-SiC films, the in-plane thermal diffusivity by electromagnetic surface modes becomes prominent and grows rapidly as the a-SiC film thickness decreases. We linked these findings to the fact that decreasing the thickness of the a-SiC film promotes interaction between electromagnetic surface waves propagating on either side of the a-SiC film, which greatly increases thermal diffusivity in the measured sample's plane. We also established a similarity between the significant enhancement of thermal radiation in the near-field limit caused by tunneling of electromagnetic surface waves between polar dielectrics and the large enhancement of thermal conduction caused by an interaction between electromagnetic surface waves propagating on either side of a polar dielectric.

General Conclusion

As a final word,

I have described in this Thesis the developed mid-IR photothermal beam deflection technique, that allowed us to measure in a non-contact manner the thermal diffusivities for different samples. The developed technique does not need any sample treatment whatsoever.

Theoretical background was explored in chapter one.

Chapter two describes non-contact thermal characterization techniques and lays the theoretical foundation for the photothermal beam deflection (Mirage effect) method.

Chapter three developed our particular setup (IR-PBD). The accuracy of the technique was demonstrated through the measurement of samples with readily known sample diffusivities (Si, AlN, α-SiO2). The subsurface imaging capability and subsurface profiling was also demonstrated by imaging defects induced in the volume of a 4H-SiC sample.

Measurement of anisotropic (in-plane and cross-plane) thermal diffusivities was also performed for proton irradiated 4H-SiC samples with different irradiation doses in chapter four.

Finally, ultra-thin layers were investigated in chapter five, showing the capability to launch surface waves and measure the thermal diffusivity of these thin layers.

As a future outlook, the thermal displacement (thermoelastic deformation) of the surface (the bump formation due to the heating pump beam), which was omitted during the measurements (by using only the transverse deflection components), and that would contribute considerably to the longitudinal deflection of the probe beam, should be modelled and introduced in the measurement of the thermal diffusivity. A deconvolution technique would be employed to separate the longitudinal deflection effect due to mirage effect, and that due to the thermoelastic deformation.

Another possible future modification of the technique would be to measure the thermoreflectance by probing the samples through mid-IR. This would allow increased sensitivity for the thermoreflectance measurements (also without the need of the addition of a metallic layer to the samples). The above would be achieved by splitting the mid-IR beam into a pump and probe beam, in a similar approach to what was introduced in Section 2.1.

Furthermore, using special gas or liquid cells, would allow measurement of gas samples for environmental applications, including pollution measurements, and measurement of the purity of solvents or fuels for energy applications.

Another potential application for this photothermal beam deflection technique, would be to use it for ultra-sensitive spectroscopy. In fact, by using special fluids above the sample, and an infrared source of variable wavelength, this would improve the sensitivity of the technique by several orders of magnitude which allows recording infrared absorption for a given wavelength, and thus the whole IR absorption spectra (by varying the wavelength of the heating source).

An additional application would be the measurement of irradiation damage induced by lasers on single or multi-layer anti reflective (AR) coatings deposited as thin films on optical lenses or mirrors, including the localization of these defects.

References

[1] M. Bertolotti and R. Li Voti, *A Note on the History of Photoacoustic, Thermal Lensing, and Photothermal Deflection Techniques*, Journal of Applied Physics.

[2] D. Fournier, A. C. Boccara, and J. Badoz, *Dichroism Measurements in Photoacoustic Spectroscopy*, Appl. Phys. Lett. **32**, 640 (1978).

[3] J. C. Murphy and L. C. Aamodt, *Photothermal Spectroscopy Using Optical Beam Probing: Mirage Effect*, J. Appl. Phys. **51**, 4580 (1980).

[4] A. C. Boccara, W. Jackson, N. M. Amer, and D. Fournier, *Sensitive Photothermal Deflection Technique for Measuring Absorption in Optically Thin Media*, Opt. Lett. **5**, 377 (1980).

[5] J. Younes, Z. Harajli, M. Soueidan, D. Fabrègue, Y. Zaatar, and M. Kazan, *Mid-IR Photothermal Beam Deflection Technique for Fast Measurement of Thermal Diffusivity and Highly Sensitive Subsurface Imaging*, J. Appl. Phys. **127**, 173101 (2020).

[6] E. D. Palik and R. T. Holm, *OPTICAL CHARACTERIZATION OF SEMICONDUCTORS.*, in *NATO Advanced Study Institutes Series, Series B: Physics*, Vol. 46 (Plenum Press, 1979), pp. 315–395.

[7] S. Nakashima and M. Hangyo, *Characterization of Semiconductor Materials by Raman Microprobe*, IEEE J. Quantum Electron. **25**, 965 (1989).

[8] E. Hecht and A. Zajac, *Optics* (Addison-Wesley, Reading, Mass., 1979).

[9] J. S. Blakemore, *Solid State Physics* (Cambridge Univ. Press, Cambridge, 2004).

[10] N. W. M. ASHCROFT N. DAVID., *SOLID STATE PHYSICS.* (CENGAGE LEARNING CUSTOM P, [S.L.], 2020).

[11] C. Kittel, *Introduction to Solid State Physics* (Wiley, New York, 2005).

[12] R. K. Willardson and A. C. Beer, *Semiconductors and Semimetals. Vol. 3, Vol. 3,* (Academic Press, New York; London, 1967).

[13] M. G. Cottam and D. R. Tilley, *Introduction to Surface and Superlattice Excitations* (IoP, Institute of Physics Publishing, Bristol, UK; Philadelphia, PA, 2005).

[14] E. Palik, *Handbook of Optical Constants of Solids* (1998).

[15] J. R. Chelikowsky and M. L. Cohen, *Nonlocal Pseudopotential Calculations for the Electronic Structure of Eleven Diamond and Zinc-Blende Semiconductors*, Phys. Rev. B **14**, 556 (1976).

[16] A. S. Barker, J. L. Merz, and A. C. Gossard, *Study of Zone-Folding Effects on Phonons in Alternating Monolayers of GaAs-AlAs*, Phys. Rev. B **17**, 3181 (1978).

[17] A. P. Flora, A. F. Rex, and S. T. Thornton, *Student Solutions Manual for Thornton & Rex's Modern Physics, Fourth Edition* (Brooks / Cole

Cengage Learning, Boston, MA, 2013).
[18] P. R. Griffiths and J. A. De Haseth, *Fourier Transform Infrared Spectrometry* (Wiley, Hoboken NJ, 2007).
[19] A. A. Christy, Y. Ozaki, and V. G. Gregoriou, *Modern Fourier Transform Infrared Spectroscopy* (Elsevier, Amsterdam, 2001).
[20] B. C. Smith, *Fundamentals of Fourier Transform Infrared Spectroscopy* (2011).
[21] D. A. Long, *Quantitative Spectroscopy: Theory and Practice.Brian C. Smith. Academic Press, Elsevier Science, 2003, Pp. 200*, J. Raman Spectrosc. **36**, 269 (2005).
[22] R. J. Bell, *Introductory Fourier transform spectroscopy* (Acad. Pr., New York, 1974).
[23] J. D. Gaskill, *Linear Systems, Fourier Transforms, and Optics* (Mei Ya, Taipei, 1979).
[24] E. O. Brigham, *The Fast Fourier Transform.* (Prentice-Hall, Englewood Cliffs, N.J., 1974).
[25] R. N. Bracewell, *The Fourier Transform and Its Applications* (McGraw-Hill, Boston, 2000).
[26] M. Tabbal, A. Said, E. Hannoun, and T. Christidis, *Amorphous to Crystalline Phase Transition in Pulsed Laser Deposited Silicon Carbide*, Appl. Surf. Sci. **253**, 7050 (2007).
[27] S. Perkowitz and R. H. Thorland, *Far-Infrared Study of Free Carriers and the Plasmon-Phonon Interaction in CdTe*, Phys. Rev. B **9**, 545 (1974).
[28] O. K. Kim and W. G. Spitzer, *Study of Plasmon—LO-Phonon Coupling in Te-DopedGa1−xAlxAs*, Phys. Rev. B **20**, 3258 (1979).
[29] S. Perkowitz, *Far Infrared Free-Carrier Absorption in n-Type Gallium Arsenide*, J. Phys. Chem. Solids **32**, 2267 (1971).
[30] R. N. Zitter and K. As'Saadi, *Far Infrared Optical Properties of Free Carriers in GaAs*, J. Phys. Chem. Solids **35**, 1593 (1974).
[31] S. Perkowitz and J. Breecher, *Far Infrared Reflectivity and Electron Scattering in GaAs*, in *International Conference on Submillimeter Waves and Their Applications, ICSWA 1974* (Institute of Electrical and Electronics Engineers Inc., 1974), pp. 193–194.
[32] V. Gopal, *Millimetric and Far-Infrared Conductivity of p-Si: A Case for Frequency-Dependent Carrier Relaxation Time*, Infrared Phys. **19**, 689 (1979).
[33] V. Gopal, *Infrared Free Carrier Reflectivity of P-Type PbTe*, Infrared Phys. **23**, 183 (1983).
[34] A. Borghesi, C. Chen-Jia, G. Guizzetti, F. Marabelli, L. Nosenzo, E. Reguzzoni, A. Stella, and P. Ostoja, *Infra-Red Properties of Bulk Heavily Doped Silicon*, Nuovo Cim. D **5**, 292 (1985).
[35] D. G. Cahill, W. K. Ford, K. E. Goodson, G. D. Mahan, A. Majumdar, H. J. Maris, R. Merlin, and S. R. Phillpot, *Nanoscale Thermal Transport*, Journal of Applied Physics.

[36] D. G. Cahill, P. V. Braun, G. Chen, D. R. Clarke, S. Fan, K. E. Goodson, P. Keblinski, W. P. King, G. D. Mahan, A. Majumdar, H. J. Maris, S. R. Phillpot, E. Pop, and L. Shi, *Nanoscale Thermal Transport. II. 2003-2012*, Applied Physics Reviews.
[37] D. G. Cahill, K. Goodson, and A. Majumdar, *Thermometry and Thermal Transport in Micro/Nanoscale Solid-State Devices and Structures*, J. Heat Transfer **124**, 223 (2002).
[38] Z. Xu, *Heat Transport in Low-Dimensional Materials: A Review and Perspective*, Theoretical and Applied Mechanics Letters.
[39] C. Shao, X. Yu, N. Yang, Y. Yue, and H. Bao, *A Review of Thermal Transport in Low-Dimensional Materials Under External Perturbation: Effect of Strain, Substrate, and Clustering*, Nanoscale and Microscale Thermophysical Engineering.
[40] Y. Zhao, Y. Cai, L. Zhang, B. Li, G. Zhang, and J. T. L. Thong, *Thermal Transport in 2D Semiconductors—Considerations for Device Applications*, Advanced Functional Materials.
[41] C. A. Paddock and G. L. Eesley, *Transient Thermoreflectance from Thin Metal Films*, J. Appl. Phys. **60**, 285 (1986).
[42] A. J. Schmidt, *PUMP-PROBE THERMOREFLECTANCE*, Annu. Rev. Heat Transf. **16**, 159 (2013).
[43] S. Huxtable, D. G. Cahill, V. Fauconnier, J. O. White, and J. C. Zhao, *Thermal Conductivity Imaging at Micrometre-Scale Resolution for Combinatorial Studies of Materials*, Nat. Mater. **3**, 298 (2004).
[44] A. J. Schmidt, R. Cheaito, and M. Chiesa, *Characterization of Thin Metal Films via Frequency-Domain Thermoreflectance*, J. Appl. Phys. **107**, (2010).
[45] P. E. Hopkins, M. Baraket, E. V. Barnat, T. E. Beechem, S. P. Kearney, J. C. Duda, J. T. Robinson, and S. G. Walton, *Manipulating Thermal Conductance at Metal-Graphene Contacts via Chemical Functionalization*, Nano Lett. **12**, 590 (2012).
[46] J. Yang, E. Ziade, C. Maragliano, R. Crowder, X. Wang, M. Stefancich, M. Chiesa, A. K. Swan, and A. J. Schmidt, *Thermal Conductance Imaging of Graphene Contacts*, J. Appl. Phys. **116**, (2014).
[47] E. Ziade, M. Goni, T. Sato, P. Czubarow, and A. J. Schmidt, *Thermal Conductance of Nanoscale Langmuir-Blodgett Films*, Appl. Phys. Lett. **107**, (2015).
[48] H. Aller, X. Yu, A. J. Gellman, J. A. Malen, and A. J. H. McGaughey, *Thermal Conductance of β-Ga2O3/Metal Interfaces*, in *2018 17th IEEE Intersociety Conference on Thermal and Thermomechanical Phenomena in Electronic Systems (ITherm)* (2018), pp. 567–571.
[49] A. Schmidt, M. Chiesa, X. Chen, and G. Chen, *An Optical Pump-Probe Technique for Measuring the Thermal Conductivity of Liquids*, Rev. Sci. Instrum. **79**, (2008).
[50] Z. Tian, A. Marconnet, and G. Chen, *Enhancing Solid-Liquid Interface Thermal Transport Using Self-Assembled Monolayers*, Appl. Phys.

Lett. **106**, (2015).
[51] J. A. Tomko, D. H. Olson, A. Giri, J. T. Gaskins, B. F. Donovan, S. M. O'Malley, and P. E. Hopkins, *Nanoscale Wetting and Energy Transmission at Solid/Liquid Interfaces*, Langmuir (2019).
[52] P. M. Norris and P. E. Hopkins, *Examining Interfacial Diffuse Phonon Scattering through Transient Thermoreflectance Measurements of Thermal Boundary Conductance*, J. Heat Transfer **131**, 1 (2009).
[53] A. Giri, J. T. Gaskins, B. F. Donovan, C. Szwejkowski, R. J. Warzoha, M. A. Rodriguez, J. Ihlefeld, and P. E. Hopkins, *Mechanisms of Nonequilibrium Electron-Phonon Coupling and Thermal Conductance at Interfaces*, J. Appl. Phys. **117**, (2015).
[54] A. Giri, J. T. Gaskins, B. M. Foley, R. Cheaito, and P. E. Hopkins, *Experimental Evidence of Excited Electron Number Density and Temperature Effects on Electron-Phonon Coupling in Gold Films*, J. Appl. Phys. **117**, (2015).
[55] O. Matsuda, M. C. Larciprete, R. Li Voti, and O. B. Wright, *Fundamentals of Picosecond Laser Ultrasonics*, Ultrasonics **56**, 3 (2015).
[56] G. A. Antonelli, B. Perrin, B. C. Daly, and D. G. Cahill, *Characterization of Mechanical and Thermal Properties Using Ultrafast Optical Metrology*, MRS Bull. **31**, 607 (2006).
[57] P. Jiang, X. Qian, and R. Yang, *Time-Domain Thermoreflectance (TDTR) Measurements of Anisotropic Thermal Conductivity Using a Variable Spot Size Approach*, Rev. Sci. Instrum. **88**, (2017).
[58] G. Pernot, H. Michel, B. Vermeersch, P. Burke, H. Lu, J. M. Rampnoux, S. Dilhaire, Y. Ezzahri, A. Gossard, and A. Shakouri, *Frequency-Dependent Thermal Conductivity in Time Domain Thermoreflectance Analysis of Thin Films*, in *Materials Research Society Symposium Proceedings*, Vol. 1347 (2011), pp. 1–7.
[59] W. S. Capinski and H. J. Maris, *Improved Apparatus for Picosecond Pump-and-Probe Optical Measurements*, Rev. Sci. Instrum. **67**, 2720 (1996).
[60] D. S. Katzer and M. Cardona, *Thermal-Conductivity Measurements of Gaas/Alas Superlattices Using a Picosecond Optical Pump-and-Probe Technique*, Phys. Rev. B - Condens. Matter Mater. Phys. **59**, 8105 (1999).
[61] A. N. Smith, J. L. Hostetler, and P. M. Norris, *Thermal Boundary Resistance Measurements Using a Transient Thermoreflectance Technique*, Microscale Thermophys. Eng. **4**, 51 (2000).
[62] N. Taketoshi, T. Baba, and A. Ono, *Development of a Thermal Diffusivity Measurement System for Metal Thin Films Using a Picosecond Thermoreflectance Technique*, Meas. Sci. Technol. **12**, 2064 (2001).
[63] K. Kang, Y. K. Koh, C. Chiritescu, X. Zheng, and D. G. Cahill, *Two-Tint Pump-Probe Measurements Using a Femtosecond Laser*

Oscillator and Sharp-Edged Optical Filters, Rev. Sci. Instrum. **79**, (2008).

[64] J. Zhu, D. Tang, W. Wang, J. Liu, K. W. Holub, and R. Yang, *Ultrafast Thermoreflectance Techniques for Measuring Thermal Conductivity and Interface Thermal Conductance of Thin Films*, J. Appl. Phys. **108**, (2010).

[65] C. Wei, X. Zheng, D. G. Cahill, and J. C. Zhao, *Invited Article: Micron Resolution Spatially Resolved Measurement of Heat Capacity Using Dual-Frequency Time-Domain Thermoreflectance*, Rev. Sci. Instrum. **84**, (2013).

[66] D. G. Cahill, *Analysis of Heat Flow in Layered Structures for Time-Domain Thermoreflectance*, Rev. Sci. Instrum. **75**, 5119 (2004).

[67] J. L. Braun, C. J. Szwejkowski, A. Giri, and P. E. Hopkins, *On the Steady-State Temperature Rise during Laser Heating of Multilayer Thin Films in Optical Pump–probe Techniques*, J. Heat Transfer **140**, (2018).

[68] Y. K. Koh and D. G. Cahill, *Frequency Dependence of the Thermal Conductivity of Semiconductor Alloys*, Phys. Rev. B - Condens. Matter Mater. Phys. **76**, 075207 (2007).

[69] A. J. Minnich, J. A. Johnson, A. J. Schmidt, K. Esfarjani, M. S. Dresselhaus, K. A. Nelson, and G. Chen, *Thermal Conductivity Spectroscopy Technique to Measure Phonon Mean Free Paths*, Phys. Rev. Lett. **107**, (2011).

[70] K. T. Regner, D. P. Sellan, Z. Su, C. H. Amon, A. J. H. McGaughey, and J. A. Malen, *Broadband Phonon Mean Free Path Contributions to Thermal Conductivity Measured Using Frequency Domain Thermoreflectance*, Nat. Commun. **4**, (2013).

[71] R. B. Wilson and D. G. Cahill, *Anisotropic Failure of Fourier Theory in Time-Domain Thermoreflectance Experiments*, Nat. Commun. **5**, 1 (2014).

[72] A. J. Schmidt, X. Chen, and G. Chen, *Pulse Accumulation, Radial Heat Conduction, and Anisotropic Thermal Conductivity in Pump-Probe Transient Thermoreflectance*, Rev. Sci. Instrum. **79**, (2008).

[73] H. S. Carslaw and J. C. Jaeger, *Conduction of Heat in Solids* (Clarendon Press, Oxford, 1959).

[74] A. Feldman, *Algorithm for Solutions of the Thermal Diffusion Equation in a Stratified Medium with a Modulated Heating Source*, High Temp. Press. **31**, 293 (1999).

[75] J. H. Kim, A. Feldman, and D. Novotny, *Application of the Three Omega Thermal Conductivity Measurement Method to a Film on a Substrate of Finite Thickness*, J. Appl. Phys. **86**, 3959 (1999).

[76] A. J. Schmidt, Optical Characterization of Thermal Transport from the Nanoscale to the Macroscale, Massachusetts Institute of Technology, 2008.

[77] D. Maillet, *Thermal Quadrupoles : Solving the Heat Equation through*

Integral Transforms (Wiley, Chichester; New York, 2000).
[78] L. A. Barragán, J. I. Artigas, R. Alonso, and F. Villuendas, *A Modular, Low-Cost, Digital Signal Processor-Based Lock-in Card for Measuring Optical Attenuation*, Rev. Sci. Instrum. **72**, 247 (2001).
[79] S. Sandell, E. Chávez-Ángel, A. El Sachat, J. He, C. M. Sotomayor Torres, and J. Maire, *Thermoreflectance Techniques and Raman Thermometry for Thermal Property Characterization of Nanostructures*, J. Appl. Phys. **128**, (2020).
[80] S. Sandell, E. Chávez-Ángel, A. El Sachat, J. He, C. M. Sotomayor Torres, and J. Maire, *Erratum: Thermoreflectance Techniques and Raman Thermometry for Thermal Property Characterization of Nanostructures (J. Appl. Phys. (2020) 128 (131101) DOI: 10.1063/5.0020239)*, Journal of Applied Physics.
[81] B. Graczykowski, A. El Sachat, J. S. Reparaz, M. Sledzinska, M. R. Wagner, E. Chavez-Angel, Y. Wu, S. Volz, Y. Wu, F. Alzina, and C. M. Sotomayor Torres, *Thermal Conductivity and Air-Mediated Losses in Periodic Porous Silicon Membranes at High Temperatures*, Nat. Commun. **8**, 1 (2017).
[82] T. Beechem, L. Yates, and S. Graham, *Invited Review Article: Error and Uncertainty in Raman Thermal Conductivity Measurements*, Rev. Sci. Instrum. **86**, 041101 (2015).
[83] T. M. Tritt, *Thermal Conductivity : Theory, Properties, and Applications* (Springer, New York; London, 2011).
[84] C. B. Reyes, *Thermal Wave Measurement of Thermal Diffusivities of Solids.*, (1988).
[85] A. C. Boccara, D. Fournier, and J. Badoz, *Thermo-Optical Spectroscopy: Detection by the "Mirage Effect,"* Appl. Phys. Lett. **36**, 130 (1980).
[86] W. B. Jackson, N. M. Amer, A. C. Boccara, and D. Fournier, *Photothermal Deflection Spectroscopy and Detection*, Appl. Opt. **20**, 1333 (1981).
[87] L. C. Aamodt and J. C. Murphy, *Thermal Effects in Photothermal Spectroscopy and Photothermal Imaging*, J. Appl. Phys. **54**, 581 (1983).
[88] N. G. C. Astrath, L. C. Malacarne, H. S. Bernabe, M. L. Baesso, and C. Jacinto, *Time-Resolved Mirage Method: A Three-Dimensional Theory and Experiments*, J. Appl. Phys. **111**, 93502 (2012).
[89] J. F. Troncoso, P. Aguado-Puente, and J. Kohanoff, *Effect of Intrinsic Defects on the Thermal Conductivity of PbTe from Classical Molecular Dynamics Simulations*, J. Phys. Condens. Matter **32**, (2020).
[90] K. A. Aissa, N. Semmar, A. Achour, Q. Simon, A. Petit, J. Camus, C. Boulmer-Leborgne, and M. A. Djouadi, *Achieving High Thermal Conductivity from AlN Films Deposited by High-Power Impulse Magnetron Sputtering*, J. Phys. D. Appl. Phys. **47**, (2014).
[91] E. Amin-Chalhoub, N. Semmar, L. Coudron, G. Gautier, C. Boulmer-

Leborgne, A. Petit, M. Gaillard, J. Mathias, and E. Millon, *Thermal Conductivity Measurement of Porous Silicon by the Pulsed-Photothermal Method*, J. Phys. D. Appl. Phys. **44**, (2011).

[92] A. A. Balandin, S. Ghosh, W. Bao, I. Calizo, D. Teweldebrhan, F. Miao, and C. N. Lau, *Superior Thermal Conductivity of Single-Layer Graphene*, Nano Lett. **8**, 902 (2008).

[93] H. Malekpour and A. A. Balandin, *Raman-Based Technique for Measuring Thermal Conductivity of Graphene and Related Materials*, Journal of Raman Spectroscopy.

[94] H. Malekpour, K. H. Chang, J. C. Chen, C. Y. Lu, D. L. Nika, K. S. Novoselov, and A. A. Balandin, *Thermal Conductivity of Graphene Laminate*, Nano Lett. **14**, 5155 (2014).

[95] V. Lysenko, S. Perichon, B. Remaki, D. Barbier, and B. Champagnon, *Thermal Conductivity of Thick Meso-Porous Silicon Layers by Micro-Raman Scattering*, J. Appl. Phys. **86**, 6841 (1999).

[96] S. Périchon, V. Lysenko, B. Remaki, D. Barbier, and B. Champagnon, *Measurement of Porous Silicon Thermal Conductivity by Micro-Raman Scattering*, J. Appl. Phys. **86**, 4700 (1999).

[97] T. R. Anthony, W. F. Banholzer, J. F. Fleischer, L. Wei, P. K. Kuo, R. L. Thomas, and R. W. Pryor, *Thermal Diffusivity of Isotopically Enriched C12 Diamond*, Phys. Rev. B **42**, 1104 (1990).

[98] L. Wei, M. Vaudin, C. S. Hwang, G. White, J. Xu, and A. J. Steckl, *Heat Conduction in Silicon Thin Films: Effect of Microstructure*, J. Mater. Res. **10**, 1889 (1995).

[99] N. Taketoshi, T. Baba, E. Schaub, and A. Ono, *Homodyne Detection Technique Using Spontaneously Generated Reference Signal in Picosecond Thermoreflectance Measurements*, Rev. Sci. Instrum. **74**, 5226 (2003).

[100] Y. Zhao, L. Liu, X. Zhao, and M. Lu, *Enhanced Photothermal Lens Using a Photonic Crystal Surface*, Appl. Phys. Lett. **109**, (2016).

[101] A. L. Glazov, V. S. Kalinovskii, and K. L. Muratikov, *Heat Transfer through Soldered and Bonded Joints of Multilayer Semiconductor Devices Studied by Laser Photothermal Beam-Deflection Method*, Int. J. Heat Mass Transf. **120**, 870 (2018).

[102] A. Dhouib, A. Khalfaoui, M. Bouaïcha, and N. Yacoubi, *Investigation of Thermal and Optical Properties on Polysilicon by the Photothermal Deflection Technique*, J. Appl. Phys. **123**, (2018).

[103] W. Dickmann, J. Dickmann, F. F. Bruns, and S. Kroker, *Key Signal Contributions in Photothermal Deflection Spectroscopy*, J. Appl. Phys. **126**, (2019).

[104] A. R. Warrier, T. Sebastian, C. Sudha Kartha, and K. P. Vijayakumar, *Transverse Photothermal Beam Deflection Technique for Determining the Transport Properties of Semiconductor Thin Films*, J. Appl. Phys. **107**, (2010).

[105] A. Mandelis, R. Bleiss, and F. Shimura, *Highly Resolved Separation of*

Carrier- and Thermal-Wave Contributions to Photothermal Signals from Cr-Doped Silicon Using Rate-Window Infrared Radiometry, J. Appl. Phys. **74**, 3431 (1993).

[106] M. E. Rodriguez, A. Mandelis, G. Pan, J. A. Garcia, and Y. Riopel, *Microelectronic Circuit Characterization via Photothermal Radiometry of Scribeline Recombination Lifetime*, Solid. State. Electron. **44**, 703 (2000).

[107] M. Pawlak and M. Maliński, *Minority Carrier Recombination Lifetimes in N-Type CdMgSe Mixed Crystals Measured by Means of the Photothermal Infrared Radiometry*, Opto-Electronics Rev. **22**, 31 (2014).

[108] A. Salnick, A. Mandelis, F. Funak, and C. Jean, *Monitoring of Ion Implantation in Si with Carrier Plasma Waves Using Infrared Photothermal Radiometry*, Appl. Phys. Lett. **71**, 1531 (1997).

[109] A. Mandelis, A. Othonos, C. Christofides, and J. Boussey-Said, *Non-Contacting Measurements of Photocarrier Lifetimes in Bulk- and Polycrystalline Thin-Film Si Photoconductive Devices by Photothermal Radiometry*, J. Appl. Phys. **80**, 5332 (1996).

[110] J. Batista, A. Mandelis, and D. Shaughnessy, *Temperature Dependence of Carrier Mobility in Si Wafers Measured by Infrared Photocarrier Radiometry*, Appl. Phys. Lett. **82**, 4077 (2003).

[111] A. Asano and M. Stutzmann, *Depth Profiling of Defects in A-Si:H by Photothermal Deflection Spectroscopy*, J. Non. Cryst. Solids **137**–**138**, 623 (1991).

[112] W. B. Jackson and N. M. Amer, *Direct Measurement of Gap-State Absorption in Hydrogenated Amorphous Silicon by Photothermal Deflection Spectroscopy*, Phys. Rev. B **25**, 5559 (1982).

[113] U. Zammit, F. Gasparrini, M. Marinelli, R. Pizzoferrato, F. Scudieri, and S. Martellucci, *Surface States Studies in Semiconductors by Photothermal Deflection Spectroscopy*, J. Appl. Phys. **69**, 2577 (1991).

[114] M. Sumiya, S. Ueda, K. Fukuda, Y. Asai, Y. Cho, L. Sang, A. Uedono, T. Sekiguchi, T. Onuma, and T. Honda, *Valence Band Edge Tail States and Band Gap Defect Levels of GaN Bulk and in x Ga1-x N Films Detected by Hard X-Ray Photoemission and Photothermal Deflection Spectroscopy*, Appl. Phys. Express **11**, (2018).

[115] T. Toyama, Y. Seo, T. Konishi, H. Okamoto, R. Morimoto, Y. Nishikawa, and Y. Tsutsumi, *Optical Absorption Spectra of P-Type Tin Monoxide Thin Films around Their Indirect Fundamental Gaps Determined Using Photothermal Deflection Spectroscopy*, Thin Solid Films **555**, 148 (2014).

[116] W. B. Jackson, D. K. Biegelsen, R. J. Nemanich, and J. C. Knights, *Optical Absorption Spectra of Surface or Interface States in Hydrogenated Amorphous Silicon*, Appl. Phys. Lett. **42**, 105 (1983).

[117] A. Khalfaoui, S. Ilahi, M. Abdel-Rahman, M. F. Zia, M. Alduraibi, B. Ilahi, and N. Yacoubi, *Photothermal Deflection Technique*

Investigation of Annealing Temperature and Time Effects on Optical and Thermal Conductivity of V/V2O5 Alternating Layers Structure, Phys. B Condens. Matter **522**, 26 (2017).

[118] D. Becker-Koch, B. Rivkin, F. Paulus, H. Xiang, Y. Dong, Z. Chen, A. A. Bakulin, and Y. Vaynzof, *Probing Charge Transfer States at Organic and Hybrid Internal Interfaces by Photothermal Deflection Spectroscopy*, J. Phys. Condens. Matter **31**, (2019).

[119] M. Sumiya, K. Fukuda, S. Takashima, S. Ueda, T. Onuma, T. Yamaguchi, T. Honda, and A. Uedono, *Structural Disorder and In-Gap States of Mg-Implanted GaN Films Evaluated by Photothermal Deflection Spectroscopy*, J. Cryst. Growth **511**, 15 (2019).

[120] M. Sumiya, K. Fukuda, H. Iwai, T. Yamaguchi, T. Onuma, and T. Honda, *Structural Evaluation of Ions-Implanted GaN Films by Photothermal Deflection Spectroscopy*, AIP Adv. **8**, (2018).

[121] M. Paulraj, S. Ramkumar, K. P. Vijayakumar, C. S. Kartha, P. Magudapathy, K. G. M. Nair, and B. Viswanathan, *Studies on Ar+ Implanted CdS Thin Films Using Photothermal Deflection Technique*, Nucl. Instruments Methods Phys. Res. Sect. B Beam Interact. with Mater. Atoms **222**, 123 (2004).

[122] U. Zammit, M. Marinelli, and R. Pizzoferrato, *Surface States and Buried Interface States Studies in Semiconductors by Photothermal Deflection Spectroscopy*, J. Appl. Phys. **69**, 3286 (1991).

[123] M. A. Proskurnin, D. Korte, O. B. Rogova, D. S. Volkov, and M. Franko, *Photothermal Beam Deflection Spectroscopy for the Determination of Thermal Diffusivity of Soils and Soil Aggregates*, Int. J. Thermophys. **39**, (2018).

[124] S. Ilahi, N. Yacoubi, and F. Genty, *Two-Layer Photo-Thermal Deflection Model to Study the Non-Radiative Recombination Process: Application to Ga0.7In0.3Al 0.23As0.77/GaSb and Al0.3Ga 0.7As0.08Sb0.92/GaSb Laser Structures*, J. Appl. Phys. **113**, (2013).

[125] D. Ferizović, L. K. Hussey, Y. S. Huang, and M. Muñoz, *Determination of the Room Temperature Thermal Conductivity of RuO 2 by the Photothermal Deflection Technique*, Appl. Phys. Lett. **94**, (2009).

[126] E. Buchaca-Domingo, K. Vandewal, Z. Fei, S. E. Watkins, F. H. Scholes, J. H. Bannock, J. C. De Mello, L. J. Richter, D. M. DeLongchamp, A. Amassian, M. Heeney, A. Salleo, and N. Stingelin, *Direct Correlation of Charge Transfer Absorption with Molecular Donor:Acceptor Interfacial Area via Photothermal Deflection Spectroscopy*, J. Am. Chem. Soc. **137**, 5256 (2015).

[127] D. Ben Hlel, M. Bouzidi, N. Sghaier, H. Fitouri, A. Gharbi, B. El Jani, and N. Yacoubi, *Photothermal Deflection Investigation of Thermally Oxidized Mesoporous Silicon*, Optik (Stuttg). **127**, 4261 (2016).

[128] S. D. George, P. Radhakrishnan, N. Nampoori, and G. Vallabhan, *Photothermal Deflection Measurement on Heat Transport in GaAs Epitaxial Layers*, Phys. Rev. B - Condens. Matter Mater. Phys. **68**,

(2003).
[129] A. Heber, M. Selmke, and F. Cichos, *Thermal Diffusivities Studied by Single-Particle Photothermal Deflection Microscopy*, ACS Photonics **4**, 681 (2017).
[130] J. Opsal and A. Rosencwaig, *Thermal and Plasma Wave Depth Profiling in Silicon*, Appl. Phys. Lett. **47**, 498 (1985).
[131] O. Hertzberg, A. Bauer, A. Küderle, M. A. Pleitez, and W. Mäntele, *Depth-Selective Photothermal IR Spectroscopy of Skin: Potential Application for Non-Invasive Glucose Measurement*, Analyst **142**, 495 (2017).
[132] M. Kazan, B. RuffÍ, C. Zgheib, and P. Masri, *Oxygen Behavior in Aluminum Nitride*, J. Appl. Phys. **98**, (2005).
[133] M. Kazan, B. Rufflé, C. Zgheib, and P. Masri, *Phonon Dynamics in AlN Lattice Contaminated by Oxygen*, Diam. Relat. Mater. **15**, 1525 (2006).
[134] M. Shamseddine, M. Kazan, and M. Tabbal, *Model for the Unpolarized Infrared Reflectivity from Uniaxial Polar Materials: Effects of Anisotropy, Free Carriers, and Defects*, Infrared Phys. Technol. **55**, 112 (2012).
[135] S. E. Bialkowski, N. G. C. Astrath, and M. A. Proskurnin, *Photothermal Spectroscopy Methods* (2019).
[136] K. Yamamoto, T. Abe, and S. I. Takasu, *Thermal Diffusivity of Crystalline and Liquid Silicon and an Anomaly at Melting*, Jpn. J. Appl. Phys. **30**, 2423 (1991).
[137] H. R. Shanks, P. D. Maycock, P. H. Sidles, and G. C. Danielson, *Thermal Conductivity of Silicon from 300 to 1400°K*, Phys. Rev. **130**, 1743 (1963).
[138] K. Fujii, M. Tanaka, Y. Nezu, K. Nakayama, H. Fujimoto, P. De Bièvre, and S. Valkiers, *Determination of the Avogadro Constant by Accurate Measurement of the Molar Volume of a Silicon Crystal*, Metrologia **36**, 455 (1999).
[139] M. Kazan, *Application of Houston's Method to the Calculation of the Direction-Dependent Thermal Conductivity in Finite Crystals at Low Temperatures*, J. Heat Transfer **139**, (2017).
[140] J. S. Danel and G. Delapierre, *Quartz: A Material for Microdevices*, J. Micromechanics Microengineering **1**, 187 (1991).
[141] P. Richet, Y. Bottinga, L. Denielou, J. P. Petitet, and C. Tequi, *Thermodynamic Properties of Quartz, Cristobalite and Amorphous SiO2: Drop Calorimetry Measurements between 1000 and 1800 K and a Review from 0 to 2000 K*, Geochim. Cosmochim. Acta **46**, 2639 (1982).
[142] G. A. Slack, *Nonmetallic Crystals with High Thermal Conductivity*, J. Phys. Chem. Solids **34**, 321 (1973).
[143] S. Burghartz and B. Schulz, *Thermophysical Properties of Sapphire, AlN and MgAl2O4 down to 70 K*, J. Nucl. Mater. **212**–**215**, 1065 (1994).

[144] C. J. Glassbrenner and G. A. Slack, *Thermal Conductivity of Silicon and Germanium from 3°K to the Melting Point*, Phys. Rev. **134**, (1964).
[145] C. Jeong, S. Datta, and M. Lundstrom, *Thermal Conductivity of Bulk and Thin-Film Silicon: A Landauer Approach*, J. Appl. Phys. **111**, (2012).
[146] H. Kanamori, N. Fujii, and H. Mizutani, *Thermal Diffusivity Measurement of Rock-Forming Minerals from 300° to 1100°K*, J. Geophys. Res. **73**, 595 (1968).
[147] P. J. Rutkowski and D. Kata, *Thermal Properties of AlN Polycrystals Obtained by Pulse Plasma Sintering Method*, J. Adv. Ceram. **2**, 180 (2013).
[148] F. Hemberger, A. Göbel, and H. P. Ebert, *Determination of the Thermal Diffusivity of Electrically Non-Conductive Solids in the Temperature Range from 80 K to 300 K by Laser-Flash Measurement*, Int. J. Thermophys. **31**, 2187 (2010).
[149] T. Yagi, N. Oka, T. Okabe, N. Taketoshi, T. Baba, and Y. Shigesato, *Effect of Oxygen Impurities on Thermal Diffusivity of AlN Thin Films Deposited by Reactive RF Magnetron Sputtering*, Jpn. J. Appl. Phys. **50**, 11RB01 (2011).
[150] R. B. Dinwiddie, A. J. Whittaker, and D. G. Onn, *Thermal Conductivity, Heat Capacity, and Thermal Diffusivity of Selected Commercial AlN Substrates*, Int. J. Thermophys. **10**, 1075 (1989).
[151] K. Watari, K. Ishizaki, and T. Fujikawa, *Thermal Conduction Mechanism of Aluminium Nitride Ceramics*, J. Mater. Sci. **27**, 2627 (1992).
[152] K. Watari, H. Nakano, K. Urabe, K. Ishizaki, S. Cao, and K. Mori, *Thermal Conductivity of AlN Ceramic with a Very Low Amount of Grain Boundary Phase at 4 to 1000 K*, J. Mater. Res. **17**, 2940 (2002).
[153] M. A. Olmstead, N. M. Amer, S. Kohn, D. Fournier, and A. C. Boccara, *Photothermal Displacement Spectroscopy: An Optical Probe for Solids and Surfaces*, Appl. Phys. A Solids Surfaces **32**, 141 (1983).
[154] H. Karakachian and M. Kazan, *Dependence of Surface Plasmon-Phonon-Polariton in 4 H-SiC on Free Carrier Concentration*, J. Appl. Phys. **121**, (2017).
[155] R. Baltaji and M. Kazan, *Modulating Near-Field Heat Transfer Using Oxygen-Contaminated Piezoelectric Aluminum Nitride Nanomaterials*, J. Appl. Phys. **125**, (2019).
[156] R. W. Gammon and E. D. Palik, *ATTENUATED-TOTAL-REFLECTION SPECTRAL LINEWIDTH: ANALYSIS OF SURFACE-POLARITON DISPERSION RELATIONS AND DAMPING RATES.*, J Opt Soc Am **64**, 350 (1974).
[157] A. De Hoogh, A. Opheij, M. Wulf, N. Rotenberg, and L. Kuipers, *Harmonics Generation by Surface Plasmon Polaritons on Single Nanowires*, ACS Photonics **3**, 1446 (2016).
[158] M. Hadi, J. Younes, M. Soueidan, and M. Kazan, *IR Photothermal and*

Spectroscopic Analysis of Proton-Irradiated 4H-SiC, Infrared Phys. Technol. **118**, 103891 (2021).
[159] M. E. Levinshtein, S. L. Rumyantsev, and M. Shur, *Properties of Advanced Semiconductor Materials : GaN, AlN, InN, BN, SiC, SiGe* (Wiley, New York, 2001).
[160] J. N. Shenoy, J. A. Cooper, and M. R. Melloch, *High-Voltage Double-Implanted Power MOSFET's in 6H-SiC*, IEEE Electron Device Lett. **18**, 93 (1997).
[161] T. Toda, M. Hata, Y. Nomura, Y. Ueda, M. Sawada, and M. Shono, *Operation at 700°C of 6H-SiC UV Sensor Fabricated Using N+ Implantation*, Japanese J. Appl. Physics, Part 2 Lett. **43**, 27 (2004).
[162] R. Madar, *Silicon Carbide in Contention*, Nature **430**, 974 (2004).
[163] T.-H. Lee, S. Bhunia, and M. Mehregany, *Electromechanical Computing at 500°C with Silicon Carbide*, Science (80-.). **329**, 1316 (2010).
[164] C. R. Eddy and D. K. Gaskill, *Silicon Carbide as a Platform for Power Electronics*, Science (80-.). **324**, 1398 (2009).
[165] D. Nakamura, I. Gunjishima, S. Yamaguchi, T. Ito, A. Okamoto, H. Kondo, S. Onda, and K. Takatori, *Ultrahigh-Quality Silicon Carbide Single Crystals*, Nature **430**, 1009 (2004).
[166] L. L. Snead, T. Nozawa, Y. Katoh, T.-S. Byun, S. Kondo, and D. A. Petti, *Handbook of SiC Properties for Fuel Performance Modeling*, J. Nucl. Mater. **371**, 329 (2007).
[167] T. Koyanagi, Y. Katoh, and T. Nozawa, *Design and Strategy for Next-Generation Silicon Carbide Composites for Nuclear Energy*, J. Nucl. Mater. **540**, 152375 (2020).
[168] Y. Katoh and L. L. Snead, *Silicon Carbide and Its Composites for Nuclear Applications – Historical Overview*, J. Nucl. Mater. **526**, 151849 (2019).
[169] A. Chakravorty, B. Singh, H. Jatav, S. Ojha, J. Singh, D. Kanjilal, and D. Kabiraj, *Intense Ionizing Irradiation-Induced Atomic Movement toward Recrystallization in 4H-SiC*, J. Appl. Phys. **128**, 165901 (2020).
[170] X. Wang, H. Zhang, T. Baba, H. Jiang, C. Liu, Y. Guan, O. Elleuch, T. Kuech, D. Morgan, J.-C. Idrobo, P. M. Voyles, and I. Szlufarska, *Radiation-Induced Segregation in a Ceramic*, Nat. Mater. **19**, 992 (2020).
[171] L. B. Bayu Aji, J. B. Wallace, L. Shao, and S. O. Kucheyev, *Non-Monotonic Temperature Dependence of Radiation Defect Dynamics in Silicon Carbide*, Sci. Rep. **6**, 30931 (2016).
[172] A. Boulle and A. Debelle, *Statistical Nature of Atomic Disorder in Irradiated Crystals*, Phys. Rev. Lett. **116**, (2016).
[173] J. B. Wallace, L. B. Bayu Aji, L. Shao, and S. O. Kucheyev, *Time Constant of Defect Relaxation in Ion-Irradiated 3C-SiC*, Appl. Phys. Lett. **106**, 202102 (2015).
[174] Y. R. Lin, C. Y. Ho, C. Y. Hsieh, M. T. Chang, S. C. Lo, F. R. Chen,

and J. J. Kai, *Atomic Configuration of Irradiation-Induced Planar Defects in 3C-SiC*, Appl. Phys. Lett. **104**, 121909 (2014).
[175] L. B. Bayu Aji, J. B. Wallace, and S. O. Kucheyev, *Radiation Defect Dynamics in SiC with Pre-Existing Defects*, J. Appl. Phys. **125**, 235706 (2019).
[176] L. L. Snead, Y. Katoh, T. Koyanagi, and K. Terrani, *Stored Energy Release in Neutron Irradiated Silicon Carbide*, J. Nucl. Mater. **514**, 181 (2019).
[177] L. B. Bayu Aji, E. Stavrou, J. B. Wallace, A. Boulle, A. Debelle, and S. O. Kucheyev, *Comparative Study of Radiation Defect Dynamics in 3C-SiC by X-Ray Diffraction, Raman Scattering, and Ion Channeling*, Appl. Phys. A **125**, (2018).
[178] T. Koyanagi, Y. Katoh, and M. J. Lance, *Raman Spectroscopy of Neutron Irradiated Silicon Carbide: Correlation among Raman Spectra, Swelling, and Irradiation Temperature*, J. Raman Spectrosc. **49**, 1686 (2018).
[179] X. Chen, W. Zhou, X. Zhang, Q. Feng, J. Zheng, X. Liu, B. Tang, J. Li, J. Xue, and S. Peng, *Mechanical Properties of 6H-SiC Irradiated by Neutron and MeV Heavy Ions: A Nanoindentation and Finite Element Method Study*, J. Appl. Phys. **123**, 25104 (2018).
[180] A. Boulle, A. Debelle, J. B. Wallace, L. B. Bayu Aji, and S. O. Kucheyev, *The Amorphization of 3C-SiC Irradiated at Moderately Elevated Temperatures as Revealed by X-Ray Diffraction*, Acta Mater. **140**, 250 (2017).
[181] X. Hu, T. Koyanagi, Y. Katoh, and B. D. Wirth, *Positron Annihilation Spectroscopy Investigation of Vacancy Defects in Neutron-Irradiated3C-SiC*, Phys. Rev. B **95**, (2017).
[182] T. Koyanagi, M. J. Lance, and Y. Katoh, *Quantification of Irradiation Defects in Beta-Silicon Carbide Using Raman Spectroscopy*, Scr. Mater. **125**, 58 (2016).
[183] M. Bruel, *Silicon on Insulator Material Technology*, Electron. Lett. **31**, 1201 (1995).
[184] G. K. Celler and S. Cristoloveanu, *Frontiers of Silicon-on-Insulator*, J. Appl. Phys. **93**, 4955 (2003).
[185] A. Baydin, H. Krzyzanowska, M. Dhanunjaya, S. V. S. Nageswara Rao, J. L. Davidson, L. C. Feldman, and N. H. Tolk, *Depth Dependent Modification of Optical Constants Arising from H+ Implantation in N-Type 4H-SiC Measured Using Coherent Acoustic Phonons*, APL Photonics **1**, 36102 (2016).
[186] X. Wang, Y.-W. Zhang, D. Han, Y.-B. Zhao, Z.-Q. Zhao, and M. Zhang, *Cross-Sectional Investigation of Radiation Damage of 2 MeV Proton-Irradiated Silicon Carbide*, Nucl. Sci. Tech. **29**, (2018).
[187] K. Huang, Q. Jia, T. You, S. Zhang, J. Lin, R. Zhang, M. Zhou, W. Yu, B. Zhang, X. Ou, and X. Wang, *Defect Formation in MeV H + Implanted GaN and 4H-SiC Investigated by Cross-Sectional Raman*

Spectroscopy, Nucl. Instruments Methods Phys. Res. Sect. B Beam Interact. with Mater. Atoms **406**, 656 (2017).
[188] X. Zhang, Q. Li, M. Wang, Z. Zhang, S. Akhmadaliev, S. Zhou, Y. Wu, and B. Guo, *Defects in Hydrogen Implanted SiC*, Nucl. Instruments Methods Phys. Res. Sect. B Beam Interact. with Mater. Atoms **436**, 107 (2018).
[189] J. Woerle, T. Prokscha, A. Hallén, and U. Grossner, *Interaction of Low-Energy Muons with Defect Profiles in Proton-Irradiated Si and 4H - SiC*, Phys. Rev. B **100**, (2019).
[190] N. Daghbouj, B. S. Li, M. Callisti, H. S. Sen, J. Lin, X. Ou, M. Karlik, and T. Polcar, *The Structural Evolution of Light-Ion Implanted 6H-SiC Single Crystal: Comparison of the Effect of Helium and Hydrogen*, Acta Mater. **188**, 609 (2020).
[191] A. Barcz, R. Jakieła, M. Kozubal, J. Dyczewski, and G. K. Celler, *Incorporation of Oxygen in SiC Implanted with Hydrogen*, Nucl. Instruments Methods Phys. Res. Sect. B Beam Interact. with Mater. Atoms **365**, 146 (2015).
[192] J. F. Ziegler, J. P. Biersack, U. Littmark, and H. H. Anderson, *The Stopping and Ranges of Ions in Matter. Vol 1 ; The Stopping and Range of Ions in Solids, by J.F. Ziegler, J.P. Biersack and U. Littmark ... Vol 6 ; Handbook of Range Distributions for Energetic Ions in All Elements, by U. Littmark and J.F. Ziegler. Vo* (Pergamon, New York, 1985).
[193] S. Hamyeh, R. Tauk, P.-M. Adam, and M. Kazan, *Publisher's Note: "Mid-IR Photothermal Measurement of Substantial Heat Transport by Surface Waves of Polar Amorphous Films Supported on Silicon" [J. Appl. Phys. 128, 095105 (2020)]*, J. Appl. Phys. **128**, 139902 (2020).
[194] J. Opsal, A. Rosencwaig, and D. L. Willenborg, *Thermal-Wave Detection and Thin-Film Thickness Measurements with Laser Beam Deflection*, Appl. Opt. **22**, 3169 (1983).
[195] P. K. KUO, L. D. FAVRO, and R. L. THOMAS, *MIRAGE DETECTION OF THERMAL WAVES*, Photothermal Investigations of Solids and Fluids.
[196] M. Kazan, *Crystal Orientation by Unpolarized Infrared Reflectivity Application to Aluminum Nitride*, J. Appl. Phys. **102**, 73532 (2007).
[197] X. Qian, P. Jiang, and R. Yang, *Anisotropic Thermal Conductivity of 4H and 6H Silicon Carbide Measured Using Time-Domain Thermoreflectance*, Mater. Today Phys. **3**, 70 (2017).
[198] N. H. Protik, A. Katre, L. Lindsay, J. Carrete, N. Mingo, and D. Broido, *Phonon Thermal Transport in 2H, 4H and 6H Silicon Carbide from First Principles*, Mater. Today Phys. **1**, 31 (2017).
[199] C. Mion, J. F. Muth, E. A. Preble, and D. Hanser, *Accurate Dependence of Gallium Nitride Thermal Conductivity on Dislocation Density*, Appl. Phys. Lett. **89**, 92123 (2006).
[200] P. Carruthers, *Scattering of Phonons by Elastic Strain Fields and the*

Thermal Resistance of Dislocations, Phys. Rev. **114**, 995 (1959).
[201] Y. Mao, Y. Li, Y. Xiong, and W. Xiao, *Point Defect Effects on the Thermal Conductivity of β-SiC by Molecular Dynamics Simulations*, Comput. Mater. Sci. **152**, 300 (2018).
[202] M. Khafizov, C. Yablinsky, T. R. Allen, and D. H. Hurley, *Measurement of Thermal Conductivity in Proton Irradiated Silicon*, Nucl. Instruments Methods Phys. Res. Sect. B Beam Interact. with Mater. Atoms **325**, 11 (2014).
[203] J.-P. Crocombette and L. Proville, *Thermal Conductivity Degradation Induced by Point Defects in Irradiated Silicon Carbide*, Appl. Phys. Lett. **98**, 191905 (2011).
[204] P. Perlin, J. Camassel, W. Knap, T. Taliercio, J. C. Chervin, T. Suski, I. Grzegory, and S. Porowski, *Investigation of Longitudinal-optical Phonon-plasmon Coupled Modes in Highly Conducting Bulk GaN*, Appl. Phys. Lett. **67**, 2524 (1995).
[205] T. Kozawa, T. Kachi, H. Kano, Y. Taga, M. Hashimoto, N. Koide, and K. Manabe, *Raman Scattering from LO Phonon-plasmon Coupled Modes in Gallium Nitride*, J. Appl. Phys. **75**, 1098 (1994).
[206] A. S. Barker and M. Ilegems, *Infrared Lattice Vibrations and Free-Electron Dispersion in GaN*, Phys. Rev. B **7**, 743 (1973).
[207] R. Kirste, S. Mohn, M. R. Wagner, J. S. Reparaz, and A. Hoffmann, *Phonon Plasmon Interaction in Ternary Group-III-Nitrides*, Appl. Phys. Lett. **101**, 41909 (2012).
[208] M. V. Balois, N. Hayazawa, A. Tarun, S. Kawata, M. Reiche, and O. Moutanabbir, *Direct Optical Mapping of Anisotropic Stresses in Nanowires Using Transverse Optical Phonon Splitting*, Nano Lett. **14**, 3793 (2014).
[209] Q. Jia, K. Huang, T. You, A. Yi, J. Lin, S. Zhang, M. Zhou, B. Zhang, B. Zhang, W. Yu, X. Ou, and X. Wang, *Freestanding Ultrathin Single-Crystalline SiC Substrate by MeV H Ion-Slicing*, Appl. Phys. Lett. **112**, 192102 (2018).
[210] M. Hofmann, A. Zywietz, K. Karch, and F. Bechstedt, *Lattice Dynamics of SiC Polytypes within the Bond-Charge Model*, Phys. Rev. B **50**, 13401 (1994).
[211] R. Loudon, *The Raman Effect in Crystals*, Adv. Phys. **13**, 423 (1964).
[212] L. Bergman, M. Dutta, C. Balkas, R. F. Davis, J. A. Christman, D. Alexson, and R. J. Nemanich, *Raman Analysis of the E1 and A1 Quasi-Longitudinal Optical and Quasi-Transverse Optical Modes in Wurtzite AlN*, J. Appl. Phys. **85**, 3535 (1999).
[213] L. Patrick, *Infrared Absorption in SiC Polytypes*, Phys. Rev. **167**, 809 (1968).
[214] D. W. Feldman, J. H. Parker, W. J. Choyke, and L. Patrick, *Phonon Dispersion Curves by Raman Scattering in SiC, Polytypes3C,4H,6H,15R, And21R*, Phys. Rev. **173**, 787 (1968).
[215] A. I. Boukai, Y. Bunimovich, J. Tahir-Kheli, J.-K. Yu, W. A. Goddard

III, and J. R. Heath, *Silicon Nanowires as Efficient Thermoelectric Materials*, Nature **451**, 168 (2008).
[216] A. I. Hochbaum, R. Chen, R. D. Delgado, W. Liang, E. C. Garnett, M. Najarian, A. Majumdar, and P. Yang, *Enhanced Thermoelectric Performance of Rough Silicon Nanowires*, Nature **451**, 163 (2008).
[217] B. L. Davis and M. I. Hussein, *Nanophononic Metamaterial: Thermal Conductivity Reduction by Local Resonance*, Phys. Rev. Lett. **112**, (2014).
[218] A. Iskandar, A. Gwiazda, Y. Huang, M. Kazan, A. Bruyant, M. Tabbal, and G. Lerondel, *Modification of the Phonon Spectrum of Bulk Si through Surface Nanostructuring*, J. Appl. Phys. **120**, 95106 (2016).
[219] I. Prigogine and S. A. Rice, *Advances in Chemical Physics. Volume XXVII. Aspects of the Study of Surfaces*, (1974).
[220] J. D. Caldwell, L. Lindsay, V. Giannini, I. Vurgaftman, T. L. Reinecke, S. A. Maier, and O. J. Glembocki, *Low-Loss, Infrared and Terahertz Nanophotonics Using Surface Phonon Polaritons*, Nanophotonics **4**, 44 (2015).
[221] C. F. Bohren and D. R. Huffman, *Absorption and Scattering of Light by Small Particles* (Wiley, 1998).
[222] S. Hamyeh, R. Tauk, P. M. Adam, and M. Kazan, *Mid-IR Photothermal Measurement of Substantial Heat Transport by Surface Waves of Polar Amorphous Films Supported on Silicon*, J. Appl. Phys. **128**, 095105 (2020).
[223] M. Francoeur, M. P. Mengüç, and R. Vaillon, *Near-Field Radiative Heat Transfer Enhancement via Surface Phonon Polaritons Coupling in Thin Films*, Appl. Phys. Lett. **93**, 43109 (2008).
[224] K. Joulain, J.-P. Mulet, F. Marquier, R. Carminati, and J.-J. Greffet, *Surface Electromagnetic Waves Thermally Excited: Radiative Heat Transfer, Coherence Properties and Casimir Forces Revisited in the near Field*, Surf. Sci. Rep. **57**, 59 (2005).
[225] S. Inampudi and H. Mosallaei, *Tunable Wideband-Directive Thermal Emission from SiC Surface Using Bundled Graphene Sheets*, Phys. Rev. B **96**, (2017).
[226] Y. Miyoshi, Y. Fukazawa, Y. Amasaka, R. Reckmann, T. Yokoi, K. Ishida, K. Kawahara, H. Ago, and H. Maki, *High-Speed and on-Chip Graphene Blackbody Emitters for Optical Communications by Remote Heat Transfer*, Nat. Commun. **9**, 1279 (2018).
[227] K. Kim, B. Song, V. Fernández-Hurtado, W. Lee, W. Jeong, L. Cui, D. Thompson, J. Feist, M. T. H. Reid, F. J. García-Vidal, J. C. Cuevas, E. Meyhofer, and P. Reddy, *Radiative Heat Transfer in the Extreme near Field*, Nature **528**, 387 (2015).
[228] B. Song, D. Thompson, A. Fiorino, Y. Ganjeh, P. Reddy, and E. Meyhofer, *Radiative Heat Conductances between Dielectric and Metallic Parallel Plates with Nanoscale Gaps*, Nat. Nanotechnol. **11**, 509 (2016).

[229] M. Francoeur, *Near-Field Radiative Transfer: Thermal Radiation, Thermophotovoltaic Power Generation and Optical Characterization*, (2010).
[230] B. Song, Y. Ganjeh, S. Sadat, D. Thompson, A. Fiorino, V. Fernández-Hurtado, J. Feist, F. J. Garcia-Vidal, J. C. Cuevas, P. Reddy, and E. Meyhofer, *Enhancement of Near-Field Radiative Heat Transfer Using Polar Dielectric Thin Films*, Nat. Nanotechnol. **10**, 253 (2015).
[231] D.-Z. A. Chen, A. Narayanaswamy, and G. Chen, *Surface Phonon-Polariton Mediated Thermal Conductivity Enhancement of Amorphous Thin Films*, Phys. Rev. B **72**, (2005).
[232] J. Ordonez-Miranda, L. Tranchant, K. Joulain, Y. Ezzahri, J. Drevillon, and S. Volz, *Thermal Energy Transport in a Surface Phonon-Polariton Crystal*, Phys. Rev. B **93**, (2016).
[233] D. Z. A. Chen and G. Chen, *Heat Flow in Thin Films via Surface Phonon-Polaritons*, Front. Heat Mass Transf. **1**, (2010).
[234] J. Ordonez-Miranda, L. Tranchant, B. Kim, Y. Chalopin, T. Antoni, and S. Volz, *Quantized Thermal Conductance of Nanowires at Room Temperature Due to Zenneck Surface-Phonon Polaritons*, Phys. Rev. Lett. **112**, (2014).
[235] A. M. Hofmeister, J. Dong, and J. M. Branlund, *Thermal Diffusivity of Electrical Insulators at High Temperatures: Evidence for Diffusion of Bulk Phonon-Polaritons at Infrared Frequencies Augmenting Phonon Heat Conduction*, J. Appl. Phys. **115**, 163517 (2014).
[236] L. Tranchant, T. Tokunaga, B. Kim, N. Takama, Y. Chalopin, and S. Volz, *Surface Phonon Polariton Mediated Thermal Conduction of a Micrometric Glass Waveguide*, J. Phys. Conf. Ser. **395**, 12087 (2012).
[237] E. J. Tervo, O. S. Adewuyi, J. S. Hammonds, and B. A. Cola, *High Thermal Conductivity in Polaritonic SiO2 Nanoparticle Beds*, Mater. Horizons **3**, 434 (2016).
[238] L. Tranchant, S. Hamamura, J. Ordonez-Miranda, T. Yabuki, A. Vega-Flick, F. Cervantes-Alvarez, J. J. Alvarado-Gil, S. Volz, and K. Miyazaki, *Two-Dimensional Phonon Polariton Heat Transport*, Nano Lett. **19**, 6924 (2019).
[239] P. Li, X. Yang, T. W. W. Maß, J. Hanss, M. Lewin, A.-K. U. Michel, M. Wuttig, and T. Taubner, *Reversible Optical Switching of Highly Confined Phonon–Polaritons with an Ultrathin Phase-Change Material*, Nat. Mater. **15**, 870 (2016).
[240] A. M. Dubrovkin, B. Qiang, H. N. S. Krishnamoorthy, N. I. Zheludev, and Q. J. Wang, *Ultra-Confined Surface Phonon Polaritons in Molecular Layers of van Der Waals Dielectrics*, Nat. Commun. **9**, 1762 (2018).
[241] A. M. Dubrovkin, B. Qiang, T. Salim, D. Nam, N. I. Zheludev, and Q. J. Wang, *Resonant Nanostructures for Highly Confined and Ultra-Sensitive Surface Phonon-Polaritons*, Nat. Commun. **11**, 1863 (2020).
[242] Y. Inoue, S. Nakashima, A. Mitsuishi, S. Tabata, and S. Tsuboi, *Raman*

Spectra of Amorphous SiC, Solid State Commun. **48**, 1071 (1983).
[243] R. Shuker and R. W. Gammon, *Raman-Scattering Selection-Rule Breaking and the Density of States in Amorphous Materials*, Phys. Rev. Lett. **25**, 222 (1970).
[244] K. K. Tiong, P. M. Amirtharaj, F. H. Pollak, and D. E. Aspnes, *Effects of As+ion Implantation on the Raman Spectra of GaAs: '"Spatial Correlation"' Interpretation*, Appl. Phys. Lett. **44**, 122 (1984).
[245] A. Iskandar, A. Gwiazda, J. Younes, M. Kazan, A. Bruyant, M. Tabbal, and G. Lerondel, *Interaction between Confined Phonons and Photons in Periodic Silicon Resonators*, Phys. Rev. B **97**, (2018).
[246] S. Gluchko, B. Palpant, S. Volz, R. Braive, and T. Antoni, *Thermal Excitation of Broadband and Long-Range Surface Waves on SiO2 Submicron Films*, Appl. Phys. Lett. **110**, 263108 (2017).
[247] S. Dai, Q. Ma, Y. Yang, J. Rosenfeld, M. D. Goldflam, A. McLeod, Z. Sun, T. I. Andersen, Z. Fei, M. Liu, Y. Shao, K. Watanabe, T. Taniguchi, M. Thiemens, F. Keilmann, P. Jarillo-Herrero, M. M. Fogler, and D. N. Basov, *Efficiency of Launching Highly Confined Polaritons by Infrared Light Incident on a Hyperbolic Material*, Nano Lett. **17**, 5285 (2017).
[248] A. Mandelis, *Photoacoustic and Thermal Wave Phenomena in Semiconductors*, (1987).

FOLIO ADMINISTRATIF

THESE DE L'UNIVERSITE DE LYON OPEREE AU SEIN DE L'INSA LYON

NOM : YOUNES DATE de SOUTENANCE :

Prénoms : JOAN

TITRE : Development of an optical setup for measuring heat diffusivity in bi-dimensional systems

NATURE : Doctorat Numéro d'ordre : 2021LYSEI078

Ecole doctorale : ED34 - Matériaux de Lyon

Spécialité : Matériaux

RESUME : Les outils de caractérisation thermique sont essentiels pour une bonne gestion thermique des semi-conducteurs. Cette thèse décrit une technique photo-thermique de déviation de faisceau (sans contact), basée sur l'effet mirage, utilisant un laser moyen IR comme faisceau de pompe, et un laser visible comme faisceau de sonde rasant la surface de l'échantillon.
Le faisceau laser modulé crée un gradient de température au voisinage de la surface de l'échantillon, provoquant ainsi une déviation du faisceau de sonde, synchronisée avec la modulation du faisceau de pompe. Un détecteur de position mesure la déviation du faisceau de sonde grâce à une amplification synchrone à verrouillage.
Pour une fréquence de modulation donnée, la distance pompe-sonde est variée et les déflexions (transversale et longitudinale) du faisceau de sonde, sont enregistrées en fonction de cette distance.
Les mesures sont répétées pour différentes fréquences. Un logiciel spécialisé permet d'obtenir la diffusivité thermique de l'échantillon.
L'utilisation du laser infrarouge permet de mesurer la plupart des types d'échantillons, sans qu'il soit nécessaire de prendre des mesures spéciales ou de déposer une couche métallique sur la surface de l'échantillon, en contraste avec d'autres techniques de caractérisation thermique sans contact.
La technique a été validée sur différents échantillons présentant des diffusivités thermiques connues. Une autre caractéristique unique est la capacité à réaliser une imagerie et un profil de la sous-surface. On a pu imager avec succès des défauts de sous-surface.
Deux autres applications ont également été étudiées :
- Mesure de diffusivités thermiques dans le plan et en travers du plan pour un ensemble d'échantillons (in-plane and cross-plane thermal diffusivity).
- Mesure de la diffusivité thermique pour des couches ultra-minces (jusqu'à 3 nm d'épaisseur), permettant également d'identifier une autre caractéristique pour cette technique: la génération d'ondes de surface qui augmentent considérablement la diffusivité thermique du matériau.

MOTS-CLÉS : Thermal diffusivity, MID-IR photothermal beam deflection, bi-dimensional systems, Optical characterization, ultra-Thin layers Thermal characterization

Laboratoire (s) de recherche : MATEIS (INSA-LYON). Thermal Physics Laboratory (AUB).

Directeur de thèse: Prof. Damien FABRÈGUE

Président de jury :

Composition du jury : Aurélien BRUYANT, Damien FABRÈGUE, Sara NAJEM, Séverine GOMES, Maher SOUEIDAN, Malek Tabbal